Dielectric studies on $MgTiO_3$ based composite ceramics and thin films for microwave applications

A Thesis Submitted to
Indian Institute of Technology Guwahati
for the Degree of

Doctor of Philosophy

By

Susmita Rabha

Under the supervision of

Prof. Pamu Dobbidi

Department of Physics
Indian Institute of Technology Guwahati
Guwahati-781039, Assam, India

August 2022

INDIAN INSTITUTE OF TECHNOLOGY GUWAHATI
Department of Physics
Guwahati – 781039

STATEMENT

The present thesis entitled, "**Dielectric studies on $MgTiO_3$ based composite ceramics and thin films for microwave applications**" has been carried out by me under the supervision of Prof. Pamu Dobiddi, Department of Physics, Indian Institute of Technology Guwahati. This work has not been submitted elsewhere for the award of any degree.

August, 2022

(**Susmita Rabha**)
Department of Physics,
Indian Institute of Technology Guwahati,
Guwahati – 781 039

INDIAN INSTITUTE OF TECHNOLOGY GUWAHATI
Department of Physics
Guwahati – 781039

CERTIFICATE

It is certified that the work described in this thesis, entitled "**Dielectric studies on $MgTiO_3$ based composite ceramics and thin films for microwave applications**", done by Ms. Susmita Rabha, a Ph.D. student of Department of Physics, Indian Institute of Technology Guwahati, for the award of degree of *Doctor of Philosophy* has been carried out under my supervision. This work has not been submitted elsewhere for the award of any degree.

August,2022

Pamu Dobiddi
Professor,
Department of Physics,
Indian Institute of Technology Guwahati
Guwahati – 781 039.

.

Dedicated to my family and Gohonzon

ACKNOWLEDGEMENTS

Years of hard work, consistent effort, and innumerable help and support from the people around me made it possible to complete the thesis work.

First, I express my sincere gratitude to my research supervisor Prof. Pamu Dobiddi for his constant support, guidance, encouragement, advice, and valuable discussions, which helped me to improve my understanding of the subject along with my skills and the successful completion of my thesis work. I must acknowledge him for providing the unconditional freedom to work, think and express whatever I have done in my research work by keeping faith in my capabilities.

I am highly thankful to my doctoral committee members, Prof. S Thota (Chairman), Prof. S. Ravi, Dr. N. Nagarjuna, and Dr. Arun Tej Mallajosyula for their constant support, guidance, and suggestions during my work progress and seminars during my whole Ph.D. period. Their valuable discussions and suggestions helped me to understand the basics of the subject and skills to improve the quality of my research work.

I would like to express my sincere gratitude to Prof. A Perumal, head of the Department of Physics, and former head of the departments, Prof. Subhradeep Ghosh, and Prof. Poulose Poulose, for giving me the opportunity to work in the department and to use departmental facilities. I am also grateful to all the faculty members of the Physics department. I would also like to thank Dr. Sidananda Sarma for his technical assistance and friendly discussions. My special thanks to all scientific officers and staff members in our department, central instruments facility, and center for nanotechnology.

I acknowledge Prof. Roy Paily Palathinkal, and Mrs. S. Josephine for providing the microwave dielectric measurement facility, without their help I would not be able to complete my thesis work.

The financial support for this thesis is provided by the Indian Institute of Technology Guwahati, and the Ministry of Human Resource and Development. Also, I would like to express my heartfelt thanks to Science and Engineering Research Board (SERB)/Department of Science and Technology (DST), New Delhi; Board of Research in Nuclear Sciences (BRNS), Mumbai; Defense Research and Development Organization (DRDO), New Delhi; and Board of Research in Fusion Science & Technology (BRFST), Gandhinagar, Gujarat through research projects for various experimental facilities. The XRD facility provided by DST, New Delhi, through the FIST program [SR/FST/PSII-020/2009] is also acknowledged.

I am also grateful to my seniors Dr. T. Santhosh Kumar, Dr. Mahesh Peddigari, Dr. Anil Kumar C, Dr. Pallabi Gogoi, Dr. Ranjan Kumar Bhuyan, and Dr. Srinivas Pattipaka for sharing their knowledge and useful discussions along with the healthy working environment. I would like to thank my research team members Apurba, Prajna, Shashi Priya, Sunil, Anil, Radhika, Sweety, and all other lab members for always being there whenever it is required and made me feel like family. I would also like to acknowledge my Ph.D. seniors: Sasmita Di, Sanjib bhaiya, Deep bhaiya, Bipul da, Pratap bhaiya from the Department of Physics for their elderly suggestions and support.

I would like to thank my best friends at IIT Guwahati, especially, Dr. Indu Kalpa, Dr. Ranjan, Anupama, Madonna, Himali, Shashi, Ankita, Dhanesh for creating a friendly and homely atmosphere. I would also like to thank my friends from different places: Mamta, Poonam, Nisha, Sristi, Birbai, Biswa, Deepjyoti for their encouraging words and mental support.

Finally, I would like to express my deepest gratitude to my family, especially, my parents (Ahmed Ch. Rabha and Jayanti), brother (Dr. Apurba Kr. Rabha), sisters (Ankita, Mridusmita, Dharitri, Uncles (Bijay Mohan Rabha, Ratneswar Rabha) and Aunties from my maternal and paternal sides and all other family members, who gave blessings, moral support and continuous encouragement.

I would finally like to acknowledge Gohonzon for helping me in creating some value through my work.

Susmita Rabha

Abstract

The development of advanced functional dielectric materials with all requisite properties for upcoming technologies is of great interest as a single dielectric material does not serve the purpose. $MgTiO_3$ (*MTO*) is one of the most extensively studied microwave dielectric ceramics owing to its excellent microwave dielectric properties. In this thesis, extensive studies have been carried out to fabricate $MgTiO_3$-based microwave dielectric composite ceramics and thin films possessing a high dielectric constant for the miniaturization of electronic components, maintaining high-quality factors and near-zero temperature coefficient resonance frequency. The solid-state reaction method and RF magnetron sputtering technique are opted for ceramic powder and thin film preparations, respectively. The ceramic samples and thin films are characterized by X-ray diffraction, Raman spectroscopy, Field effect electron microscopy, atomic force microscopy and UV-visible spectroscopy. Further, dielectric and electrical properties are studied by using LCR meter, RF impedance analyser, Krupka cavity equipped with vector network analyser and Keithley meter. The 0.9 $MgTiO_3$- 0.1$Ba_5Nb_4O_{15}$ composite ceramics exhibited a maximum relative density of 98% as well as suitable dielectric properties: dielectric constant (ε_r) ~20, loss tangent ($tan\delta$) ~ $10^{-4,}$ and quality factor ($Q \times f_o$) = 60,230 GHz at 8.25 GHz with τ_f ~ -5 ppm/^{o}C for microwave resonator. The thickness-dependent structural, microstructural, and dielectric properties of 0.9*MTO*-0.1*BNO* thin films revealed improvement with an increase in film thickness. Further, the 0.96$MgTiO_3$-*0.04*$SrTiO_3$ composite ceramics exhibited the best microwave dielectric properties with moderate quality factor ($Q \times f_0$) ~ 26,154 GHz at 8.08 GHz and better thermal stability ~τ_f ~ 1.76 ppm/K are suitable for microwave communication applications as microwave filters, resonators, etc. The bilayer thin film of MTO and STO (*STMT3*) film exhibited excellent dielectric properties: loss tangent (1.89×10^{-3}) and considerable dielectric constant ~65 at 10 GHz. Furthermore, the 0.7$MgTiO_3$ – 0.3$Ba_{0.5}Sr_{0.5}TiO_3$ composite ceramics exhibited high dielectric permittivity ε_r ~ 57, and quality factor, $Q \times f_0$ = 19,30 GHz at 4.16 GHz and τ_ε ~54% and found to be promising for type -II capacitors in integrated circuits of de-couplers and filters. The bi-layer thin films of *MTO* and *BST*: *MTO/BST* and *BST/MTO* with alternate stacking order showed role of stacking order. As theoretical estimation, *BST/MTO* bilayer exhibited intermediate dielectric constant and loss (27.3 and~10^{-2}) to *BST*, *MTO* monolayer whereas *MTO/BST* showed anomaly attributed to generation of dipoles in the interface of individual layers at 100 kHz. Both *MTO/BST* and *BST/MTO* films exhibited tunable dielectric responses. These findings of

this report provide perspective insight into the design of multilayer structured smart materials.

List of publications

Refereed Journal Publications

1. Rabha, S., Das, A., Gone, S., & Dobbidi, P. (2023). Investigation of dielectric and electric behavior of $MgTiO_3$ and $Ba_{0.5}Sr_{0.5}TiO_3$ bilayer films by RF sputtering method. *Applied Surface Science*, *608*, 154972.
2. Rabha, S., Das, A., Gonne, S., Mohapatra, P. P., Balmuchu, S. P., Radhika, E., & Dobiddi, P. **(2022).** "Dielectric and leakage characteristics of MTO/STO bilayer films deposited by RF magnetron sputtering technique for optical and electronic applications." ***Materials Science and Engineering: B,*** *282*, 115790.
3. Rabha S, Dobbidi P.(**2021**) "Optical and electrical studies on $MgTiO_3$–$Ba_5Nb_4O_{15}$ composite thin films for integrated microwave circuit applications". ***Ceramics International***. *47*(14), 20428-20437.
4. Rabha S, Dobbidi P.(**2021**) "Structural, electrical properties and stability in microwave dielectric properties of (1− *x*) $MgTiO_3$-*x* $SrTiO_3$ composite ceramics". ***Journal of Alloys and Compounds, 872, 159726.***
5. Rabha, S. & Dobbidi, P. (**2019**). Structural, electrical, and dielectric studies on (1− *x*) $MgTiO_3$− *x*$Ba_{0.5}Sr_{0.5}TiO_3$ composite ceramics for type-II capacitor applications. Journal of ***Materials Science: Materials in Electronics***, 30(6), 5327-5341.
6. Rabha, S., & Dobbidi, P. (**2019**). The impact of thickness on the optical, electrical and dielectric properties of nanocrystalline 0.9 MTO-0.1 BNO composite thin films. ***Applied Surface Science***, 489, 831-840.
7. Rabha, S., & Dobbidi, P. (**2019**). Enhanced microwave dielectric and electrical properties of Zn substituted Mg_2TiO_4 ceramics for RF/microwave applications**.** ***Journal of Materials Science: Materials in Electronics***, 30(15), 14600-14610.
8. Rabha, S., Chikkala, A. K., & Dobbidi, P. (**2017**). Structural and dielectric properties of (1-x) $MgTiO_3$-x $Ba_5Nb_4O_{15}$ composites by microwavesintering process. ***Ferroelectrics***, 519(1), 145-151.

Patent:

"Synthesis and processing of ST sputtering target material to obtain single phase thin films", Pamu Dobbidi, Susmita Rabha, and Apurba Das, Indian Patent Application No. 202131004326 dated 01/01/2021.

Publications outside thesis:

1. Das, A., Saxena, V., Bhardwaj, A., Rabha, S., Pandey, L. M., & Dobbidi, P. **(2022**). "Microstructural, interfacial, biological and electrical activity in sputtered Hydroxyapatite-Barium Strontium Titanate bilayered thin films." ***Surfaces and Interfaces****, 102063.*
2. Das, A., Bhardwaj, A., Rabha, S., Pandey, L. M., & Dobbidi, P. **(2022).** "Physical, chemical, and biological investigations of composites for biomedical applications." ***Journal of the American Ceramic Society,*** *105(3), 1790-1808.*
3. Das, A., Rabha, S., Saxena, V. et al. The role of electrical property in determining the response of 20H-80S composite thin films fabricated for biological applications. **J Mater Sci** 57, 13586–13602 (2022).

List of attended conferences and workshops with details:

1. International Conference on Technologically advanced materials & Asian meeting on ferroelectricity (ICTAM-AMF10). November 7-11,2016.
2. International conference on advanced ceramics and nanomaterials for sustainable development. ACeND-2018.September 19-21,2018.
3. National symposium on vacuum electronic devices and applications. VEDA-2018.November 22-24,2018.
4. One-Day workshop on Vacuum Technology and its application in optical Science. August 19, 2017.
5. International conference on advanced materials and mechanical characterizations. ICAMMC-2021.December 02-04,2021.

Table of Contents

List of figures

List of tables

List of Symbols and Abbreviations

Units of measurement

m	Meter
cm	Centimeter
μm	Micrometer
nm	Nanometer
Å	Angstrom
^{o}C	Centigrade (degree)
kHz	Kilo Hertz
MHz	Mega Hertz
GHz	Giga Hertz
h	Hour
F	Farad
pC	Pico Coulomb
μC	Micro Coulomb
N	Newton
V	Volt
eV	Electron-volt
GPa	Giga Pascal
g	Gram
W	Watt
esu	Electrostatic unit
A	Ampere

Electrical measurements

ε_r	Relative permittivity
tan δ	Loss tangent
A	Area of the electrodes
ε'	Real part of permittivity
ε''	Imaginary part of permittivity
ε_0	Permittivity of vacuum
σ_{ac}	AC-conductivity
χ_e	Electric susceptibility

J	Leakage current density
E	Electric field
C	Capacitance
d	Thickness
σ	Stress
η	Strain
P	Polarization
p	Dipole moment
V	Unit cell volume
Z	Impedance
Z'	Resistance
Z''	Reactance
f_0	Resonant frequency
f_a	Anti-resonance frequency
Q	Quality factor
τ	Relaxation time
DC	Direct current
AC	Alternating current
γ	Degree of diffuseness
E_A	Activation energy
ω	Angular frequency
k_B	Boltzmann constant
T_C	Curie temperature
ρ_{ac}	AC-resistivity
ξ	Decay length
$N(E_F)$	Density of states
R_H	Hopping length
W_H	Hopping energy

Optical measurements

α	Absorption coefficient
n	Refractive index
E_g	Optical bandgap

h	Planck's constant
z_0	Rayleigh length
λ	Wavelength
c	Velocity of light
hv	Photon energy

Other parameters

θ	Angle
D	Crystallite size
FWHM	Full width at half maximum
a, b, c	Lattice parameters
χ^2	Chi-square
R_{Bragg}	Bragg factor
R_f	Profile factor
F	Orientation factor
ρ	Density
wt.	Weight
rms	Root mean square
CSSR	Conventional solid-state reaction
RT	Room temperature
RF	Radio frequency
FE	Ferroelectric
OMP	Oxygen mixing percentage
O_2	Oxygen partial pressure
VRH	Variable range hopping
CCD	Charge coupled device
SCLC	Space charge limited conduction
SE	Spectroscopic ellipsometry
SEA	Spectroscopy ellipsometry analyzer
SPDR	Split post dielectric resonator
MIM	Metal-insulator-metal
XRD	X-Ray diffraction
AFM	Atomic force microscopy

SEM	Scanning electron microscopy
FESEM	Field emission scanning electron microscopy
FETEM	Field emission transmission electron microscope
HRTEM	High resolution transmission electron microscope
SAED	Selected area electron diffraction
EDS	Energy dispersive X-ray spectrometer
MTO	$MgTiO_3$
BNO	$Ba_5Nb_4O_{15}$
STO	$SrTiO_3$
BST	$Ba_{0.5}Sr_{0.5}TiO_3$

CHAPTER 1: INTRODUCTION

1.1 Background of microwave dielectrics:

Development and innovations in microwave communication technology and the internet of things has brought revolutionary changes in human civilization in various aspects at the societal and personal level. Microwave dielectrics are regarded as one of the key functional materials in the microwave communication industry: cellular phones, direct broadcasting satellites (DBS), and global positioning systems (GPS). Microwave dielectrics are a special type of material that show extraordinary properties at radio frequency waves. Microwave dielectrics have been explored for various functions such as electromagnetic resonance, electromagnetic wave shortening, electromagnetic wave delay, electromagnetic wave absorption, etc. depending upon their dielectric properties at the microwave frequency range as depicted in figure 1.1 [1].

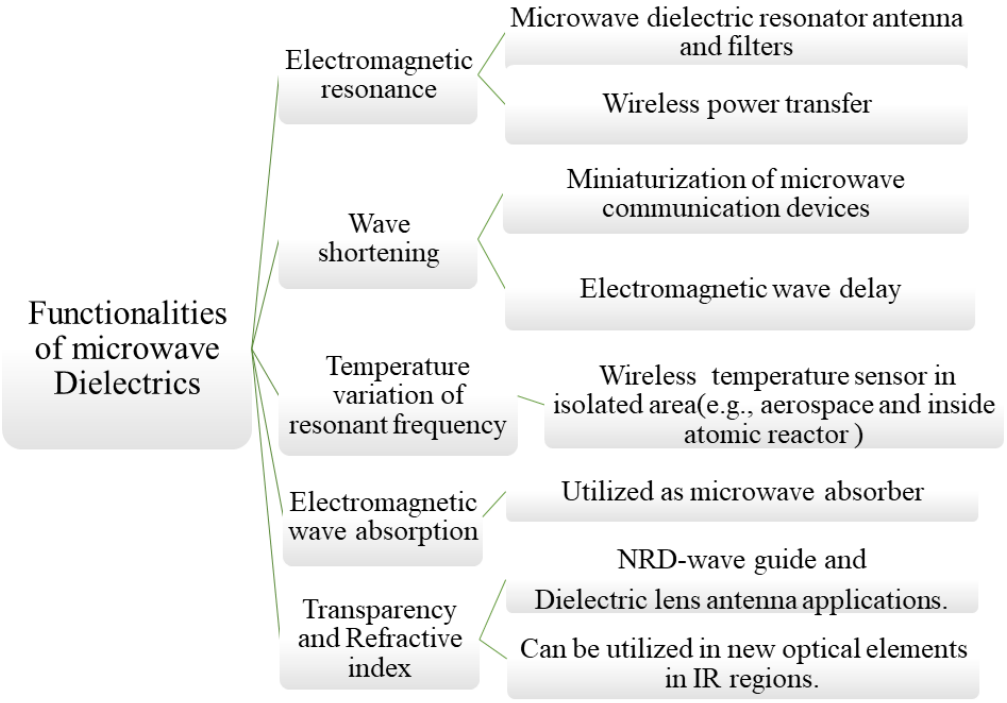

Figure 1.1 *Schematic diagram for different functionalities and their related applications of microwave dielectric materials.*

The recent research in this field mainly focused on the development of advanced materials for dielectric resonator (DR), electromagnetic interference shielding, tunable dielectric, higher temperature cofired ceramics (HTCC), low temperature cofired ceramics (LTCC), polymer-rubber ceramic composites, dielectric inks, and microwave ferrites[2]. DRs had played a vital role in recent progress in the telecommunication industry and satellite broadcasting technology by scaling down the device dimension and better performance.

In the year 1873, James Clerk Maxwell predicted the existence of electromagnetic waves of shorter wavelength, later, in 1888 Heinrich Hertz demonstrated the existence of radio waves[3]. In the year 1894, Indian Physicist Jagadish Chandra Bose was successfully able to produce microwaves in a laboratory experiment. Later in the year 1897 Lord Rayleigh mathematically solved the necessary boundary condition and cut-off frequency for the propagation of an electromagnetic wave through dielectric rods[4]. During the time of world war-II microwave radiation is utilized as radar for military purposes by US and UK. The commercialization of microwave technology started post world war-II. Microwave technology is widely used in the wireless communication domain. In the beginning days, invar air cavities are used as microwave resonators and filters for both base stations and mobile handsets. In 1939 Richtmyer of Scotland University theoretically demonstrated that dielectric materials also act as microwave resonators[5]. After a long gap of 30 years in 1960, Okaya and Barash from Colombia University rediscovered rutile TiO_2 based DR and also reported in detail about the shape of DR and related electromagnetic modes for the first time[6]. However, TiO_2 based DR was not regarded as a microwave dielectric resonator because of its low thermal stability. In the early 1970s, Murata manufacturing company from Japan commercialized DRs based on (Zn, Sn) TiO_4 ceramics[7]. The first-generation ceramic resonators are based on (Mg, Ca) TiO_3, $ZrTiO_4$, and $BaTi_4O_9$ ceramic resonators and are used in both transmitter and receiver ends [8,9]. By 1990, the development of miniaturized user-`friendly handsets diverged the ceramic technology of handsets from base stations. $CaTiO_3$-$NdAlO_3$ (CTNA), $ZrTiO_4$-$ZnNb_2O_6$ (ZTZN) based ceramics are widely utilized as resonators in base stations[10][11]. Later, Ba $(Co, Zn)_{1/3}Nb_{2/3}O_3$ (BCZN) ceramics are regarded as a cheaper replacement for existing ceramic resonators [12–14]. Recently, the bulky electronic components were replaced by printed strips and known as microwave integrated circuits (MIC). The microwave integration circuit made it possible to scale down the overall dimension[3].

1.2 Introduction to dielectric resonators (DR):

1.2.1 Working principle of DRs:

A dielectric resonator (DR) is a puck of dielectric material which acts as a resonator at the microwave (300 MHz -30 GHz) and millimeter wave (300 GHz- 3THz). DRs have been utilized in the fabrication of oscillators, and filters in microwave integrated circuits replacing the bulky metallic cavities in microwave antennas and filters

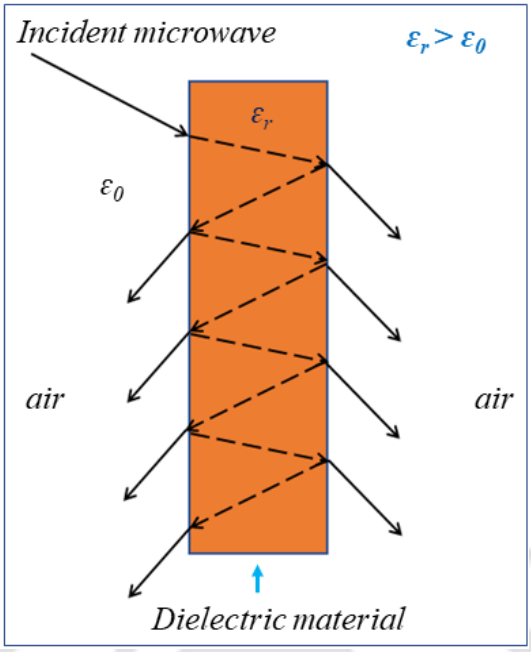

Figure 1.2: Schematic diagram of total internal reflection inside dielectric material with dielectric constant, $\varepsilon_r > \varepsilon_o$.

The development of dielectric oxide ceramic-based DRs had brought a revolutionary change in the microwave communication industry by reducing the size and cost of the filter, oscillator, and antenna components in applications ranging from cellular phones to global positioning systems. Lord Rayleigh demonstrated the applicability of a long dielectric cavity as a waveguide for microwaves for the first time[4]. As shown in figure 1.2, microwave gets confined inside the dielectric material upon multiple internal reflections due to abrupt change in dielectric constant at the air to dielectric material interface as depicted in figure 1.2[2]. Also, at certain frequencies known as resonant frequency, the microwaves form standing waves in the resonator, oscillating with large amplitude inside the dielectrics and decays as it moves away from the sample. The resonant frequency of a DR depends on its physical property, physical dimension, and surrounding environment. In general, the resonant frequency shifts towards the lower side with an increase in the dielectric constant value.

Microwave dielectric properties can be determined by studying transmitted electromagnetic waves through DR. There are some critical characteristics of dielectrics that decide the applicability of a DR. Firstly, the dielectric constant (ε_r). The dielectric constant is defined as the ratio of electrical permittivity through the substance to its electrical permittivity in the free space. Electrical storage in a dielectric is directly proportional to the value of the dielectric constant. The wavelength of an electromagnetic wave transmitted through a dielectric material decreases by the square root of the dielectric constant of the dielectrics. This physical phenomenon facilitates the confinement of microwaves inside a

dielectric material (with ε_r>1) within a smaller dimension as compared to a metallic cavity. The minimum required dimension of a DR to confine an electromagnetic wave is half of the wavelength of the propagated electromagnetic wave inside it. The critical relationship between the dielectric constant and the device dimension(l) can be expressed as follows

$$l = \frac{\lambda_0}{4}\frac{1}{\sqrt{\varepsilon_r}} \text{ ; for operating frequency } f < 3 \text{ GHz} \quad (1.1)$$

$$l = \lambda_0 \frac{1}{\sqrt{\varepsilon_r}} \text{ ; for operating frequency } f > 3 \text{ GHz} \quad (1.2)$$

where λ_0 is the wavelength of the microwave while propagating through free space. However, a higher dielectric constant is not suitable for resonator and filter applications for their narrowed frequency window as such materials exhibit larger loss as a result of their intrinsic property. Also, the higher confinement of electromagnetic waves prevents the efficient coupling of DRs with microstrip lines.

Secondly, the quality factor of DR is desired to be higher for the acuteness of the resonator at a given frequency. It is also the inverse of the dielectric loss tangent. In other words, it is a measure of the energy loss or dissipation per cycle to the energy stored in the fields inside the resonator and can be expressed as

$Q = 2\pi$ (maximum energy stored)/(average energy dissipated per cycle) (1.3)

$$Q = \frac{\omega_0 W_0}{P} \quad (1.4)$$

where, W_0, ω_0, and P denote energy stored, resonant angular frequency, and dissipated power, respectively. Experimentally, this dimensionless parameter defined is defined as the ratio of resonant frequency (f_0) and bandwidth (Δf) of the resonant peak at 3 dB down. Thus, the value of the quality factor depends inversely on the width of the resonant peak. The high-quality factor is desired for low-noise oscillators and narrow-band microwave filters to avoid cross-talk for a range of frequencies. For dielectric material, Q is a frequency-dependent term and hence, $Q \times f_0$ is used for conventional microwave dielectric properties. Lastly, thermal stability is necessary for a DR from a practical application point of view.

The temperature coefficient of resonant frequency is defined as the deviation in resonance frequency (f_0) of DR with a change in operating temperature (T) from room temperature (RT). i.e.,

$$TCF(\tau_f) = \frac{1}{f_0}\frac{\Delta f}{\Delta T} \quad (1.5)$$

where Δf is the change in resonant frequency over temperature difference of ΔT. In practice, the surrounding temperature at base stations is a variable parameter and for the unwavering performance of oscillators and filters irrespective of the temperature coefficient of the resonance frequency is desired to be near zero. On the other hand, non -zero temperature coefficient of the resonant frequency of a dielectric can be used as a temperature sensor in space and isolated places. Microwave technology is developing rapidly to fulfill the user's demand. The development of microwave technology includes development in advanced materials and development of engineering in microwave device performances. In addition, different components of microwave communications viz: base station, handset, and internet connectivity need to be compatible with each other. Great attention has been given to the development of new materials with the desired properties by various research institutes, educational organizations, and companies as well[15,16].

1.2.2 Resonant modes in DRs:

Various specifications such as the resonant frequency, the field distribution inside the resonator, the radiated field, and also the bandwidth play an important role in the design of DRs. Depending upon the field distribution (electric and magnetic field) resonator modes are classified as follows:

i. Transverse Electric Modes (TE)
ii. Transverse Magnetic Modes (TM)
iii. Hybrid Electromagnetic Modes (HEM)

TE and TM modes are always referred to by a coordinate axis (X, Y, and Z with an integer *n, l,* and *m,* respectively). Many resonator modes can be excited for DRs depending upon their geometry, measurement setup, and measured frequency range. The variations of fields along the azimuthal, radial, and Z - direction inside the resonator, are denoted by indices: *m, n,* and *p* as subscripts to each family of modes. The field distributions are axisymmetric for TE and TM modes and vary azimuthally for hybrid modes. The resonant modes of a cylindrical resonator can be divided into constituent modes with azimuthal variation given by $\cos(m\varphi)$ or $\sin(m\varphi)$, (where m = 0, 1, 2, 3) [17].

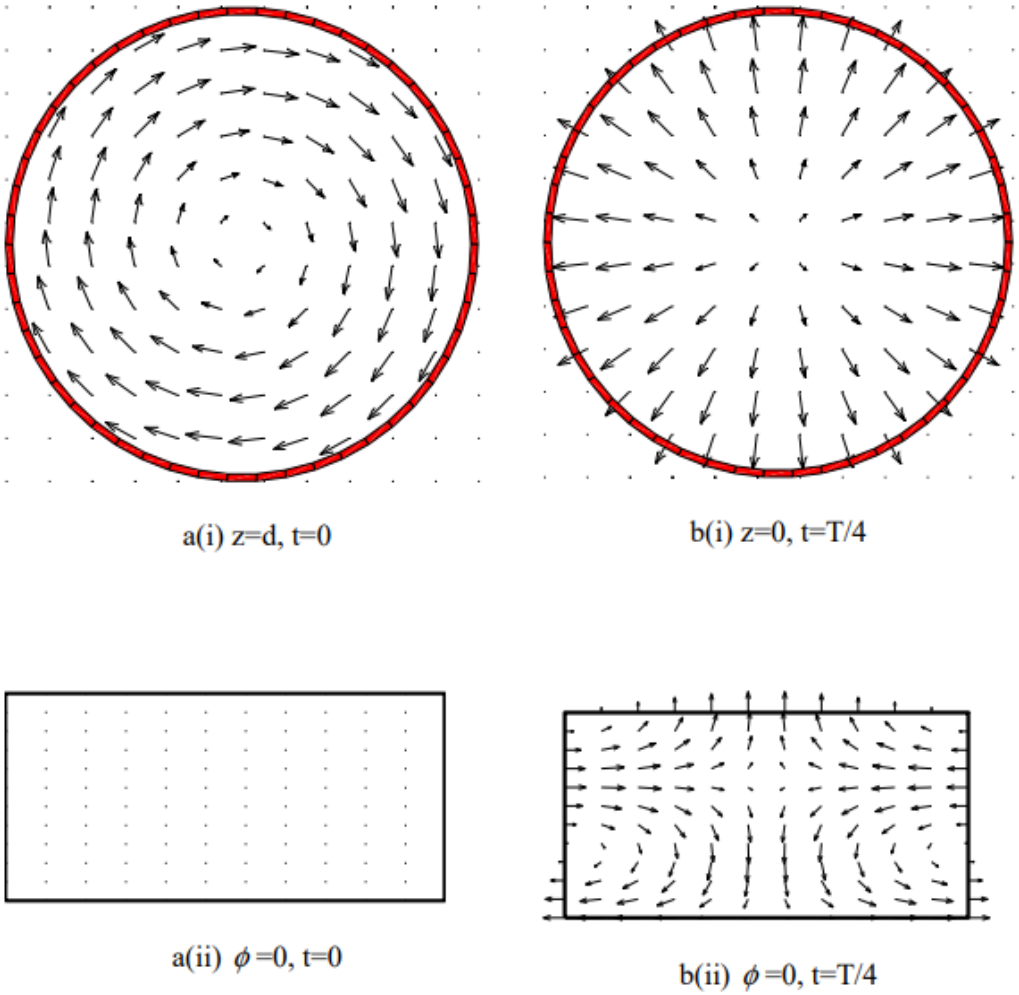

Figure 1.3: Fields inside the cylindrical DRA for the mode $TE_{011+\delta}$, with an (i), (ii) showing E-field in the top, side views respectively, and b(i), (ii) showing H-field in the top, side views, respectively (T is the time period of one resonant cycle) [18].

Generally, the resonant frequency of the hybrid mode: $HEM_{11\delta}$ is lower than that of the widely used $TE_{01\delta}$ mode. The separation between $HEM_{11\delta}$ mode to $TE_{01\delta}$ mode depends on the width to height ratio of the DR and the gap between perturbing metallic surface to the DR. Proper separation of $HEM_{11\delta}$ mode to $TE_{01\delta}$ mode is desired as the $HEM_{11\delta}$ mode exhibits lower *Q* value. The $HEM_{21\delta}$ mode has a lower resonant frequency and falls right between $TE_{01\delta}$ and $TM_{01\delta}$ modes. Thus, when operating in either of these modes, $HEM_{21\delta}$ mode will interfere. Coupling to TM modes requires special arrangement as compared to TE modes. In both TE and TM coupling arrangements HEM mode is possible to couple. HEM modes are highly leaky (i.e., radiative) in nature and can cause difficulties in using TE and

TM modes. The interference of HEM modes grows as the integer's m and n take higher values. DRs of aspect ratio 2.5 provides well separated $TE_{01\delta}$ mode. The mode which is most commonly used for material characterization is $TE_{01\delta}$ mode. Fig.1.3 a(i-ii) and b(i-ii) present the electric field and magnetic field lines for $TE_{011+\delta}$ for top and side views, respectively. Some part of the electromagnetic energy gets stored within the DR and the rest energy is dispersed in the air around the DR which decays as it moves away from the DR vicinity. An exact solution of Maxwell's equations for an isolated DR is difficult to achieve and hence, approximated solutions are considered for such cases.

For a value of dielectric constant (ε_r) a standard mode chart is corresponding to a particular diameter (D) to the height (L) ratio i.e., D/L (aspect ratio) is available. Kobayashi et. al,[17] reported a mode chart ($\varepsilon_r (D/\lambda_0)^2$ vs. $(D/L)^2$) for a dielectric rod resonator short-circuited at both ends, where λ_0 is the free space wavelength corresponding to the resonant frequency of the mode. Thus, for known ε_r, D, and L values the resonant frequencies corresponding to the resonant modes and their respective orders of a DR can be estimated with the help of a mode chart. This information helps in designing a DR for a particular application without any interference from unwanted (lossy) resonating modes. The following equation is utilized for an approximate estimation of the resonant frequency of an isolated DR

$$f_{GHz} = \frac{34}{D_{mn}\sqrt{\varepsilon}}\left[\frac{D}{L} + 3.45\right] \qquad (1.6)$$

where D and L refer to the width and height of the DR, respectively.

Ceramic resonators are prepared in different geometries (examples: cylindrical, tubular, toroids, spheres, parallelepiped, cubes, etc.) as per the requirement. In practice, DRs are kept within a silver-coated square cavity for use.

1.3 Current status and future of microwave dielectrics

In the present century, the integrated circuit of multifunctional components has served the purpose of today's miniaturized, user-friendly modern technologies such as cell phones, i-pods, palMTOps, automobile power electronics, safety robotics, medical instruments, etc. IC-based electronics is widely utilized in passive things as well including walls, pavements, roofs, etc. Based on their characteristics ceramics are widely utilized in electronics as insulators, semi, super and ionic conductors, varistors, capacitors, thermistors, etc. Dielectric ceramics have been used as capacitors, resonators, filters, and substrates for different

purposes. The ongoing research in this field is mainly focusing on the development of new functional materials with requisite properties to fit upcoming technologies. Research is going on composite ceramics of two or more different phases (e.g., polymer, ceramic, metal) has found to be a potential approach in this regard.

1.4 $MgTiO_3$-based composite ceramics and thin films for microwave communication

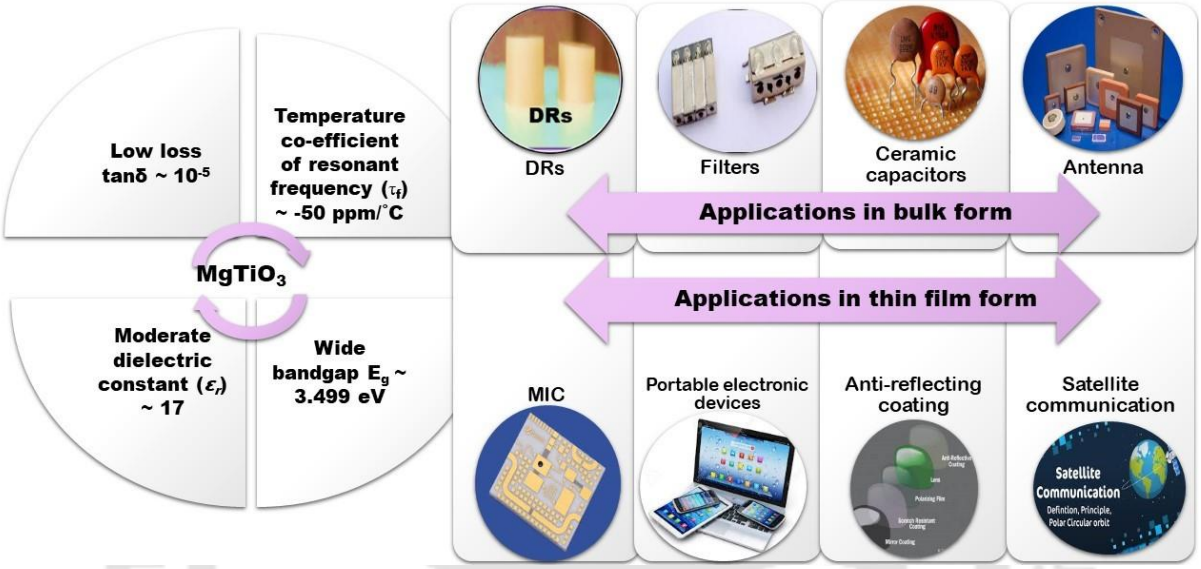

Figure 1.4: *Schematic representation of various applications based on $MgTiO_3$ ceramics and thin films*

$MgTiO_3$ (*MTO*) is one of the most extensively studied microwave dielectric ceramics. $MgTiO_3$ shows excellent microwave dielectric properties exhibiting high-quality factor ($Q \times f_0$ ~ 160,000 at 8 GHz), permittivity (ε_r ~17), and a non-zero temperature coefficient of resonant frequency τ_f = - 50 ppm/^{o}C [19]. Non-zero τ_f value limits the use of *MTO* ceramics in base stations. In addition, *MTO* ceramics require a high sintering temperature when prepared in the solid-state reaction method and usually form the $MgTi_2O_5$ phase (metastable state of Magnesium Titanium oxide) due to the hygroscopic nature of MgO. Since *MTO* exhibited extremely low dielectric loss, it has been extensively studied to compensate for the negative temperature coefficient value. In communication technology, temperature-stable *MTO*-based ceramics has found application as an integrated part of filters, antennas radars, multilayer capacitors, 90˚ hybrid coupler, planar patch antenna, and direct broadcasting satellite and global positioning systems operating at microwave frequencies [20–22]. The areas where *MTO* has been potentially explored for applications were schematically represented in figure 1.4.

1.5 Brief literature survey on $MgTiO_3$ based ceramics for microwave application

The research on $MgTiO_3$ ceramics mainly focused on two aspects firstly lowering the sintering temperature and secondly, tunning of temperature coefficient to near zero. These two aspects are discussed in detail in the subsequent sections.

1.5.1 Single Phased $MgTiO_3$ based ceramics with low sintering temperature:

The high sintering temperature for $MgTiO_3$ makes it not suitable for many other applications. There are several research articles on lowering sintering temperature for *MTO* ceramics. The sintering temperature of the ceramics can be lowered by adding glass phases such as Bi_2O_3 etc and following the chemical route for preparation. Some of the reports on lowering sintering temperature are tabulated in Table.1.1,

Table 1.1: *Brief literature on MgTiO3 based Ceramics for lowering sintering temperature.*

Serial No.	***Material composition***	***Sintering temperature (T) in ˚C***	***Preparation Method***	***Dielectric constant (ε_r)***	***Quality Factor ($Q\times f_0$) in GHz***	***Temperature coefficient of resonant frequency (τ_f) in ppm/˚C***	***References***
1	MTO	1200	Aqueous sol-gel process	17.5	156,000	-44	[23]
2	6 wt% CuO–Bi_2O_3–V_2O_5 added MTO	900	Solid state reaction method	18.1	20,300	-57	[24]
3	B_2O_3 doped MTO	1100	sol-gel	17.63	33,768	-48	[25]
4	V_2O_5 doped non stoichiometric MTO	1100	Solid state reaction	15.8	85,600	-	[26]

From the table, we can see that the use of sintering aid has deteriorated the quality factor, of $MgTiO_3$ ceramics. Whereas dielectric permittivity has increased and decreased depending on the type of sintering aid. So, maintaining the quality factor, and lowering the sintering temperature would be a challenging task.

1.5.2 Tunning of temperature coefficient of resonant frequency, τ_f by composite approach:

A composite approach is an efficient approach for tuning dielectric properties. A composite of two or more ceramics can offer promising dielectric properties for intended applications. Table 1.2 presents important parameters corresponding to various composites of *MTO*. This section discusses the development of $MgTiO_3$ based composite ceramics with near-zero τ_f value. J.B. Huang, et. al [27] have obtained near-zero τ_f for $CaTiO_3$- $MgTiO_3$ composite ceramics, and 1% ZnO addition has lowered the sintering temperature to 1260 ˚C.

Table 1.2*:Brief literature on MgTiO3 based Ceramics with near-zero τ_f value*

Sl. No.	**Material composition**	**Dielectric constant (ε_r)**	**Quality Factor ($Q\times f_0$) *in* GHz**	**Temperature coefficient of resonant frequency (τ_f) in ppm/ ˚C**	**Sintering temperature (T) in ˚C**	**References**
1	$0.95MgTiO_3$-$0.05CaTiO_3$ with 1% ZnO addition	21	56,000	-5	1260	[28]
2	$0.90MgTiO_3$–$0.05CaTiO_3$ 0.05LiF	12.7	93,000	-3	950	[29]
3	$0.95MgTiO_3$-$0.05CaTiO_3$ with 3wt% addition of B_2O_3	20.3	68,000	-5	1210	[30]
4	$0.92(Mg_{0.95}Zn_{0.05})TiO_3$ $0.8(Ca_{0.8}Sr_{0.2})TiO_3$	21.9	42,800	-0.15	1300	[31]
5	$0.964MgTiO_3$-$0.036SrTiO_3$ 2wt% addition of B_2O_3	19	75,300	-8.7	1170	[32]

Akinori Kan, et. al [29] has achieved a very good dielectric response at a low sintering temperature of 950˚C due to the addition of 5 wt% LiF as a sintering aid in $0.90MgTiO_3$–$0.05CaTiO_3$ composite ceramics. Su Hao et. al [30] also achieved near-zero τ_f value and excellent microwave dielectric properties at 1210˚C sintering temperature for $0.95MgTiO_3$-$0.05CaTiO_3$ ceramics with 3wt% sintering aid B_2O_3 by solid-state reaction method.

Shailendra Singh Rajput et. al [31], reported $0.92(Mg_{0.95}Zn_{0.05})TiO_3$ -$0.8(Ca_{0.8}Sr_{0.2})TiO_3$ composite by solid-state reaction method to tune the τ_f near zero and achieved 0.15 ppm/˚C at sintering temperature of 1400˚C. Won Woo Cho et. al [32], reported the microwave dielectric properties of $0.964MgTiO_3$-$0.036SrTiO_3$ with 2 wt% B_2O_3 addition and got ε_r of 19, $Q \times f_0$ value of 75,300 GHz (at 9 GHz) and τ_f of −8.9 ppm/ ◦C.

1.5.3 $MgTiO_3$-based composite for tunable microwave dielectrics

The trend in wireless communication systems broadband applications such as multimedia file transfer, video transmission, and internet access require much higher data transmission rates than the existing one at an affordable price. To achieve these higher data rates, substantially larger bandwidth and higher carrier frequencies are required. Electrically tunable microwave dielectrics thin films can be useful resonators, filters, phase shift antennas, and tunable oscillators which utilize nonlinear tuning in a control element. Miniaturization of electronic circuits in the mobile application can be facilitated by tunable capacitors by exploiting the DC bias dependence[33]. Ferroelectrics, and piezoelectric show tunable microwave dielectric properties. Piezoelectricity is the ability of a material to produce electricity when it is subjected to mechanical stress or the production mechanical strain by applying the electric field. Only the materials that do not have a center of symmetry in their crystal structure possess piezoelectricity. The microwave dielectric property of a piezoelectric can be realized by the application of mechanical stress. Ferroelectricity is the ability of the material that can change the direction of polarization with the application of an electric field. Ferroelectric materials have spontaneous polarization (P_s) even in the absence of an electric field. When a small amount of electric field is applied to the ferroelectric crystal, it shows the linear relationship between P and E, because the field is not large enough to induce any domain switching. As the field increases, the domains with polarization opposite to the direction of the applied field will flip to align with the field direction, and the polarization increases rapidly until all the domains align in the same direction. When the field is removed, some domains do not go back to their original polarization direction and the material possesses remanent polarization (P_r). The remanent polarization can be removed, when the electric field is applied in the opposite direction. The critical strength required to reduce the remanent polarization back to zero is called the coercive field (E_c). As ferroelectricity is caused by the existence of dipole moment, a unit cell needs to be non-centrosymmetric i.e; the center of positive charge and the center of negative charge does not coincide in ferroelectric crystal. In normal ceramics, the domains are oriented randomly and therefore,

unable to exhibit piezoelectricity. It is desirable to have a low permittivity for good impedance matching, a low dielectric loss to minimize the insertion losses of devices, and a high dielectric tunability, which is the change of permittivity with dc field, for less power driving and high speed of phase shift for the tunable ceramic capacitor. Barium strontium titanate (*BST*) ferroelectric materials have shown great promise for application as phase-shifting elements in phased array antennas and as tuning elements in devices operating at microwave frequencies because of their high tunability and low dielectric losses[34]. However, in the case of pure *BST,* its high permittivity value makes it difficult for impedance matching and high power for tunable capacitors. Strontium titanate (*STO*) possesses piezoelectric behavior at low temperatures, but the introduction of strain (<1%) can shift the transition temperature of strontium titanate up to more than room temperature [35]. which made it a very attractive candidate for tunable electronic circuits. B. Su and T. W. Button reported Mg-doped barium strontium titanate (< 2%) and suppressed the permittivity and dielectric loss to fit for tunable microwave device by mixed titanate route [36]. L. Tang et al, reported (1-*x*) $Ba_{0.5}Sr_{0.5}$ TiO_3-*x*$MgMoO_4$ Ceramics by solid-state reaction method up to x = 30%, with x =20% is the best optimized composite with tunability =10% and dielectric constant of 111 and Q value 183 (2.24 GHz) is suitable for electrically tuneable microwave device[37].

1.5.4 $MgTiO_3$ and $MgTiO_3$ based composite thin film:

Thin film is a 3-dimensional structure, where the dimension in one direction is negligible as compared to the other two dimensions. Due to the confinement of electrons in 2 dimensions, it exhibits extraordinary physical and chemical responses. Thin film is the basic requirement of integrated circuit technology. Compact and cost-effective handy electronic devices and gadgets are being realized through the development of thin film science and technology. The ever-increasing demand for device performance and data transfer speeds requires further development of functional materials. Thin films scale down the material cost as it uses 10^7 times less material and exhibits comparable surface responses as the bulk one. The thin film technology consists of the fabrication of thin film followed by characterization and application. Apart from electronic components thin films also found application in catalysis and surface coating. From the beginning of the evolution of integrated circuit technology to the end of the 19^{th} century SiO_2 was the sole gate material for the fabrication of Si-based complementary metal oxide semiconductor (CMOS) devices as well as dynamic random-access memory (DRAM) devices. In the year 1997 electronic industries proposed an

International Technology Roadmap on Semiconductors (ITRS) on necessary materials, equipment, and design for the development of IC technologies. The requisite characteristics for gate dielectrics are low leakage current and high dielectric constant. The existing SiO_2 films could not maintain the maximum leakage current limit at 0.7 nm thicknesses[38]. SiO_2 on Si-based metal-oxide-semiconductor field-effect transistors is still widely used because of its fundamental characteristics such as dielectric constant, barrier height, morphology and stability in Si contact, and device properties: processing, integration, and reliability. From then to date, many materials with high dielectric constant and low leakage current have been investigated to meet the equivalent properties of SiO_2 with less leakage current. Both nitrides: Si_3N_4 (ε_r ~7.5) and oxides: Al_2O_3 (ε_r ~9.1) are proposed to be a potential replacement for SiO_2 for future generation electronics [39]. $MgTiO_3$ possesses a high dielectric constant (17) and optical bandgap (3.05eV),[40] and is studied as a potential replacement of SiO_2 [41,42]. $MgTiO_3$ thin films are also investigated for optical modulation, protective layer for plasma displays, and monolith microwave integrated circuits [43]. Because of excellent microwave dielectric properties and constant demands for cost-effective, thinner, and lighter devices, *MTO* films were studied extensively for monolith microwave integrated circuits[44,45]. *MTO* and $CaTiO_3$-based composite films were also explored for low dimensional temperature stable microwave resonators[30,46–48]. In low dimensional room temperature tunable microwave devices including phase shifters, voltage controlled oscillators, and steerable antenna array applications *MTO* has been considered as an integrated part along with ferroelectric and piezoelectric materials and obtained low loss tunable microwave thin films[49–52].

Based on the above literature survey, we have formatted some of the literature gaps which are described in the subsequent section.

1.6 Literature gap:

- High *Q*-value and moderate dielectric constant with near zero τ_f value are essential for the application of *MTO*-based composite ceramics as microwave dielectrics. Comprehensive studies on the optimization of these parameters are therefore important. The existing literature, however, primarily focuses only on the τ_f tunability. A detailed study on the degradation of the *Q*-value for the *MTO*-based composite ceramics is not available so far.

- Most of the available pieces of literature on temperature stable *MTO* based composite ceramics have reported microwave dielectric characteristics. Whereas, *MTO* based composites can have applications in other ranges of frequency such as type-I and type-II capacitors along with microwave antenna and filter applications. A detailed study of *MTO* based composite ceramics in a broad frequency region is required to get a better insight into the related scope.
- Temperature stable *MTO*-based composite ceramics are not yet explored in thin film form.
- Further, *MTO* based thin films for electronic applications and monolith microwave integrated circuits are still in the initial stage, and very few reports are available on their microwave dielectric properties.
- In addition, the physical responses of a thin film greatly depend on its structural and microstructural properties, and precise control over the fabrication method to achieve requisite responses needs an in-depth understanding of the different characteristics of the deposited film.

1.7 Motivation of the present thesis:

Pure and doped *MTO* ceramics and thin films have been extensively studied by our research group and obtained promising dielectric properties for DR applications. All the dielectric parameters such as dielectric constant, quality factor, and temperature coefficient of resonant frequency are related to each other. Alteration of one property causes changes in other parameters as well. Therefore, a detailed study on the various characteristics of *MTO* based ceramics applications. The present thesis focuses on the tuning of the temperature coefficient of resonant frequency near zero and the introduction of dielectric tunability via a composite approach. For the composite approach ceramics with a large positive co-efficient of resonant frequency: $Ba_4Nb_4O_{15}$ (τ_f ~+78 ppm/˚C), and $SrTiO_3$ (τ_f ~+1100 ppm/˚C) are chosen. Similarly, a ferroelectric composite of *MTO* with $Ba_{0.5}Sr_{0.5}TiO_3$ is chosen for tunable microwave dielectric response. The thin film of proposed *MTO*-based composites would also be interesting materials for microwave integrated circuits, tunable capacitors, and filter applications.

1.8 Theory and fundamental Physics associated with microwave dielectrics:

1.8.1 Dielectric Polarization:

Dielectric materials are unique types of electric substances. Dielectrics are electrically resistive matter, and charges cannot pass across the dielectrics in presence of an applied electric field but rather get stored by the phenomenon called dielectric polarization. Dielectric materials cannot conduct electricity as they do not contain free charge carriers and all the charge carriers or electrons are tightly bound to their nucleus/atoms. It can be imagined as a positively charged nucleus surrounded by electron clouds exactly canceling out the net charge. However, an interesting phenomenon is found to occur when dielectric materials are placed in an external electric field. Depending upon the strength of the externally applied field the negatively charged electron cloud would shift to the positively charged nucleus and thus each atom acts as a tiny dipole resulting in an induced dipole moment. This phenomenon is called electronic polarization. Apart from this, three other types of polarization mechanisms can be observed in a dielectric material. The collective dipole moment ($\vec{\mu}$) per unit volume (V) of the dielectric material is known as polarization $\vec{P}$ = ($\vec{\mu}$/V). In total four types of dielectric polarization mechanisms can be found in a dielectric material viz: electronic polarization ($\vec{P_e}$), ionic polarization ($\vec{P_i}$), dipolar polarization ($\vec{P_{dp}}$), and space charge polarization($\vec{P_{sc}}$). Solids formed by ionic covalent bonds exhibit ionic polarization. Ionic polarization is defined as the polarization of ions. The cations and anions of the solids get displaced to each other in presence of an electric field resulting in a net dipole moment per unit volume. In presence of electric field ions present in dielectric materials displace from each other in the direction of the field inducing a dipole moment and this mechanism is called ionic polarization. Dipolar polarization is the polarization of permanent dipoles intrinsically present in the dielectric material due to asymmetric crystal structure. In absence of an electric field net dipole moment per unit volume from intrinsic dipoles is zero because of the dipole's random orientations. The magnitude of dipole moment in such a case is much larger than electronic and ionic polarization. The origin of space charge polarization is extrinsic charges which get accumulated in the interfaces of electrodes resulting in a dipole moment. Dielectric polarization is a frequency-dependent phenomenon. When the applied electric field is replaced with an alternating current electric field the effect can be directly observed. When the frequency of the applied AC field is increased gradually from a very low value at around 10^5 Hz, the heaviest dipole corresponding to space charge polarization gets relaxed resulting

in a sharp drop in dielectric constant value. At 10^9 Hz the second most heavy dipole corresponding to dipolar polarization is unable to follow the frequency of the AC field and cease its contribution towards net dipolar polarization. At 10^{12} Hz ionic polarization also gets relaxed as the alteration of the electrode terminal becomes too fast to follow by the ionic dipoles. That is why for the high-frequency electric field only electronic polarization contributes toward net dipole polarization in the dielectric material. Further dielectric materials can be classified into two types based on the dependency of dipolar polarization with applied field strength: linear dielectric and nonlinear dielectrics. The polarization ($\vec{P}$) in linear dielectric materials is proportional to the field ($\vec{E}$). Whereas, the nonlinear dielectric materials possess inherent dipoles and show a non-zero spontaneous polarization even after the removal of the external electric field. The basic difference between linear dielectrics and non-linear dielectrics is their crystal structure. Linear dielectrics do not have permanent dipoles as the ions of opposite charges are perfectly balancing each other because of their symmetric structure. Therefore, the presence of a non-centrosymmetric structure is a basic requirement to fall into nonlinear dielectric materials. Generally, the dielectric constant is calculated using the parallel plate capacitance method by the following equation,

$$\varepsilon_r = \frac{\varepsilon}{\varepsilon_0} = \frac{Cd}{\varepsilon_0 A} \qquad (1.7)$$

where *C* is the capacitance, *d*, and *A* is the thickness of the sample and area of the electrodes, respectively. The dielectric constant of the material depends on the ability to polarize. Based on polarization ability the dielectric materials are classified as, linear dielectric, ferroelectric, piezoelectric, and pyroelectric materials.

1.8.2 Dielectric loss:

It is defined as the ratio of the imaginary (ε″) part of the dielectric permittivity to the real permittivity (ε′), i.e., $\tan\delta = \frac{\varepsilon''}{\varepsilon'}$. Therefore, the high dielectric constant and low dielectric loss materials are key parameters for the electrical/electronics industry applications. Dielectric loss is the loss of electromagnetic energy inside a dielectric material. Dielectric loss is broadly classified into two types based on their origin namely intrinsic and extrinsic. Intrinsic loss is the dissipation of the electric field due to its interaction with the phonon system in a perfect crystal. The altered phonon system corresponding to the perfect crystal undergoes relaxation in the presence AC electric field, which dissipates the energy of

electromagnetic waves. The intensity of interaction depends on crystal structure and single-crystal will exhibit minimum intrinsic loss[53]. In particular, the microwave frequency is much smaller than the phonon frequency, so, the low-frequency relaxations originate from harmonic oscillations. Relaxations in the electric field cause dissipation of heat leading to heating the system and affecting the overall performance of the device performance. The intrinsic loss also depends on crystal symmetry, frequency of AC field, and temperature. Whereas extrinsic loss comes from external factors such as impurities, vacancies, grain boundary structure, porosity, dislocations, etc. The extrinsic loss depends greatly on fabrication methods and engineering.

1.8.3 Temperature coefficient of resonant frequency:

The deviation of resonant frequency as a function of temperature defines as the temperature coefficient of the resonant frequency (τ_f). This parameter depends on two temperature-dependent parameters of dielectric materials as the following expression

$$\tau_f = -\alpha_L - \frac{\tau_\varepsilon}{2} \tag{1.8}$$

where α_L is the linear thermal expansion coefficient and is usually positive for a dielectric material, τ_ε denotes the temperature coefficient of the dielectric constant.

In the subsequent sections, a brief introduction about the chosen compositions in the current study is discussed.

1.8.4 Crystal structure and properties of $MgTiO_3$

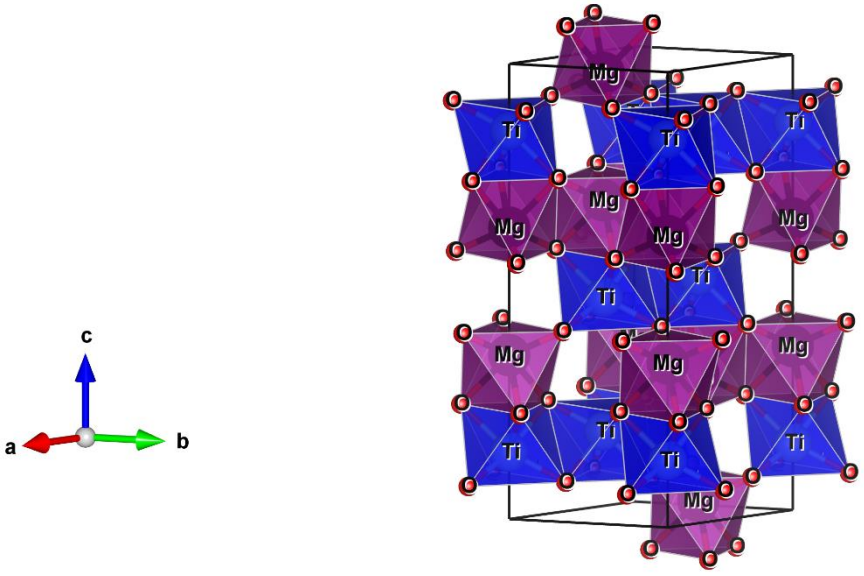

Figure 1.5:Crystal structure of $MgTiO_3$.

$MgTiO_3$ has an ilmenite type structure and crystallizes to rhombohedral symmetry with $R\bar{3}$ the space group. Typically, A^{2+} Ti^{4+} O_3 (where A is a first-order transition metal, Fe, Mn, Zn, and Mg) compounds adopt an ilmenite structure when the ionic radii of A ($^{vi}R_A$) and Ti ($^{vi}R_{Ti}$) are comparable and are smaller than oxygen anion[22]. The Goldschmidt tolerance factor of ilmenites is less than 1 and can be defined as,

$$t = \frac{(R_A + R_O)}{\sqrt{2}(R_B + R_O)} \tag{1.8}$$

where, R_A, R_B, and R_O signify ionic radius of A, B, and oxygen, respectively. A pair of MgO_6 and TiO_6 octahedra share a (001) face and each octahedron in the ilmenite structure shares one edge with the same type of octahedral and three edges with the other octahedral. As shown in figure 1.5, the stacking sequence along $[001]_h$ of this structure is "*Mg-Ti- [ ]-Ti-Mg-[ ]"* and either "*Ti-Ti-[ ]"* or "*Mg-Mg-[ ]"* parallel to (111), resulting in the centrosymmetric $R\bar{3}$ rhombohedral cell. The typical, lattice parameters of MTO *are a = b = 5.0567* Å and *c* = 13.9034 Å with the number of atoms per unit cell (Z) = 8. The Goldschmidt tolerance factor for $MgTiO_3$ is 0.88. This is the reason Ti octahedra gets tilted with temperature which results in a negative temperature coefficient of the resonant frequency. $MgTiO_3$ exhibits excellent microwave dielectric properties with quality factor ($Q \times f_0$ ~ 160,000 at 7 GHz), permittivity (ε_r ~ 17) and temperature co-efficient of resonant frequency τf = - 50 ppm/^oC [45].

1.8.5 Crystal structure and properties $Ba_5Nb_4O_{15}$:

Among various other oxide materials, $Ba_5Nb_4O_{15}$ (*BNO*) ceramics have been found useful for microwave communication technology [54]. Although $Ba_5Nb_4O_{15}$ ceramics possess superior dielectric properties i.e., ε_r ~39–40 and $Q \times f_0$~26,000GHz, its applicability is limited as $Ba_5Nb_4O_{15}$ ceramics show large positive τ_f ~78 *ppm/˚C*. Temperature stable microwave ceramics were obtained in the composite form of $Ba_5Nb_4O_{15}$ ceramics with other ceramics such as $BaNb_2O_6$ and $BaWO_4$ with considerable ε_r and $Q \times f_0$ values for the applications in $Ba_5Nb_4O_{15}$ ceramics microwave communication technology [55][56][57]. Temperature stable $Ba_5Nb_4O_{15}$ - $BaWO_4$ composites are also investigated in thin film form for smart window applications[58]. Similarly, a composite of $MgTiO_3$ ceramics with $Ba_5Nb_4O_{15}$ ceramics would also exhibit temperature stability. In the present work, composite of $MgTiO_3$ and $Ba_5Nb_4O_{15}$ ceramics were prepared by solid-state reaction method to obtain temperature stable smart material without degradation of other dielectric properties such as quality factor and dielectric constant. Further, the best-optimized composition is carried

forward for thin film deposition and characterization for microwave integrated circuit applications. $Ba_5Nb_4O_{15}$ exhibits a five-layer hexagonal perovskite structure with vacant octahedra layers as shown in figure 1.6 and belongs to $A_nB_{n-1}O_{3n}$ compound family. The missing octahedra layer produces anharmonicity in the crystal and results in a large dielectric constant.

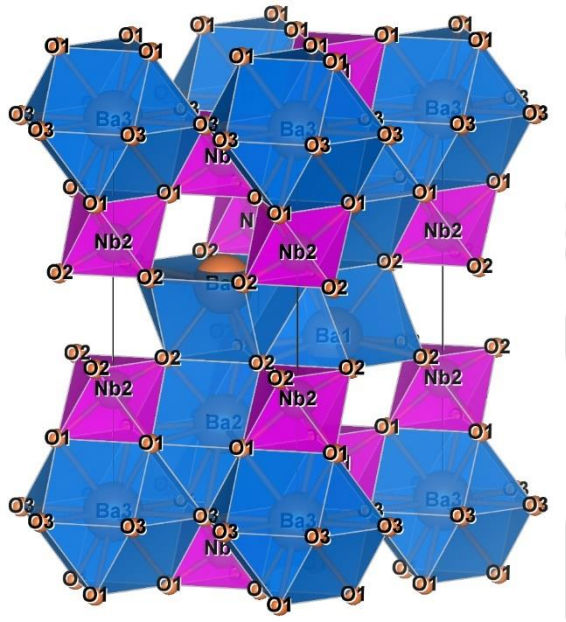

Figure 1.6:Crystal structure of $Ba_5Nb_4O_{15}$

1.8.6 Crystal structure of $SrTiO_3$:

Strontium titanate is a well-known perovskite structured material and possesses a cubic paraelectric phase above 105 K with lattice parameter 0.3905 nm. $SrTiO_3$ (*STO*) is another widely explored material with a simple cubic structure at room temperature with a lattice parameter of 0.395 nm as shown in figure 1.7. *STO* exhibits a high dielectric constant (~300) and extensively studied material for energy storage devices, electronic sensors, dynamic random-access memories, and multilayer ceramic capacitors. Whereas, *STO* has not been explored for microwave communication technology because of its low-quality factor (~3000 GHz) and a large positive temperature coefficient of resonant frequency (~1200 ppm/˚C). Since *MTO* exhibits a significantly high-quality factor and negative coefficient of resonant frequency (~ -50 ppm/˚C), a composite of *MTO* with *STO* ceramics has the potential to offer temperature-stable microwave ceramics.

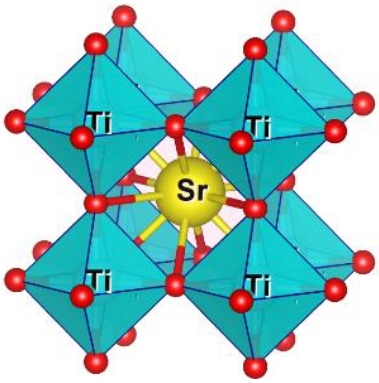

Figure 1.7: Crystal structure of $SrTiO_3$

1.8.7 Crystal structure of $Ba_{0.5}Sr_{0.5}TiO_3$:

Barium strontium titanate $Ba_{0.5}Sr_{0.5}TiO_3$ (*BST*) is ferroelectric material that has shown great promise for application as the phase-shifting element in phased array antennas and as tuning elements in devices operating at microwave frequencies because of their high tunability and low dielectric losses[34]. However, in the case of pure *BST*, its high dielectric constant value makes it difficult for impedance matching and high power for tunable capacitors. *MTO* ceramics exhibits minimum insertion loss (high *Q* value) and comparatively low dielectric constant (17). Thus, the issues owing to a high dielectric constant of *BST* can be resolved by the addition of *MTO* in an optimized fraction to sustain tunability. At room temperature *BST* exhibits cubic structure with Pm-3m space group and lattice parameters ($a=b=c=0.394$ nm)

1.9 Objectives

The main objective of this work is to fabricate microwave ceramic possessing a high dielectric constant for the miniaturization of electronic components maintaining high-quality factor and near-zero temperature coefficient resonance frequency. The proposed works are listed as follows:

1. Development of temperature stable $MgTiO_3$ - $Ba_5Nb_4O_{15}$ composite ceramic and thin film for microwave applications.
2. To study the tunability behavior in microwave dielectric properties of $MgTiO_3$ - $SrTiO_3$ composite ceramics, and study the structural, optical, electric, and dielectric properties of $MgTiO_3$ -$SrTiO_3$ composite thin films.
3. Development of $MgTiO_3$- $Ba_{0.5}Sr_{0.5}TiO_3$ composite ceramics and thin films for tunable microwave dielectric property.

CHAPTER 2: SYNTHESIS AND CHARACTERIZATION TECHNIQUES

In the present work, bulk and thin film *MTO* based composites were prepared by conventional solid-state reaction method and RF magnetron sputtering technique, respectively. Further, their structural, microstructural, optical, dielectric, and electrical properties were characterized by using various experimental setups. The preparation methods and characterization techniques are discussed in detail in the following sections.

2.1 Synthesis of bulk MTO based composite ceramics

Ceramics are inorganic crystalline materials and are often associated with metal ions along with oxygen. Ceramics are widely utilized in many applications such as the communication industry, electronics, and appliance industries because of their unique characteristics. The physical and mechanical properties of ceramics mainly depend on their crystallinity and chemical composition. For fixed chemical composition, the physical property of the ceramics can be altered by controlling the crystal structure. Ceramic systems are often associated with one or more types of defects namely inclusions, voids, pores, and irregular grain sizes, and significantly deteriorate their physical (electrical and dielectric properties) and mechanical properties (e.g., hardness).

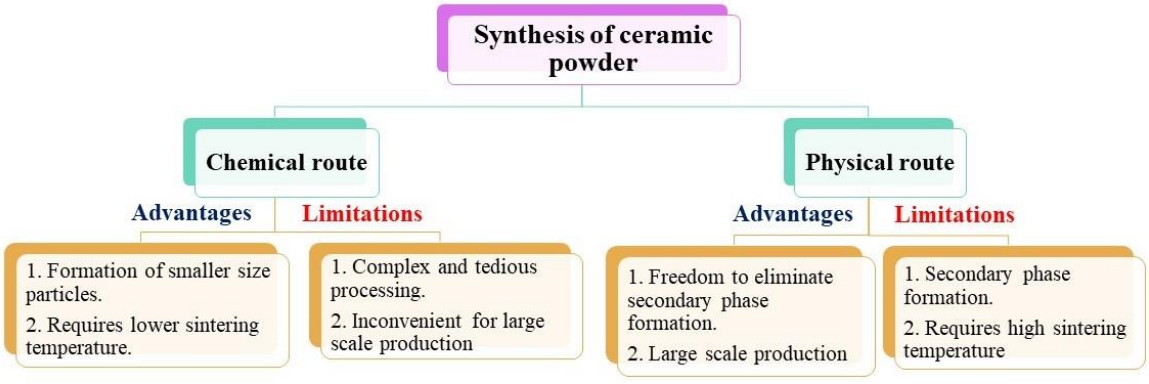

Figure 2.1:Schematic diagram for ceramic powder synthesis methods and corresponding advantages and limitations.

Therefore, it has been always a challenge to fabricate ceramics with minimal defects to achieve the best physical and mechanical properties. The *MTO* based composite ceramics are polycrystalline in nature and grain boundaries also act as a type defect in such systems.

There are various methods to prepare ceramic powders broadly: physical and chemical routes. Both physical and chemical routes have their advantages and limitations as shown in figure 2.1. In the present work conventional solid-state reaction method is used for *MTO* and *MTO* based composite ceramics powder preparation. The conventional solid-state reaction method is explained in detail in figure 2.2.

2.1.1 Conventional solid-state reaction method (CSSR)

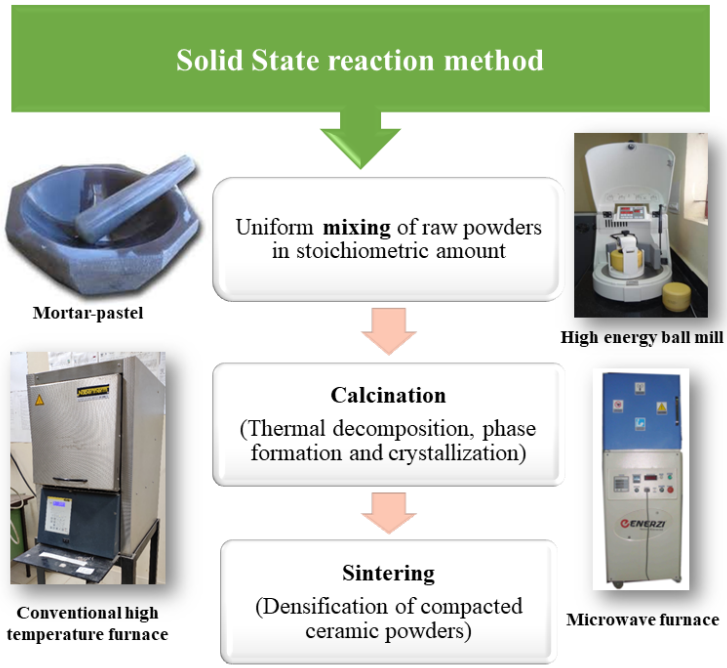

1.

Figure 2.2 Flowchart of the various steps of the synthesis procedure in a conventional solid-state reaction.

Synthesis of desired quality material for the intended application is the first and foremost requirement for research in the field of experimental condensed matter Physics. The conventional solid-state reaction method is one of the well-known techniques for the fabrication of polycrystalline samples in bulk quantity. The conventional solid-state reaction method is a user-friendly, cost-effective, and thermodynamically stable technique. The conventional solid-state reaction method consists of two main stages: uniform mixing of raw powders in stoichiometric quantity followed by calcination of as mixed raw powders. Later the pure phased ceramic powders are carried forward for palletization to obtain densified ceramics.

2.1.2 Preparation of ceramic powders

(a) Stoichiometric weighing of starting materials

The quality and phase of ceramic powders depend on the quality and quantities of initial raw powders. In the presented work, highly pure (> 99.9%) raw oxide powders: MgO, $SrCO_3$, $BaCO_3$, Nb_2O_5, and TiO_2 were procured from Sigma Aldrich. The initial raw powders are weighed (AG135, Mettler Toldo), accuracy ~0.01 mg) as per the stoichiometric ratio as the following chemical reactions for the preparations of *MTO, BNO, STO, BST*, respectively.

$$1.05MgO + TiO_2 \rightarrow Mg_{1.05}TiO_3 + 0.025O_2 \quad (2.1)$$

$$5BaCO_3 + 2Nb_2O_5 \rightarrow Ba_5Nb_4O_{15} + 5CO_2 \quad (2.2)$$

$$SrCO_3 + TiO_2 \rightarrow SrTiO_3 + CO_2 \quad (2.3)$$

$$0.5SrCO_3 + 0.5BaCO_3 + TiO_2 \rightarrow Ba_{0.5}Sr_{0.5}TiO_3 + CO_2 \quad (2.4)$$

(b) Uniform mixing of starting materials

Before the high-temperature treatment, the initial raw powders need to be mixed homogeneously. Since the reactants used are different from each other, a homogeneous mixer can be obtained by high-energy milling and grinding. In this step, the initial reactants (powders) tend to agglomerate, and rapid milling of the reactants stops the formation of agglomeration by the introduction of defects in the grains to enable faster diffusion among the particles. In the present work, the stoichiometrically weighed reactants were homogeneously mixed with zirconia balls of 5 mm diameter in a 1:5 powder to ball weight ratio in a zirconium jar with the help of a planetary ball mill (Pelverisette 6, Fritsch GmbH, Germany) using distilled water as milling media. The speed of the ball mill is set at 120 rotations per minute throughout the mixing process (i.e., 5-10 h). In the milling process, the initial micron-sized particles break down into smaller sizes and come into contact. However, crystallization of the desired phase does not occur at such a low temperature.

(c) Calcination

After uniform mixing of initial reactants in a distilled water medium, the obtained slurry is dried in an oven at 120˚C. The mixed powder is then carried forward to high-temperature treatment (below the melting point) to initiate crystallization as well as phase formation before the sintering process. The required temperature for the ceramic powders varies depending upon their chemical compositions. That heat treatment and temperature are called calcination process and required temperature, respectively. Generally, the calcination process leads to (1) thermal decomposition, (2) phase transitions, and (3) removes volatile

fractions such as carbides, nitrides, etc. In the calcination process crystallite growth and formation of larger particles takes place by bonding and fusing smaller particles. In addition, the carbonates, nitrides, sulfates, and acetate decompose to form solid or volatile gas. The product from the post-calcination process depends on the calcination temperature, environment, heating, and cooling rate. The crystallinity and phase purity of calcined ceramic powders were confirmed by structural characterizations such as X-ray diffraction and Raman spectroscopy.

2.1.3 High density green cylindrical disc preparation:

(a) Particle size reduction

After the confirmation of ceramic phase and crystallinity, the powders were carried forward to cylindrical disc formation and sintering (high-temperature treatment) for electrical and dielectric studies. The Physical properties of the sintered ceramics are related to the structural and microstructural properties of the ceramics. The desired microstructures of the ceramics are possible to attain by proper control of the synthesis process. To get maximum density ceramic discs with minimal defects uniform particle size is desired and further smaller particle size enables better compaction at a significantly lower temperature. Since smaller particles provide a greater surface-to-volume ratio, the reactivity between different particles enhances leading to a lowering of the required sintering temperature. In the present work, the phase pure powders obtained post calcination process were milled in a ball mill maintaining a 1:5 powder to ball weight ratio for another 10 h.

(b) Use of binding agent:

The obtained ceramic powders are non-elastic which made it difficult to press into discs of desired shape and size. Binding agents such as polymers, and clays provide appropriate elasticity and mechanical strength to green discs to sustain throughout the subsequent processes: high-temperature sintering and handling. Among various binders, polymer polyvinyl alcohol (PVA) and polyethylene glycol (PEG) is regarded as best for dry pressed ceramics. Literature suggests, that 3-4 wt% of PVA or PEG transparent solutions are ideal for the fabrication of microwave dielectrics. Low-level usage of PVA does not affect the dielectric properties as it evaporates at around 400˚C. In the current work 5 wt% PVA solution is used as a binder.

(b) Uniaxial die pressing:

The PVA was added to the fine powders and pressed into cylindrical-shaped discs of 10 mm in diameter and 1-5 mm in thickness using KBr hydraulic press (M-20, Technosearch Instruments, India). The applied pressure on the upper part of the die is given by the following equation,

$$P_x = P_a \exp^{\frac{-4\mu KL}{D}} \quad (2.5)$$

where P_x is the pressure gradient; P_a is the applied pressure, μ is the friction coefficient, K is a constant, L and D, are the length and diameters of the die, respectively [59]. In this study, the pressure was applied in uniaxial pressing to prepare the green cylindrical discs.

2.1.4 Sintering:

Sintering is a process where powder compacts and discs are treated at high temperatures to achieve densification and grain growth. Achievement of higher density while maintaining the crystalline phase is crucial to achieving desired dielectric responses. There are two types of sintering processes namely solid-state sintering and liquid phase sintering. In solid-state sintering, process densification takes place by coalescence of solid particles process without any rearrangements, whereas in the liquid phase sintering process a liquid phase will be present during the sintering process. Liquid phase sintering is advantageous in terms of control over microstructures and low processing cost as compared to the solid state sintering process. However, the mechanical properties of the ceramics might get affected in the liquid phase sintering process. In the present thesis work, the solid-state sintering process is adopted. High-temperature microwave furnace (MH1516-000-V6, Enerzi heating reinvented, India) and conventional furnace (LHT 04/18, Nabertherm GmbH, Germany; Temperature range: 25˚C-1800˚C). In timeline sintering process can be divided into three distinguished stages: (i) initial stage: Surface polishing and connections between different particles or grains take place to form neck structure. By the end of this stage, 60-65% relative density can be achieved, (ii)intermediate stage: the neck formed between the different particles and grains grows rapidly through surface diffusion, lattice diffusion and grain boundary diffusion and relative density improved from 65%- 90% at the end of the intermediate stage., and (iii) final stage: densification is much slower in this stage as compared to initial and intermediate stages. In this stage, isolated pores in the grain boundaries and within the grains are removed through the process of grain boundary diffusion and lattice diffusion, respectively. The maximum removal of porosity is possible

when all of the void spaces are connected to fast and short diffusion paths along the grain boundaries. The final stage of sintering begins around 90 - 95 % of theoretical density. The pictorial representation for grain or particle distribution and growth in three different phases is presented in figure 2.3.

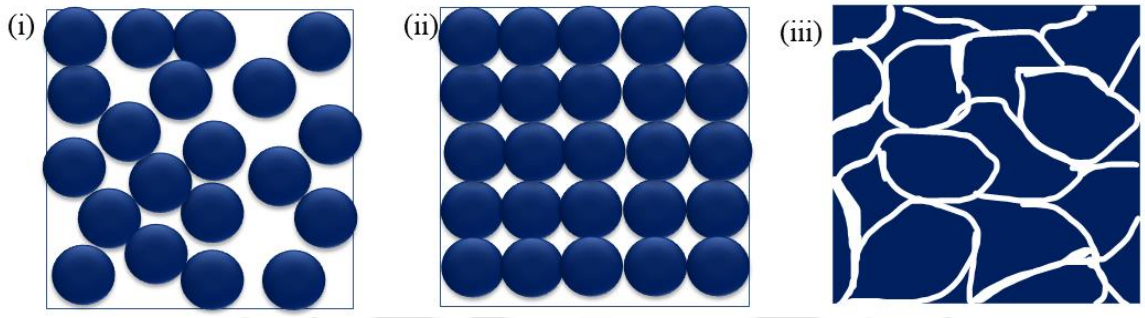

Figure 2.3:(i-iii) initial, intermediate and final stages of the sintering process, respectively.

2.2 *MTO*-based composite thin-film deposition:

Thin films are three-dimensional structures where one dimension is negligible as compared to the other two. Due to the quantum confinement effect in the third dimension (typically ~nm), thin films exhibit interesting and distinguished properties from bulk structures. As miniaturization of structures enables smaller and compact devices, the demand for thin films of requisite characteristics is rapidly increasing. The microstructural characteristics of the deposited thin films significantly affect the physical and mechanical properties. Further, the microstructures of deposited films depend on deposition technique and conditions. Therefore, an optimized deposition technique and methodology are crucial to obtaining desired quality of thin films. Broadly thin film deposition techniques are classified into chemical vapor deposition (CVD) method and physical vapor deposition (PVD) method, respectively.

2.2.1 Chemical vapor deposition method (CVD):

The CVD method is a process of thin film growth where the precursors react in the vapor phase with other gases and gets deposited atom by atom on the substrate. This method can be associated with the production of chemical by-products that are exhausted out of the chamber along with the other unreacted precursor gases. This method is useful for easily volatile precursors.

2.2.2 Physical vapor deposition method (PVD):

The PVD method is used to deposit the thin films by the condensation of vaporized material onto the substrate. This method deals with a purely physical process such as thermal evaporation and sputtering rather than involving a chemical reaction in the case of the CVD technique. In the evaporation technique, the atoms are removed from the source material by heating, whereas in the case of sputtering the atoms are dislodged from the target material by the bombardment of ions. In thermal evaporation, the thermally released atoms move onto the substrate in straight trajectories without any collisions under a high vacuum. Different methods were used to heat the source material such as direct and indirect resistive heating, inductive heating, electron evaporator, arc discharges, laser ablation, and flash evaporation.

2.2.3 Sputtering:

Sputtering is the process where surface atoms are impinged out of a target surface through impact upon the bombardment with high-energy particles: positive ions. Ideally, the free atoms are supposed to be transferred to the substrate surface in a controlled manner atom by atom. For the first time in the year, 1852 Grove discovered the sputtering phenomenon for metals in a cathode glow environment. Generally, for film deposition, the sputtering process requires a chain of atoms through the impact of ions on the target's surface atom. In other words, sputtering of atoms from the target surface arises via the transfer of momentum from energetic projectile (positive ions) to the atoms of the target surface. The chain of free atoms is dependent on both the target material characteristics and the energy of ions. The efficiency of the sputtering technique is measured by sputter yield. The sputter yield (S_Y) is defined as the number of atoms or molecules ejected from a target surface per incident ion and can be expressed as,

$$S_Y = \frac{3\alpha}{4\pi^2} \frac{4m_1 m_2}{(m_1 + m_2)^2} \frac{E_1}{E_b} \qquad (2.6)$$

where, m_1 and m_2 (amu) are the masses of the projectile and target atoms, respectively; α is a dimensionless parameter, which depends on the ion energy and mass ratio, E_1 and E_b are the kinetic energy of the projectile and the binding energy of the surface atoms, respectively. At lower energies, an incoming ion transfers the maximum momentum to target atoms when both masses are equal ($m_1 = m_2$).

Generally, the positive ions (projectiles) used to sputter the target surface are obtained through the glow discharge produced due to the potential difference between the anode and cathode at significantly low pressures in a closed chamber. At a minimum potential difference, the gas present inside the chamber breaks down to conduct. The nature of glow discharge depends on both the applied voltage and ionization current. When the glow is maintained at constant applied voltage is known as a normal glow whereas in an abnormal glow along with ionization current applied voltage also increases. In the discharge tube, the whole region from cathode to anode can be divided into a number of regions as shown in figure 2.4. Firstly, the cathode glow: a luminous region, which covers the cathode partially in the normal glow and completely in the abnormal glow. Next to the cathode glow, a region with relatively low luminosity is known as a cathode dark space. It is the most important region because most of the applied voltage will drop across it. Further in the sequence, a bright negative glow region, Faraday dark space, and positive column region appear.

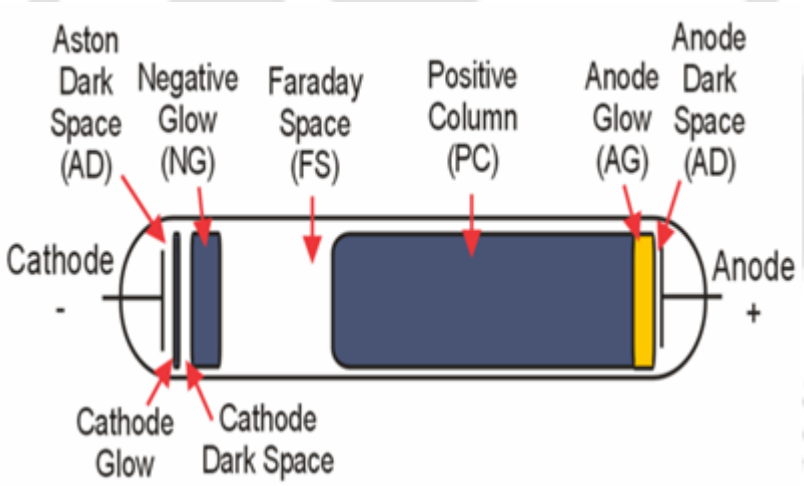

Figure 2.4:A schematic representation of different glow discharge regions.

At the beginning of the discharge, the primary electrons from the cathode are accelerated by the electric field near the cathode and ionize the gas molecules. If the energy of the primary electrons is more than the ionization energy the gas molecules generate positive ions upon collision before they reach the anode. When produced positive ions energetically bombard the cathode surface, they knock out the target atoms and secondary electrons. These secondary electrons will also create more positive ions leading to a self-sustained discharge.

There are four different types of sputtering: (a) direct current (DC) sputtering, (b) radio frequency (RF) sputtering, (c) magnetron sputtering, and (d) reactive magnetron sputtering.

(a) DC sputtering:

DC sputtering method is the simplest form of cathodic or diode sputtering. In this method, the target material is connected to the negative terminal of a DC power supply, whereas the substrate is placed on an anode, which may be biased. The sputtering chamber will be filled with an inert gas, typically argon (Ar), which serves as a medium in which the glow discharge is initiated under the application of DC voltage. The Ar atoms will be ionized (Ar^+) in the applied potential and accelerated towards the cathode and eject the atoms from the target material. These sputtered atoms transfer through the glow discharge and deposit onto the substrate. However, the main disadvantages are low deposition rates, high discharge voltages, high gas, and low plasma densities, and used only for conducting targets.

(b) RF sputtering:

In DC sputtering method for a conducting target, when Ar ions bombard the target surface makes electrons free along with sputtered atoms, and, Ar ions convert into neutral Ar gas after accepting generated free electrons. However, for an insulating target, Ar ions accelerated towards the target will eject out sputtered atoms and remain there leading to the formation of a layer of positive ions on the target surface since unlike metals insulators do not contain free electrons to neutralize the positive ions. This layer of positive ions near the target surface will repel the positive ions and puts an end to the sputtering process. The application of RF signal to the cathode solves this problem, where each terminal will alter its polarity periodically. This type of sputtering is called RF sputtering. In this technique, a frequency of 13.56 MHz is applied to the cathode via an impedance matching network.

RF voltages can be coupled with any kind of impedance and thus removes restrictions on the choice of electrode material. Therefore, in RF sputtering technique insulating target and the substrate holder can also act as electrodes. As the RF power is applied, then electrons follow the RF signal and oscillate between the electrodes and acquire sufficient energy for ionizing collisions and sustaining the plasma. A blocking capacitor will also be connected in between the RF power supply and cathode to avoid shorting the target to the ground. In the positive half cycle, the target acts as an anode and acquires electrons and during the negative

half cycle, it will acquire enough ions and resulting in the sputtering as well as deposition of the target material.

(c) Magnetron sputtering:

In usual DC or RF sputtering techniques, the efficiency of the ionization process decreases when electron energy exceeds an optimum value as those electrons reach the anode without taking part in the ionization process. These limitations can be conquered in the magnetron sputtering systems by trapping electrons near the cathode surface using permanent magnets. In magnetron sputtering, a magnetic field (B) is applied parallel to the cathode surface, while the electric field (E) acts normal to the surface. The magnets are arranged in such a way that one of the poles is positioned at the center of the target, and the other pole is placed near the edge of the target, which can form the magnetic field lines.

The electrons emitted from the cathode and moving with velocity component perpendicular to the magnetic field will spiral around the magnetic field lines and be trapped by the field. The trapping of electrons can significantly enhance the probability of ionization efficiency, which results in a high rate of deposition onto the substrate even at lower working pressures. This technique can be used in both DC and RF sputtering.

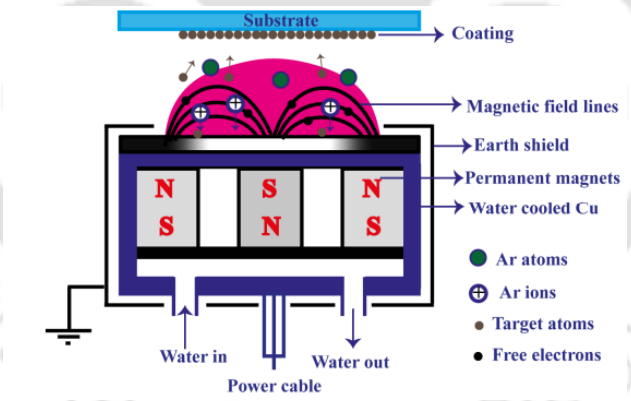

Figure 2.5: Schematic diagram for magnetron sputtering system.

(d) Reactive magnetron sputtering:

In general, an inert gas (argon) is used as sputtering gas to avoid the chemical reactions between the target and sputtered gas to retain the chemical composition. However, for the deposition of nitrides and oxides, reactive gases are added with argon to induce reactions with sputtered materials. This type of sputtering process is called reactive magnetron sputtering. The addition of reactive gases to the sputtering chamber can significantly affect the deposition rate and stoichiometry of the compound. In the present

thesis, RF reactive magnetron sputtering system (M/s Advanced Process Technologies, Pvt. Ltd., India) has been used for the deposition MTO based composite thin films. The photographic image of the RF reactive magnetron system is shown in Figure 2.6.

Figure 2.6: RF reactive magnetron sputtering system.

The sputtering system consists of a vacuum chamber equipped with pumping systems, a sputtering source, a heating assembly, and a rotating substrate holder. A two-inch target is power-driven by an RF generator (M/s RF VII, Inc. RF-3-XIII) through an impedance matching network. The high vacuum (~10^{-6} mbar) in the system is achieved by a turbo molecular pump (M/s Leybold vacuum, TD20). In the present work, both reactive (Ar and O_2) and non-reactive (Ar) type sputtering techniques were followed to deposit MTO-based composite thin films.

2.3 Characterization techniques

2.3.1 X-Ray diffraction

X-ray diffraction (XRD) is one of the most widely used non-destructive material characterization tools. The diffraction pattern obtained by XRD provides about the material's crystal structure, crystallinity, and chemical composition both qualitative and quantitively. Bragg's Law is regarded as the governing equation for the X-ray diffraction technique and can be expressed as

$$n\lambda = 2d \sin\theta \qquad (2.7)$$

where n is (integer) the order of reflection, d, λ, and θ are the interplanar spacing of crystal, the wavelength of incident X-ray, and angle of incidence of the X-rays, respectively.

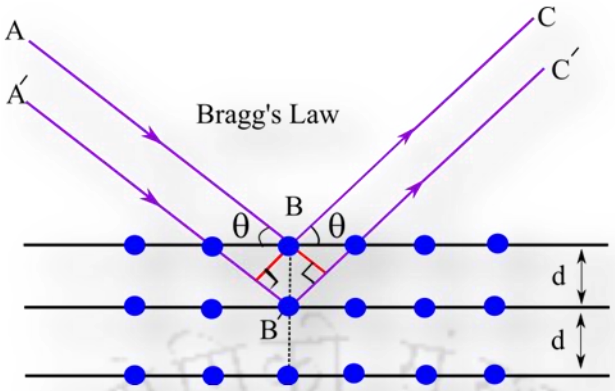

Figure 2.7: *Bragg's law for X-ray diffraction in a crystal lattice.*

Figure 2.7 and Figure 2.8 present Bragg's Law of diffraction from perfectly crystalline lattice and schematic representation for X-ray diffractometer, respectively. The diffracted X-rays exhibit constructive interference when the distance between ABC and A'B'C' paths ($2d\sin\theta$) is differed by an integer number of λ.

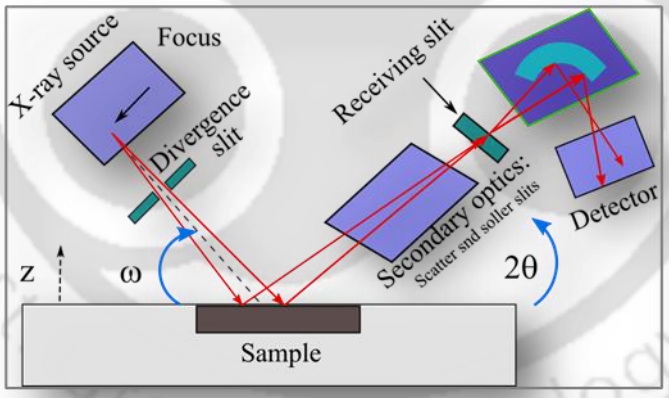

Figure 2.8: Schematic diagram for X-ray diffractometer.

In this thesis, X-ray diffractometer (TTRAX-III 18 kW, Rigaku,) with Cu K_α (λ = 1.5406 Å) radiation was used to characterize the MTO-based ceramics and thin films. Figure 2.9 shows the photographic image of the X-ray diffractometer employed in the present work. The XRD patterns of the prepared *MTO*-based ceramics and thin films were measured with a scanning step size 0.03° and a scanning rate 3°/minute between the 2θ range of 15-80°. The 2θ calibration was performed using a standard Si sample to account for the instrumental line

broadening approximately equal to the 0.15°. Furter, Rietveld refinement is employed using FullProf software for qualitative and quantitive analysis of X-ray diffraction patterns for MTO-based composite ceramics and thin films [60]

Figure 2.9: Photograph image of the X-ray diffractometer.

2.3.1 Density measurement

Archimedes' method is used to evaluate the relative density of the sintered pellets of *MTO*-based composite ceramics. The Archimedes principle states that "a body (pellet) fully or partially sink in a fluid is lifted by an upward force equal to the weight of the fluid displaced". The difference between the actual weight of the body to the magnitude of the buoyance force (upward force) is equal to the apparent weight of the body. The apparent density (ρ_a) of the sintered pellets can be estimated by using the following equation,

$$\rho_a = \left(\frac{w_1}{w_2 - w_3} \right) \times \rho_w \qquad g/cm^3 \tag{2.8}$$

where, ρ_w is the density of the liquid, and w_1, w_2, and w_3 denote the weight of the body in the air, sunk in the liquid medium, and weight of the body after being removed from the liquid medium, respectively. In the thesis work, distilled water is (ρ_w = 1 gm/cm^3) used as the liquid medium. In addition, the relative density of the pellets was by using apparent density (ρ_a) and theoretical density (ρ_{th}) determined as the following equation

$$relative\ density = \frac{\rho_a}{\rho_{th}} \times 100\% \tag{2.9}$$

2.3.2 Raman spectroscopy

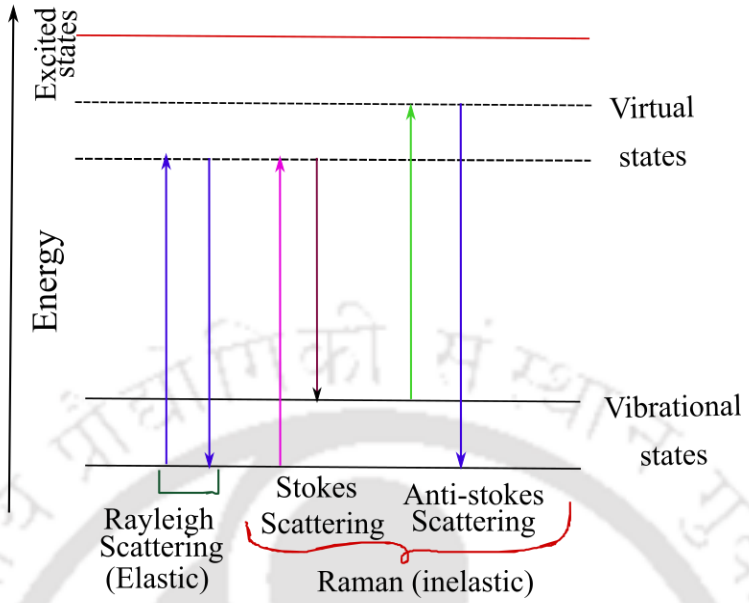

Figure 2.10: Energy level diagram for Rayleigh and Raman Scattering.

Raman spectroscopy is a technique used to detect molecular vibrations based on Raman scattering. The phenomenon of inelastic scattering of light was first postulated by Smekal in 1923, and Raman and Krishnan observed the Raman scattering phenomenon for the first time in the year 1928 [2]. The spectral pattern obtained by Raman spectroscopy is unique to a substance. Raman spectroscopy provides information about chemical structures and physical forms chemical composition of the material and does not require any sample preparation. Thus, Raman spectroscopy is a user-friendly tool to characterize material as a sample of any form such as solids, liquids, and gases.

As shown in figure 2.11, the monochromatic laser beam falls and interacts with the molecule of the sample and a small fraction of light may be scattered either elastically or inelastically. The wavelength of inelastically scattered light is either higher or lower than incoming light, which is called a Raman effect. The Raman spectra are composed of two types of scattered lights namely Stokes and anti-Stokes. As shown in figure 2.10 the inelastically scattered lights having higher energy and lower energy compared to the incident beam are known as Stokes and anti-Stokes, respectively. . The fraction of incident light exhibiting elastic scattering possesses energy equal to the energy of the incident radiation and such radiations are known as Rayleigh lines. At room temperature, the Stokes lines are more intense than that of anti-Stokes lines. Therefore, in conventional Raman spectroscopy, Stokes

lines are utilized. The magnitude of the Raman shift is basically independent of the wavelength of the incident radiation

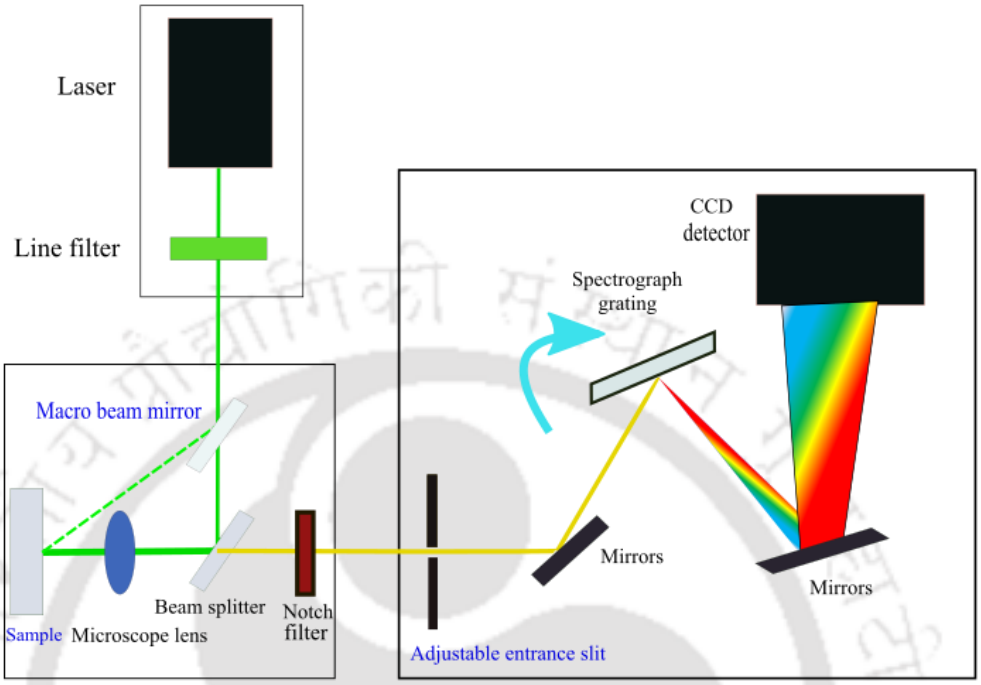

Figure 2.11:Schematic experimental setup for Raman spectroscope.

. For liquid samples, water is used as an ideal solvent as water exhibits negligible Raman scattering.

Figure 2.12: Photograph of Raman spectrometer (LBRAM HR800).

However, the solid samples can be directly mounted on a glass substrate to perform the measurements equipped with optical components (mirror, lens, sample cell) in a Raman spectrophotometer[61–63]. In the present thesis, the room temperature Raman spectra of *MTO*-based composite ceramics and thin films were recorded by using the LABRAM HR800 Raman spectrometric analyzer developed by Horiba Jobin Yvon with an excitation wavelength of 488 nm of an Ar-ion laser and spectral resolution of 1 cm^{-1}

Figure 2.12 presents the photograph of a Raman spectrometer. The setup is equipped with a separate heating/cooling sample stage (THMS600, Linkam). The Raman spectra were recorded in a backscattered geometry furnished with a 50× objective, an edge filter, and a Peltier-cooled charge-coupled device detector. An Ar^{+} ion excitation (λ = 514 nm) laser source equipped with a high-resolution dispersive geometry and an 1800 mm^{-1} grating is utilized for low-temperature micro-Raman measurements. The grating was fixed during the entire temperature scan for a high degree of positional accuracy.

2.3.3 Scanning electron microscopy

The morphology and elemental composition analysis for prepared MTO-based composite ceramics and thin films were obtained by scanning electron microscopy (SEM) (1430 VP, LEO) equipped with an energy dispersive X-ray spectrometer (EDS) and field emission scanning electron microscope (FESEM) (Sigma 300, Zeiss). The schematic diagram of the SEM is shown in Figure 2.13. In scanning electron microscope provides images of surface morphology with high-energy electrons in a raster scan pattern. The high-energy electrons are generated by thermionic emission from a tungsten filament and accelerated towards an anode with sufficient kinetic energy. FESEM is a new version of electron microscope where field emission electrons are utilized to scan the sample surface. When a highly energetic electron beam incident on the sample surface it undergoes both elastic and non-elastic scattering and produces a number of signals such as secondary electrons, backscattered electrons, Auger electrons, photons, characteristic X-rays, diffracted and transmitted electrons. For surface morphology secondary electron and backscattered electron signals are utilized whereas, photons are used for chemical composition estimation. Energy analysis of Secondary electrons and backscattered electrons provide topographic images and composition details of the test sample, respectively. The energy dispersive spectrometer utilizes the characteristic X-rays obtained from the sample electron interaction and produces a spectrum of the peaks that correspond to the energy levels of detected X-rays. The intensity

of the individual peak signifies the concentration of elements present in the test sample. Figure 2.14 shows a photograph of the field emission scanning electron microscope that was used in the present study.

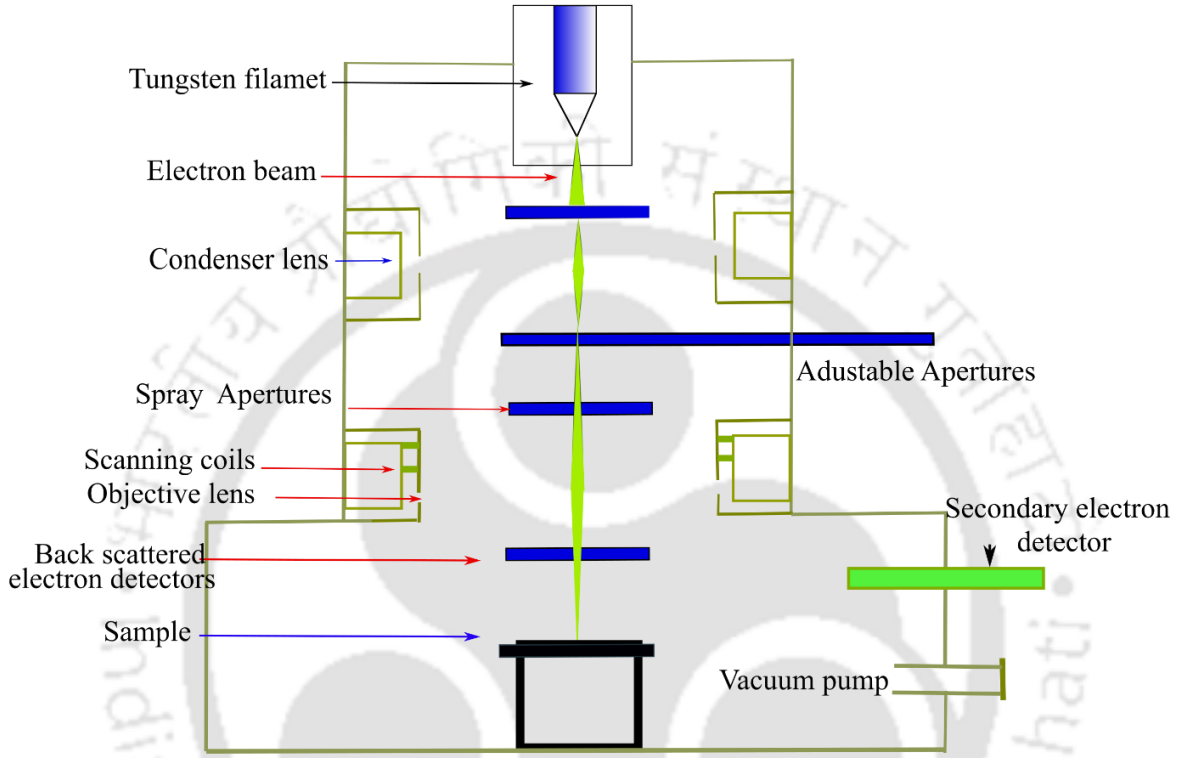

Figure 2.13: The schematic diagram of a scanning electron microscope setup.

Figure 2.14: Photograph of field emission scanning electron microscope.

2.3.4 Field emission transmission electron microscopy

The field emission transmission electron microscope (FETEM) is one type of electron microscope that utilizes transmitted electrons through the material to characterize it. FETEM characterizes the crystal structure, dislocation, and grain boundaries of nanoparticles or nanocrystals. As shown in figure 2.15 complete FETEM setup can be classified into four different parts: (a) electron gun: is the source of highly energetic electrons and tungsten filament is used for this purpose. It has a cathode and anode pair to accelerate the emitted electrons from tungsten filaments (b) electromagnetic lens system: consists of an electromagnetic lens and metal aperture to focus the electron beam, (c) the sample holder; is a stage equipped with a mechanical arm to hold and control the position of the specimen, (d) imaging system.

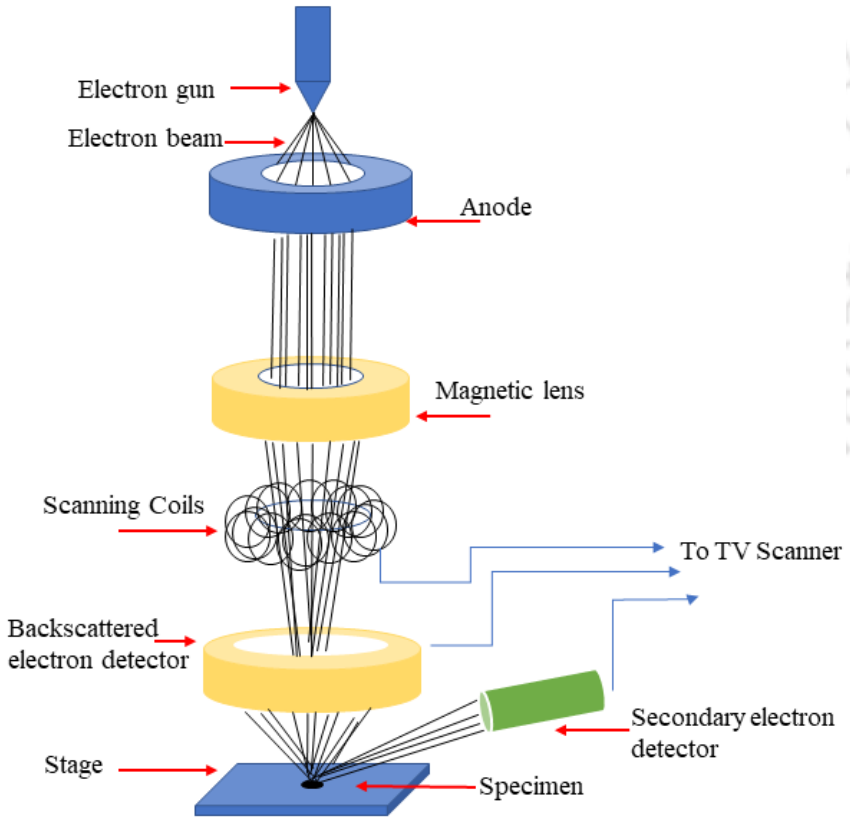

Figure 2.15: The schematic outline of a FETEM.

The FETEM works like a slide projector. A projector shines a beam of light that transmits through the slide. The patterns painted on the slide only allow certain parts of the light beam to pass through. Thus, the transmitted beam replicates the patterns on the slide, producing an enlarged image of the slide when it falls on the screen. In the present thesis, the

FETEM instrument (2100F, JEOL) is employed to study morphology and the crystallographic structure of the prepared samples was analyzed by bright-field TEM image, high-resolution transmission electron microscopy (HRTEM), and selected area electron diffraction (SAED) in some of the papers. Figure 2.15 shows the schematic diagram of the TEM instrument used in the present study. The figures themselves explain in detail the individual parts of the instrument and the arrangements of the TEM instrument. The resolution of the instrument is 1.9 Å to 1.4 Å (lattice) with accelerating voltage 60 to 200 kV in 50 V steps and a tilt of ± 25^{o}. The magnification range of standard specimens goes from 50 X to 1,500,000 X which is a very sophisticated instrument for the characterization of nanomaterial. It also has a high-resolution CCD (charge-coupled device) camera with 2.672 x 2.672 K resolution providing very high-resolution images of the samples.

2.3.5 Dielectric measurements and impedance spectroscopy

The relative permittivity (ε_r) and loss tangent ($tan\delta$) are the most important parameters to understand the various types of polarization mechanisms (e.g., electronic, atomic, dipolar polarization, and space charge polarization) present in the sample. Frequency-dependent dielectric studies provide information about dielectric relaxation of various polarization mechanisms such as space charge polarization, ionic polarization, atomic polarization, and dipolar polarization. In addition, temperature-dependent dielectric response exhibits phase transitions present in the sample. In the present thesis work, to record dielectric response, sintered 1-2 mm thick MTO based composite ceramics were coated with the silver paste to make metal-insulator-metal (MIM) capacitors. For *MTO* based composite thin films n-type Si substrate and Al coating are used as bottom and top electrodes, respectively. The low frequency (20 Hz -1 MHz) dielectric properties of the prepared *MTO* based composite ceramics and thin films were measured in the temperature range of 25 ˚C - 300 ˚C employing an LCR meter (1J43100, Wayne Kerr Electronics Pvt. Ltd.) controlled by PID controller (3216, Eurotherm) with an accuracy of ± 1.5 ^{o}C. The high frequency (1 MHz -1 GHz) dielectric properties of the *MTO* based composite ceramics were measured using the RF impedance material analyzer (E4991A, Agilent Technologies,) in the wide temperature range of -160˚C – 400 ˚C with the stability of 0.01 ^{o}C due to the 4 channel Quatro controller containing PID control algorithms (Novocontrol, Concept 70). The low-temperature measurements were carried out using liquid nitrogen as a cooling or heating medium.

Impedance spectroscopy is an extensively utilized technique to understand the electrical properties of the material. The AC voltage and current of an electrical network can be expressed in the following equations

$$V(t) = V_0 \exp(j\omega t) \tag{2.10}$$

$$I(t) = I_0 \exp(j\omega t + \varphi) \tag{2.11}$$

where, j = √-1, ω and φ represent an angular frequency and the phase angle, respectively. The complex impedance (Z*) can be expressed in terms of both magnitude ($|Z|$) and phase angle (φ) as,

$$Z^*(\omega) = |Z| \exp(-j\varphi) \tag{2.12}$$

$$Z^*(\omega) = |Z| \cos(\varphi) - j|Z| \sin(\varphi) \tag{2.13}$$

$$Z^*(\omega) = Z'(\omega) - jZ''(\omega) \tag{2.14}$$

where, $Z'(\omega)$ and $Z''(\omega)$ are the real and imaginary parts of complex impedance, and

$$|Z| = \sqrt{[Z'(\omega)^2 + Z''(\omega)^2]} \tag{2.15}$$

2.3.6 Atomic force microscope

Figure 2.16 presents a schematic diagram of an atomic force microscope (AFM). Atomic force microscope (AFM) is a powerful imaging technique to produce topographical images that quantify surface morphology, size, the surface roughness of nanoscale samples. A 3-dimensional profile of the sample surface can be obtained from AFM [64,65]. AFM consists of a flexible cantilever with a sharp tip (silicon or silicon nitride), scanner, controller, and signal processing unit. The tip scans the sample surface and produces the surface topography depending on the interactions between the tip atoms and surface atoms. The Van der Waals forces between atoms at the tip and the sample surface lead to a deflection of the cantilever according to Hooke's law. This deflection is measured using a laser reflected from the top surface of the cantilever to a photodetector shown in Figure 2.16. Further, the detected signals send to the signal processing unit to produce the topography image along with amplitude and phase. In this thesis, the atomic force microscope (Cypher, Oxford) was used

to obtain AFM images of the *MTO*-based thin films, and further, the surface roughness, 3D and 2D image processing were done using WSxM 4.0 Beta software [64].

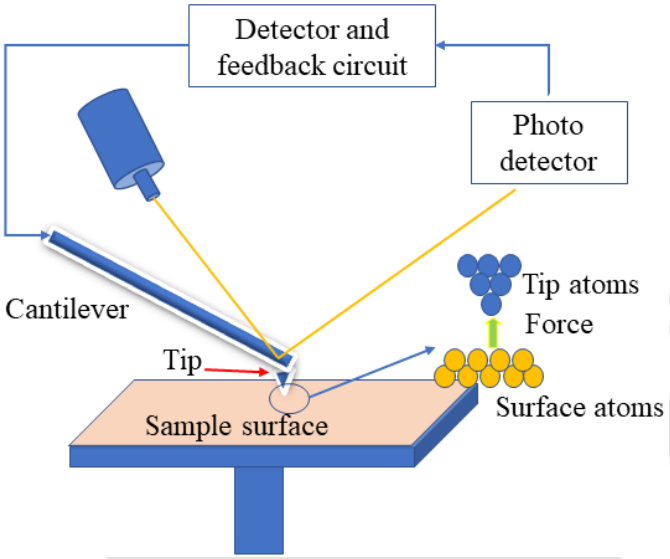

Figure 2.16: Schematic diagram of the atomic force microscope.

2.3.7 Optical characterization

In the present work, the optical properties of *MTO* based composite thin films have been analyzed by employing a UV-VIS-NIR spectrophotometer (UV 3101PC, SHIMADZU)

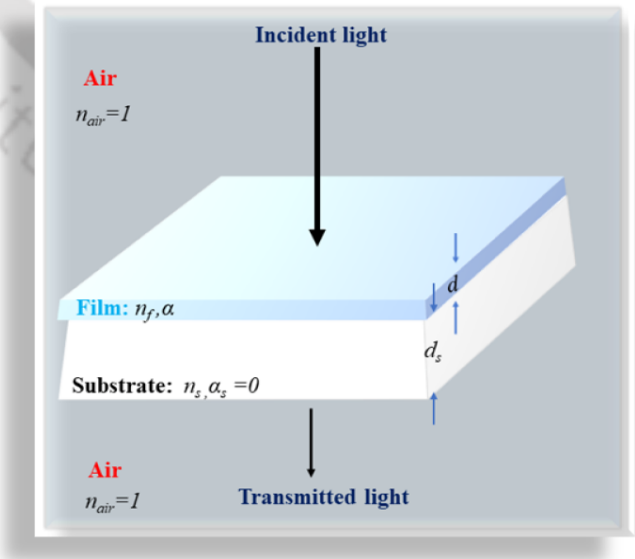

Figure 2.17: Schematic diagram of light transmittance through different interface mediums of the thin film.

The fundamental optical constants such as linear refractive index (n), packing density (p), absorption coefficient (α), and optical bandgap (E_g) can be calculated from transmission spectra. In addition, the film thickness can also be calculated by this method. The optical parameters of thin films can be calculated by using transmittance spectra by the Swanepoel envelop technique [65]. Optical transmission through a film of refractive index n with the thickness d deposited onto any transparent substrate having the refractive index n_s and thickness d_s as shown in Figure 2.17. When a light incident on the film, then some fraction of an incident is reflected and the rest is transmitted at the interfaces of air-film, film-substrate, and substrate-air. The reflected and transmitted light exhibit the interference pattern since the beams originated from a single coherent source. The typical transmittance spectrum of a film deposited onto a transparent substrate measured in the wavelength range of 200 -1000 nm is shown in Figure 2.18.

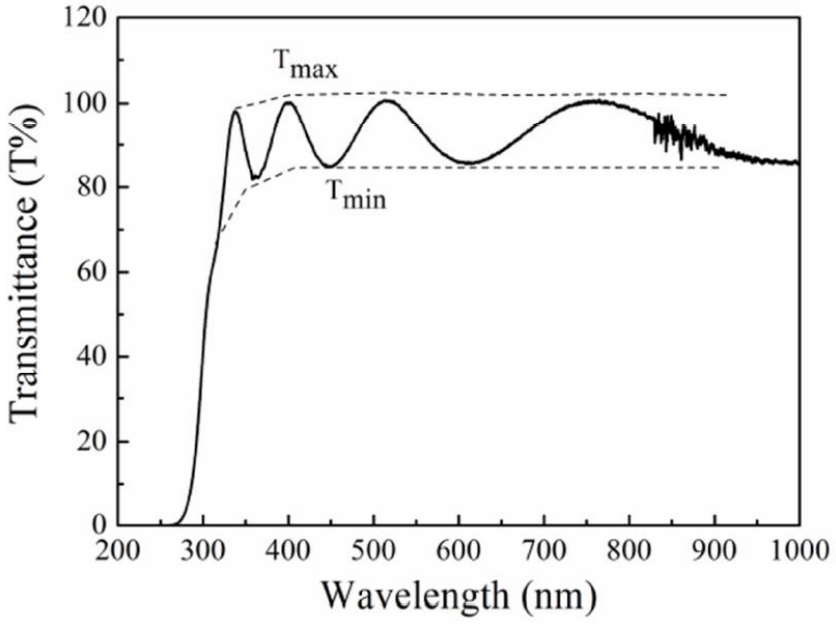

Figure 2.18: Fabry-Perot transmittance spectrum of a thin film.

The refractive index (n) of the film can be calculated by using Swanepoel's envelop method based on the following expressions.

$$n = \left[N + (N^2 - n_s^2)^{0.5} \right]^{0.5} \qquad (2.16)$$

where,
$$N = 2n_s \left(\frac{T_M - T_m}{T_M T_m} \right) + \left(\frac{n_s^2 + 1}{2} \right) \qquad (2.17)$$

$$n_s = \frac{1}{T_s} + \sqrt{\frac{1}{T_s^2} - 1} \tag{2.18}$$

here, n_s is the substrate refractive index, T_M and T_m are the transmittances at maxima and minima at certain wavelength λ, respectively.

The thickness of the film (d) can be estimated by the following expression,

$$d = \frac{\lambda_1 \lambda_2}{2(n_1\lambda_2 - n_2\lambda_1)} \tag{2.19}$$

where, n_1 and n_2 are the refractive indices of two adjacent maximum and minimum at wavelengths λ_1 and λ_2, respectively.

According to Beer-Lambert's law,

$$I = I_0 \exp(-\alpha d) \tag{2.20}$$

where I_0 is the incident light intensity, I is the intensity of the light at wavelength λ, d is the thickness of the film and α is the absorption coefficient, which can be related to the transmittance as,

$$\alpha = \frac{-\ln T_\alpha}{d} \tag{2.21}$$

where, $T_\alpha = (T_M T_m)^{0.5}$.

Further, the optical bandgap (E_g) of the films can be estimated using the Tauc relation by the following relation[66].

$$(\alpha h\nu)^m = B(h\nu - E_g) \tag{2.22}$$

where, $h\upsilon$ is the incident photon energy, m (m =2 for direct transition and m = 0.5 for indirect transitions) determines the type of electronic transition between the valence band and conduction band and B is the measure of crystalline order. The E_g of the films can be calculated from the extrapolated linear portion of $(\alpha h\upsilon)^m$ versus ($h\upsilon$) curve, In the present study, the E_g has been calculated by assuming an allowed direct electronic transition (m=2). The error associated with the measurement of n and d is ±0.02 and ±10 nm, respectively.

2.3.8 Microwave dielectric characterization

With an increase in demand for the development of high-speed, high-frequency devices complete understanding of the properties of materials functioning at microwave frequencies is necessary. In general, the microwave methods for materials characterization are categorized into two types: non resonant methods and resonant methods. Non resonant methods are often used to obtain a general knowledge of electromagnetic properties over a wide frequency range, while resonant methods are used for low loss dielectric materials to get accurate knowledge of dielectric properties at a single microwave frequency or several discrete microwave frequencies[67]. The presence of air gaps is one of the most important factors limiting the measurement accuracy of high permittivity solid materials unless the electric field of the mode of interest does not have a component perpendicular to the surfaces of the sample. This is the situation for TE_{0np} modes of cylindrical cavities and dielectric resonators. Therefore, methods employing these modes are considered to be among the most accurate[68]. The quasi -$TE_{01\delta}$ mode of operation (often called the TE_{011} - mode) is the mode most commonly used by manufacturers of dielectric materials for making dielectric loss tangent measurements.

The important characteristics of a dielectric resonator (DR) are dielectric constant, loss tangent, and temperature dependence of resonant frequency. The permeability of most of these materials is equal to that of free space, as they are nonmagnetic materials. A parallel plate dielectric resonator structure known as the Courtney setup is used to measure the dielectric constant of the bulk dielectric material. The principle involved in the measurement is rather simple. The resonant frequency of a $TE_{01\delta}$ mode is measured for a dielectric resonator radius '*a*' and height '*L*'. Afterward, the dielectric constant is computed using the Courtney procedure. Hakki and Coleman first introduced the procedure. The error analysis and investigation of temperature effects were later made by Courtney[69]. Another cylindrical cavity made of invar is used to measure the temperature coefficient of the resonant frequency of the cylindrical DR. The negligible coefficient of thermal expansion of invar material helps to increase the accuracy of this measurement.

2.3.8.1 Vector network analyzer

In microwave engineering, a network analyzer is a major instrument used to investigate a wide variety of materials, components, circuits, and systems. A measurement of the reflection from or transmission through a material along with knowledge of its physical

dimensions provides the information to characterize the permittivity and permeability of the material. Network Analyzer is a swept frequency measurement equipment to completely characterize the complex network parameters in comparatively less time without any degradation in accuracy and precision. Two types of network analyzers are available: scalar and vector network analyzers. Scalar network analyzer measures only the magnitude of reflection and transmission coefficients while the vector network analyzer measures both the magnitude and phase. Note that the magnitude and phase of a component can be critical to the performance of a communication system. A vector network analyzer can provide information on a wide range of these devices, i.e., from active devices such as amplifiers and transistors to passive devices such as capacitors and filters.

A basic network analyzer is designed to show graphically a plot of the voltage gain or loss of a network versus frequency. The network analyzer measures the magnitude, phase, and group delay of two-port networks to characterize their linear behavior. A vector network analyzer consists of a signal source, a receiver, and a display. The source launches a signal at a single frequency to the material under test. The receiver is tuned to that frequency to detect the reflected and transmitted signals from the material. The measured response produces the magnitude and phase data at that frequency. The source is then stepped to the next frequency and the measurement is repeated to display the reflection and transmission measurement response as a function of frequency. The ratio of the output to the input level is displayed as dB which is the voltage gain or loss of the network.

Consider a circular cylindrical rod of relative dielectric constant ε_r, permeability μ_0, length L, and radius placed between two large perfectly conducting plates. If the dielectric material is isotropic, then the characteristic equation for this resonant structure operating in the TE_{0nl} mode is

$$\alpha \frac{J_0(\alpha)}{J_1(\alpha)} = -\beta \frac{K_0(\beta)}{K_1(\beta)} \tag{2.23}$$

where $J_0(\alpha)$ and $J_1(\alpha)$ are the Bessel functions of the first kind of orders zero and one, respectively, $K_0(\beta)$ and $K_1(\beta)$ are the modified Bessel functions of the second kind of orders zero and one. The parameters α and β depend on the geometry, the resonant wavelength, and dielectric properties. Thus,

$$\alpha = \frac{2\pi a}{\lambda_0}\left[\varepsilon_r - \left[\frac{c}{v_p}\right]^2\right]^{1/2} \tag{2.24}$$

$$\beta = \frac{2\pi a}{\lambda_0}\left[\left(\frac{c}{v_p}\right)^2 - 1\right]^{1/2} \tag{2.25}$$

c is the velocity of light and v_p the phase velocity in the structure so that

$$\frac{c}{v_p} = \left(\frac{l\lambda_0}{2L}\right) \tag{2.26}$$

where l is the number of longitudinal variations of the field along the axis, L is the Length of the DR, D is the Diameter of the DR, λ_0 is free space resonant wavelength. It is seen that the characteristic equation is a transcendental equation and hence, a graphical solution is necessary. The resulting mode charts are given by Hakki et al.[69] where each value of β_l corresponds α_n. The characteristics equation and the resulting charts are universal as per as permittivity is concerned.

In the present investigation, a vector network analyzer (VNA, Rohde & Schwarz, P50282A) was used to the measurement of microwave dielectric properties of *MTO* ceramics.

2.3.8.2 Measurement of dielectric constant (ε_r)

This can be done by using the transmission method introduced by Hakki and Coleman and modified by Courtney. This setup is having two parallel plates with an adjustment for the varying distance between the two plates. Two bent monopoles (rigid coaxial cables) are provided for coupling electromagnetic waves to the DR and are suitably mounted to move in any of the *x*, *y*, and *z* directions. One can identify the modes of the DR by moving the bent monopoles in all three directions. The number of standing waves in *z* - directions indicates the third subscript of resonant mode. By rotating the rigid coaxial cables around their axis, it is possible to find the maximum field in the horizontal direction or vertical direction. Subsequently, the first subscript can be found by placing the coaxial cable at different angles in the plane of parallel plates. Once the resonant frequency of $TE_{01\delta}$ mode is measured, the relative dielectric constant for the dielectric resonator with known dimensions can be calculated using the equations (2.27) and (2.28).

$$\beta_l = \frac{2\pi a}{\lambda_0}\left[\left(\frac{l\lambda_0}{2L}\right)^2 - 1\right]^{\frac{1}{2}} \tag{2.27}$$

$$\varepsilon = \left(\frac{\alpha_n \lambda_0}{2\pi a}\right)^2 + \left(\frac{l\lambda_0}{2L}\right)^2 \qquad (2.28)$$

where β_l corresponds to α_n, which can be obtained from the mode chart given in [25] one of the characteristic equations.

2.3.8.3 Measurement of unloaded quality factor (Q_u)

To measure the Q factor of microwave resonators, various methods are applied. However, all the existing methods do not take an account noise, crosstalk, coupling losses, transmission line delay, and impedance mismatch related to real measurement setup. Thus, significant uncertainty is associated with the measured Q factor of the DR.

In the present study, a transmission mode cavity was proposed by Krupka et al.[70] is utilized to measure the unloaded quality factor of the DR. This measurement is done using the reflection method by placing the sample over a low loss quartz spacer with a height of 4 mm inside a cylindrical copper cavity having 10 mm height and 24 mm diameter (inner dimensions). The inner side of the cavity was finely polished and silver plated to reduce radiation loss. The use of a low-loss single quartz spacer reduces the effect of losses due to the surface resistivity of the cavity. Samples with a diameter/length (D/ L) ratio of 1.8 – 2.2 are preferable to get maximum mode separation and to avoid interferences from other modes. Microwaves are fed into the sample using the loop coaxial antennas, which provide a magnetic coupling to excite the transmission mode resonance spectrum of the dielectric cylinder. The rigid coaxial cable is provided at the center of the cavity (as shown in Fig. 2.19 (a)) for electromagnetic field coupling and it can be moved in and out for adjusting between the weak and strong coupling.

The cavity is connected to the VNA through a rigid coaxial cable with connectors on both ends (THRU). The network analyzer is set in S_{21} mode and performs calibration. The coaxial cable is adjusted in such a way that weak coupling exists between the rigid coaxial cable and DR. By identifying the $TE_{01\delta}$ mode, the resonant frequency can be obtained. The 3 dB bandwidth of the spectrum to calculate the loaded Q factor (Q_l), from the resonance spectrum (Fig. 2.19(b)) is given by,

$$Q_l = \frac{f_0}{\Delta f} \qquad (2.29)$$

One can assume that the unloaded *Q* factor is equal to the loaded *Q* factor if the coupling is weak (S_{21} at resonance < 45 dB, and couplings are symmetric). The unloaded Q_u value is calculated using the coupling coefficient β_c, and the loaded Q_l value using the relation [30],

$$Q_u = \frac{Q_l}{(1-\beta_c)} \tag{2.30}$$

where β_c is the coupling coefficient is equal to $10^{\frac{-S_{21}}{20}}$. A further rigorous electromagnetic analysis must be performed to evaluate the dielectric constant of the sample under test. Rayleigh-Ritz's method has been used in the computer program for calculating the dielectric constant.

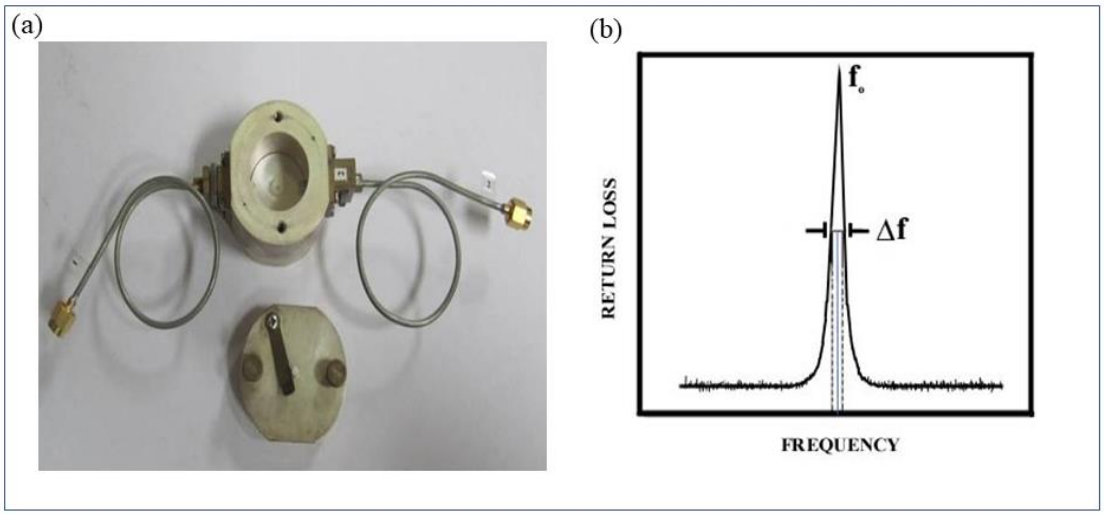

Figure 2.19: (a) QWED Krupka resonator cavity used to measure the Q- factor and dielectric constant (b) the method of calculating Q- factor from resonant mode using Eq. 2.29.

2.3.8.4 Measurement of temperature coefficient of resonant frequency (τ_f)

The temperature coefficient resonant frequency (τ_f) is an important parameter to determine the performance of the device. Since the resonators are used in communication systems, temperature stability is an important factor and should nearly be zero.

The temperature-dependent resonant frequency can be measured using the cavity made up of invar material having the least thermal expansion coefficient. The cavity is kept on a hot plate and the entire system is insulated in an isothermal enclosure. The setup is then slowly heated (1° per min.) from room temperature to 80 ˚C to obtain the temperature coefficient of resonant frequency defined as,

$$\tau_f = \frac{1}{f_0}\frac{\Delta f}{\Delta T}\ ppm/^oC \qquad (2.31)$$

where f_o is the resonant frequency at room temperature and Δf is the change in resonant frequency for a temperature variation ΔT .

2.3.8.5 Microwave dielectric properties of thin films:

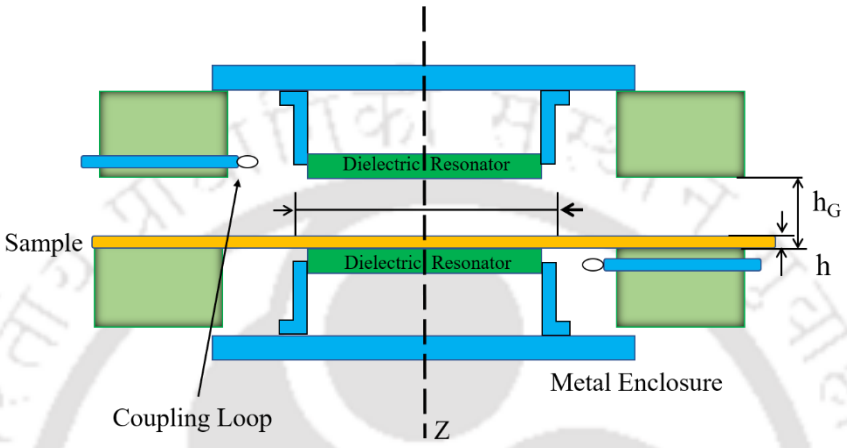

Figure 2.20: The cross-sectional view of SPDR fixture [30-31].

The split post dielectric resonator (SPDR) technique is a well-established, non - destructive, and accurate technique for the measurement of complex permittivity of low loss dielectric substrates and thin films at spot frequencies in the microwave region of 5, 10, and 15 GHz. In the present thesis, the microwave dielectric properties such as dielectric permittivity and loss of the prepared films were measured in the frequency range of 5 - 15 GHz using a vector network analyzer (8722 ES, Agilent Technologies,) and (ZVA24, Rohde & Schwarz) by employing SPDR technique. The dielectric resonators are typically operated with $TE_{01\delta}$ mode, that mode has only an azimuthal electric field component. Thus, the electric field remains continuous across the dielectric interfaces, which makes the measurement insensitive to the presence of air gaps perpendicular to the z-axis of the fixture. Figure 2.20 presents the schematic cross-section of an SPDR.

The relative permittivity (ε_r) and loss tangents ($tan\delta$) of the films and substrates are mainly dependent on the resonant frequency and quality factor. Initially, the resonant frequency and quality factor of the empty resonator (f_{01}, Q_{01}) and resonant frequency and quality factor of the substrate (f_0, Q_0) are measured before the deposition of the film. When the deposited film is placed in SPDR, which results in a shift in resonant frequency. The shift of resonant frequency and its quality factor (f_s, Q_s) of the film is measured. The Rayleigh-Ritz

method was employed to calculate the resonant frequencies, unloaded *Q*-factors, and other parameters. Therefore, the relative permittivity and loss tangent of the films were calculated based on the thickness and resonant frequencies by following equations [67],

$$\varepsilon_r = 1 + \frac{(f_0 - f_s)}{h f_0 K_s(\varepsilon_r, h)} \tag{2.32}$$

where h is the thickness of the film, f_0 and f_s are the resonance frequencies of the bare substrate and film-coated substrate of the SPDR. K_s is a slowly varying function of the samples ε_r and h.

$$\tan\delta = \frac{Q^{-1} - Q_{Dr}^{-1} - Q_c^{-1}}{P_{es}} \tag{2.33}$$

where Q is related to the unloaded quality factor of SPDR containing dielectric thin film, Q_{Dr} is related to the dielectric losses in the empty resonators, and Q_c belongs to the metal losses for the resonant cavity containing the thin film. The uncertainty in ε_r and $tan\delta$ is calculated as,

$$\frac{\Delta\varepsilon_r}{\varepsilon_r} \le 0.15\% + T\frac{\Delta h}{h} \tag{2.34}$$

where, 1<T<2, and $\Delta tan\delta = \pm 2.0\times10^{-5}$.

2.3.9 I-V characteristics

The leakage currents analysis is one of the most important characterizations for device applications. Most of the applications are based on the application of an external voltage on the ceramic capacitors either bulk ceramics or thin films, leading to the occurrence of leakage current. The leakage current might originate due to the presence of defects (oxygen vacancies, nonstoichiometric, defect states, etc.) which leads to degradation in properties. The solutions to reducing the leakage current can be found by understanding the conduction mechanism in the samples. Therefore, it is very important to study the charging mechanism in samples to identify the conduction mechanisms responsible for the leakage current. In the present thesis, the Keithley parameter analyzer (4200A-SCS, Tektronix, USA) was used to measure the leakage current versus applied voltage at room temperature.

CHAPTER 3: Structural and Dielectric Properties of (1-x) $MgTiO_3$-x $Ba_5Nb_4O_{15}$ Composites Ceramics and their Thin Films

This chapter deals with the structural, microstructural, dielectric, and electrical properties of (1-*x*) $MgTiO_3$-*x* $Ba_5Nb_4O_{15}$ (*MTO-BNO*) composite ceramics and their thin films for temperature-stable microwave applications. The first part of the chapter deals with the synthesis, characterization (Structural and microstructural), and physical property analysis of *MTO-BNO* composite ceramics. The second part of the chapter presents the deposition of *MTO-BNO* composite thin film by RF magnetron sputtering and characterization (structural and microstructural) and analysis of its physical property based on film thicknesses.

3.1 Introduction:

In recent decades advancement in technology has brought remarkable changes to human civilization. One of the most significant developments is cellular technology and microwave dielectric resonators had played a vital role in all these advancements. With passing times, telecommunication devices are desired to become handy as well as cost-effective. This is the reason the number of users of this technology is above 1033.20 million and growing (May 2016) in India itself [71]. Preparation of sophisticated material for this technology is one of the biggest challenges for the research areas all over the globe, for cheaper and better microwave devices. Resonators used in microwave technology are preferred to have a combination of high dielectric constant ($\varepsilon_r >$ 15), good quality factor ($Q >$ 5000), and near zero-temperature co-efficient of resonant frequency [72].In the field of broad band satellite communication technology where high power is required and control of temperature fluctuation is difficult, so temperature co-efficient of resonant frequency is desired to be near zero. So, in this report, the addition of $Ba_5Nb_4O_{15}$ (*BNO*) ceramic exhibiting hexagonal perovskite structure having positive temperature co-efficient for resonant frequency, τ_f = +79 ppm/^{o}C, with high dielectric constant $\varepsilon_r \sim$ 39, and quality factor, $Q \times f_0 \sim$ 26,300 GHz with $MgTiO_3$ (*MTO*) is carried out to get near zero temperature co-efficient of the resonant frequency. Both *MTO* and *BNO* ceramics exhibit different crystal structures with independent phases[73]. J. B. Huang, et. al[28] carried out similar studies and reported that the addition of $CaTiO_3$ with $MgTiO_3$ to get near zero τ_f [74]. Another limitation

of $MgTiO_3$ ceramics is that it requires a high sintering temperature ~ 1400 - 1470^oC in the conventional solid-state reaction method[75]. In the current study, the microwave sintering route is adopted to achieve highly densified ceramics at a lower sintering temperature with less processing time as compared to the conventional sintering method [76]. Various dielectric ceramics were being studied in thin film form for microwave integrated circuits and optical communications. *MTO-BNO* ceramic exhibited excellent microwave dielectric properties, and no literature is available on the thin film of *MTO-BNO* composition. This motivated us to pursue the present study. In the current study, thickness-dependent optical, structural and dielectric properties of 0.9 $MgTiO_3$ - 0.1$Ba_5Nb_4O_{15}$ composite thin films deposited by the RF reactive magnetron sputtering technique have been investigated. The microwave dielectric properties of these films were also measured at microwave frequencies.

3.2 Sample preparation:

3.2.1 $MgTiO_3$-$Ba_5Nb_4O_{15}$ composite ceramics preparation:

The samples were prepared using the conventional solid-state reaction method using highly pure oxide powders. $MgTiO_3$ ceramics were prepared by using high purity powders of MgO (99%) and TiO_2 (99%) (M/s Sigma Aldrich, St. Louis, MO) by following the non-stoichiometric $MgTiO_3$ preparation method to avoid secondary phase formation of *MTO* at higher sintering temperatures[77]. These powders were weighed and ball milled in distilled water (used as a mixing medium) for 5 h using a planetary ball mill (M/s Fritsch GmbH, Germany). Similarly, $Ba_5Nb_4O_{15}$ powders were prepared by using highly pure powders of $BaCO_3$ (> 99.9%) and Nb_2O_5 (> 99.9%). These raw powders were weighed and ball milled for 5 h, according to desired stoichiometry in a planetary ball mill. Later, the slurry is dried in a magnetic stirring hot plate and the obtained powder is calcined at 1050^oC for 3 h. Now, (1-*x*) $MgTiO_3$-*x*$Ba_5Nb_4O_{15}$ (where x = 0.0, 0.1, 0.2, 0.3, 0.4) composite were prepared by using calcined $MgTiO_3$ and $Ba_5Nb_4O_{15}$ powders. The powders were pressed into discs, which were sintered at 950^oC, 1000^oC, 1030^oC, and 1050^oC for 15 minutes by using a high-temperature microwave furnace and whereas above 1030^oC sintering temperature melted discs were obtained.

3.2.2 $MgTiO_3$-$Ba_5Nb_4O_{15}$ composite thin film preparation

3.2.2.1 Sputtering target preparation:

The best optimized 0.9*MTO*-0.1*BNO* composite ceramic and ceramic target for the RF Sputtering system are indigenously prepared in the lab as illustrated in figure 3.1. The phase pure 0.9*MTO*-0.1*BNO* powders were mixed with 5 wt% PVA solution and pressed into a 60 mm diameter and 3-5 mm thickness cylindrical compact. sintered at 1350 ˚C for 4 h.

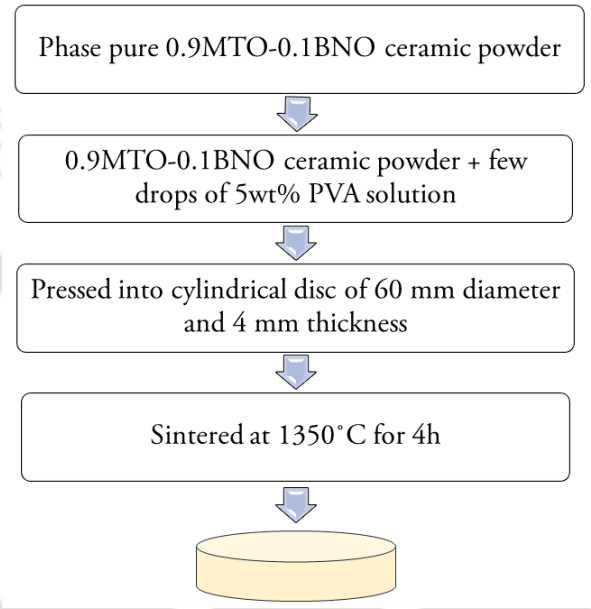

Figure 3.1: *Target preparation in steps*

3.2.3 Thin film deposition:

The thin films were deposited on SiO_2 and n-type Si substrate using radio frequency (RF) reactive magnetron sputtering at 400^{o}C substrate temperature. Initially, the deposition chamber was evacuated up to ~ 1×10^{-6} mbar. The sputtering chamber pressure was maintained at ~ 3×10^{-2} mbar throughout the deposition process by purging reactive gases argon (99.99%) and oxygen (99.99%) in 50:50 ratio. All the depositions were carried out at a fixed 40 W RF power. Later, the as-deposited films were annealed at 800^{o}C for 2h to induce crystallinity. For the electrical measurements, the sample was prepared in a capacitive structure.

3.3 Results and Discussion:

3.3.1 $MgTiO_3$-$Ba_5Nb_4O_{15}$ composite ceramics:

3.3.1.1 XRD analysis:

Figure 3.2 (a) presents the experimentally obtained XRD pattern of pure *MTO* ceramics. The obtained XRD pattern exhibited polycrystalline nature and crystallizes into the rhombohedral lattice with R-3 symmetry and diffraction peaks corresponding to lattice planes were indexed according to JCPDS no# 790831 file.

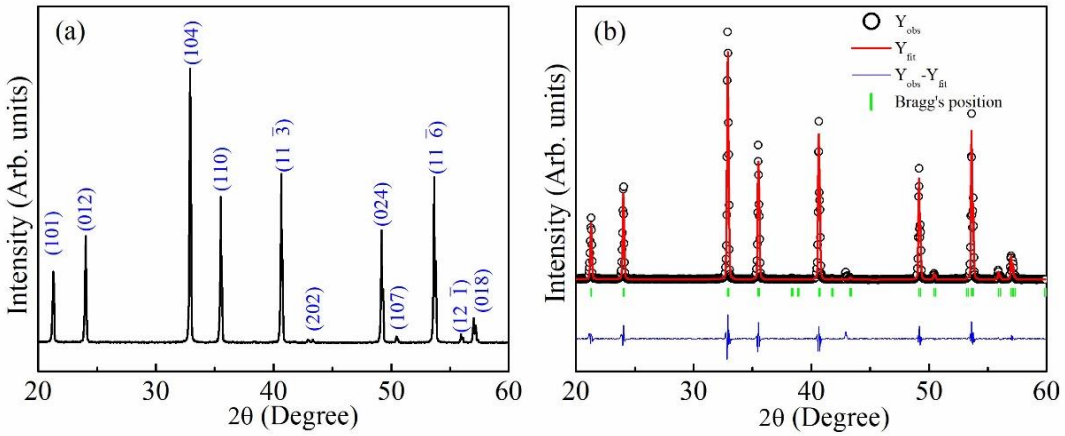

Figure 3.2: *(a-b) Experimentally obtained XRD pattern and Rietveld refined XRD pattern for MTO ceramics.*

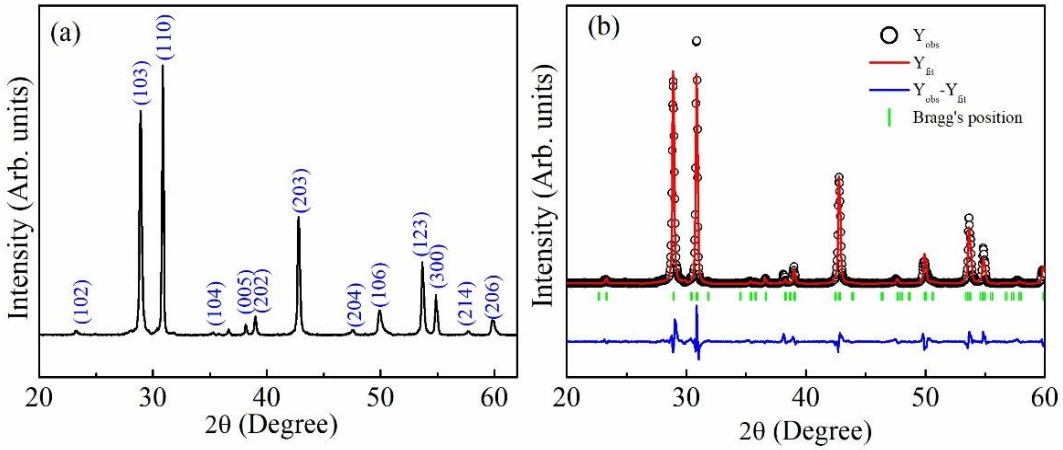

Figure 3.3: *(a-b): Experimentally obtained XRD pattern and Rietveld refined XRD pattern for BNO ceramics*

This is further confirmed with Reitveld refinement results and extracted its lattice parameters. As shown in figure 3.2(b) the Reitveld refined XRD pattern fit well with the experimentally obtained XRD pattern in the present case signifying the phase

purity of *MTO* ceramics. The obtained lattice parameters of *MTO* ceramics are listed below in table 3.1.

Table 3.1: Obtained lattice parameters of MTO crystal lattice from Reitveld refinement

χ^2 value	Lattice parameters		Lattice volume, V ($Å^3$)
	a = b (Å)	c (Å)	
2.16	5.0624 ± 0.89E-05	13.9191 ± 0.10E-05	308.9216

Figure 3.3(a-b) presents experimentally obtained XRD pattern and Rietveld refined XRD pattern for *BNO* ceramics, respectively. The obtained XRD pattern of *BNO* revealed that the calcined *BNO* ceramic is pure in phase and polycrystalline in nature**.** The Rietveld refinement for *BNO* ceramic was carried out considering a hexagonal lattice system with P-3m1 lattice symmetry and obtained a considerable chi-square value (χ^2) ~2.43. The lattice parameters for *BNO* crystal lattice are evaluated from the Reitveld refinement results and tabulated in table 3.2.

Table 3.2: *Obtained lattice parameters of BNO crystal lattice from Reitveld refinement.*

χ^2 value	Lattice parameters		Lattice volume, V ($Å^3$)
	a = b (Å)	c (Å)	
2.43	5.7935 ± 0.79E-05	11.7556 ± 0.21E-05	341.7081

The XRD patterns of (1-*x*) $MgTiO_3$(*MTO*) - *x* $Ba_5Nb_4O_{15}$(*BNO*) (for *x* = 0.1, 0.2, 0.3 and 0.4) composite ceramics sintered at 1000˚C for 15 minutes in a high temperature microwave furnace are presented in Figure 3.4. The XRD patterns of *MTO-BNO* composite ceramics suggested the presence of both independent *MTO* and *BNO* phases, respectively. In addition, some of traces of secondary phase: $BaNb_2O_6$ (JCPDS # 140027), $Ba_2Nb_5O_9$ (JCPDS # 821919) and Nb_2O_5 (JCPDS # 721121) also identified. These minor secondary peaks are found to be increased in number with an increase in a value of *x* from 0.1 to 0.4. This would lead to degradation in the dielectric and microwave dielectric properties of the *MTO-BNO* composites. So, further studies were carried out by taking the composite *x* =0.1, and studied

the effect of sintering temperature on the structural, microstructural, and dielectric properties of the composite

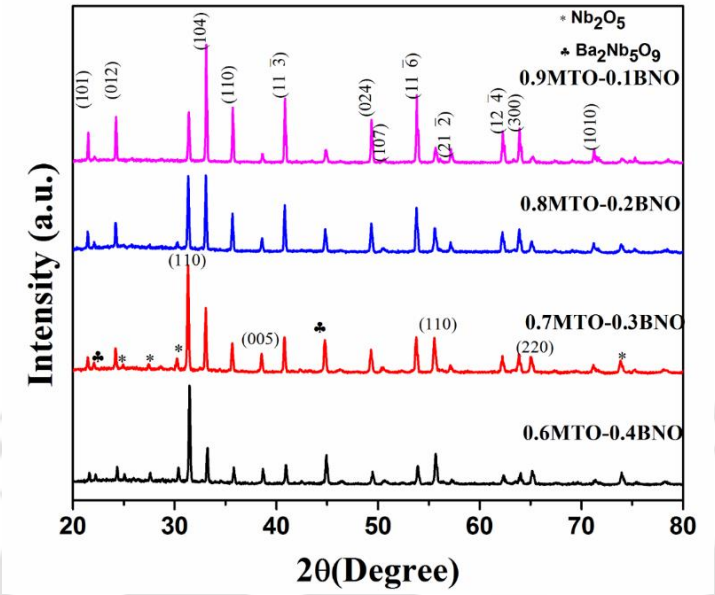

Figure 3.4: XRD patterns of (1-x) MTO-xBNO (for x =0.1,0.2,0.3 and 0.4) composite pellets sintered at 1000˚C sintering. Peaks for MTO and BNO are indexed in x=0.1 and x =0.2 patterns, respectively

.

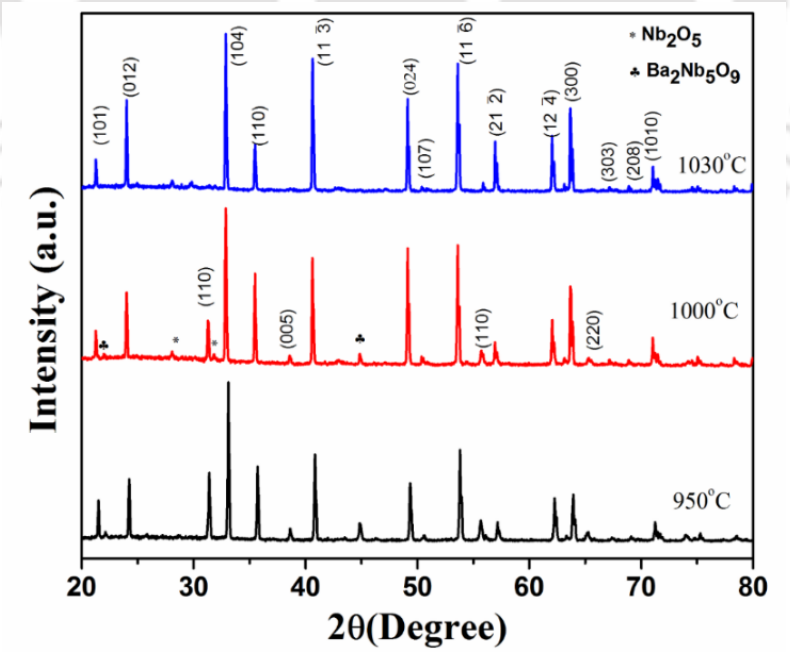

Figure 3.5: XRD patterns of 0.9MTO-0.1BNO composite at different sintering temperatures. Peaks for MTO and BNO are indexed for sintering temperatures 1030 °C and 1000 °C, respectively

Figure 3.5 shows the XRD patterns of $0.9MgTiO_3$ - $0.1Ba_5Nb_4O_{15}$ composite ceramics sintered at 900 ˚C, 1000 ˚C, and 1030 ˚C for 15 minutes, respectively. As the sintering temperature increased from 950 to 1030˚C, the intensity of diffraction peaks corresponding to the *MTO* phase grows prominently with a decrease in secondary peaks intensities of *BNO*. These XRD patterns revealed that the structural property depends on the sintering temperature and 1030˚C is the optimum sintering temperature for *MTO-BNO* composite ceramics.

3.3.1.2 Raman Spectroscopy:

Figure 3.6, displays the Raman spectra of 0.9*MTO* - 0.1*BNO* composite sintered at 1030ºC for 15 minutes along with calcined *MTO* and *BNO* powder. All the theoretically observed peaks of *MTO* have appeared along with one peak of *BNO*. The Raman spectra revealed that all the atoms are involved in each vibrational mode. The origin of peak (A_g) 225 cm^{-1} and (A_g) 308 cm^{-1} is due to the vibration of Mg and Ti along the Z-axis. (A_g) 500 cm^{-1}, (A_g) 717 $cm^{-1}$and (A_g) 398 cm^{-1} modes represent breathing-like vibration (each of them shows liberation direction) and stretching breath-like vibration O (octahedra) atoms respectively. Mode 398 cm^{-1} (A_g) arises from the combination of $a_g^{(1)}$ and $a_g^{(2)}$, which is the key reason for this nearly isotropic stretching vibration.

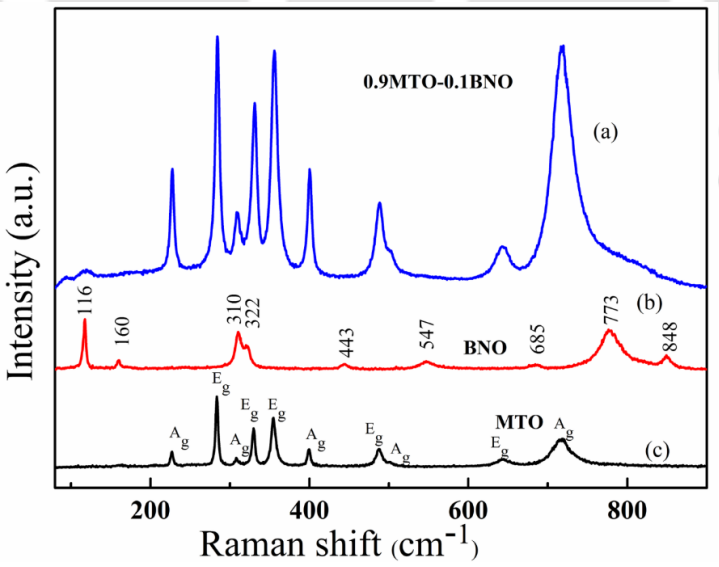

Figure 3.6: *Raman spectra of (a) 0.9MTO-0.1BNO composite sintered at 1030ºC and (b, c) calcined MTO, and BNO powders, respectively.*

The anti-symmetric breathing vibration represented by E_g, 328 $cm^{-1,}$ and 353 cm^{-1} originated from the twisting of the O octahedron with the vibration of Mg and Ti atoms parallel to XY planes. Similarly, 486 cm^{-1} and 641 cm^{-1} also represent a mix of anti-symmetric breathing and twisting vibration mode of the O octahedra with cationic vibrations parallel to the XY plane. In 486 cm^{-1} both Mg and Ti are involved in vibration and 641 cm^{-1} involvement of the Ti atom dominates [78]. Whereas 160 cm^{-1} of BNO represents weak metal oxygen vibration[79].

3.3.1.3 Microstructural analysis

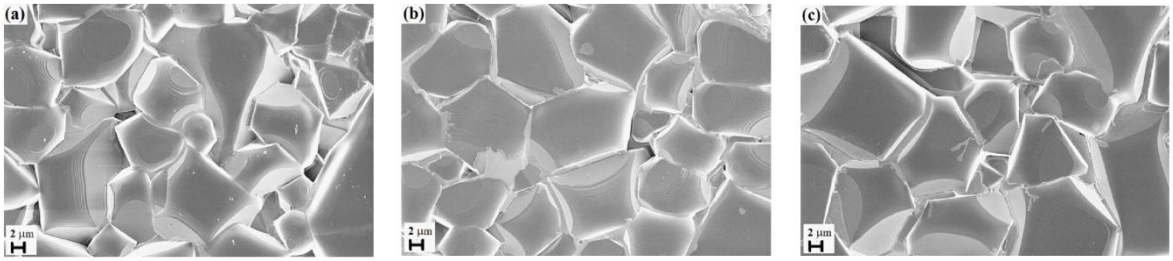

Figure 3.7: (a-c): FESEM images of 0.9MTO-BNO composite ceramics sintered at 950, 1000, and 1030˚C for 15 minutes, respectively.

Figure 3.7 (a-c) shows the FESEM images for 0.9*MTO* - 0.1*BNO* composite sintered at 950, 1000, and 1030˚C for 15 minutes, respectively. All the ceramics showed brick-layer arrangements of almost similar sizes (~15-20 µm) of grains. As the sintering temperature increased from 950 - 1030˚C, due to higher thermal energy the fine grains recrystallized [80] to form larger grains and packed tightly. As observed from the microstructures the maximum relative density (96%) was found at 1030ºC measured by the Archimedes formula. Whereas, due to the small amount of *BNO* addition to *MTO* ceramics, FESEM images show only one type of grains. This might be due to the segregation *BNO* phase into the grain boundaries of *MTO* grains.

3.3.1.4 Microwave dielectric properties:

Figure 3.8 presents the microwave dielectric constant (ε_r) and quality factor ($Q \times f_0$) of 0.9*MTO*-0.1*BNO* composite ceramics sintered at 950˚C, 1000 ˚C, and 1030 ˚C.

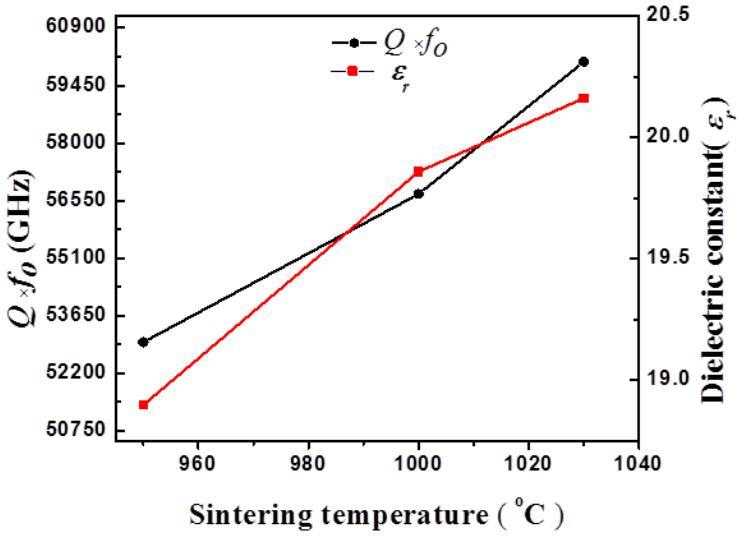

Figure 3.8:Variation of quality factor ($Q \times f_0$) and dielectric constant (ε_r) of 0.9MTO-0.1BNO composite as a function of sintering temperature

It is found that with an increase in sintering temperature both ε_r and $Q \times f_0$ values also increased. The improvement in microwave dielectric properties can be attributed to better crystallinity and microstructure. The observed ε_r and $Q \times f_0$ values are found to be in the range of 18.7 - 20.3 and 52925 - 60175 GHz for sintering temperatures 950°C -1030°C. The temperature coefficient of resonant frequency (τ_f) is known to be related to the composition. The obtained τ_f values for 0.9 *MTO*-0.1*BNO* composite ceramics decreased from -10 to -5 ppm/°C with an increase in sintering temperature from 950-1030 ˚C. The 0.9*MTO* - 0.1*BNO* composite ceramic sintered at 1030 ˚C exhibited the lowest τ_f value ~ -5 ppm/˚C.

3.3.1.5 Low-frequency dielectric properties:

Figure 3.9(a, b) shows the variation of dielectric constant (ε_r) and loss tangent ($tan\delta$) with frequency (at different temperatures) for sintered 0.9*MTO*- 0.1*BNO* composite ceramics. The dielectric constant decreases with an increase in frequency and becomes almost constant after 10 kHz attributing to the relaxation of space charge polarization. Space charge polarization originated from the accumulation of charges at the grain boundaries and the interface of samples and electrodes. As shown in figure 3.8 (b) loss tangent also exhibited a similar type of variation with frequency at all different measurement temperatures. Further, figure 3.8(c, d) shows the variation of dielectric constant and loss tangent ($tan\delta$) with temperature (at a different frequency) for 0.9*MTO* - 0.1*BNO* composite ceramics sintered at 1030°C for 15 minutes. Both the dielectric constant and loss tangent showed slow increment

with an increase in measurement temperature attributed to thermally activated conduction in the sample.

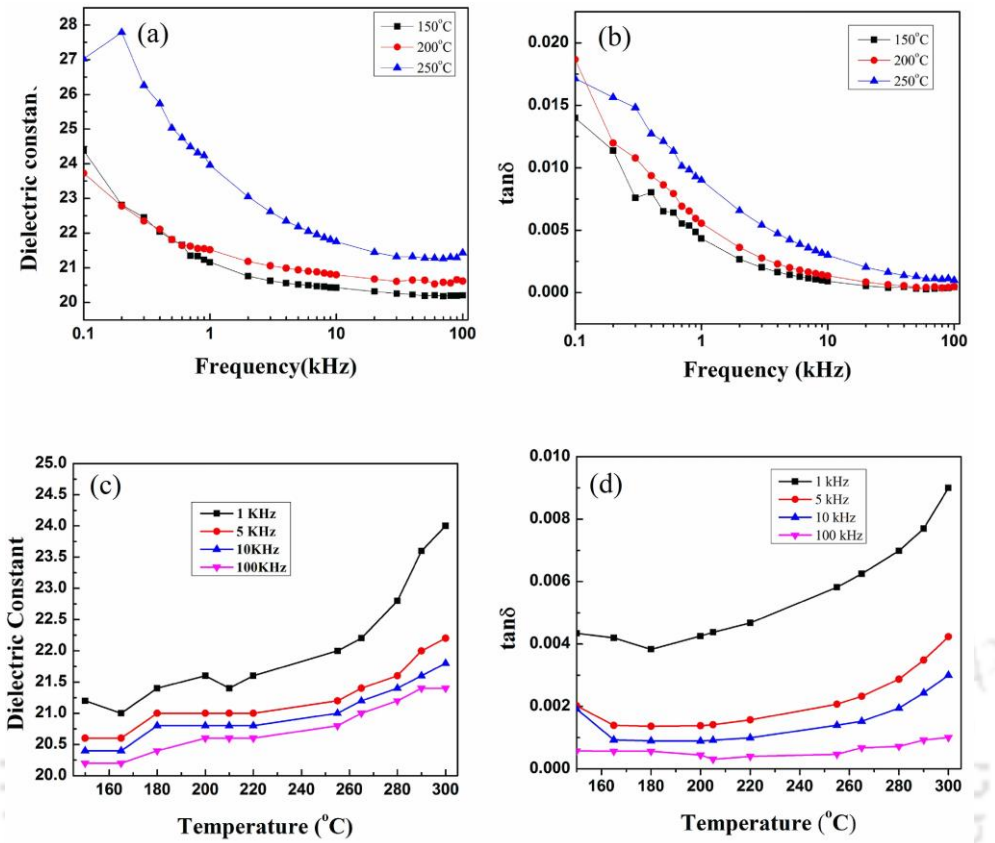

Figure 3.9:Variation of (a) dielectric constant, (b) loss tangent as a function of frequency, and Variation of (c) dielectric constant, (d) loss tangent as a function of temperature for 0.9MTO-0.1BNO composite, sintered at 1030°C for 15 minutes.

From the above analysis, 0.9*MTO*- 0.1*BNO* composite ceramics are found to be promising for dielectric resonator applications. Therefore, the composition is deposited in thin film form. The results and discussion for 0.9*MTO* - 0.1*BNO* composite thin film are presented in the subsequent section.

3.3.2 0.9 $MgTiO_3$-0.1$Ba_5Nb_4O_{15}$ composite ceramic thin films:

3.3.2.1 XRD analysis:

The as-deposited films at 400˚C were found to be amorphous, and these films were post-annealed at 800 ˚C for 2 h to induce crystallinity. Oxide films grow in amorphous form due to insufficient deposition temperature and the lattice mismatch between the substrate and film.

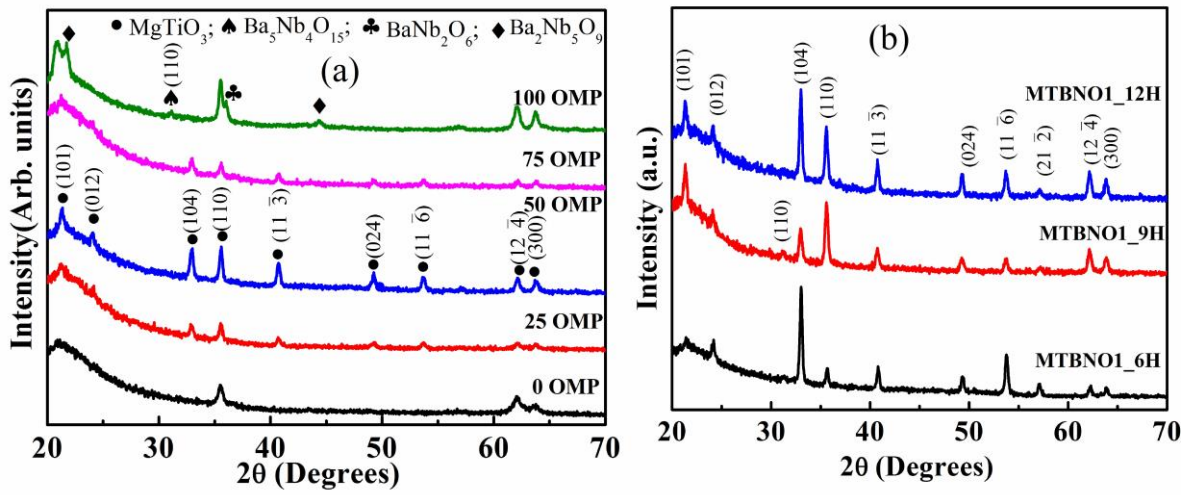

Figure 3.10: XRD spectra of annealed 0.9MTO-0.1BNO thin films deposited for (a) different oxygen mixing percentages (OMP) and (b) different thicknesses.

In figure 3.10(a), the XRD pattern of annealed 0.9*MTO* - 0.1*BNO* thin films deposited on SiO_2 substrate under different oxygen mixing percentages (OMP) is demonstrated. Interestingly, as the target material is an oxide material, the amount of oxygen mixed has been seen to play an important role in phase formation. The crystallinity of the films showed an improvement with an increase in oxygen mixing percentage (OMP). In a pure argon atmosphere, up to 75% of only peaks corresponding *MTO* phase were observed. The films deposited at 50% of the oxygen atmosphere exhibited better crystallinity without any secondary phase. Whereas, the XRD pattern of thin film deposited in 100 OMP showed a better crystallinity in the *MTO* phase with some secondary phases of *BNO*. It is interesting to note that the films deposited in pure oxygen plasma exhibited both the phases along with minor secondary phases of *BNO*. The presence of the secondary phases can be attributed to the variations in the energies in oxygen plasma. Further, the presence of the secondary phases of *BNO* may be due to its formation at lower energies. From this study, it's very clear that the composite thin films can be deposited by using RF magnetron sputtering. Furthermore, it is very difficult to achieve plasma in pure oxygen purging but in the present case, the films with a uniform thickness are obtained, which showed that the target is not fully oxidized, even in the pure oxygen plasma. After the preliminary studies on the phase and crystallinity of deposited thin films, further depositions were carried out in 50 OMP atmospheres for different deposition times to study the effect of thickness on structural, optical, and dielectric properties of 0.9*MTO* - 0.1*BNO* thin films, because the films deposited under 50 OMP exhibited both the phases and better crystallinity. Figure 3.10(b) depicts the XRD spectra of

annealed 0.9*MTO* - 0.1*BNO* thin films deposited on SiO_2 substrates for different deposition times.

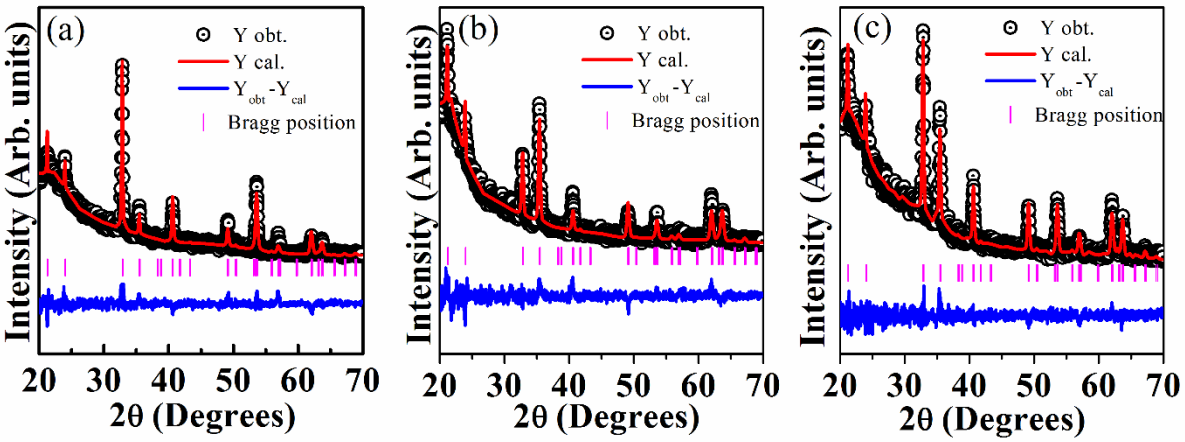

Figure 3.11: Rietveld refinement XRD patterns for (a) 150 nm, (b) 235 nm and (c) 340 nm 0.9MTO-0.1BNO thin films.

Table 3.3: Numerical values of lattice parameters, density, bond length, angles, crystallite sizes, and strains corresponding to the different

Film thickness (nm)	*Lattice Parameters obtained from Rietveld refinement*						*Obtained from W-H plot*	
	a = b (Å)	c (Å)	Density (g/cm^3)	Bond length (Å)		Angle (Degree)	Crystallite size, D (nm)	Strain, $\eta\times10^{-3}$
				Mg - O	Ti - O	Ti – O - Mg		
150	5.0587	13.9250	3.88	2.04	2.04	116.09	55	2.8
235	5.0618	13.9216	3.87	2.25	1.87	111.01	34	1.9
340	5.0617	13.9158	3.87	2.18	1.67	116.63	46	1.7

Further, for the confirmation of phase formation, Rietveld refinement is carried out considering $R\bar{3}$ Space group in rhombohedral crystal structure for *MTO* by using FullProf software as shown in figure 3.11. The refinement parameters for all the films were tabulated in Table 3.3.

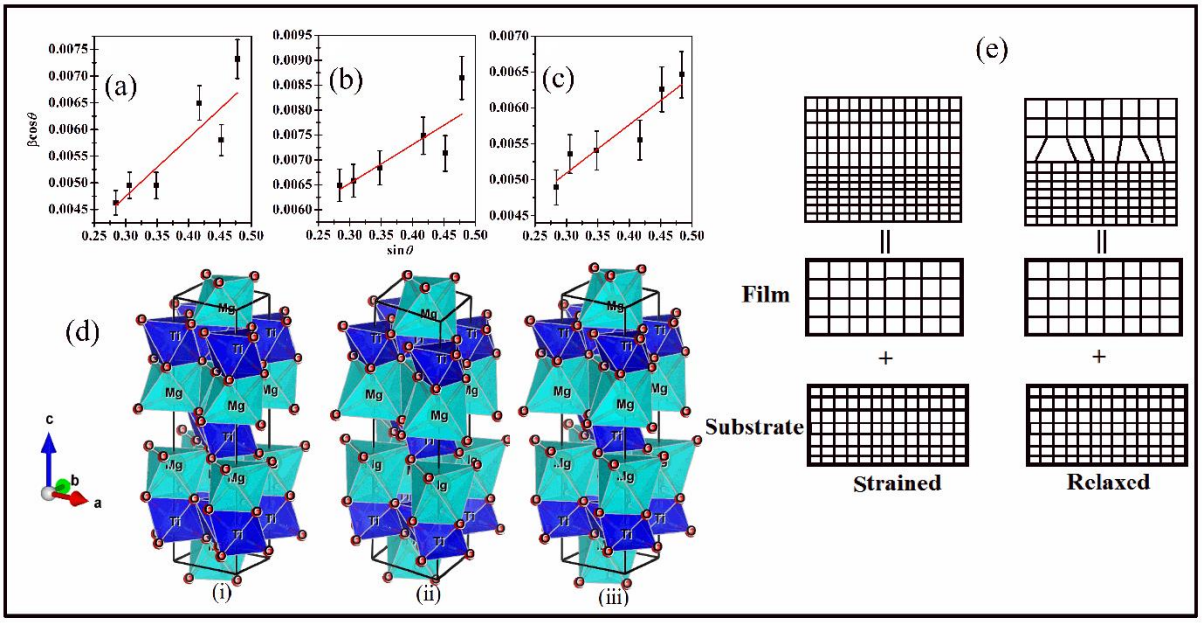

Figure 3.12:(a-c) W-H plot and d (i- iii) 3d crystal structures for 150 nm, 235 nm, and 340 nm thin films, respectively. And (e) Schematic demonstration of defects related to hetero-epitaxial films.

From the XRD patterns, it is observable that both the *MTO* and *BNO* phases prepared are more likely to align along (104) and (110) planes, respectively. With an increase in film thickness, the diffraction peak for *BNO* is found to be suppressed compared to the *MTO* phase. The deposited films are non-epitaxial and the expected strain associated with the films was evaluated by using Williamson-Hall plots and are shown in figure 3.12(a-c) and the obtained parameters are given in Table 3.3. Similarly, by using the Rietveld refinement data 3- dimensional crystal structures of *MTO* have been generated as shown in figure 3.12(d) and the corresponding bond lengths and angles were calculated by using Vesta software and summarized in Table 3.3. From the 3-D crystal arrangements, any kind of visual distortion in *MTO* crystals could not be detected. Whereas, slight variation in calculated bond length and bond angle values are evident. It is interesting to note that the calculated bond length between Ti and O showed systematic change with film thickness towards a lower value owing to the compressive strain experienced. However, the bond length of Mg and O did not follow a particular trend and this result was expected attributed to the hygroscopic and volatile nature of Mg and O, respectively. Similarly, the bond angle between Mg – O – Ti also changed according to Mg and O bond lengths with film thickness. In thin film technology, when the lattice parameter of the film is not the same as the substrate, there is a lattice mismatch, which causes strain and other defects. Depending upon the mismatch different kinds of

defects in the film would be introduced as shown in figure 3.12(e), and for some applications, i.e., optical, and protective technologies a minimum strain in the film is desirable[81]. In the present case, the strain in the films is found to be reduced with an increase in film thickness. The lattice parameter of the SiO_2 substrate (a ~ 0.491 nm) and the film (a ~ 0.505 nm) is not the same, which leads to the accumulation of strain in initial atomic layers, and as the thickness increases, the strain on the top layers of the films would gradually be minimized.

In the present work due to the very low concentration of *BNO*, it was difficult to detect by XRD analysis. To study the presence of *BNO*, a FETEM analysis has been carried out. FETEM images for 0.9*MTO* - 0.1*BNO* thin film deposited for 6 h are shown in Figure 3.13.

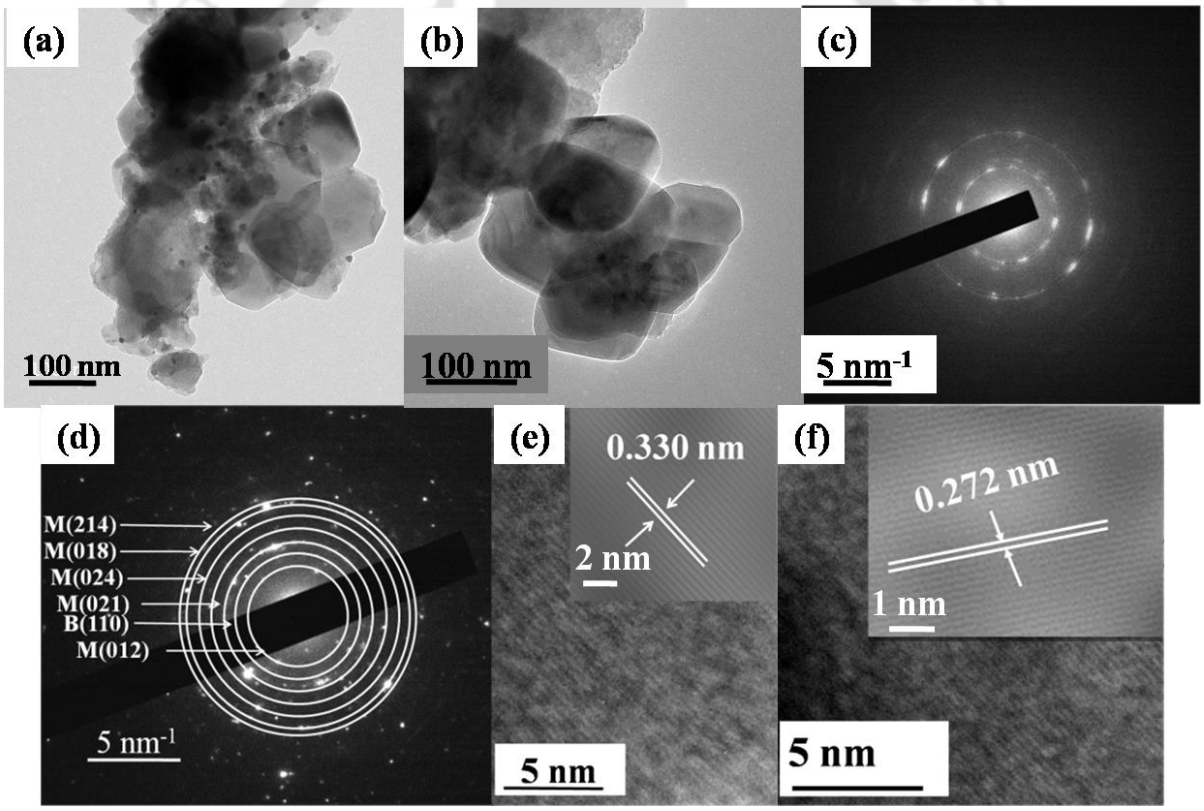

Figure 3.13: (a – b) FETEM images, SAED patterns for (c) as deposited, (c) annealed, and (e –f) HRTEM images for 0.9 MTO-0.1BNO thin films

The FETEM images clearly signify the formation of polyhedral particles with sizes < 200 nm. Again, selected area electron diffraction (SAED) pattern and HRTEM images were analyzed for as-deposited and annealed films to study the crystallinity of the film. The SAED pattern for the as-deposited film is partially crystalline which will be difficult to

detect by XRD analysis. Whereas the obtained SAED pattern for the post-annealed films signified the polycrystalline nature of the film, and all the fringes were indexed accordingly. From the SAED pattern, only one fringe of *BNO* is obtained for the (110) plane. The HRTEM images shown in figure 3.13(e-f) have lattice spacing of 3.30 and 2.72 Å, corresponding to (110) and (110) planes of *BNO* and *MTO* phases, respectively. The presence of a lower concentration of *BNO* might be due to the variations in the rate of deposition of *MTO* and *BNO*. From this study, it's evident to note the co-existence of *MTO* and *BNO* phases and it could be possible to obtain the composite thin films using RF sputtering technique.

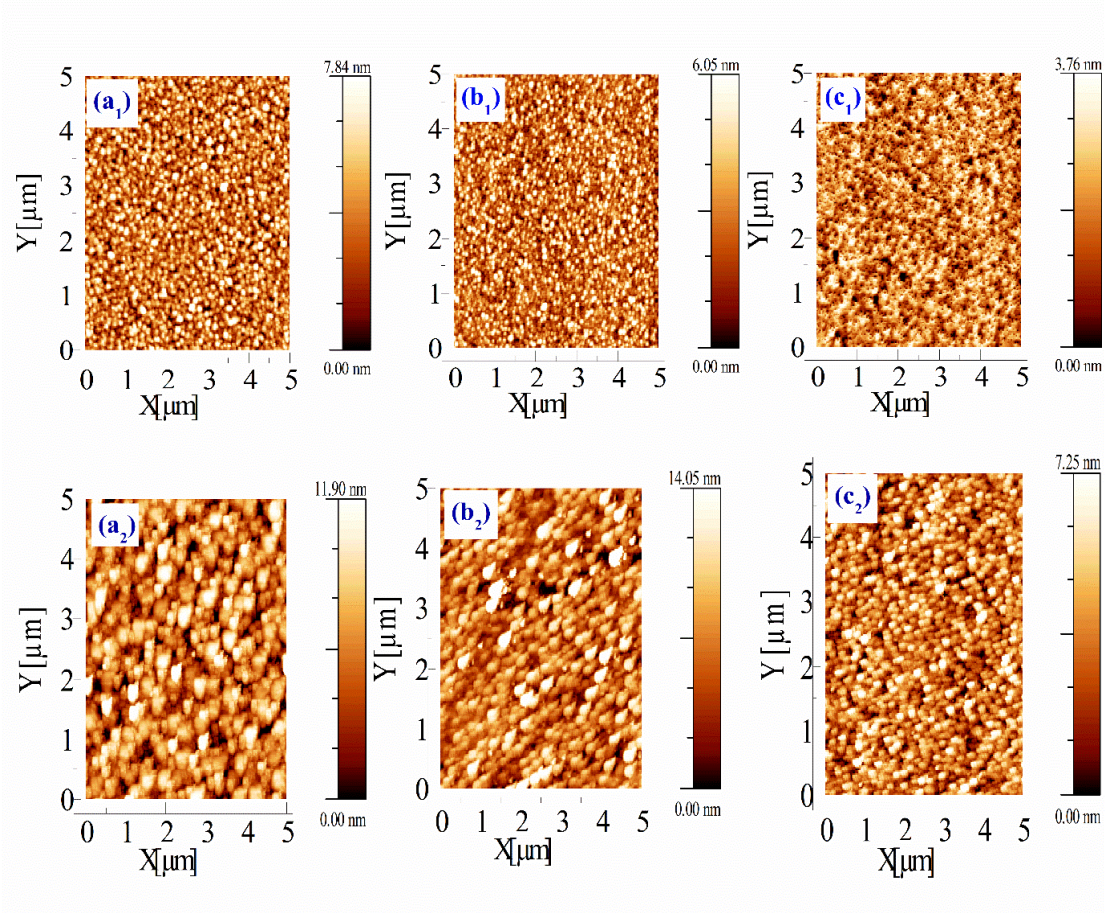

Figure 3.14: AFM images of, (a_1, b_1, c_1) as-deposited and (a_2, b_2, c_2) annealed 150 nm, 235 nm, 340 nm MTO-BNO thin films, respectively.

. The thin films deposited by RF sputtering showed variation in morphology depending on the deposition conditions and the post-heating treatment. Atomic force microscopy (AFM) has been opted to study the topography of the as-deposited and post-annealed thin films and is shown in Figure 3.14. The AFM topography indicates the formation of different kinds of morphology for the thin films of different thicknesses. For the as-deposited films, the AFM

images are evident of uniform spherical particle growth over a large scale ~ 5 µm and whereas, for the thin film of 340 nm showed ruptured topography. When the films were treated at 800˚C for 2 h, the particle sizes of the films improved as well as the ruptured surface also recovered. The roughness of the post-annealed films is analyzed by using WSxM software and found to be minimized with thickness from 2.9 nm to 2 nm. The obtained low RMS roughness values of these films suggest these films are suitable for optical applications

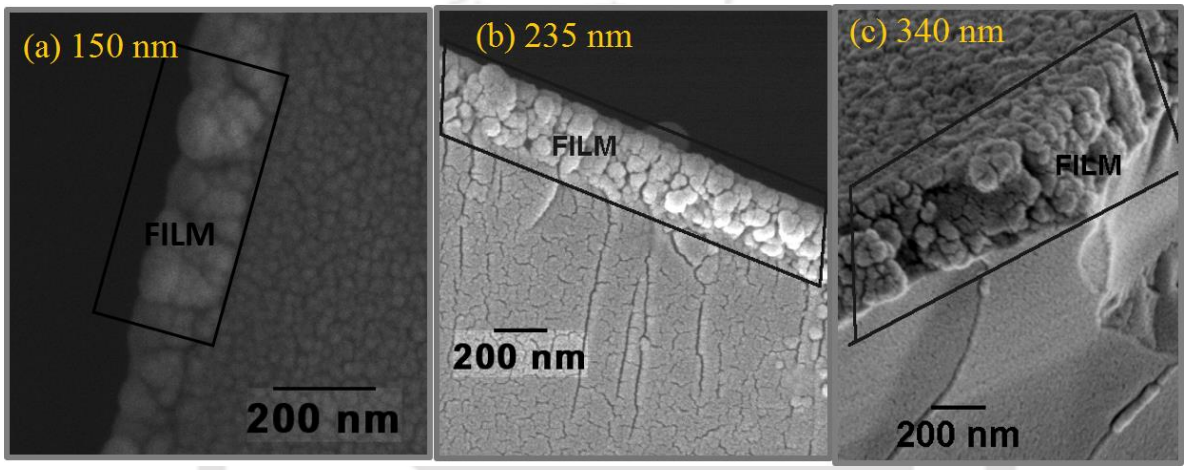

Figure 3.15: Cross-sectional morphology of MTO-BNO thin films.

Figure 3.15 demonstrates a cross-sectional FESEM image of the films and the estimated thicknesses of the films are also found to be nearly equal to the thicknesses calculated from the Swanepoel envelope method.

3.3.2.2 Optical properties:

Figure 3.16(a), represents the optical transmittance of the post-annealed *MTO-BNO* composite thin films as a function of wavelength (200- 1450 nm), deposited on SiO_2 substrates, and all the films exhibited > 70% transmittance in the visible range with Fabry-Pérot kind of interference pattern as a result of multiple reflections between air- film and film-substrate interface. The obtained interference patterns represented the uniform and flat nature of the films. The sharp fall of transmittance near 270-265 nm wavelengths corresponds to the fundamental absorption edge of the films. The absorption edge of the films exhibited a red shift with an increase in film thickness. The optical parameters of the films are determined by using envelop method[65].

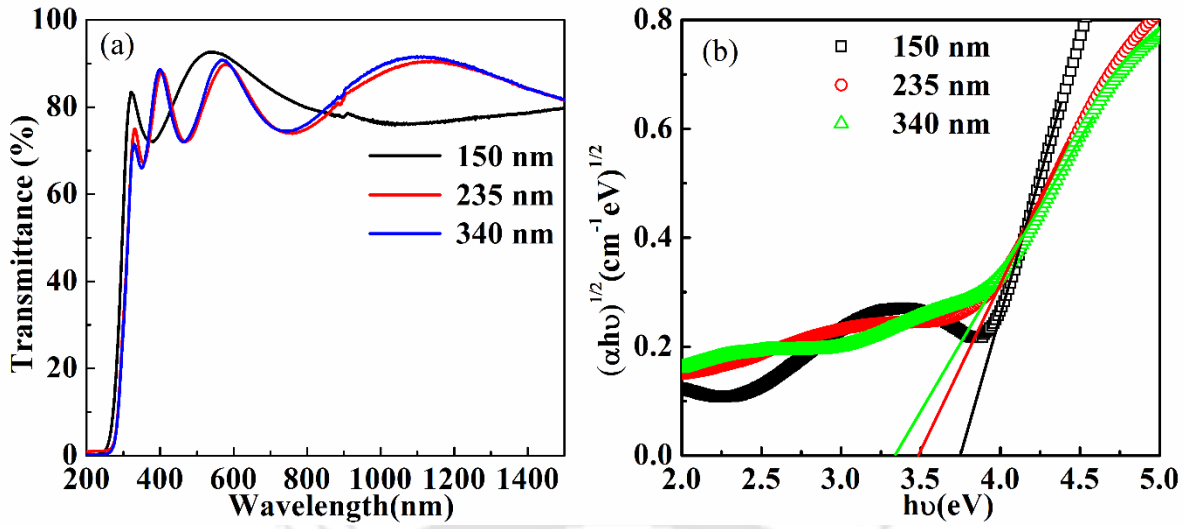

Figure 3.16: (a) Transmittance spectra and (b) Tauc's plot of the MTO-BNO films of different thicknesses.

The refractive index (*n*) and film thicknesses were determined by using equations 2.16 and 2.19 of the previous chapter. The thicknesses of the films are obtained as 150 nm, 235 nm, and 340 nm, respectively. The calculated optical refractive index (*n*) was slightly increased from 2.02- 2.07 with film thickness, which is an indication of increased density and minimization of defects in the films. Further, the optical bandgap of the films is obtained from the extrapolated linear portion of the $(\alpha h\upsilon)^{n}$ vs $h\upsilon$ curve in Figure 3.16(b), considering indirect optical transition (where, n=1/2). The optical bandgap decreased from 3.75 to 3.34 eV with an increase in film thickness from 150 to 340 nm. This can be attributed to the reduction of the *BNO* phase with film thickness which might also cause a reduction in the bandgap since the bandgap of *BNO* (~ 4.2 eV) is higher as compared to *MTO* (~3.7 eV)[82][83]. However, there are not many variations in the obtained values of optical results because their parent compounds also exhibited similar optical constant[84]. The refractive index (*n*) of the films as a function of wavelength is shown in Figure 3.17(a) and single electronic oscillator model is applied to understand the dispersion of the refractive index in the thin films. The single electronic oscillator model defines that the materials consist of a series of independent oscillators and those oscillate when light energy impinges on them [85,86]. The relation between refractive index (*n*)and incident photon energy (λ) can be expressed with the following equation,

$$n^2 - 1 = \frac{S_o \lambda_o^2}{\left(1 - \lambda_o^2 / \lambda^2\right)} \tag{3.1}$$

where, S_o and λ_o are the average oscillator strength and wavelength, respectively. The dispersion energy, E_d, and average oscillator strength, S_o determines the strength of inter-band transition. If E_o, h, and c are the average oscillator energy gap, Planck's constant and speed of light in vacuum, respectively then, $S_o\lambda^2 = (E_d/E_o)$ and $E_o = hc/\lambda_o$. These all-optical parameters S_o, E_o, and E_d are extracted from the $1/(n^2-1)$ vs $1/\lambda^2$ plot (figure 3.17 (c-d)) and the obtained values were listed in Table 3.4.

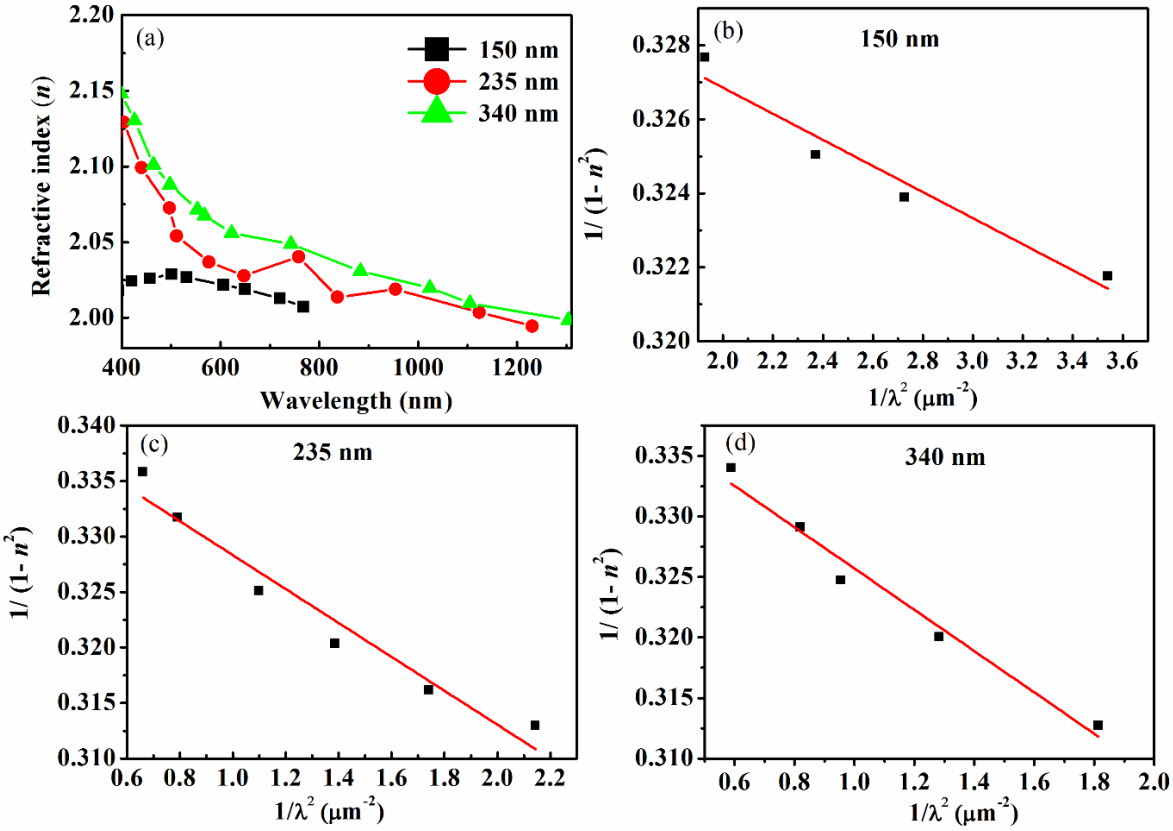

Figure 3.17: (a) Dispersion of refractive index with wavelength, (c-d) $1/(1-n^2)$ vs $1/\lambda^2$ plots for 150 nm, 235 nm, and 340 nm MTO-BNO thin films.

Table 3.4: Extracted numerical values of optical parameters of 0.9MTO-0.1BNO films for different thickness.

Film thickness (nm)	***n***	***P* (%)**	***E_g* (eV)**	***E_o* (eV)**	***E_d* (eV)**	***S_o* (10^{14} m^{-2})**	***E_U* (eV)**
150	2.02	85.82	3.75	12.10	36.32	2.83	0.21
235	2.04	86.93	3.51	5.92	17.09	0.65	0.44
340	2.07	88.54	3.36	5.58	16.25	0.59	0.46

The optical parameters S_o, E_o, and E_d are found to be reduced and become comparable with six coordinated oxides with an increase in film thickness which is an indication of enhancement in packing density and reduction of defects in the films [67].

3.2.3.3. Microwave dielectric properties:

The microwave dielectric properties of the films were measured using the SPDR method at a spot frequency of 5 GHz and 10 GHz.

Table 3.5: Microwave dielectric constant and loss tangent of 0.9MTO-0.1BNO films for different thicknesses.

Film thickness (nm)	*5 GHz*		*10 GHz*	
	ε_r	tanδ	ε_r	tanδ
150	16.042	1.69×10^{-3}	12.111	3.65×10^{-4}
235	16.067	2.88×10^{-3}	12.655	2.87×10^{-4}
340	16.825	4.41×10^{-3}	14.166	1.45×10^{-4}

The permittivity and loss tangent of the films were calculated by using the equations 2.32 and 2.33, respectively. The measured ε_r and *tanδ* of the films are listed in Table 3.5. The dielectric constant (ε_r) has shown an improvement with an increase in film thickness, and in addition to that, the loss tangent (*tanδ*) was also found to be reduced with film thickness. These observed responses can be attributed to better microstructure and low roughness of the thicker films. It is significant to note that the dielectric constants of the films are comparable to their bulk counterparts whereas the loss tangents are higher and this can be attributed to the smaller grains, higher grain boundaries, and strains in the films. In the case of bulk, the samples would be free from strain and also have larger grain sizes

3.2.3.4. Dielectric properties:

The dielectric response of the 0.9*MTO* - 0.1*BNO* composite films, recorded in the frequency range of 1k - 1MHz measured at different temperatures, are shown in Figure 3.18(a-d). The dielectric constant exhibited a large dispersion in the low-frequency region (1kHz- 10 kHz), indicating the presence of space charge polarization in the films further the dielectric constant gradually falls and became almost constant up to 1MHz, which is a natural response of a linear dielectric.

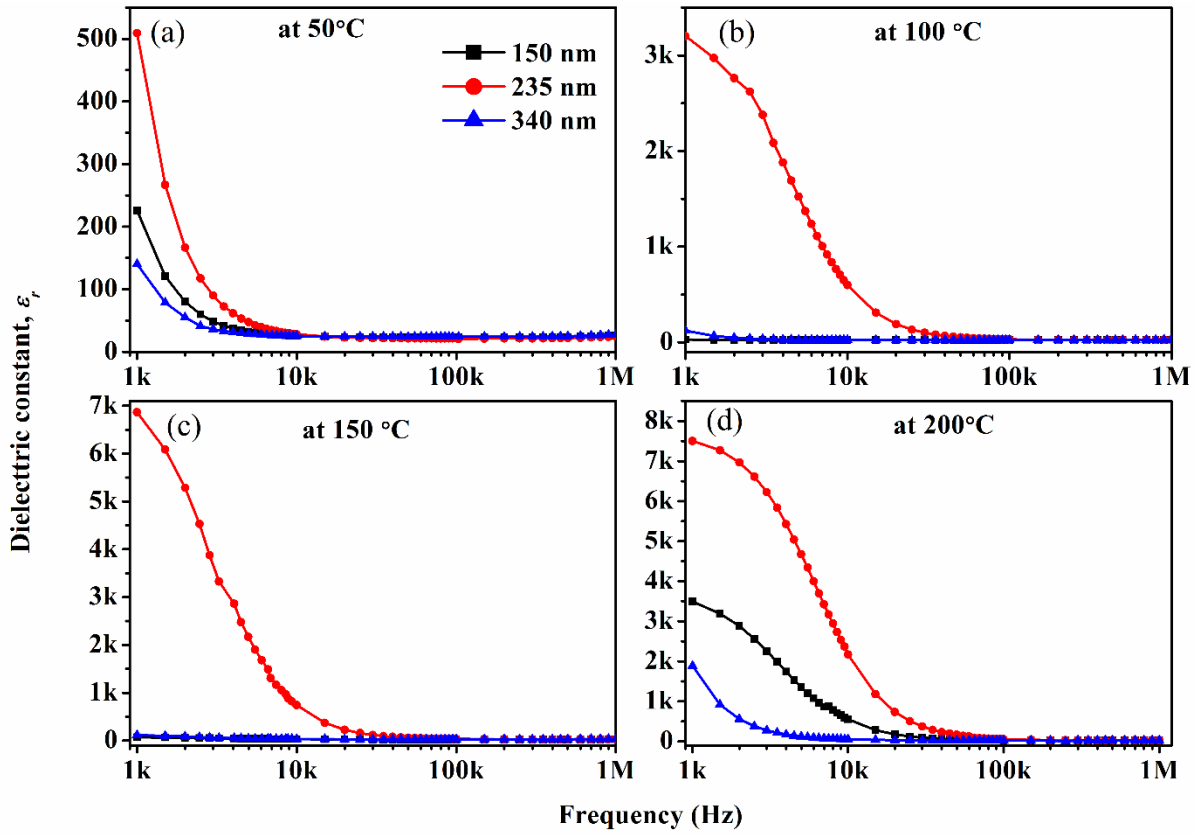

Figure 3.18: Dielectric constant as a function of frequency measured at different temperatures.

Frequency-dependent dispersion of dielectric constant can be understood by Maxwell-Wagner's two-layer and Koop's phenomenological theory [87]. The space charge polarization is a consequence of an accumulation of charge carriers at the interface of electrode and film surface. Among all the three films, the film with higher thickness showed an almost stable dielectric constant throughout the measurement frequency range. The dielectric constant of the films also exhibited an enhancement from 20 to 24 with an increase in film thickness from 150 nm to 340 nm. These might be due to the better microstructure and uniformity in the film. At the same time, the enhancement in dielectric constant with an increase in measurement temperature is a result of the thermally activated orientation of dipoles. The dipoles will freeze at lower temperatures but as the temperature rises, they align much faster in the field direction.

3.2.3.5. Impedance analysis:

The variation in the real part of the impedance (Z') of the films measured at different temperatures is presented in Figure 3.19(a-c). As the measurement temperature and frequency raised, the real part of impedance (Z') reduced for all the films as an indication of

enhancement in the conduction process due to the increase in thermal energy and release of space charge polarization.

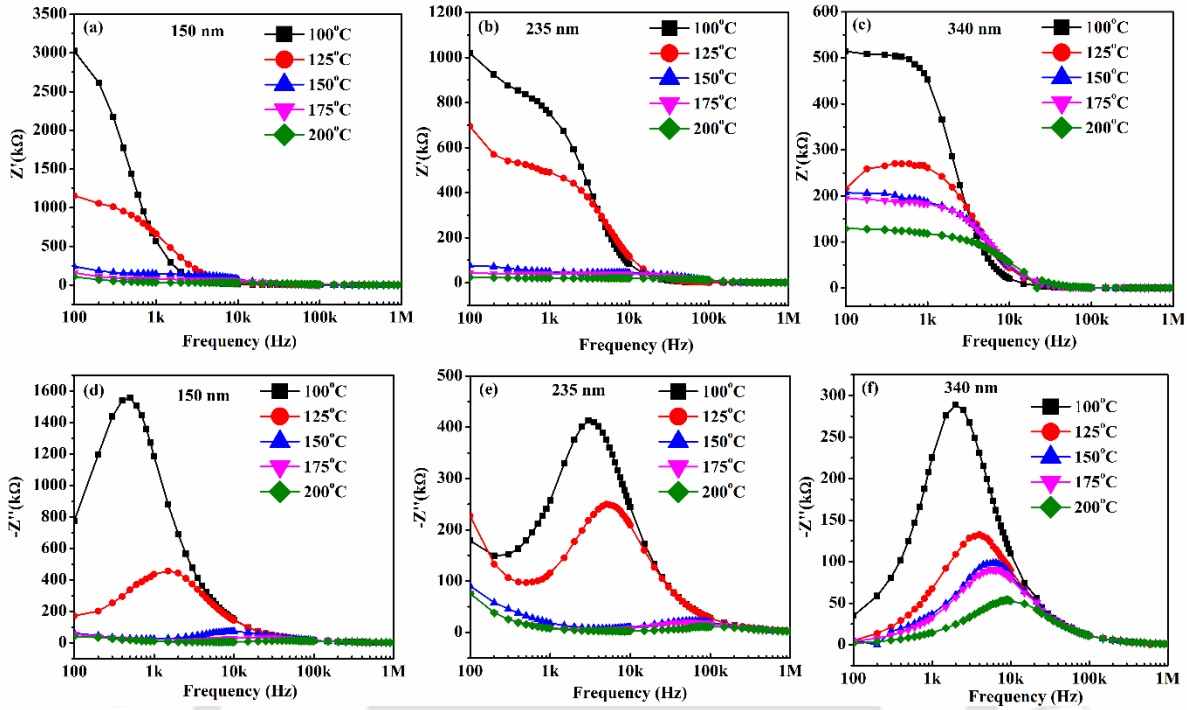

Figure 3.19: Variation of the real and imaginary impedance of MTO-BNO thin films with different thicknesses measured at different measuring temperatures.

Further, this response of the films exhibited a negative temperature coefficient for real impedance (Z') (i.e., resistance) and which is a typical nature of semiconductors [88]. Similarly, the imaginary part of impedance (Z'') as a function of frequency at different measurement temperatures is shown in Figure 3.19(d-f). A peak of Z'' has been observed for all the films, which has been shifted towards the higher frequency side with an increase in measurement temperature. In oxide films, the peak and nature of the peak in the imaginary part of impedance (Z'') reveal the relaxation process present in the film. In addition to that, the peaks were also broadened with measurement temperature, which can be attributed to the temperature-dependent relaxation process[89]. Various electrical phenomena present have a strong correlation with the microstructure of the dielectric films, and complex impedance spectroscopy is a vital tool to probe it.

In Figure 3.20, complex impedance spectra of the films measured at three different temperatures were plotted along with best-fitted curves considering two parallel R||C components connected in series and displayed in Figure 3.20(d). The impedance spectra followed the Cole-Cole phenomenon indicating the non-Debye conduction process in the film[90]. For the films of thickness 150 nm and 235 nm displayed only one semicircle is

observed at lower temperatures. This single semicircle signifies the grain (bulk) electrical phenomenon of the test specimen.

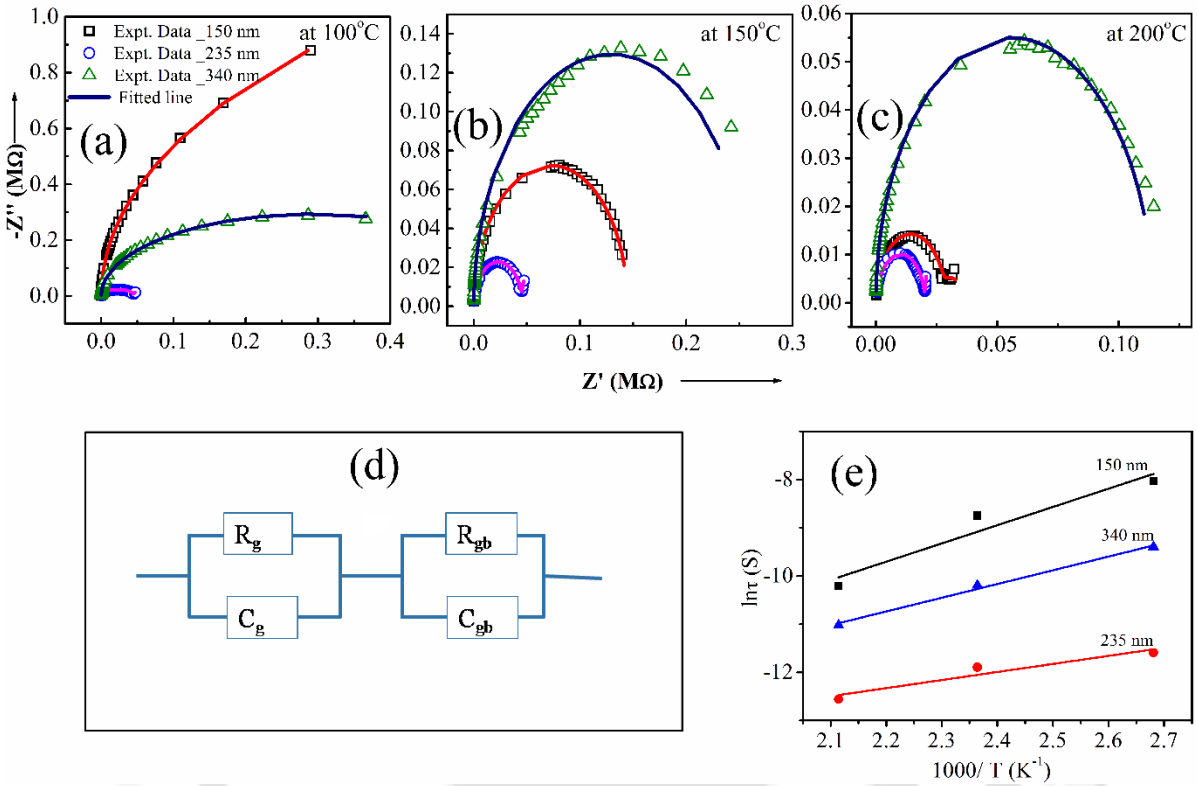

Figure 3.20: (a-c) Cole- Cole Plot, (d) equivalent electrical circuit and (c) lnτ vs. 1000/T plot for MTO-BNO thin films.

Further, the complex spectra recorded at a higher measurement temperature (200˚C), showed the second semicircular arc, which indicates the compound response of grain (first arc) and grain boundary (second arc) to the electrical response of the films[91,92]. The films of thickness 235 and 340 nm showed unusual responses as compared to the film of 150 nm. The complex impedance spectra of 235 nm film, showed two semicircular arcs for all the measurement temperature ranges (100 to 200˚C) and which can be attributed to the compact microstructure or complete coverage in the film. On the other hand, 340 nm film did not show up in the second semicircular arc for all the temperature ranges of (100 to 200˚C) which again can be attributed to the uniform film growth and larger grain sizes present in the film. From the above analysis, the film with a thickness of 340 nm has the highest resistance compared to the other two films, and that might be due to fewer defects present in the film. All the electrical parameters (R and C) corresponding to grains are obtained. The temperature-dependent relaxation times were also estimated using the equation, $\tau = R_gC_g$.

These relaxation times (τ) are plotted as a function of 1000/T, which followed Arrhenius Law [93],

$$\tau = \tau_o \exp\left(\frac{E_a}{k_B T}\right) \tag{3.2}$$

where, τ_o, E_a, and k_B are the prefactor, activation energy for the response, and Boltzmann constant, respectively. The activation energies for the corresponding plots were extracted from the slope of the linearly fitted curve as shown in Figure 3.20(e). The obtained values of activation energies were found to be in the range of 0.313 eV to 0.144 eV.

3.3.2.3 Conductivity analysis:

The frequency-dependent conductivity plots at different measuring temperatures are shown in Figure 3.21. In the measured frequency range, ac conductivity revealed two regions, frequency independent plateau region at lower frequencies as a result of direct conduction of charge carriers and the dispersion region towards higher frequency region corresponding to ac conduction, respectively[94]. At higher temperatures, the plateau region is found to be enlarged, moreover, the dispersive region is shifted towards the higher frequency side. This kind of conduction process is generally governed by hopping of charge carriers and understood by Jonscher's Power Law,

$$\sigma_{AC}(\omega) = \sigma_{DC} + A\omega^S \tag{3.3}$$

where, σ_{DC} is the frequency independent conductivity, which can be obtained by extrapolating the low-frequency plateau to zero frequency, A is a constant depending upon temperature and determines the strength of polarization and s is a frequency exponent that lies between 0 and 1[95]. Generally, the study of ionic conductivity is carried out by a.c. techniques, because it does not require a non-blocking electrode and to separate grain and grain boundary phenomenon[96]. Many models have been proposed based on the classical hopping of a carrier over the potential barrier between energetically favorable two sites and quantum mechanical tunneling through the barrier through the studies of temperature-dependent frequency exponent[97]. The variation of frequency exponent with temperature can be related to the conduction mechanism of any polycrystalline system. For Quantum mechanical tunneling (QMT), the frequency exponent (s) is almost equal to a derived value ~ 0.8 and increases slightly with an increasing temperature[98]. In the overlapping large polaron (OLPT) model, the frequency exponent (s) depends on both frequency and

temperature and drops with rising temperature to a minimum value and then increases as the temperature rises[99].

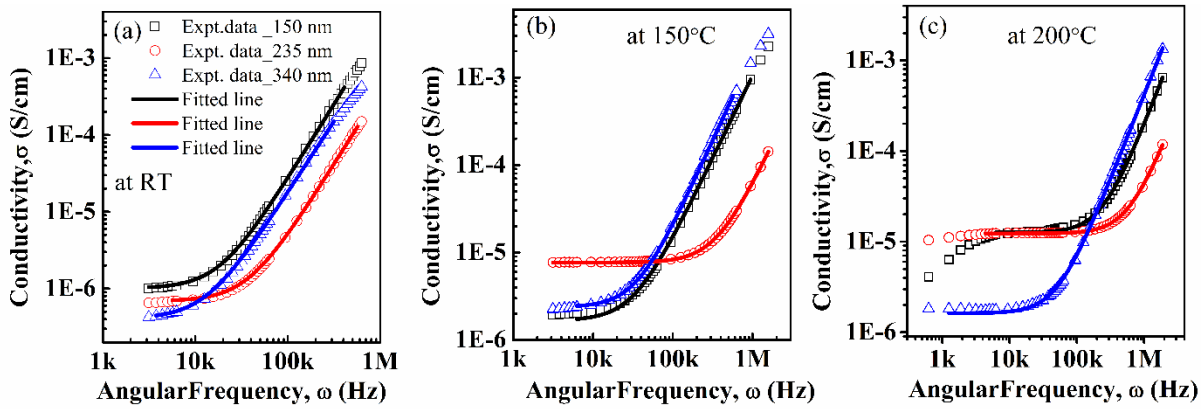

Figure 3.21: (a-c) Variation of conductivity to the angular frequency of MTO-BNO thin films with different thicknesses.

For Correlated Barrier hopping (CBH) model, the exponent decreases with a rise in temperature[100]. And for the non-overlapping small polaron hopping (NSPT) model the exponent (*s*) is temperature dependent and increased with the increase in temperature[101]. In the present case, the frequency exponent, *s* found to be in the range of 1.8 to 1.9 and it is found to be increasing with temperature. These variations in frequency exponent suggest that the conduction process in the films took place due to non-overlapping small polaron hopping. The activation energy associated with such conduction was also evaluated from the lnσ vs 1000/ T plot. The obtained numerical values are found to be in the range of 0.25 eV to 0.12 eV which are also comparable with the activation energy evaluated from relaxation time.

3.3.2.4 Leakage current measurement:

The leakage current densities of the *MTO-BNO* composite films were measured for various thicknesses at room temperature and are shown in figure 3.22. All deposited films showed symmetric leakage current behavior under an electric field of ± 100 kV/cm and it was found to be increased with the electric field. The film with the lower thickness (150 nm) exhibited a higher leakage current (4.51×10^{-5} A/cm^2 at 100 kV/cm). With increasing film thickness, the leakage current density gradually decreased to 8.83×10^{-6} A/cm^2 for 340 nm film. The leakage current density is dependent on the grain size, crystallinity, and RMS roughness associated with film and the measure of storage in the capacitor. The reduction in the leakage current with a rise in the thickness effectively enhanced electrical properties in 0.9*MTO*-0.1*BNO* thin films.

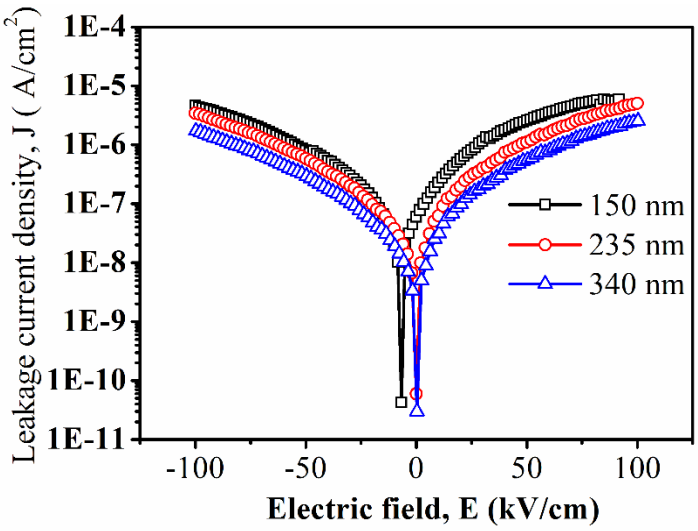

Figure 3.22: Variation of leakage current density (J) with applied voltage (V) for different thickness films.

3.4 Summary:

(1-*x*) $MgTiO_3$(*MTO*) - *x*$Ba_5Nb_4O_{15}$(*BNO*) composite of dielectric ceramics were prepared by using solid-state reaction route. All the composites are crystallizing into polycrystalline *MTO* and *BNO* phases with some minor secondary phases. With an increase in *BNO* concentration structural properties are found to be degraded resulting in degradation in microwave dielectric responses. The best dielectric properties were observed for 0.9*MTO*-0.1*BNO*, with the dielectric constant (ε_r)~ 20, loss tangent (*tanδ*) ~ 10^{-4}, and quality factor ($Q \times f_0$) ~ 60,230 GHz at 8.25 GHz with τ_f ~5 ppm/˚C. The improvement in dielectric constant and degradation in quality factor is observed for 0.9*MTO*-0.1*BNO* as compared to pure *MTO* ceramics. The 0.9$MgTiO_3$-0.1$Ba_5Nb_4O_{15}$ (0.9*MTO*-0.1*BNO*) thin films were successfully deposited onto Pt (111)/TiO_2/SiO_2/Si (100) and SiO_2 substrates by RF magnetron sputtering. The best crystallization of the films was obtained in post annealed 50/50, O_2/Ar_2 atmosphere with a substrate temperature of 400℃. The thicknesses also played a significant role in the crystal orientation of the films. The XRD spectra revealed crystallization of the films into independent *MTO* and *BNO* phases. The SAED patterns and HRTEM studies also complement XRD results. The strain associated with these non-epitaxial films was found to be reduced with an increase in the film thickness. The obtained optical bandgaps are 3.751 eV, 3.505 eV, and 3.365 eV for 150 nm, 235 nm, and 340 nm thin films, respectively. The morphology of the films was dense and uniform and the roughness of the films was found to

be in the range of 2.9 nm to 1.9 nm. The microwave dielectric properties recorded at microwave frequencies showed an improvement with an increase in film thickness and these values are found to be equal to the bulk counterparts. The dielectric properties are studied in the frequency range of 1 kHz -100 kHz, showed a large dispersion in lower frequency range < 10 KHz, and became almost constant with further increase in frequency. The dielectric constant of the films also exhibited enhancement from 20 to 24 with an increase in film thickness from 150 nm to 340 nm. The impedance analysis opted by the Cole-Cole plot signifies non -The Debye correlated conduction process in the films. The film, with 340 nm thickness, showed the best optical, structural, microstructural, and low leakage current properties with dielectric constant (ε_r) ~ 14.66 and $tan\delta$ ~ 10^{-4} at 10 GHz. These obtained properties of 340 nm *MTO-BNO* thin film, make it suitable for microwave-integrated electronic and optical applications.

CHAPTER 4: Structural, Electrical, and Dielectric Properties of $MgTiO_3$- $SrTiO_3$ Composite Ceramics and $MgTiO_3$/ $SrTiO_3$ Bilayer Thin Films

This chapter deals with the synthesis of the $MgTiO_3$- $SrTiO_3$ composite ceramics, and $MgTiO_3$/ $SrTiO_3$ bilayer thin films, and the characterization of various physical parameters viz., structural, electrical, microstructural, and dielectric properties for microwave applications. The chapter is divided into two parts. The first part presents the synthesis of *MTO-STO* composite ceramics, followed by results and a discussion on the characterization of relevant properties. The second part introduces the *MTO/STO* bilayer thin films as a potential microwave material for integrated circuit applications.

4.1 Introduction

Microwave ceramics have been exploited extensively in recent decades to achieve the requisite properties for emerging microwave technology. Among various ilmenite titanates, $MgTiO_3$ (*MTO*) is considered a promising microwave material for integrated circuit applications. In particular, *MTO* has been proposed for use in various components of microwave devices such as dielectric resonators (SDRs), filters, antennas, and type-I and type-II RF capacitors[47]. As discussed in chapter 1, *MTO* possesses extremely low dielectric loss (10^{-4}) and moderate dielectric constant (ε_r ~16), making it a suitable candidate for microwave device applications. However, the large temperature coefficient of resonant frequency (τ_f ~ -50 ppm/˚C), and the probability of secondary phase $MgTi_2O_5$ formation due to the hygroscopic nature of MgO and high processing temperature are the main drawbacks associated with *MTO* ceramics[102,103]. The term τ_f defines a shift in resonant frequency with a change in the operating temperature (RT to 85˚C), and its value is desired to be zero[104]. The composite approach is effective in tailoring various physical parameters viz., dielectric constant, magnetic susceptibility, and bandgap energy in the material production[31,88,105,106]. The microscopic responses such as structural, electrical, dielectric, and magnetic properties are material specific and can vary depending upon the composite material's compositional characteristics. A study on the microscopic responses of the ceramic composite material is, therefore, of great interest in the field of material development. Therefore, the composite of *MTO* with $SrTiO_3$ (*STO*) would be promising for this purpose.

Further, hetero structural growth of *MTO* on top of *STO* thin film is carried out. Thickness-dependent structural properties were investigated with 3 different thicknesses of the *MTO* layer. The evaluation of crystallinity with an increase in *MTO* thickness and its corresponding optical, electric, and dielectric properties are comprehensively discussed

4.2 Experimental details:

4.2.1 MTO-STO composite ceramic preparation:

(1-*x*) *MTO-x STO* composite ceramics were synthesized by the two-step solid-state reaction method. The 99.99% pure metal oxide powders: MgO, $SrCO_3$, and TiO_2 (Sigma Aldrich, St. Louis, MO, USA) were used as the raw materials for the ceramic powder preparation. In the first step, the $MgTiO_3$ and $SrTiO_3$ ceramic powders were separately prepared and optimized for the single phases. A non-stoichiometric approach is followed for $MgTiO_3$ preparation[26,107]. The raw metal oxide powders were weighed and mixed in a planetary ball mill (Pulverisette 5, Fritsch), maintaining a 1:5 powder and ball weight ratio for 5 h in a distilled water medium. The powder of mixed oxides was obtained after drying the slurry at 120˚C followed by calcined at 1100˚C for 3h for phase formation and crystallization. Similar steps followed for $SrTiO_3$ ceramic powder preparation taking the raw materials in stoichiometric amounts. In the second step, both the ceramic powders were further ground for 10 h to obtain finer initial particle size and proceeded for (1-*x*) *MTO-x STO* composite ceramics preparation by mixing in a ball mill for 5 h. Afterward, the composite powders were mixed with 5 wt% polyvinyl alcohol (PVA) solution and pressed into a cylindrical disc of the desired dimension (1-2 mm, 5 mm thick, and 10 mm diameter) using a KBr press.

4.2.2 MTO/STO bilayer thin films:

4.2.2.1 Preparation of sputtering targets:

Green compacted ceramic cylindrical discs of *MTO* and *STO* were prepared using a KBr press and 60 mm cylindrical die, and sintered at 1350˚C for 4 h for further densification.

4.2.2.2 . Preparation of MTO/STO thin film:

The deposition of *MTO/STO* bilayer on Si and quartz substrates were carried out by the R.F. magnetron sputtering technique. R.F. sputtering technique is chosen for the purpose as it provides uniform growth of film and is regarded as one of the best methods for the growth of oxide films[108,109]. Before the deposition of films, a base pressure of 1×10^{-6} mbar is

maintained in the chamber. At first, the films were deposited in different argon (Ar) to oxygen (O_2) gas mixed environments to optimize deposition conditions. The best-optimized deposition conditions for individual films of *MTO* and *STO* are listed in Table 4.1.

Table 4.1: Best optimized deposition conditions for STO and MTO thin film growth by R.F. magnetron sputtering

Deposition conditions	*$SrTiO_3$*	*$MgTiO_3$*
Base pressure	1×10^{-6} mbar	1×10^{-6} mbar
Deposition pressure	3×10^{-2} mbar	3×10^{-2} mbar
Ar: O_2 ratio (%)	75:25	50:50
RF power	40W	40W
Substrate to target separation	6 cm	6 cm

In the present study, *MTO* films of three different thicknesses were deposited on 150 nm *STO* film in optimized deposition conditions. The terminology for deposited *MTO/STO* bilayer films is in table 4.2, concerning different *MTO* film thicknesses. As deposited films were amorphous in nature and post-annealed at 750˚C for 2 h for crystallization of films.

Table 4.2: Nomenclature of prepared bilayer films along with detailed deposition conditions.

Sl. No.	*Sample name*	*Details of the bottom layer*	*Details of the top layer*
1	STMT1	150 nm $SrTiO_3$	100 nm $MgTiO_3$
2	STMT2	150 nm $SrTiO_3$	133 nm $MgTiO_3$
3	STMT3	150 nm $SrTiO_3$	165 nm $MgTiO_3$

4.3 The Results and discussions:

4.3.1 MTO-STO composite ceramics:

4.3.1.1 Structural and microstructural analysis:

Figure 4.1(a) depicts XRD patterns of *MTO-STO* composite ceramic discs with different *STO* concentrations, sintered at 1350˚C for 3h. The obtained diffraction peaks signify the formation of the polycrystalline *MTO* and *STO* phases. The *MTO* and *STO* phase are indexed as a rhombohedral system with $R\bar{3}$ symmetry and as a cubic system with a pm3m

space group, respectively [110][111]. All the patterns revealed the formation of the independent polycrystalline phase of *MTO* and *STO* crystals without any trace of the mixed or secondary phase, which might be attributed to significantly different crystal structure and symmetry possessed by *MTO* and *STO* ceramics. *MTO* and *STO* ceramics' crystal planes are mostly oriented along (104) and (110) directions, respectively. A shift towards the higher angle side as well as broadening in diffraction peaks are observed with an increase in *STO* concentration as shown in Figure 4.1(b), which signifies non-uniform strain in the crystal lattice as a result of ionic substitution. A small amount of Sr^{2+}(1.13Å) might get a substitute in Mg^{2+} (0.72Å) site and vice versa during high-temperature treatment for compaction of discs resulting in non-uniform strain in the crystal.

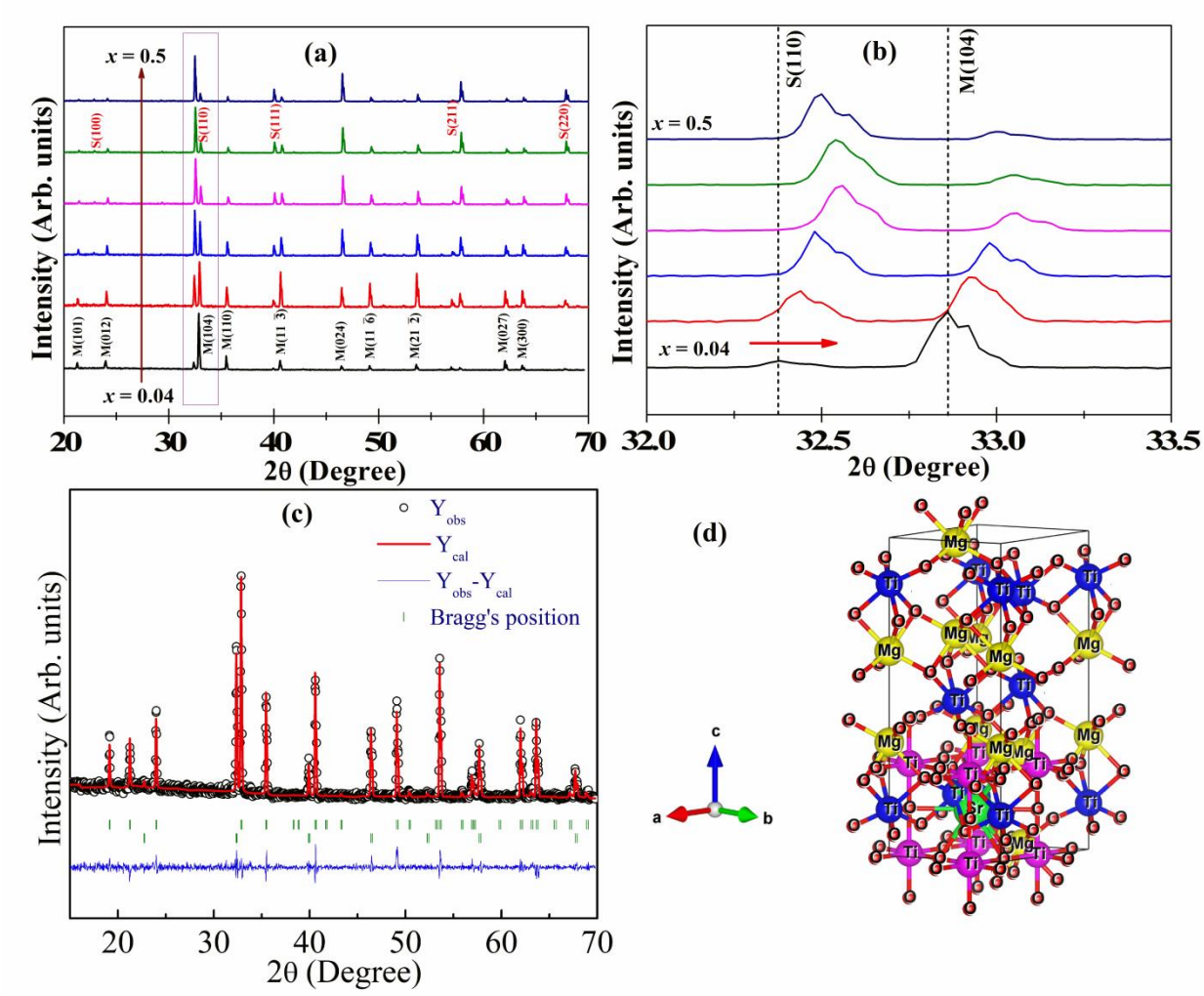

Figure 4.1: (a) The XRD patterns of sintered (1-x) MTO-x STO (for x=0.04,0.1, 0.2…0.5) composite ceramics with the lattice plane index corresponding to MTO and STO are indicated as M and S, respectively. (b) Magnified view of fig(a) in 2θ~32˚-33.5˚region. (c) Fitted XRD pattern with Reitveld refinement and (d) 3-D crystal illustration for x =0.1.

Further, qualitative and quantitative analysis for (1-*x*) *MTO-x STO* (for *x*=0.04,0.1,0.2…0.5) composite ceramic discs are performed based on Reitveld refinement of diffraction profiles using Fullprof software. The XRD profile fitting of the composite ceramics was carried out considering a two-phase system and acquired considerable chi-square (χ^2 ~2-3) values. The Rietveld refined XRD pattern is presented in Figure 4.1I for 0.9*MTO*-0.1*STO* composite ceramic disc. The circular black dots, red line, blue line, and scattered vertical green lines denoted the experimental data points, calculated pattern, difference between the computed pattern to experimental pattern, and Bragg's position. Obtained nature of the blue line confirmed the excellent quality of fitting

Table 4.3: *lattice parameters and volumes of MTO and STO with χ^2 obtained from Rietveld refinement and obtained fraction (xI) of STO with experimentally used fractions(xI)*

x I	*x I*	*MTO*		*STO*	*V (Å^3)*		χ^2	R_p	R_{wp}
		a (Å) = b (Å)	c (Å)	a = b = c (Å)	MTO	STO			
0.04	0.043	5.0569 ±0.0002	13.9108 ± 0.0008	3.9072 ±0.0002	308.1	59.6	2.12	13.6	18
0.1	0.12	5.0614 ±0.0002	13.9152 ± 0.0008	3.9111 ±0.0002	308. 7	59.8	1.78	14.3	19.5
0.2	0.25	5.0616 ±0.000 2	13.9173 ±0.0008	3.9122 ± 0.0001	308. 9	59.9	2.10	13.7	18.3
0.3	0.36	5.0601 ±0.000 2	13.9169 ±0.0008	3.9121 ± 0.0001	308. 6	59.9	2.21	13.3	17.7
0.4	0.46	5.0566 ±0.000 2	13.9108 ±0.0008	3.9102 ± 0.0001	308. 1	59.8	1.93	14	18.7
0.5	0.55	5.0593 ±0.000 2	13.9167 ±0.0009	3.9118 ± 0.0001	308. 5	59.9	2.33	13.2	17

In Table 4.3, the crystal lattice information and a quantitative fraction of *STO* ceramics obtained from Rietveld refinement are presented. The overall lattice volumes were increased with an increase in *STO* concentration up to $x < 0.3$. However, the variation in lattice parameters exhibited random behavior, which might be attributed to the crystal lattice's non-uniform strain due to A-site metallic cation (Sr^{2+} in Mg^{2+} or vice-versa) substitution. A similar conclusion is also possible to draw from the diffraction peak shift. However, there is no trace of impurity phase and mixed-phase, which agrees with earlier reports that solids with different crystal symmetry do not form a solid solution The *MTO* and *STO* crystals would present independently in the composite particle. The derived *STO* concentrations are slightly higher than that of analytical values, and that might be attributed to the fact that XRD patterns of perovskite-type oxides are usually dominated by the contributions of heavier elements (i.e., Sr)[110]. The 3-D crystal illustration for x =0.1, (1-x) *MTO-x STO* composite ceramic portrayed in figure 4.1(d) revealed that the crystals of *MTO* and *STO* diffused to form a single crystal [112].

Figure 4.2(a) presents the Raman spectra of (1-x) *MTO-x STO* (for x=0.04,0.1…0.5) composite ceramic discs sintered at 1350˚C. A Raman spectrum displays various vibrational modes corresponding to a molecular structure under monochromatic light irradiation and is a tool to characterize short-range symmetry. As per group theory, trigonal *MTO* with $R\bar{3}$ symmetry exhibits ten Raman-active vibrational modes ($\Gamma_{Raman}= 5A_g + 5E_g$), where each E_g mode is double degenerated $(E_g = E_g^1 + E_g^2)$ [111]. The obtained Raman spectra for composite ceramics exhibited all the 10 (226 cm^{-1}, 282 cm^{-1},306 cm^{-1}, 327 cm^{-1}, 357 cm^{-1},397 cm^{-1},485 cm^{-1}, 506 cm^{-1}, 637 cm^{-1}, 715 cm^{-1}) theoretically predicted modes, signifying presence of local symmetry in the crystal lattice [113]. Further, modes observed around 177 cm^{-1}, 246 cm^{-1} and 629 cm^{-1} were belong to $SrTiO_3$ crystal lattice [110]. The above-mentioned 13 Raman modes were observed for all the composite ceramics, however depending upon individual phase concentrations, Raman's intensity corresponding to *MTO/STO* was suppressed or grew accordingly. The obtained Raman spectra for composite ceramics reflected the presence of local symmetry in the composite ceramics. Among the 10 vibrational modes of *MTO* crystal, modes around 328 cm^{-1} and 353 cm^{-1} are attributed to O octahedra's twisting with Mg and Ti atoms, respectively.

As shown in Figure 2(b), there is no significant change in the profile of mode ~ 353 cm^{-1} corresponding to TiO_6 with an increase in *STO* concentration. However, the profile for mode ~328 cm^{-1} originated from MgO_6 octahedron showed a blue shift with an increase in

STO concentration till x = 0.3. With a further increase in *STO* concentration, the mode's peak profile got broadened, as shown in Figure 2(d). The replacement of Sr in the Mg site might be the cause behind the blue shift of the Raman mode originating from twisting of MgO_6 and observed broadening revealed inhomogeneous distortion in the vicinity of MgO_6 for x >0.3. The characteristic observed from Raman spectroscopy complements the XRD spectra analysis.

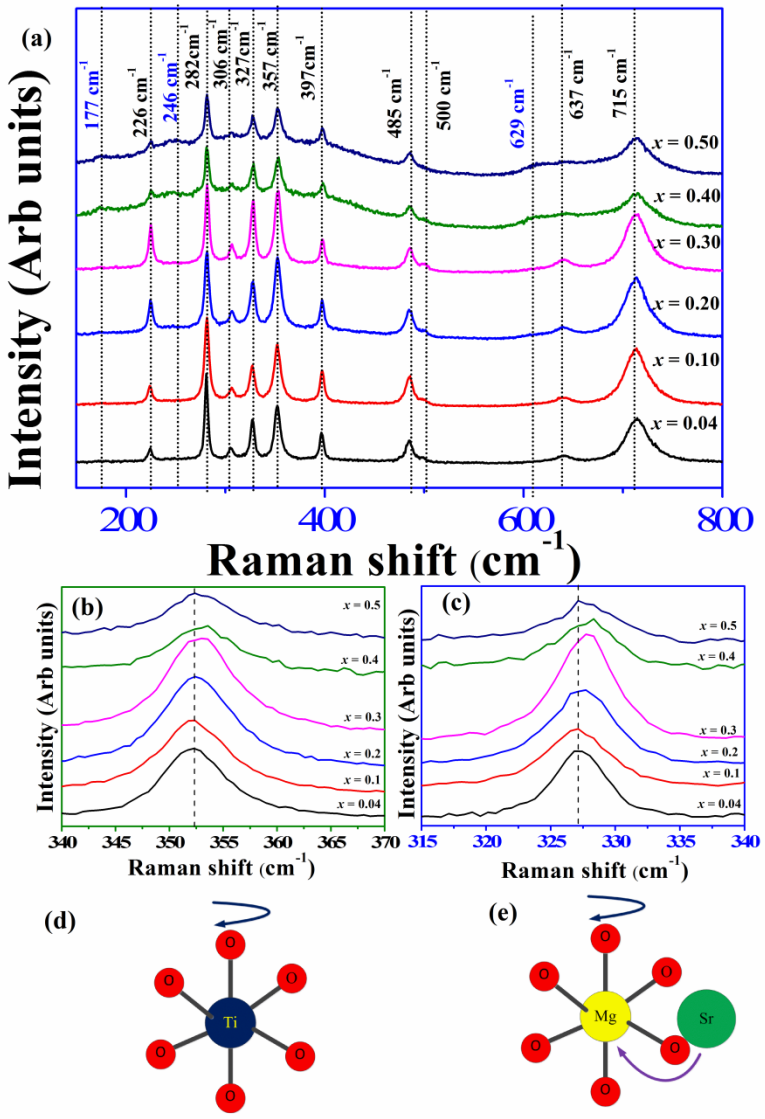

Figure 4.2: *(a) Raman spectra of (1-x) MTO-x STO (for x=0.1, 0.2…0.5) composite ceramic discs sintered at 1350˚C. The vibrational modes for MTO and STO are indexed in black and blue, respectively. (b) and (c) presents the enlarged view of 358 cm^{-1}mode and 328 cm^{-1}mode, respectively. (d)and I the twisting of TiO_6 and MgO_6 octahedron, respectively.*

In ceramic technology, the ceramic disc's microstructure is a significant characteristic and determining factor, which provides a qualitative outlook of the grain distribution. The

microstructures and histograms of grain size distribution for the sintered (1350˚C) (1-*x*) *MTO-x STO* (for *x*=0.1, 0.2 and 0.3*)* composite ceramic discs are presented in figure 4.3 (a-c).

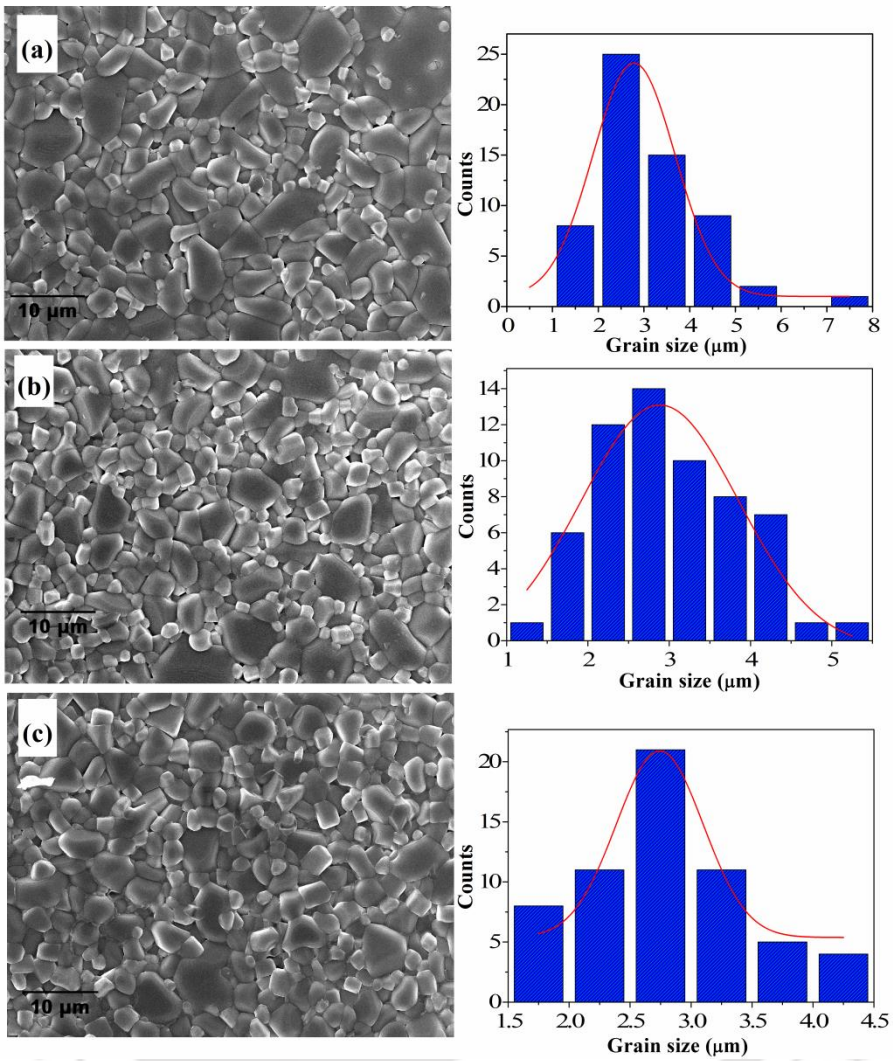

Figure 4.3*: FESEM images of (1-x) MTO-x STO (for x=0.1, 0.2,0.3) composite ceramic discs sintered at 1350˚C, along with histograms of grain size distribution.*

The observed microstructures revealed that *MTO* and *STO* ceramics grains were well packed together to form a highly dense composite ceramic. In the present study, the individual calcined ceramic powders were re-grinded to reduce the particle sizes. Particles with smaller sizes would enhance the sintering velocity and promote grain boundary diffusion and lattice diffusion from the surface leading to uniform grain growth and densified microstructure at lower sintering temperature. Based on the sizes obtained, grains can be classified into two categories: type-I (4-6 μm) and type-II (~1-4 μm). The FESEM images, along with the histograms of grain size distributions, revealed that the type-I and type-II grains are almost evenly distributed. Further, the type-I grains ceased in

number compared to a growing number of type-II grains with an increase in *STO* concentration.

4.3.1.2. **Microwave dielectric properties:**

The microwave dielectric properties of (1-*x*) *MTO-x STO* (where *x* = 0.1– 0.5) composite ceramic discs are recorded at a spot frequency using the resonant method. Figure 4.4 presents the variation of key microwave dielectric parameters for (1-*x*) *MTO-x STO* (where, *x* = 0.04,0.1 – 0.5*)* composite ceramic pellets with respect to *x*.

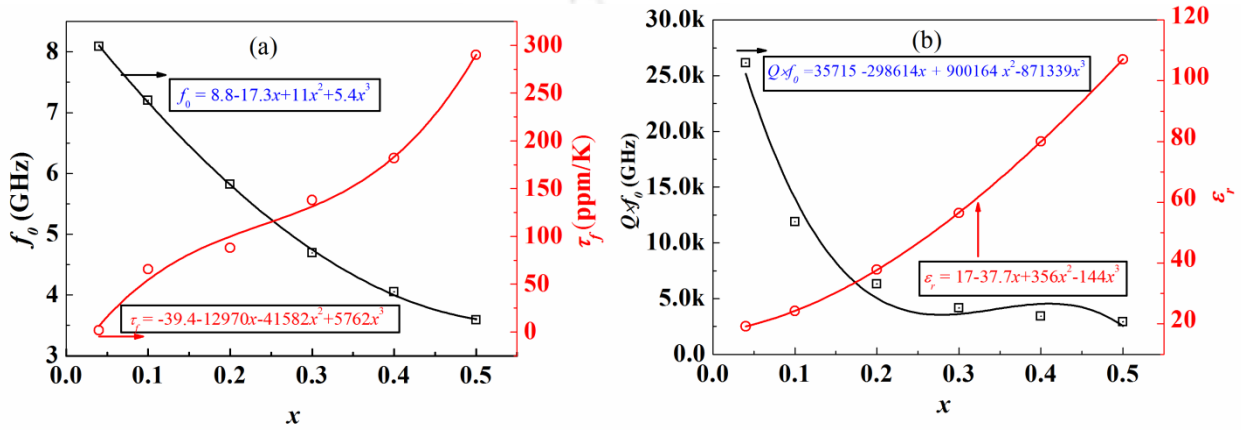

Figure 4.4:*Variation of (a) resonant frequency (f_0) and temperature coefficient of resonance frequency(τ_f), (b)quality factor ($Q \times f_0$) and dielectric constant(ε_r) at room temperature with respect to STO concentration for (1-x) MTO-x STO (where, x= 0.1 – 0.5) composite ceramic discs.*

The variations of microwave dielectric parameters could fit a cubic polynomial, and the obtained cubic equations are presented in the inset of figures 4.4(a) and figure 4.4(b). The dielectric constant for the *MTO-STO* composites increased from ~18.74 to 107.98 for *x* =0.04 to 0.5. The resonant frequency is shifted towards the lower side (8.08 GHz to 3.592 GHz) as the resonant frequency is inversely proportional to the dielectric constant [67]. The stability in microwave dielectric properties with temperature is vital for the endeavor of practical applications. The measure of temperature stability in terms of the dielectric constant defined as the temperature coefficient of the dielectric constant (τ_ε) was estimated using equation (4.1)

$$\tau_\varepsilon = \frac{1}{\varepsilon_r}\left[\frac{\Delta f_0}{\Delta T}\right] \qquad (4.1)$$

where, $\Delta\varepsilon_r = \varepsilon_r$(85˚C) – ε_r (30˚C) and ΔT = 85˚C-30˚C [114]. The $\tau_\varepsilon$increased from 214 to 1897 ppm/K for *x*= 0.04, 0.1 to 0.5. The temperature coefficient of resonance frequency (τ_f) is calculated following the expression[115],

$$\tau_f = \frac{1}{f_0}\left[\frac{\Delta f_0}{\Delta T}\right] \qquad (4.2)$$

where, $\Delta f_0 = f_0(85^\circ C) - f_0(30^\circ C)$ and f_0 is the resonant frequency. All the composite ceramics exhibited a positive temperature coefficient of resonance frequency and increased *STO* concentration. The temperature coefficient of resonance frequency tuned to near-zero ~ 1.72 ppm/K for x =0.04. The quality factor $(Q \times f_0)$ *also* found to be ceased from $(Q \times f_0)$ ~ 26,154 GHz at 8.08 GHz to 2911 GHz @ 3.592 GHz for x= 0.04 to 0.5, respectively. The (1-x) $MgTiO_3 - x\ SrTiO_3$ (for x = 0.04) composite ceramics exhibited best microwave dielectric properties with quality factor $(Q \times f_0)$ ~ 26,154 GHz at 8.08 GHz and near-zero temperature coefficient for resonance frequency τ_f ~ 1.76 ppm/K.

4.3.1.3 Temperature and frequency-dependent dielectric properties:

Physical properties exhibited by a material depend on the operating temperature. At a lower temperature regime (cryogenic temperature), the loss introduced by phonon scattering would be minimal compared to other temperature ranges where phonon scattering would be higher due to thermal activation. Figure 4.5(a) presents the variations of dielectric constant from cryogenic temperature (125 K) to elevated temperature (475K) at 10 MHz for *MTO-STO* composite ceramic discs. The dielectric constant of (1-x) MTO-x STO (for $x \leq 0.1$) composite ceramic disc remained almost constant with measuring temperature. Unlike that case, for (1-x) *MTO-x STO* with other compositions, at a low-temperature regime (125 K to 400 K), the dielectric constant exhibited a sharp fall ascribed to ferroelectric to paraelectric transition (at ~105 K) and later gradually increased with measuring temperature due to thermally activated polarization [116].

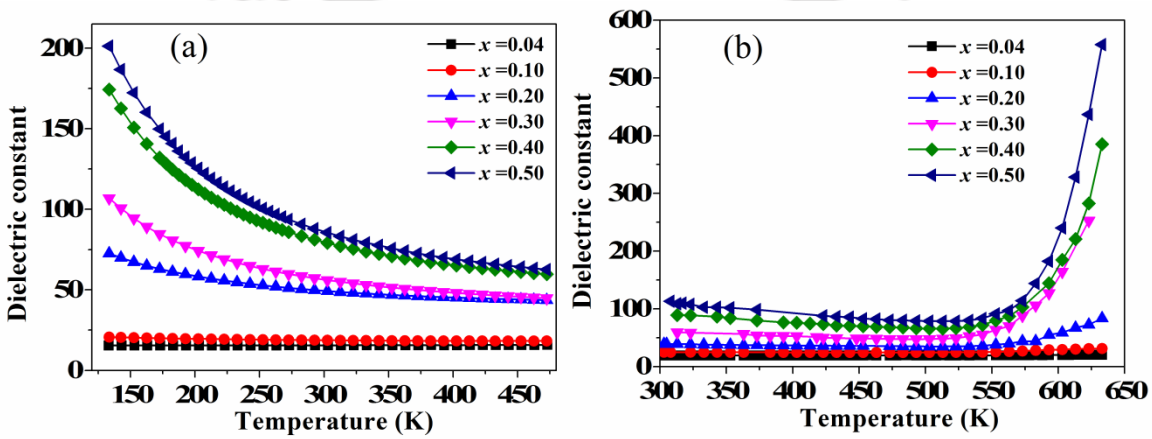

Figure 4.5: Temperature dependent dielectric constant (a) from cryogenic temperature 125K to 478K, and (b) room temperature 300K to elevated temperature 650K, for (1-x) MTO-x STO (for x=0.04, 0.2…0.5) composite ceramic discs sintered at 1350˚C.

Further, with an increase in *STO* content, the dielectric constant for the *MTO-STO* composite ceramic discs improved monotonically (18.74 -85.55), attributed to higher dielectric polarization in *STO* ceramics as compared to *MTO* ceramics [23,117]. The obtained values of dielectric constants are comparable with the theoretical values attributed to a maximum density of the prepared ceramic discs. Figure 4.5(b) depicted the variation of the dielectric constant by measuring temperature from room temperature to 630 K at 100 kHz. The observed rapid growth in dielectric constant above 400 K ascribed to thermally activated charge carriers.

Figure 4.6 (a) and (b) represent the frequency-dependent dielectric constant of (1-*x*) *MTO-x STO* composite ceramics measured in the low frequency (100-100 kHz) and high frequency (1MHz -1 GHz) regime, respectively. Interestingly, the dielectric constant showed no variation over a broad frequency range for all the compositions. This attributes to the absence of space charge polarization in the measured frequency range. However, at a higher frequency region ~ 1 GHz, the dielectric constant showed a hump-like feature, which might contribute to the relaxation of ionic polarization[118].

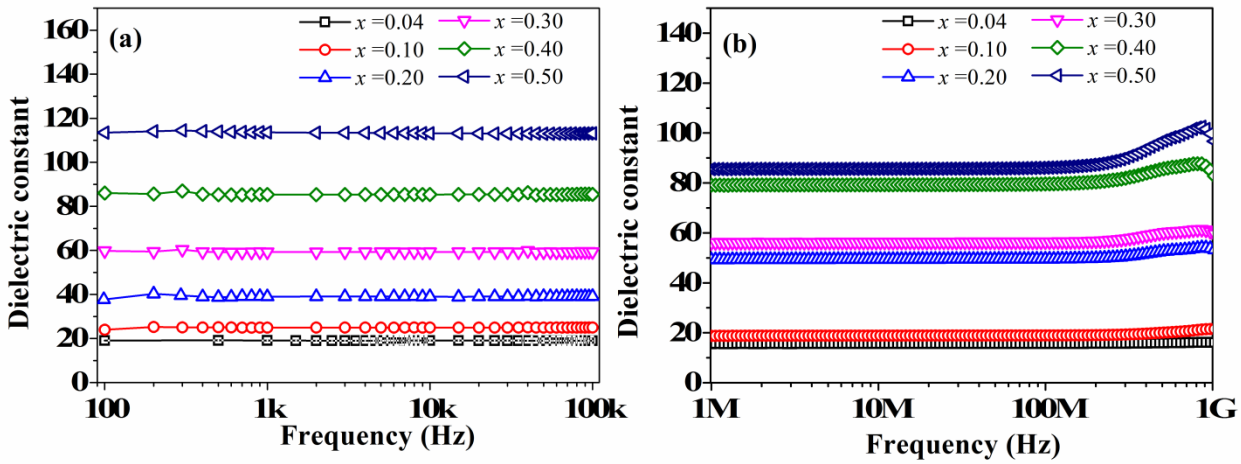

Figure 4.6*: Frequency-dependent dielectric constant measured at room temperature for (1-x) MTO-x STO composite ceramic discs sintered at 1350˚C in (a) 100Hz -100 kHz and (b) 1MHz- 1GHz regime, respectively*

4.3.1.4 Conductivity analysis:

Figure 4.7 depicts the variation of complex conductivity (σ_{ac}) with the frequency of applied field for the (1-*x*) *MTO-x STO* composite ceramic discs at 573 K. The conductivity plot can be distinctly divided into three different regions. In the I-region, conductivity rapidly decayed with a decrease in applied frequency (< 1 kHz), which can be attributed to the non-uniform distribution of interfacial polarization. Such characteristics are evident when the

charges (positive and negative) pile in the interface of electrode and sample interface known as space charge polarization, prohibiting further conduction in the sample and would cease the conductivity [119]. The second region is a plateau region, and literature suggested it contributes to dc electrical conduction in the sample. The third region preceding the plateau region of complex conductivity is highly dispersive, and this characteristic response can be defined by an empirical equation known as the Jonschers power law. The Jonschers power law can be expressed as follows,

$$\sigma_{ac} = A\omega^{n} \tag{4.3}$$

where, $\omega = 2\pi f$ is the angular frequency of the applied electric field, and A and n are fitting parameters of observed nature.

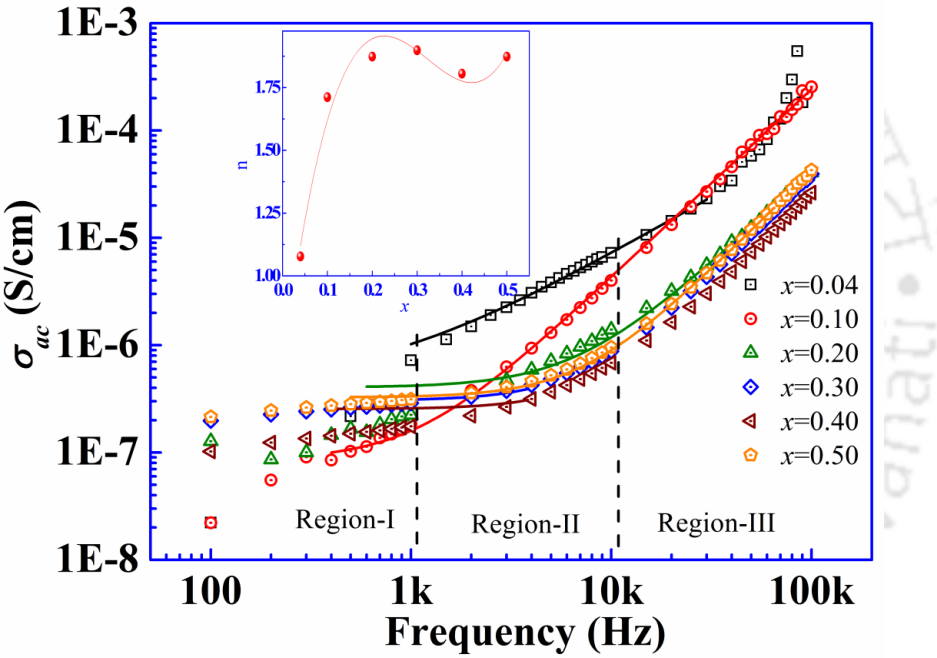

Figure 4.7*: Dispersion of AC-conductivity with the applied frequency of (1-x) MTO-x STO (for x=0.04,0.1-0.5) composite ceramic discs measured at 573 K.*

Generally, n lies between 0 to 1; however, it often deviates from this range, as evident in many studies reported earlier [94]. The obtained value of n defines the nature of electrical conduction by mobile charge carriers present in the sample. The characteristic response of conductivity with applied frequency for the (1-x) *MTO-x STO* composite ceramic discs for all compositions is found to be similar. Further, the conductivity plots were fitted with the Jonschers' power law, and the extracted values of n were found to be greater than 1 for all the compositions. These signified hopping charge carriers contributed to electrical conduction in

composite ceramics. The value of *n* followed cubic relation with *STO* concentration as presented in the inset of figure 4.7

4.3.1.5 Temperature-dependent Resistivity and VRH model analysis:

Figure 4.8(a) presents the temperature-dependent ac resistivity of (1-*x*) *MTO-x STO* (where, *x* = 0.04, 0.1 – 0.5) composite ceramic discs. At a lower temperature range (< 250 K), observed dispersion in resistivity can be attributed to dispersion in dielectric polarization due to ferroelectric to the paraelectric transition of *STO* ceramics, at ~105 K. After a certain temperature, the resistivity decreases with measuring temperature, as typical semiconducting nature exhibited by *MTO* ceramics[84]. In the case of thermally activated conduction across the band, conductivity can be expressed with the empirical equation given by Arrhenius as follows,

$$\sigma_{ac} = \sigma_0 \exp(-\frac{E_a}{k_B T}) \qquad (4.4)$$

where σ_0, k_B, and E_a are the notations for a proportionality constant, Boltzmann constant, and activation energy, respectively [120]. Since $\sigma_{ac} = 1/\rho_{ac}$, the equation (2) can be re-written as

$$\rho_{ac} = \rho_0 \exp(E_a / k_B T) \qquad (4.5)$$

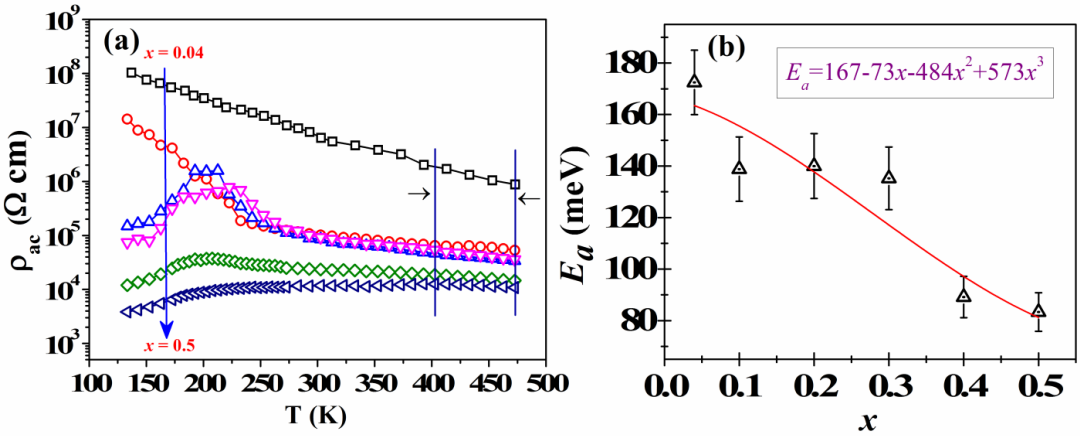

Figure 4.8: (a)Ac resistivity with respect to temperature and (b) Cubic variation of activation energy with respect to STO concentration for(1-x) MTO-x STO (for x=0.04,0.1-0.5) composite ceramic discs.

As shown in Figure 4.8 (a-f), the ln ρ_{ac} vs. 1/T plots a straight line perfectly fitted for these Arrhenius plots in the measuring temperature regime ~ 400 K- 470 K for (1-*x*) *MTO-x STO* (where *x* = 0.04 – 0.5) composite ceramic discs. As presented in figure 4.8(b), the evaluated activation energies reduced from 172 meV to 83 meV for *x* = 0.04 – 0.5, (1-*x*) *MTO-x STO* composite ceramics and found to follow a cubic equation with *STO*

concentration(*x*). In thermally activated conduction, the activation energy decreases as the charge carrier concentration increases, leading to a decrease in the energy gap between the Fermi level and free energy level [121]. Both the ceramics *MTO* and *STO* are insulating in nature; however, they exhibit a certain amount of electrical conduction because of some microstructural defects such as vacancies, impurities, etc. These charge carriers cannot contribute to band-to-band conduction processes at low temperatures but would hop from one state to another energetically favorable state within the impurity band. Further, this hopping-like conduction can be limited to a fixed hopping range (nearest-neighbor hopping) or variable hopping range (variable range hopping).

According to Mott's proposed 3-d VRH model, the resistivity (ρ_{ac}) follows a relation with measuring temperature (T) as follows,

$$\rho_{ac} = \rho_0 \exp(T_0/T)^{1/4} \qquad (4.6)$$

where ρ_o is the pre-exponential factor, and T_0 is the characteristic temperature co-effcient [120]. In the present case, a measuring temperature (T) ~ 400 K- 470K regime has been chosen to study the effect of STO concentration (*x*).

$$N(E_F) = \frac{16\alpha^3}{k_B T_0} \qquad (4.7)$$

The plots for temperature variation resistivity concerning $T^{-1/4}$ as presented in figure 4.9 (a-f) are well fitted linearly (R > 0.9), and thus, the conductivity of the composite ceramics is analyzed in detail using Mott's variable range hopping 3-d model. From equation (4.6), understandably, the slope of $\ln[\ln(\rho_{ac}/\rho_o)]$ vs. lnT should be ¼, and the obtained values of the slopes for the same as shown in figure 4.10 (a-f) verified the validation of Mott's 3-d VRH model in this temperature regime. The density of states ($N(E_F)$) can be determined using temperature co-efficient (T_o) and the inverse localized length of localized states (α) using the relation given below. Here, the inverse localized length of localized states was considered as 1.66 nm^{-1}, k_B is the Boltzman constant. The density of states increased from 1.65 $\times 10^{19} eV^{-1}cm^{-3}$ to 3.413$\times 10^{20} eV^{-1}cm^{-3}$ with increase in *STO* concentration from *x*= 0.04 to 0.5 and this observation justified the reduction in activation energy with *x*. Besides, the most probable average hopping length (R_H) and average hopping energy (W_H) are also determined from equations (4.8) and (4.9).

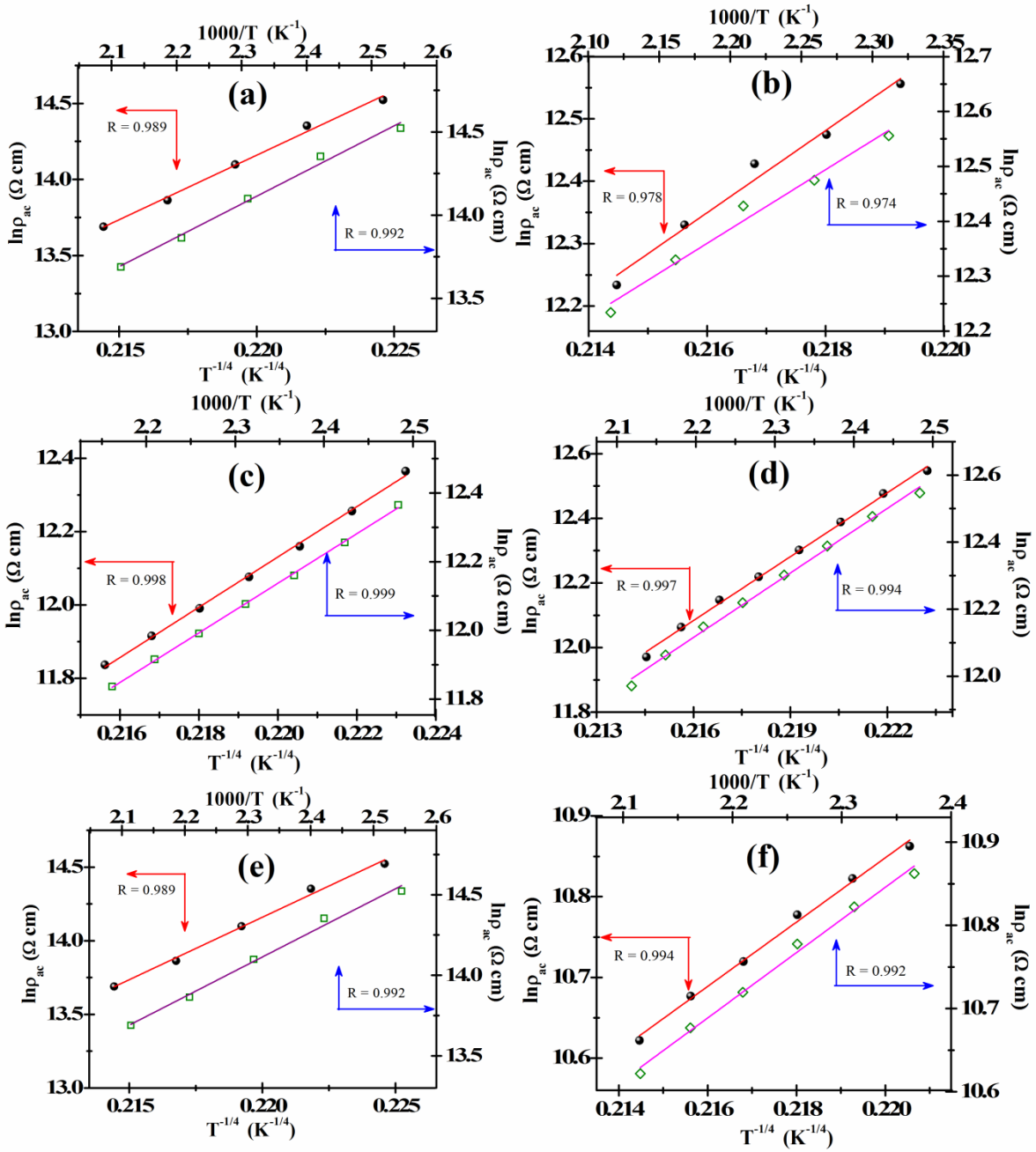

Figure 4.9*: (a-f) Temperature-dependent electrical resistivity for (1-x) MTO-x STO (where, x= 0.04,0.1 – 0.5) composite ceramics with respect to 1/T and $T^{-1/4}$, respectively.*

$$R_H = 0.75 \times [3/2\pi\alpha N(E_F)k_B T]^{1/4} \quad (4.8)$$

$$W_H = [3/(4\pi R_H^3 N(E_F))] \quad (4.9)$$

The derived values of R_H and W_H values for the composite ceramics fulfilled the prerequisite condition of Mott's 3-d VRH conduction model, i.e., $\alpha R_H > 1$ and $W_H > k_B T$. The

most probable average hopping length (R_H) decreases with an increase in measuring temperature, and in contrast to it, average hopping energy (W_H) increases with measuring temperature. These can be attributed to the fact that with a temperature rise, the immobile charge carriers' thermal energy increased, leading to growth in average hopping energy and a reduction in average hopping length (R_H).

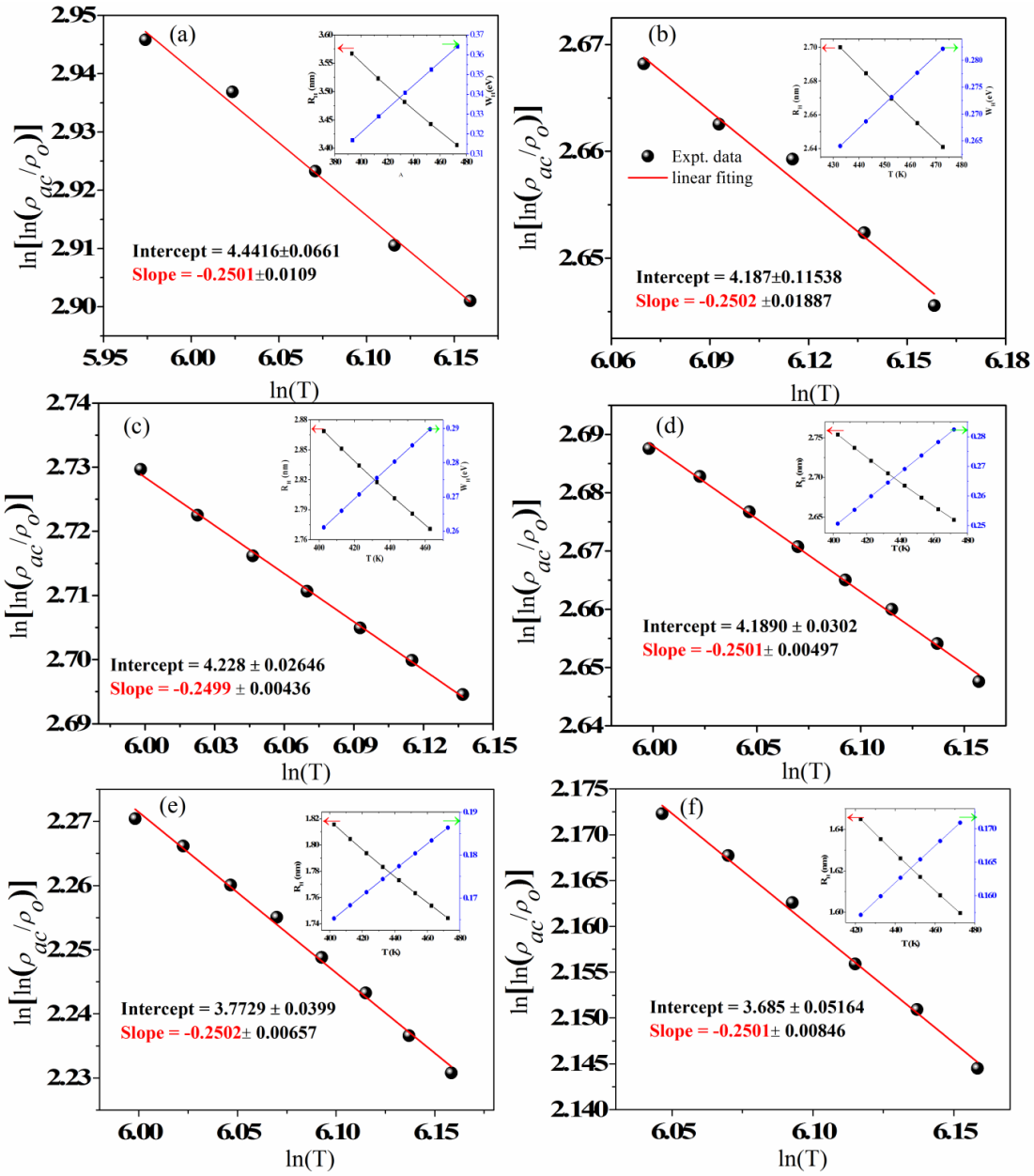

Figure 4.10 ☹a-f) ln[ln(ρ_{ac} /ρ_o)] vs. lnT scattered plot of experimentally obtained data for (1-x) MTO-x STO (where, x= 0.04,0.1 – 0.5) composite ceramics and linearly fitted to obtain slope represented by the solid lines. Variation of hopping length (R_H) and average hopping energy (W_H) with measuring temperature plotted as shown in the inset of figure 9(a-f).

4.3.2 STO/MTO bilayer thin films

4.3.2.1 Structural and microstructural analysis:

Figure 4.11 (a) presents XRD patterns for annealed *STO* films deposited on Si substrate in different Ar and O_2 mixed environments.

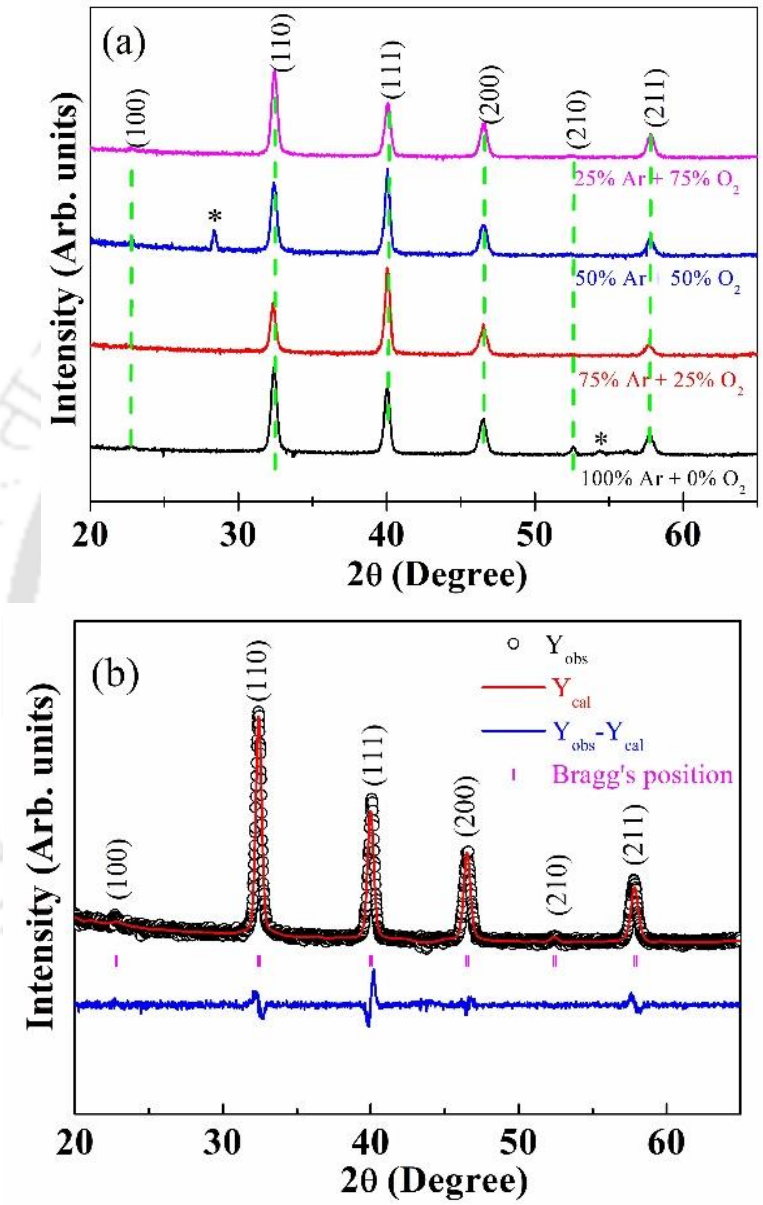

Figure 4.11*: (a) XRD patterns of STO film deposited on Si (STO/Si) at different Ar and O_2 mixed environments, (b) Reitveld refined XRD pattern for STO/Si film deposited at 75% Ar +25% O_2 environment.*

All the films exhibited polycrystalline cubic *STO* phase and the lattice planes are indexed in the XRD pattern of *STO* film deposited at 75% Ar +25% O_2 mixed environment. As seen in figure 4.11(a) *STO* films deposited in 100% Ar, and 50:50 Ar: O_2 environments

possess a secondary phase, and a pure *STO* phase is obtained for 75:25 and 25:75 Ar: O_2 environments. Further, the XRD pattern of *STO* film deposited in 75% Ar +25% O_2 environment exhibited the best crystallinity and the phase purity is further confirmed with Rietveld refinement as presented in figure 4.11(b). The XRD patterns for annealed STMT bilayer films deposited on Si substrate are shown in figure 4.12 for three different thicknesses. In all the films, *STO* and *MTO* crystallized into polycrystalline cubic and rhombohedral phases, respectively, upon annealing at 750˚C. In addition, obtained XRD diffraction patterns also revealed the formation of a secondary phase corresponding to $MgTiO_3$. This attributed to a deficiency of Mg atom or excessive Ti atom transfer from the sputtering target to the substrate as given in the following chemical reaction

$$MgO + 2TiO_2 \rightarrow MgTi_2O_5 \qquad (4.10)$$

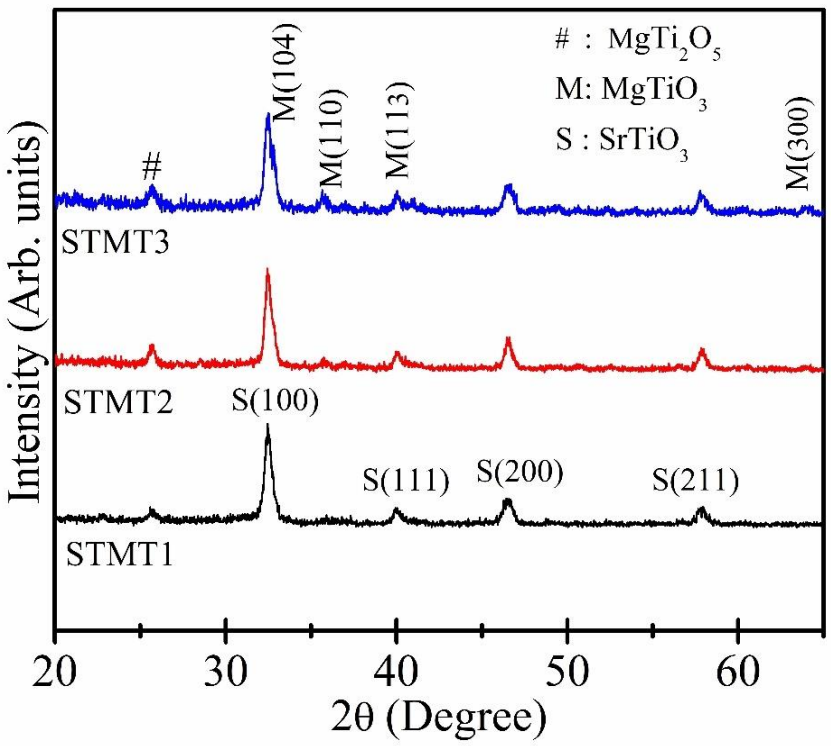

Figure 4.12: XRD patterns for annealed STMT bilayers deposited on Si substrate scanned at room temperature.

Reitveld refinement of diffraction patterns is carried out for STMT bilayer films, considering the pm3m space group with cubic symmetry and R-3 space group with rhombohedral symmetry for *STO* and *MTO* phases, respectively. As presented in Figure 4.13 the obtained refined pattern almost traced the experimental pattern as a sign of good quality fitting. The details of the crystal lattice, such as lattice parameters and volumetric phase

concentrations for the STMT films, were extracted from Rietveld refinement data as tabulated in Table 4.4. As the film thickness of *MTO* increases, the corresponding volumetric fraction for the *MTO* phase increases in the diffraction pattern of STMT films attributing to the rise in *MTO* atomic layers in the overall penetration depth of X-ray. In non-epitaxial growth of films, lattice parameters of top and bottom layers either get compressed or enlarged to match their lattice units depending upon their lattice misfit [81]. In the present study, in-plane lattice parameters of *MTO* and *STO* films were found to be compressed and elongated, respectively, as *MTO* has a more significant lattice parameter (5.056 Å) compared to *STO* (3.914Å).

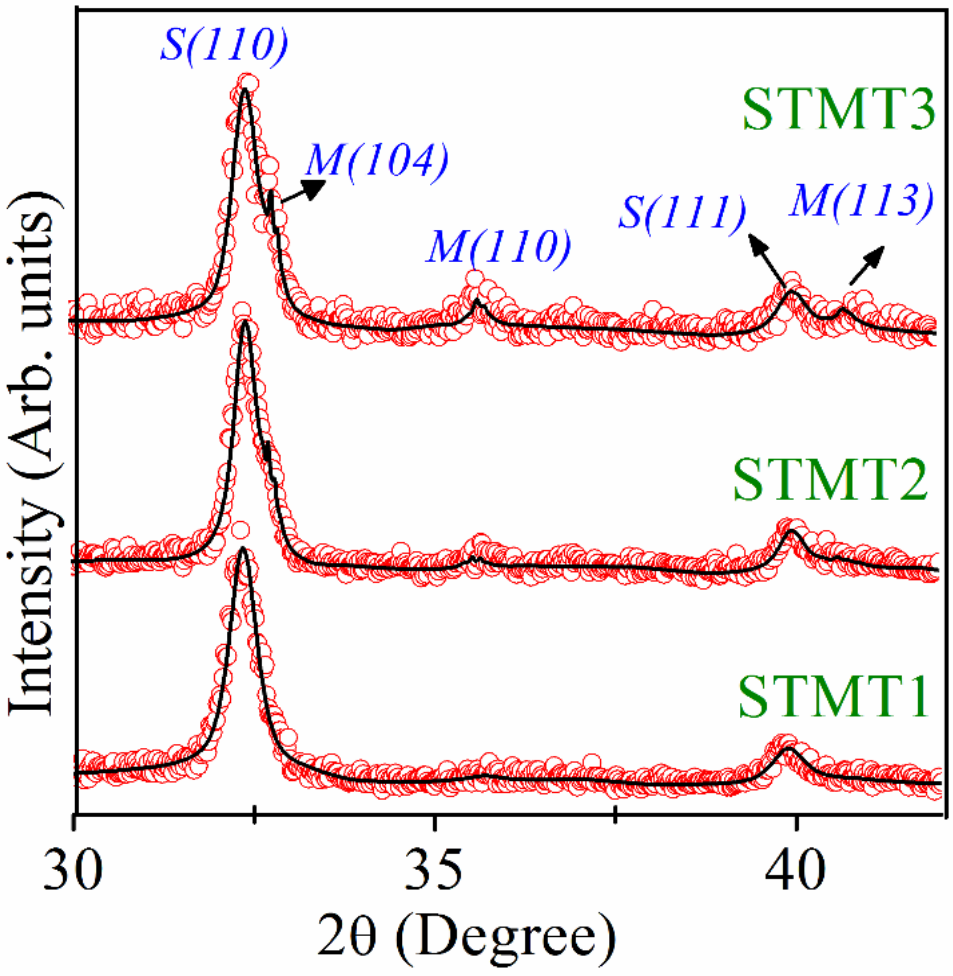

Figure 4.13: Rietveld refined XRD patterns for STMT bilayers.

As predicted in theory, as the film thickness of *MTO* increases, compressive strain in the lattice parameter is found to be ceasing and for STMT3 obtained lattice parameter (5.0505 Å) is almost close to the theoretical one (5.056 Å) [122]

Table 4.4: Obtained lattice parameters and volumetric concentration of the STMT films from Rietveld refinement.

Sample	***MTO phase***			***STO phase***	
	Volumetric Fraction (%)	*a = b (Å)*	*C (Å)*	*Volumetric Fraction (%)*	*a=b=c (Å)*
STMT1	*9.72*	*5.0336 ± 0.0031*	*14.3475 ± 0.0075*	*98.28*	*3.9145± 0.0018*
STMT2	*36.93*	*5.0459 ± 0.0042*	*14.0222± 0.0118*	*63.07*	*3.9071± 0.0032*
STMT3	*45.27*	*5.0505 ± 0.0065*	*13.9872± 0.0274*	*54.73*	*3.9096± 0.0028*

Figure 4.14 presents the surface topography for STMT bilayer films. The granular particles of size < 100 nm are found to be formed in all the films. Further, the surface topography was modified with an increase in *MTO* thickness as observed from the AFM images.

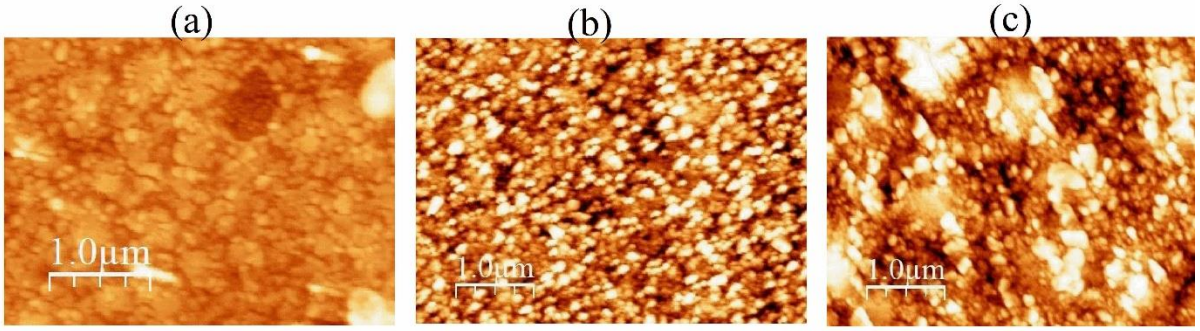

Figure 4.14: Surface topography of STMT bilayer films.

4.3.2.2 Optical properties:

Figure 4.15(a) presents the transmittance spectra for STMT bilayer films in the UV-visible region. All the films exhibited more than 70% transmittance and Fabry-Perrot pattern. At around 300 nm, the transmittance dropped sharply for all the films corresponding to the characteristics of the band structure. The optical bandgap is the energy gap between the maximum (highest of occupied molecular orbital) valance band and the minimum conduction bandgap (lowest of unoccupied molecular orbital). In 2D material, the optical bandgap gets altered due to quantum confinement and is considered a critical parameter in various device

applications such as solar cells and LEDs [123]. The bandgap of the STMT bilayer films was estimated by using Tauc's and Woods's relation as follows,

$$h\upsilon\alpha = A(h\upsilon - E_g)^n \qquad (4.11)$$

where, *A and Eg* are proportional constant and optical bandgap, and *v* and *h* represent the optical frequency and the Planck constant, respectively [124]. The power factor *n* is a constant for an optical transition. (*n* = ½, 2, 3/2, or 3 for direct allowed, indirect allowed, direct forbidden, and indirect forbidden transitions, respectively).

Figure 4.15(b-d) shows Tauc's plots of STMT1, STMT2, and STMT3 for direct allowed transitions. The estimated optical bandgap value is in the range of reported bandgap values 3.735 eV – 3.727 eV intermediate to $MgTiO_3$ and $SrTiO_3$, attributing to the crystalline sample. The bandgap value decreases with an increase in *MTO* thickness since the bandgap of *MTO* (~3.51eV) [125]is smaller than *STO*(3.75eV)[126].

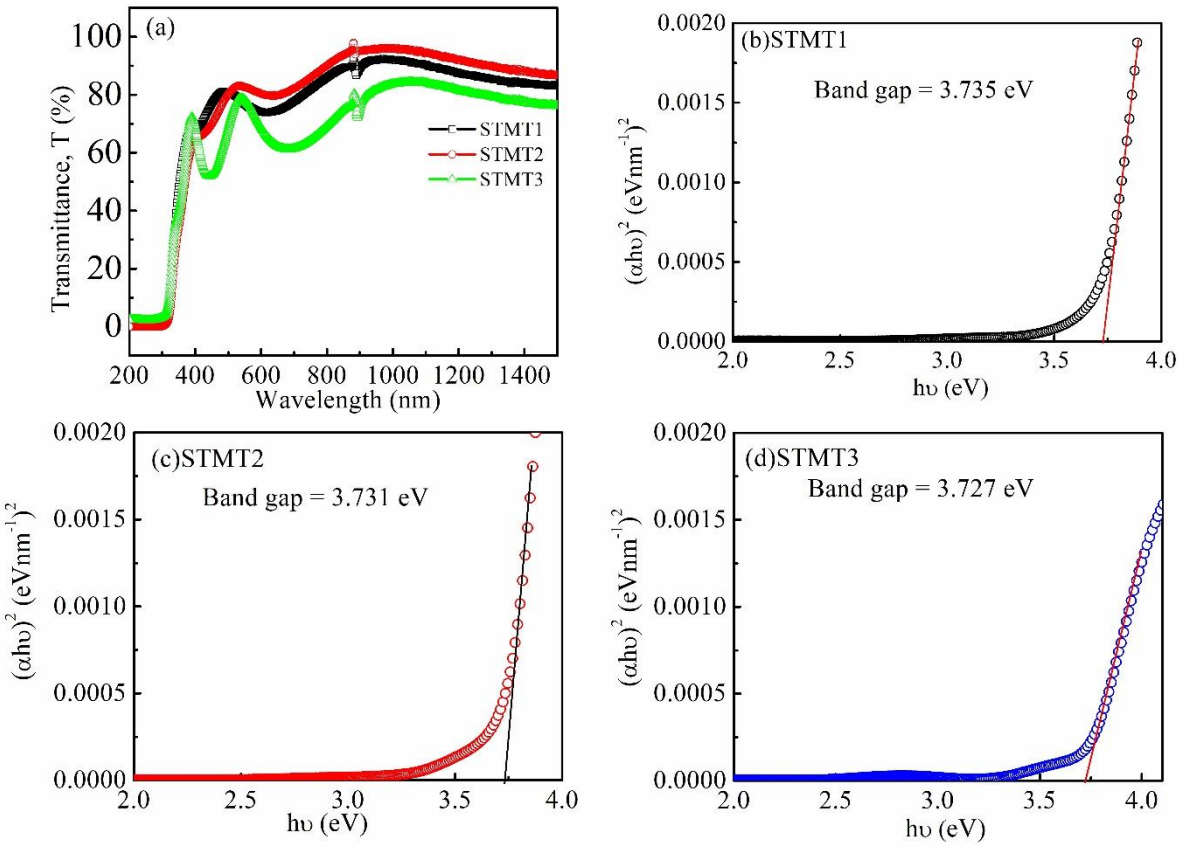

Figure 4.15: (a) UV-visible transmittance spectra for STMT1, STMT2 and STMT3 films and (b-d) Tauc's plot for STMT1, STMT2 and STMT3 films, respectively.

4.3.2.3 Dielectric properties:

The frequency-dependent dielectric constant represents a measure of dielectric polarizability of dipoles in the sample on the application of an ac field. Figure 4.16 presents the frequency-dependent dielectric constant for STMT thin films at room temperature. Maxwell-Wagner and Koop's phenomenological theory explained in the present case dielectric constant drops as the frequency of applied field rises attributed to the relaxation of space charge polarization [127]. The dielectric constant of STMT film is found to be increasing with an increase in *MTO* thickness which can be ascribed to the lower dielectric constant of *MTO* (~17) as compared to *STO*(~300)[128,129].

Figure 4.17(a) presents the frequency-dependent dielectric constant of STMT3 at different measuring temperatures. The dispersion in the dielectric constant remained almost invariant in the measured temperature range, which is an interesting observation from the application point of view

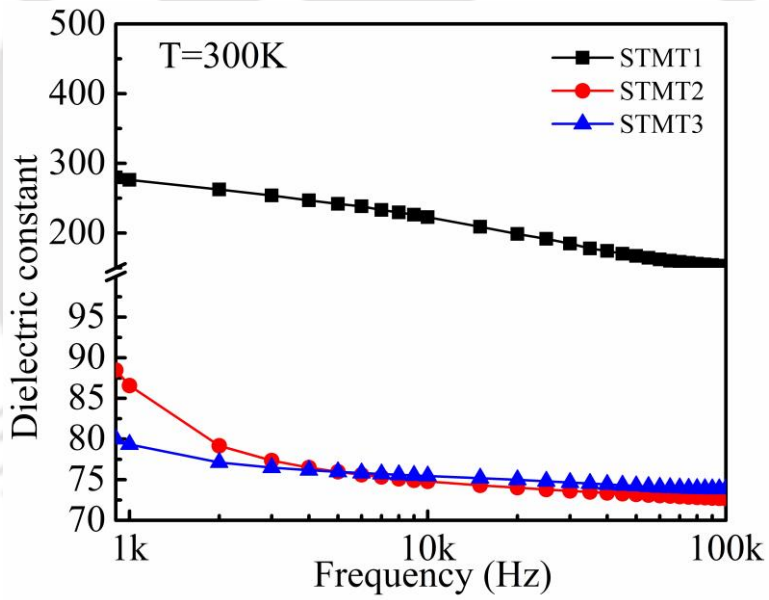

Figure 4.16: Frequency-dependent dielectric constant for STMT thin films.

The Complex impedance spectra reflect different relaxation mechanisms associated with a dielectric material and hence, are treated as an effective tool to probe relaxation mechanisms [97]. A dielectric sample can undergo more than one relaxation process depending upon the dipolar species present in it. Typically, each dipolar relaxation impedance spectra exhibit a semi-circular arc. In general, a polycrystalline material possesses two electrically active regions, viz: grains and grain boundaries, and each of them shows a

different relaxation time. Relaxation frequency for grains is at a higher frequency than grain boundary[90].

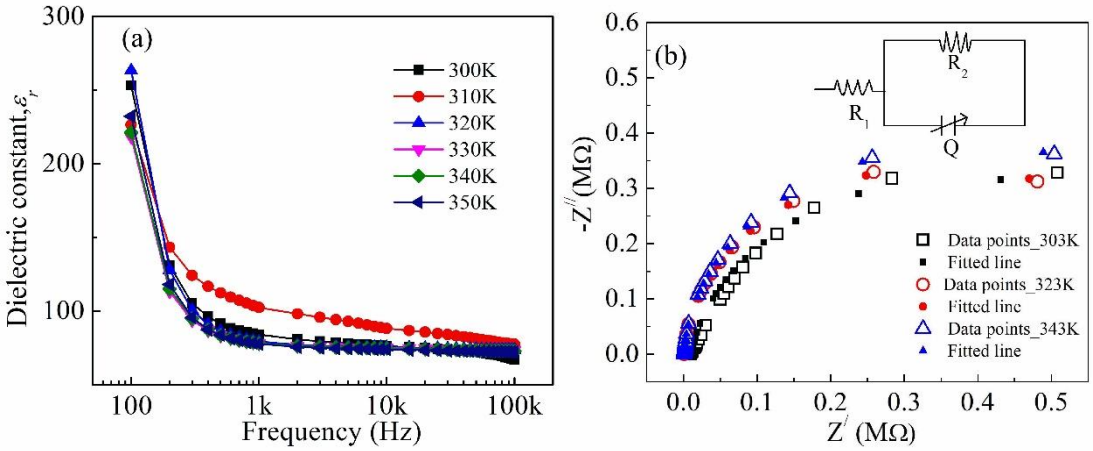

Figure 4.17: (a) Frequency-dependent dielectric constant of STMT3 at different measuring temperatures. (b) Cole- Cole plot for STMT3 to varying temperatures along with equivalent model circuit.

Figure 4.17(b) presents complex impedance spectra for STMT3 at three different measuring temperatures. Due to insufficient data points, only one semi-circular arc is evident, corresponding to grains of the samples. A combination of parallel resistance and constant phase element (CPE) in series with a resistive component fitted well for the obtained impedance spectra. The constant phase element is a frequency-dependent quantity, which possess both resistive and capacitive element as given in following expression of impedance corresponding to CPE element can be represented as,

$$z^* = [A(j\omega)^n]^{-1} \qquad (4.12)$$

For n=1 and 0, Z is completely capacitive and resistive, respectively[130]. The obtained electrical circuit for STMT films: Series combination of one resistor with a parallelly connected constant phase element (Q) and a resistor R(RQ), suggests that both grain and grain boundaries contributed to electrical polarization in the present measuring condition viz: frequency of applied field and temperature. The dielectric tunability test for STMT3 film is performed using an alternating electric field at 20 Hz. As shown in figure 4.18, the capacitance of STMT3 film increases as an increase in the voltage of the applied AC field. This can be attributed to an enhancement in polarizability at a higher voltage. The slope of the C vs. V is found to be 259 µF/V. These characteristics of STMT3 can be utilized in tunable electronic device applications.

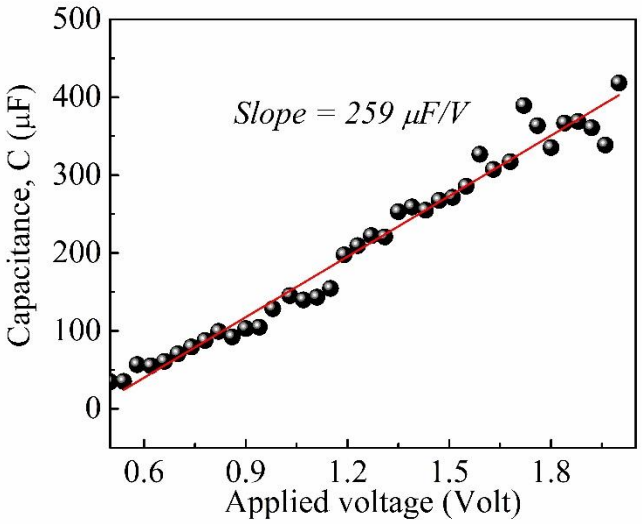

Figure 4.18: Capacitance versus applied ac voltage.

Microwave dielectric properties for the STMT thin films deposited on quartz substrate are measured by the SPDR method at 10 GHz. The obtained dielectric parameters are listed in table 4.5. The obtained dielectric constant is found to be decreasing with an increase in *MTO* film thickness. On the other hand, loss tangent is reduced with an increase in *MTO* film thickness. The values dielectric constant (table 4.5) for STMT2 and STMT3 are found to be higher as compared to the dielectric constant measured at a lower frequency range using the MIM structure which can be attributed to the different measurement techniques used in both cases.

Table 4.5: Obtained dielectric constant (ε_r) and loss tangent ($tan\delta$)

Sl. No.	**Sample name**	**At 10 GHz**	
		ε_r	$tan\delta$
1	STMT1	240	8.57×10^{-3}
2	STMT2	150	6.48×10^{-3}
3	STMT3	103	2.86×10^{-3}

4.3.2.4 Leakage current:

Leakage current is the allowed current flow through the dielectric material when subjected to the applied field. It has been found that in a critical field, leakage current rises abruptly due to avalanche breakdown and the Joule heating effect [131]. Therefore, leakage current study is crucial to understand the strength of a capacitor. In the present work, the

characteristics of leakage current density (J) vs. the applied field I for STMT3 (dielectric) thin film is tested for a maximum field of ~200kV/cm as depicted in figure 4.19(a). Maximum leakage current density, J of ~10^{-6}Acm$^{-2,}$ is recorded for the 200 kV/cm field. Several mechanisms are found to be responsible for current conduction in dielectric materials, such as Poole-Frenkel emission, Fowler-Nordheim unnelling ionic hopping conduction, Space-charge limited conduction, and the Schottky effect [132].

Generally, electrode(metal) and dielectric film form a Schottky junction and conduction through Schottky emission, as shown in figure 4.19 (b). As shown in figure 4.19(c), For E > 64 kV/cm, the lnJ vs. lnE plot exhibited linear behavior, and the slope is found to be greater than 2, which indicates space-charge limited conduction [120]. Further, the lower field region (E < 64), lnJ vs. $E^{1/2}$ showed linear variation as shown in figure 4.19(d) ascribed to Schottky emission.

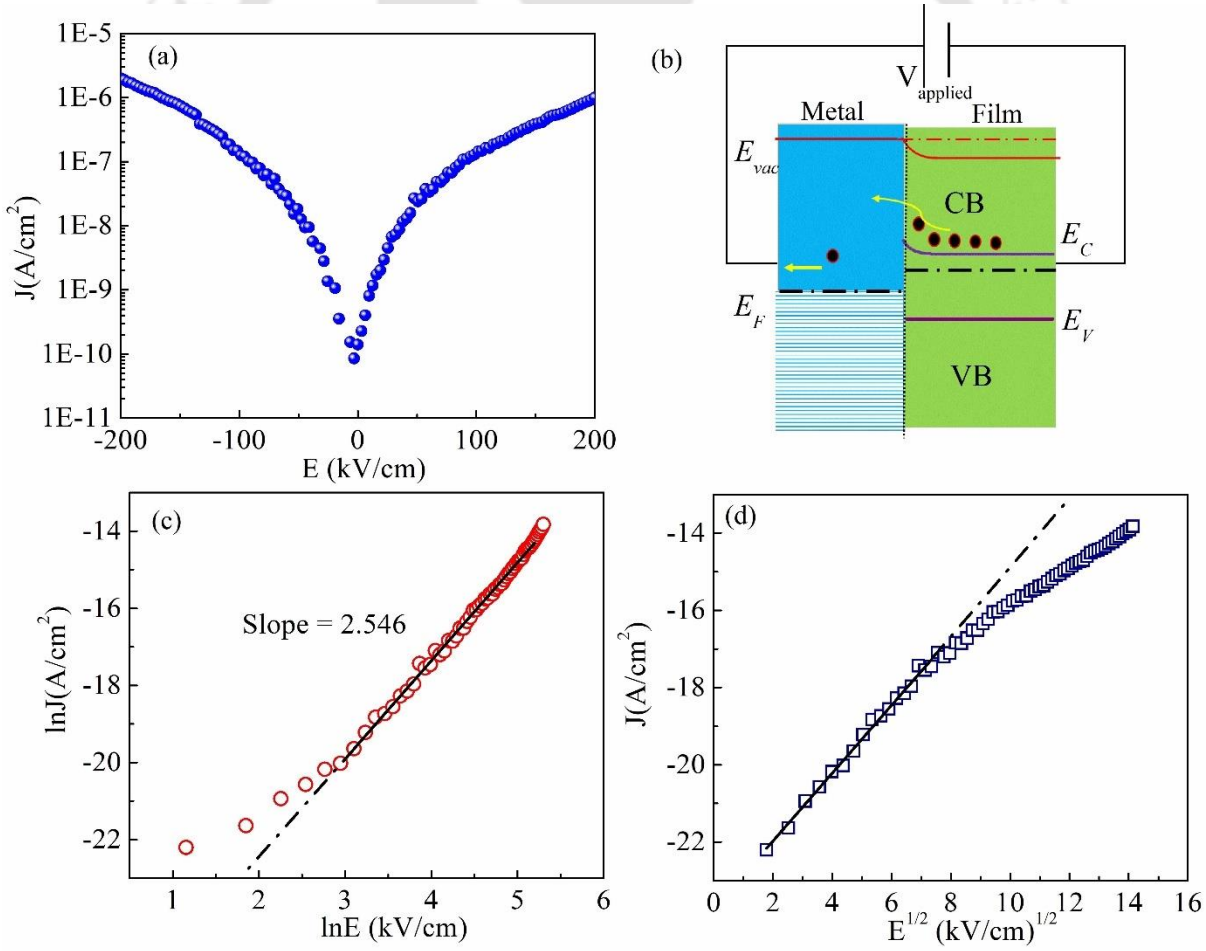

Figure 4.19 *a) Leakage current density (J) vs. the applied field I of STMT3 measured at room temperature, (b) schematic representation of leakage current flow through the film to*

metallic contact junction, leakage current density analysis of STMT3 for (c)space charge limited conduction (SCLC) and (d) Schottky mechanism, respectively.

4.4 Summary:

The phase pure *MTO-STO* composite ceramics were successfully synthesized by using the solid-state reaction method. The (1-*x*) $MgTiO_3$-*x* $SrTiO_3$ composite with x =0.04 exhibited the best microwave dielectric properties with moderate quality factor ($Q \times f_0$) ~ 26,154 GHz at 8.08 GHz and better thermal stability (τ_f ~ 1.76 ppm/K). The XRD spectra revealed that the individual ceramic *MTO* and *STO* were present in dispersed form instead of in a solid solution form, attributed to different crystal structures of the constituent ceramics. The 3-D crystal representation is illustrated from Vesta using Rietveld refinement data. Raman spectra analysis is also in good agreement with the XRD results. FESEM images revealed compact microstructures. The overall dielectric constant increased for the *MTO-STO* composite ceramic pellets and followed a cubic (polynomial) relation with *STO* concentration. The dispersion in frequency-dependent complex conductivity was analyzed by Jonscher's power Law and obtained power factor values (n) indicated hopping-like conduction of charge carriers.

Further, temperature-dependent resistivity was investigated by using the Arrhenius equation and Mott's 3-d variable range hopping model. The thermal stability of microwave dielectric constant and resonance frequencies was found to be degraded with *STO* concentration. *MTO/STO* bi-layer films deposited by using RF sputtering technique exhibited a polycrystalline phase upon post-annealing treatment at 750˚C for 2 hours. In an attempt to grow *MTO* film on *STO* film due to heteroepitaxy at the interface, both the crystal lattice undergoes lattice compression and elongation, respectively. The surface topography of the STMT films showed granular nanograins and with an increase in *MTO* thicknesses topography of the films deviated from the granular structure. The dielectric dispersion at room temperature for all the STMT films exhibited traditional Maxwell-Wagner and Koop's phenomenon. Impedance spectra for STMT3 film showed a distorted semi-circular arc corresponding to grain and grain boundary polarization. The STMT3 film showed considerable tunability to AC field voltage. The leakage characteristics for STMT3 film are studied at room temperature and found maximum leakage current density of order 10^{-6} A/cm^2 for a 200 kV/cm field. The obtained dielectric properties of *MTO-STO* composite ceramic and thin films are promising for microwave application.

CHAPTER 5: Structural, Electrical, and Dielectric Properties of $MgTiO_3$-$Ba_{0.5}Sr_{0.5}TiO_3$ Composite Ceramics and $MgTiO_3$/$Ba_{0.5}Sr_{0.5}TiO_3$ Bilayer Thin films

This chapter deals with the synthesis of the $MgTiO_3$- $Ba_{0.5}Sr_{0.5}TiO_3$ composite ceramics, and the $MgTiO_3$/ $Ba_{0.5}Sr_{0.5}TiO_3$ bilayer thin films, and the characterization of various physical parameters viz., structural, electrical, microstructural, and dielectric properties for tunable dielectric properties. The chapter is divided into two parts. The first part presents the synthesis of *MTO-BST* composite ceramics, followed by results and a discussion on the characterization of relevant properties. The second part presents the deposition of *MTO/BST* bilayer thin films altering their stacking order and their results and discussion based on structural, microstructural, dielectric, and electric property analysis.

5.1 Introduction:

In the telecommunication industry, electric field tunable ferroelectric ceramics were widely studied for applications in phase shifters, tunable dielectric filters, delay lines, and other microwave devices [133]. Materials with high permittivity ($30 < \varepsilon_r < 1500$) and low loss ($< 0.01$) are required for high-performance compact IC applications [133]. Further, the ceramic capacitors were categorized into two types type-I and type-II capacitors. For a type-I capacitor, moderate dielectric constant, low loss tangent, and high thermal stability is required and are used in resonant circuit applications. The type-II capacitors need a high dielectric constant, which minimizes the device size and is promising for de-couplers and filters.

$MgTiO_3$, a linear dielectric ceramic has been widely investigated due to its excellent dielectric responses at microwave frequencies: extremely low insertion loss (~10^{-4}), moderate dielectric permittivity ($\varepsilon_r \approx 17$), and considerable thermal stability ($\tau_f \approx$ -50 ppm/˚C) [26]. On the other hand, $Ba_{0.5}Sr_{0.5}TiO_3$, a ferroelectric ceramic has high dielectric permittivity and low loss along with tunable dielectric permittivity (with DC biasing) [133,134]. $Ba_{0.5}Sr_{0.5}TiO_3$ modified by Mg doping is potential material for tunable phase shifters, filters, and antenna applications with reduced dielectric loss and permittivity value [135]. A maximum solubility limit of Mg in $Ba_{0.8}Sr_{0.2}TiO_3$ is found as 2wt% as per the reports of Su et al.[36]. Shanming Ke et al. [136], reported the effect of $MgTiO_3$ on $Ba_{0.6}Sr_{0.4}TiO_3$ ceramics and achieved a

significant reduction in the dielectric loss (0.003) for 8 mol% addition of $MgTiO_3$. In the present study effect of $Ba_{0.5}Sr_{0.5}TiO_3$ addition in $MgTiO_3$ ceramic and proper optimization of composition is carried out to enhance dielectric permittivity with the least effect on the *Q* value of $MgTiO_3$ ceramics for microwave tunable applications. Further, the best optimized composite sample was chosen to study the impedance spectra at different temperatures to understand the relation between the dielectric responses and microstructure.

Technologies are heading towards the realization of device miniaturization, and integrated circuits are key to accomplishing these developments[137]. Smart materials are crucial in such areas to fulfill multi-dimensional applications and excellent performance of the devices. Multilayer thin films have demonstrated tremendous potential, as by making a proper choice of layers, hybrid characteristics can be achieved in a single device [138]. In this regard, Kahn *et. al.* [139] reported $SrTiO_3/Y_2O_3$ bilayer for MIM capacitor applications and achieved better C(V) linearity in comparison to individual $SrTiO_3$ film. In field effect transistors (FET) oxide based multilayer films are explored to overcome the scaling limits of Si-based FET [140]. The idea propelling the research is the utilization of 2-dimensional electron gas (2DEG) generated in the interface. In a similar context, $LaAlO_3$- $SrTiO_3$ bilayer was investigated by Forg *et. al.* [140] for the fabrication of low dimensional FET, where 2DEG acted as the drain-source channel and $LaAlO_3$ as the gate layer. Menglin *et. al.* [109] obtained 61% efficiency in $BiFeO_3/BaTiO_3$ bi-layer thick films integrated on Si. Hirai *et. al.* [141] reported a magnetically insulated ground state of $Ca_{0.5}Sr_{0.5}IrO_3/SrTiO_3$ superlattice films attributing to electron correlations in Ir perovskites and topological effect [124,142]. Similarly, $MgTiO_3$ ceramics and thin films exhibited extremely low dielectric loss ~10^{-4} facilitating negligible insertion loss, and moderate dielectric constant 17 at microwave frequency [74]. Therefore, characteristics of *MTO* and *MTO*-based ceramics have been extensively explored for microwave filter, oscillator, and capacitor applications in microwave technology [143,144]. Furthermore, $Ba_{0.5}Sr_{0.5}TiO_3$ (*BST*) has been explored for energy storage applications [23]. In addition, *BST* exhibits tunable microwave dielectric properties and is found to be of potential interest in microwave tuning device applications. Jain *et al.* [23] reported sol-gel-based *BST: MTO* composite thin films for tunable microwave devices and achieved a higher figure of merit as compared to *BST* films. As reported by Sahoo *et. al.* [145], multilayered $Ba_{0.8}Sr_{0.2}TiO_3/ZrO_2$ can be an excellent candidate for providing temperature stability in microwave devices. The findings of multilayer film-related research suggest that unlike bulk composites, for a fixed composition their composite response can be

tuned by varying thickness ratio, stacking order and substrates. However, the deposition or fabrication of such bilayers itself is presents a challenge for thin film technology. RF sputtering technique is well known deposition technique for uniform film growth of oxide materials. In present work, a comprehensive report on composite effect of *BST* and *MTO* bilayers is presented for the first time using the versatile radio frequency (RF) sputtering technology. At first *MTO/BST* and *BST/MTO* bilayers were deposited on n-type Si substrate keeping 1:1 thickness ratio. An extensive structural analysis on the effect of stacking order is carried out based on theoretical assumptions and obtained diffraction characteristics. In addition, established a correlation between microstructural properties.

5.2 Sample preparation:

5.2.1 (1-*x*) $MgTiO_3$-*x* $Ba_{0.5}Sr_{0.5}TiO_3$ composite ceramic:

The composite ceramics were prepared via the molten salt reaction method using $MgTiO_3$ (*MTO*) and $Ba_{0.5}Sr_{0.5}TiO_3$ ceramic powders. $MgTiO_3$ (*MTO*) ceramics were prepared by using highly pure powders of MgO (99.99%) and TiO_2 (99.99%) from M/s Sigma Aldrich, USA. To avoid secondary phase formation of *MTO* at higher sintering temperatures, the non-stoichiometric composition of $MgTiO_3$ was used [26]. The powders were first weighed in appropriate proportions and ball milled in distilled water for 5 h using a planetary ball mill (Pulversitte 6, M/s Fritsch GmbH, Germany). For preparing $Ba_{0.5}Sr_{0.5}TiO_3$, high purity powders of $BaCO_3$ (99.99%), $SrCO_3$ (99.99%), and TiO_2 (99.99%) m/s Sigma Aldrich, USA, were first weighed and then ball milled for 5 h, according to the desired stoichiometry. The obtained slurry is then dried at 150˚C and the powders obtained are calcined at 1100˚C for 3hrs.

Table 5.1: *Sample name corresponding to different values of x.*

Serial number	*x*	*Sample name*
1	0.1	MTBS1
2	0.2	MTBS2
3	0.3	MTBS3
4	0.4	MTBS4
5	0.5	MTBS5

Further for the preparation of (1-*x*) $MgTiO_3$- *x* $Ba_{0.5}Sr_{0.5}TiO_3$ (*x* = 0.1, 0.2, 0.3, 0.4, 0.5) composite, the calcined $MgTiO_3$ and $Ba_{0.5}Sr_{0.5}TiO_3$ powders were ball milled for 5 h. The powders were pressed into cylindrical discs of a diameter of 10 mm and thickness ranging from 1-5 mm using polyvinyl alcohol as a binder. The prepared pellets were finally sintered at 1250˚C 1300˚C, 1350˚C, and 1400˚C for 4 h in air. The prepared composite ceramics have been named accordingly and tabulated in Table 5.1.

The Archimedes method has been adopted to measure the density of the samples and the values obtained were compared with the theoretical density obtained from the following relation

$$\rho = \frac{w_1 + w_2}{\frac{w_1}{\rho_1} + \frac{w_2}{\rho_2}} \qquad (5.1)$$

where W_1 and W_2 are the molecular weight fraction of *MTO* and *BST* ceramics respectively. P_1 and ρ_2 represent the theoretical densities of *MTO* and *BST* ceramics accordingly.

5.2.2 Deposition of MTO/BST bilayer

The obtained pure phased $MgTiO_3$ and $Ba_{0.5}Sr_{0.5}TiO_3$ powders were used for sputtering target preparation. The powders were mixed with 5 wt.% Polyvinyl alcohol (PVA) binder and pressed into cylindrical compacts of 60 mm diameter and 5 mm thickness followed by high-temperature sintering at 1350˚C for 4 h. *MTO/BST* and *BST/MTO* each of 100 nm were deposited on SiO_2 and n-type Si substrate using the RF sputtering technique.

The individual layers were deposited and optimized for the deposition conditions. The deposition chamber was evacuated to achieve a base pressure of ~ 1×10^{-6} mbar before the deposition of the films. A pressure of ~ 3×10^{-2} mbar was maintained throughout the deposition process by purging gases of argon (Ar) (99.999%) and (O_2) oxygen (99.999%) through mass flow controllers. Both *MTO* and *BST* monolayers were deposited at 45 W RF power in 50/50 Ar/O_2 environment. The as-deposited films were further annealed at 750˚C to obtain crystallinity.

5.3 . Result and Discussions:

5.3.1 (1-*x*) $MgTiO_3$-*x* $Ba_{0.5}Sr_{0.5}TiO_3$ composite ceramic:

5.3.1.1. Structural and microstructural analysis:

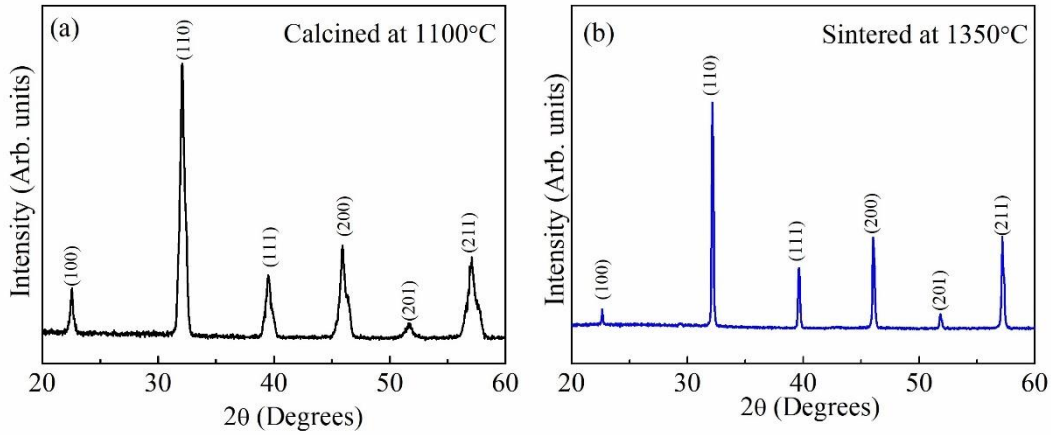

Figure 5.1: XRD pattern of (a) calcined BST powder and (b) sintered disc of BST, respectively.

Figure 5.1(a-b) presents XRD patterns for calcined *BST* powder and sintered pellet, respectively. The obtained XRD pattern confirmed the formation of the polycrystalline *BST* phase upon calcination at 1100˚C. Further, the XRD pattern of sintered *BST* ceramic disc revealed improved crystallinity and phase purity.

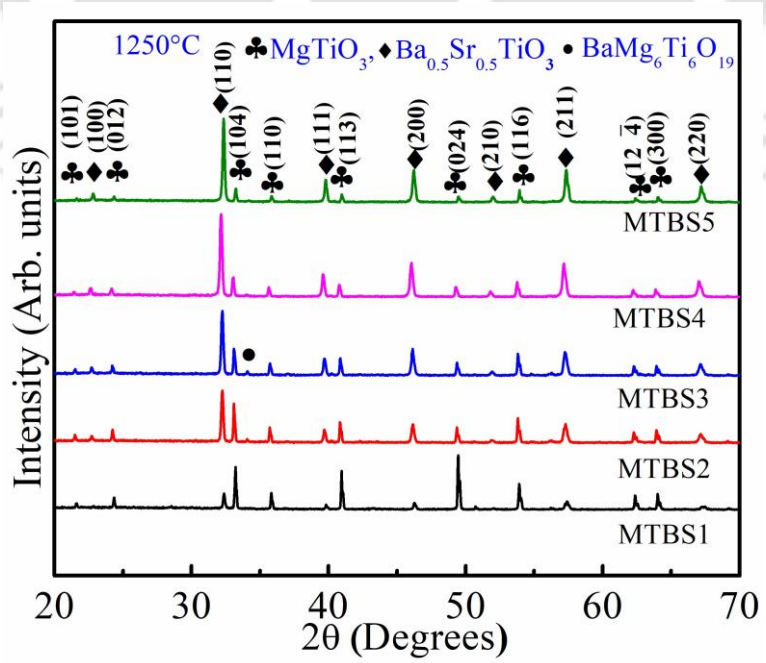

Figure 5.2: XRD patterns of MTO-BST composite ceramics, sintered at (a) 1250 °C.

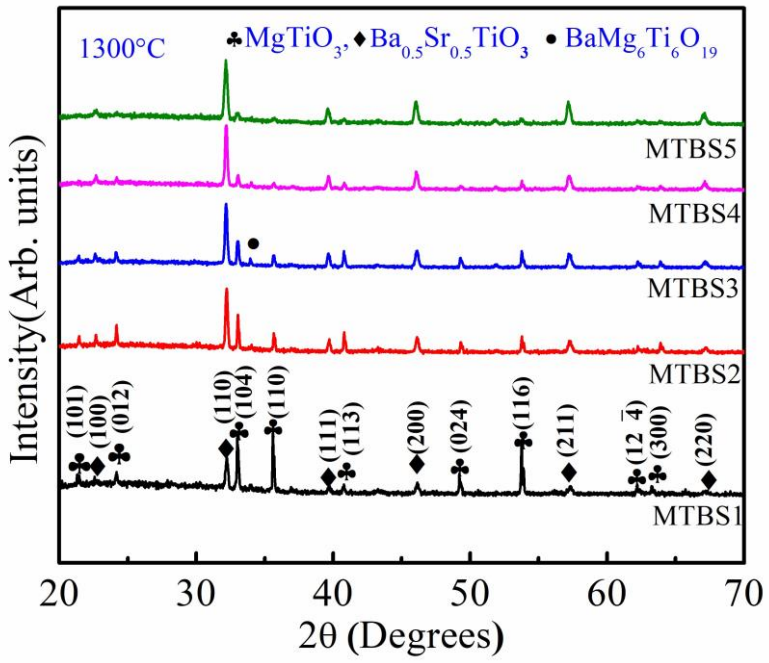

Figure 5.3: XRD patterns of MTO-BST composite ceramics, sintered at 1300 °C.

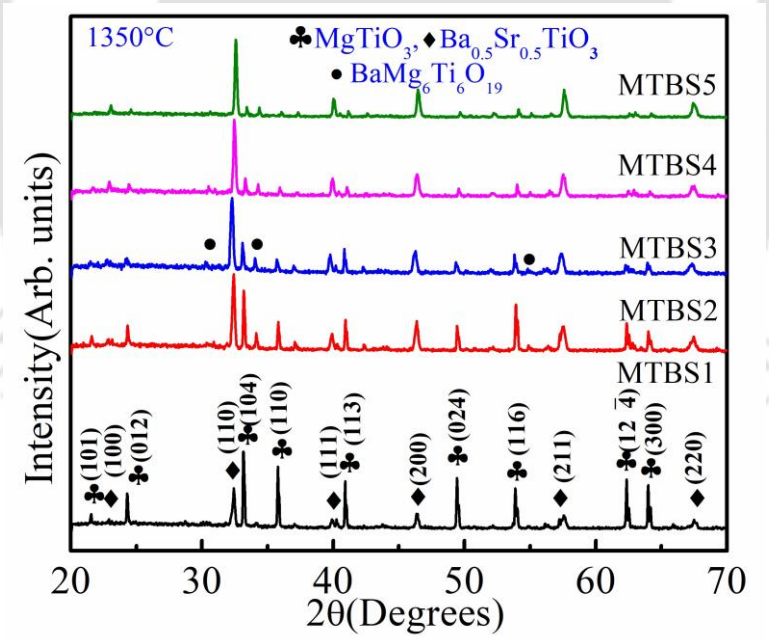

Figure 5.4: XRD patterns of MTO-BST composite ceramics, sintered at 1350 °C.

XRD patterns of the *BST-MTO*-based composite ceramics, sintered at different temperatures (1250- 1400^{o}C) are shown in Figures 5.2-5.5. The analysis of XRD patterns revealed the presence of individual phases of polycrystalline *MTO* (JCPDS # 790831) with rhombohedral structure and *BST* (JCPDS no: 00-0390-1395) with cubic structure. Apart from *MTO* and

BST, some peaks belonging to the mixed phase *MTO-BST*: $BaMg_6Ti_6O_{19}$ were also observed and indexed according to JCPDS no: 42-441.

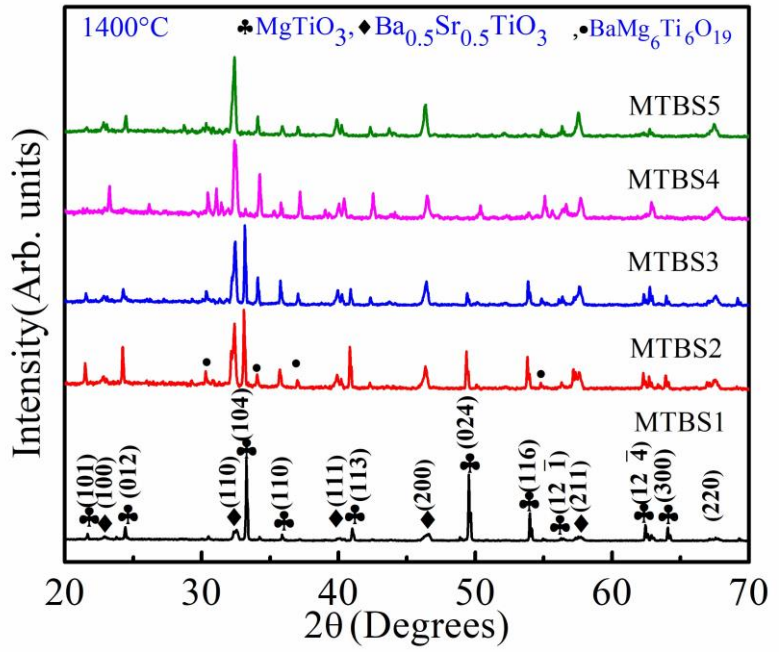

Figure 5.5: XRD patterns of MTO-BST composite ceramics, sintered at 1400 °C.

The sintering temperature strongly affected the intensities of the corresponding peaks. For a sintering temperature (T_s) corresponding to 1250˚C, MTBS1 and MTBS5 had no signs of a mixed phase. This indicates that *MTO* and *BST* can co-exist independently at that temperature. On the other hand, the MTBS2, MTBS3, and MTBS4 samples showed a low intensity of the mixed phase peak. The appearance of this peak can be attributed to the similar coordination numbers shared by the cations of these two ceramics. An increase in sintering temperature from 1250 ˚C to 1400˚C leads to a rapid improvement in the intensities of the mixed phase. Higher thermal energy is the key factor that facilitates the growth of mixed phases in these composite ceramics.

To understand the effect of sintering temperature on the structural properties of the *MTO-BST* ceramics, Rietveld refinement has been carried out using FullProf Program by considering the rhombohedral phase of *MTO* belonging to *R-3* the space group, and the cubic phase of *BST* belonging to Pm-3m space group.

Table 5.2 Obtained parameter and volume from Rietveld refinement for MTO phase:

x	T_S (°C)	*a = b (Å)*	*c (Å)*	*V (Å^3)*	*Density(g/cm^3)*	χ^2
	1250	5.0540	13.881	307.067	3.885	5.70
0.1	1300	5.0542	13.892	307.240	3.890	3.74
	1350	5.0560	13.905	307.845	3.891	6.50
	1250	5.0537	13.904	307.489	3.892	4.75
0.2	1300	5.0537	13.906	307.579	3.894	3.91
	1350	5.0546	13.905	307.699	3.896	4.85
	1250	5.0528	13.880	306.891	3.895	4.70
0.3	1300	5.0531	13.892	307.197	3.902	3.68
	1350	5.0535	13.900	307.432	3.912	4.70
	1250	5.0529	13.890	307.266	3.894	3.93
0.4	1300	5.0528	13.900	307.332	3.896	3.31
	1350	5.0559	13.904	307.904	3.897	4.18
	1250	5.0566	13.907	307.948	3.890	3.47
0.5	1300	5.0551	13.920	308.058	3.897	3.39
	1350	5.0563	13.920	308.193	3.898	5.35

The obtained parameters have been listed in Table 5.2 and Table 5.3 for *MTO* and *BST*, respectively. These variations might be due to the strain exhibited by the samples as a result of Ba^{2+}(1.35Å) substitutions in the *MTO* lattice. Since Ba^{2+} (1.35Å) has much larger ionic radii compared to Mg^{2+} (0.720Å) it is most likely to sit on the interstitial position of the *MTO* crystal lattice leading to distortion in the *MTO* crystal structure. On the other hand, in the case of *BST* crystals, as shown in Table 5.3, lattice parameters and lattice volumes were enhanced with an increase in sintering temperature. This again refers to the substitution of Mg^{2+} (0.720Å) in some Ba^{2+}(1.35Å) and Ti^{4+}(0.605Å) sites of BST lattice due to similar ionic radii shared by both.

In Figure 5.6 (a-c) Rietveld refined plots for x = 0.3 at different sintering temperatures are shown, which were well fitted with experimental XRD patterns. An increase in the broadening of the XRD diffraction peaks as well as a shift towards lower 2θ is seen

with a rise in sintering temperature from 1250 to 1300˚C for both *MTO* and *BST* and are shown in Figure 5.6(f).

Table 5.3: Obtained parameter and volume from Rietveld refinement for BST phase.

x	T_S (°C)	*a = b = c (Å)*	*V (Å^3)*	*Density(g/cm^3)*	χ^2
	1250	3.9503	61.646	4.943	5.70
0.1	1300	3.9422	61.262	4.974	3.74
	1350	3.9419	61.253	4.975	6.50
	1250	3.9505	61.654	4.942	4.75
0.2	1300	3.9487	61.569	4.948	3.91
	1350	3.9431	61.307	4.970	4.85
	1250	3.9507	61.663	4.941	4.70
0.3	1300	3.9475	61.513	4.954	3.68
	1350	3.9444	61.368	4.965	4.70
	1250	3.9530	61.772	4.933	3.93
0.4	1300	3.9505	61.654	4.942	3.31
	1350	3.9497	61.604	4.943	4.18
	1250	3.9550	61.886	4.923	3.47
0.5	1300	3.9544	61.836	4.927	3.39
	1350	3.9524	61.741	4.935	5.35

However, above 1300˚C characteristic peaks of *MTO* shifted towards lower 2θ without any peak broadening whereas, *BST* peaks showed only peak broadening. The shift in XRD peak towards lower 2θ values is attributed to tensile strain in the sample and the broadening is due to inhomogeneous strain in the sample [146]. To study the lattice strain induced by BST in the *MTO-BST* ceramics, Williamson- Hall (W-H) plots have been plotted, as shown in figure 5.6 (d-e). The crystallite sizes and strains for both the phases were calculated from the W-H plots using equation (5.2) and are listed in Table 5.4 For both *MTO* and *BST* phases, the average crystallite size (L) decreased when the sintering temperature has

raised from 1250 to 1300 °C, however, above 1300 °C, crystallite size again enhanced with sintering temperature.

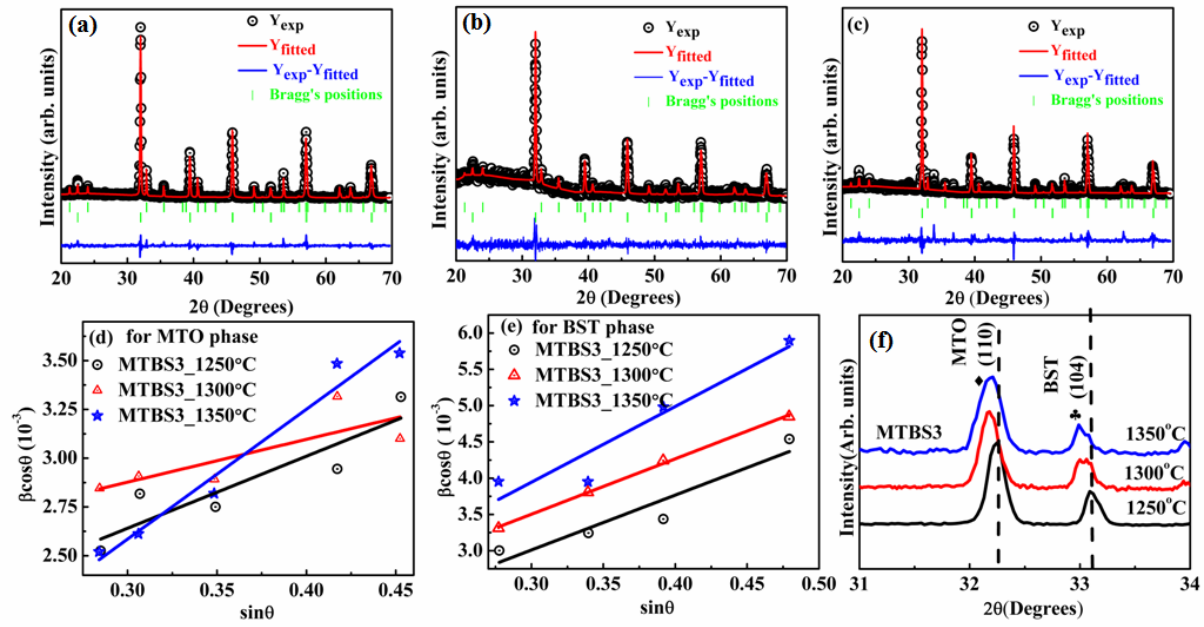

Figure 5.6: Rietveld refined XRD patterns of 0.7MgTiO$_3$-0.3 Ba$_{0.5}$Sr$_{0.5}$TiO$_3$ (MTBS3) composite ceramics sintered at (a) 1250 °C, (b) 1300 °C and c 1350 °C for 4 h and Williamson-Hall plots of (d) MTO and e BST phases at different sintering temperatures for MTBS3 composite ceramics. (f) Magnified XRD spectra for MTBS3 composite ceramics, sintered between 1250 and 1350 °C 4 h.

The strain (η) in the *MTO* phase was also found to follow the same trend as crystallite size, but in the case of the *BST* phase, strain increased with sintering temperature. Both crystallite size and strain contribute to the broadening (FWHM) of XRD peaks as follows,

$$B_{hkl} = B_{CS} + B_S \tag{5.2}$$

$$\beta = \frac{k\lambda}{D\cos\theta} + 4\eta\tan\theta \tag{5.3}$$

where, β =*Full width half maximum of diffraction peak,* D = crystalline size, k = shape factor (0.9), and λ= wavelength of Cu k$_\alpha$- radiation. The XRD analysis of these *MTO-BST* composites revealed that the sintering temperature had played a significant role in all the variations observed in structural parameters as well as associated strain of the samples. At 1250˚C, densification of samples initiated without formation of mixed phase with minimal strain effect and further rise in sintering temperature induced formation of mixed phase. This

might be attributed to thermal energy which is not sufficient for Mg^{2+} and Ba^{2+} to replace Ti^{4+} site in BST lattice and to sit in the interstitial site of MTO lattice, respectively. As, the sintering temperature is raised to 1300˚C, there is sufficient thermal energy to form the mixed phase and this leads to the reduction in the crystallite size due to improvement in strain in the crystals. Further, with increasing the sintering temperature, the intensity of mixed phase as well as crystallite sizes were found to be enhanced.

Table 5.4: Obtained values of crystallite size (D) and strain (η) for MTO phase from Williamson-Hall plot.

T_S (˚C)	*Crystallite size (Å)*		***Strain***	
	MTO	*BST*	*MTO*	*BST*
1250	*950*	*1969*	9.22×10^{-4}	1.89×10^{-3}
1300	*655*	*1201*	5.55×10^{-4}	1.91×10^{-3}
1350	*2474*	*1790*	1.65×10^{-3}	2.61×10^{-3}

Figure 5.7 (a) shows Raman spectra of (1-*x*) *MTO-x BST* (*x* =0.1 to 0.5) composite ceramics, sintered at 1350˚C for 4 hours. To study the effect of sintering temperature Raman spectrum for MTBS3 composite ceramic, sintered at three different temperatures are plotted and are shown in Figure 5.7(b). The E_g modes observed at 490 cm^{-1} and 644 cm^{-1} belong to a combination of antisymmetric breathing and twisting vibrations of oxygen octahedral with the cationic vibrations parallel to the X-Y plane. For E_g (490cm^{-1}) mode both Mg^{2+} and Ti^{4+} ions are involved in the vibrations, while the E_g (644cm^{-1}) mode primarily involves Mg^{2+}. Raman modes for BST observed at 179 cm^{-1} may originate from A site ions oscillation due to Mg^{2+} ion substitution [147]. The Raman peak at 233cm^{-1} is attributed to rotations of the oxygen cage and ordering of B site ions [148], while the broad peak at 576 cm^{-1} originates from TiO_6 octahedron stretching. The effect of composition for composite ceramics is visible from the Raman spectra, which are shown in Figure 5.7 (a). For $x \geq 0.3$, ten intense peaks corresponding to the theoretical Raman active modes of *MTO* are observed along with some minor peaks for *BST* [78,149]. In *MTO* both Mg and Ti metal atoms are bonded to O atom by covalent bonds, and it results in a high dependency of TiO_6^{4-} and TiO_6^{2-} on Mg. This also

results in the involvement of all atoms in the vibrational mode [113], and most of the vibrational modes are found to be combinations of symmetry coordinates [150].

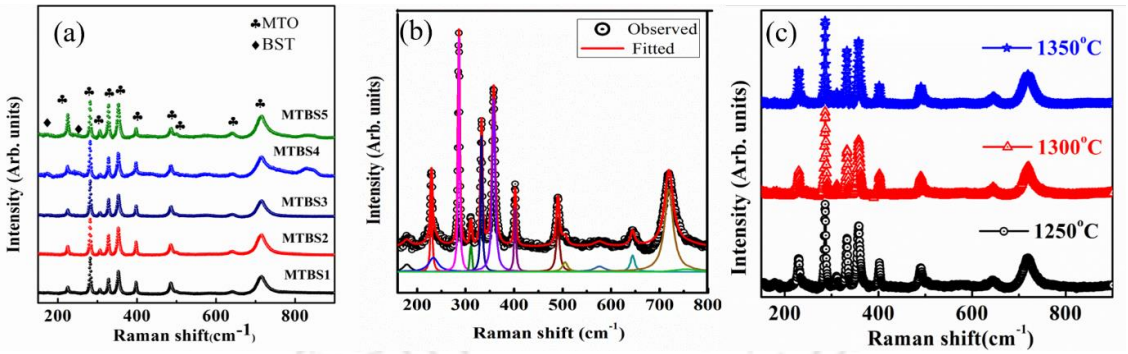

Figure 5.7:: Raman spectra of (a) MTO–BST composite ceramics, sintered at 1350 °C and (b) Fitted Raman spectra for MTBS3 sample, sintered at 1350 °C for 4 h. And (c) MTBS3 sintered at different sintering temperatures.

Table 5.5: Obtained Raman shift peak and corresponding FWHM for MTBS3 composite ceramics, sintered at 1350˚C.

Serial No	*Peak position (cm^{-1})*	*FWHM (cm^{-1})*
1	179.06±1.02	18.16±2.03
2	229.63± .05	4.51±0.03
3	233.71±1.13	23.51±2.23
4	286.22±0.02	3.72±0.04
5	310.99±0.15	5.88±0.04
6	332.74±0.03	4.13±0.07
7	357.87 ±0.03	6.87±0.08
8	402.21±0.06	4.33±0.15
9	490.48±0.10	7.61±0.34
10	505.13±0.71	12.45±2.50
11	576.16±1.81	26.71±3.25
12	644.46±0.39	10.39±1.02
13	719.17±0.01	21.39±0.40
14	754.92±1.25	54.34±0.20

However, the *MTO* modes seemed to be dominating over *BST* modes for all the compositions, and hence to filter out the modes, fitting for Raman spectra was carried out using origin software.

. The Raman spectra with fitted peaks are shown in Figure 5.7(c) and details of the peak's position and full width at half maxima are presented in Table 5.5. The mode at 229 cm^{-1} (A_g) and 311 cm^{-1} (A_g) correspond to the vibration of Mg^{2+} and Ti^{4+} ions, respectively along the Z-axis, whereas, A_g (402 cm^{-1}), A_g (505 cm^{-1}), and A_g (719 cm^{-1}) are originated from independent vibration of O^{2-} ions. The A_g (505 cm^{-1}) and A_g (719 cm^{-1}) modes exhibit the symmetric breathing-like vibrations of six O^{2-} ions corresponding to different degrees of freedom of oxygen octahedron. In the case of E_g modes, the mode at 286 cm^{-1} resulted from anti-symmetric breathing vibrations of oxygen octahedrons. The E_g (332 cm^{-1}) and E_g (357 cm^{-1}) modes represent the twisting of oxygen octahedron with the vibrations of the M_g^{2+} and Ti^{4+} ions parallel to the X-Y plane, respectively.

The surface morphologies of (1-*x*) *MTO-x BST* (*x* =0.1 to 0.5) composite ceramics obtained by FESEM sintered at 1300˚C for 4 hours are presented in Figure 5.8(a-e). The FESEM images showed two distinct types of grains. One type of grain is larger with an approximate size of 2-3 μm whereas in the other type grains are less than 1 μm. All the samples have shown a well-packed microstructure. As the *BST* concentration increases in the samples, the number of smaller grains is surpassed. At the same time, the larger grains scaled down in size with an increase in *BST* concentration, which might be attributed to the uniform mixing of *BST-MTO* ceramics and *BST* grains which acts as a barrier between *MTO* grains for further growth. From the observation, it can be concluded that larger grains are composed of *MTO* and smaller grains are composed of *BST* ceramics. As shown in Figure 5.8(f), elemental distribution on a large area of the ceramics is found to be nearly equal to the calculated value. In addition to it, the EDS analysis also confirmed that grains A and B belong to *MTO* and *BST* ceramics, respectively.

Further, to study the effect of sintering temperature on the microstructural properties of *MTO-BST* ceramics the FESEM images of MTBS3 samples, sintered at 1250 to 1350˚C are obtained and are shown in Figure 5.9(a–c). An enhancement in the grain size, as well as packing of grains, have observed with a rise in sintering temperature. At 1350 °C, MTBS3 exhibited a highly compacted and uniform microstructure. The density plays a significant role in the dielectric properties of a ceramic composite. The relative density of the ceramics was

estimated by the Archimedes method and the relative densities are found to be ~95%, ~95.8%, and ~97% for the composites sintered at 1250, 1300, and 1350 °C, respectively.

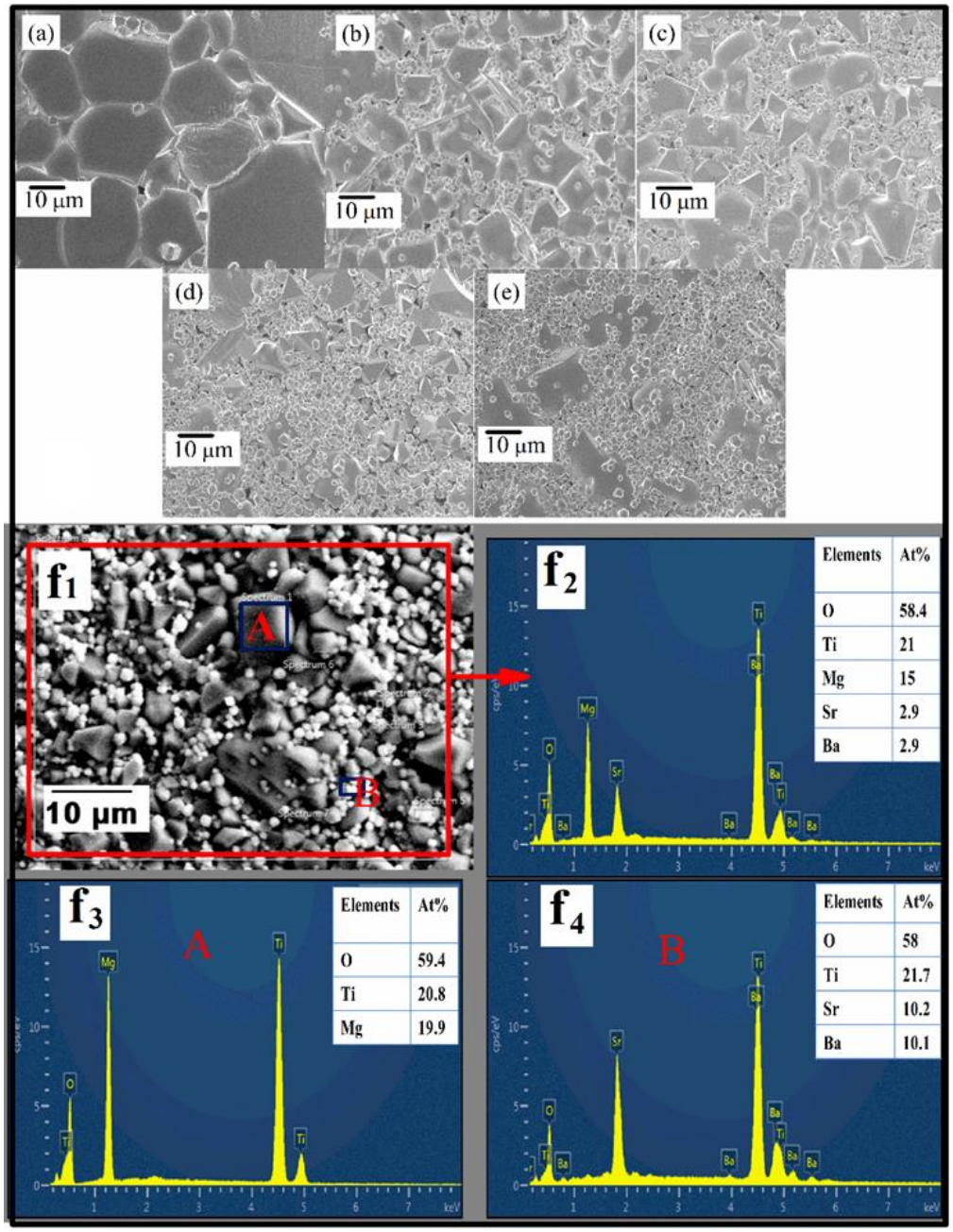

Figure 5.8: FESEM micrographs of MTO-BST composite ceramics are shown from (a) to (e) for MTBS1–MTBS5, respectively, sintered at 1300 °C for 4 h. (f) EDS elemental distribution spectra of the MTBS3 composite at selected area.

.

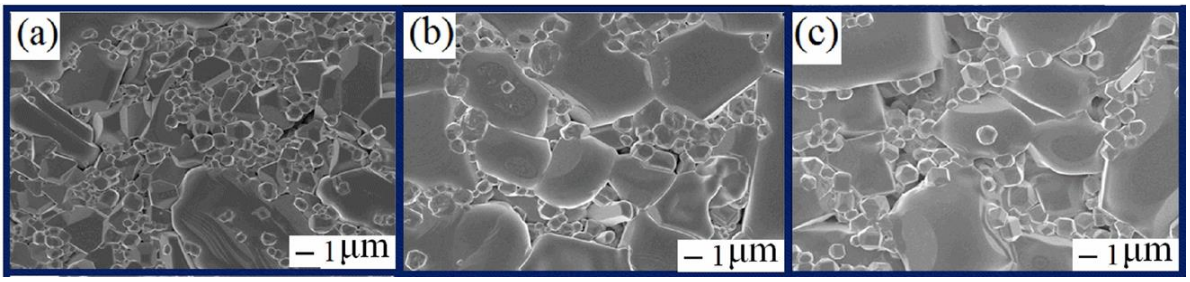

Figure 5.9: (a–c) FESEM images of MTBS3 composite ceramics, sintered at 1250 °C, 1300 °C, and 1350 °C for 4 h, respectively.

The relative densities of all the composite ceramics sintered at 1350 °C are given in Table 5.6 calculated value.

5.3.1.2. Microwave dielectric properties:

To study the effect of *BST* on *MTO*, the microwave dielectric parameters of the composite ceramics were extracted at a spot frequency by using the Hakki–Coleman method considering $TE_{01\delta}$ mode as discussed in chapter section 2.3.8.5 of chapter 2. The *BST* ceramic was found to have a significant effect on the microwave dielectric properties of the *MTO-BST* composites.

The obtained microwave parameters are summarized and plotted in Table 5.6 and Figure 5.10, respectively. The *Q* value and the resonant frequency for the composites were found to be decreased with an increase in *BST* concentration. Whereas, dielectric permittivity value has shown a significant enhancement with *BST* concentration. The $Q \times f_0$ value of the composite ceramics exhibited a drastic change from ~17,806 to 988 GHz for x = 0.1 to 0.5, respectively. The observed degradation in *Q* value may be attributed to relaxation polarization present in *BST* at higher frequencies[151].

Table 5.6: Obtained microwave parameters for MTO-BST composite.

Sample name	***Resonant frequency (GHZ)***	***Dielectric permittivity(ε_r)***	***Quality factor (Q)***	***Loss tangent***	***$Q \times f_O$ (GHZ)***	***Relative density (%)***
MTBS1	7.262	20 ± 0.2	2452	8.158×10^{-4}	17,806	97.90
MTBS2	4.928	29 ± 0.3	486	0.002	2395	97.84
MTBS3	4.160	57 ± 0.57	464	0.004	1930	97.69
MTBS4	3.686	97 ± 0.97	400	0.005	1474	97.30
MTBS5	2.548	200 ± 4	388	0.006	988	97.06

The resonant frequency (f_0) has also shown dependency on *BST* concentration and varied from 7.262 to 2.54 GHz for, x=0.1 to 0.5. At, the microwave frequency range the MTBS composites exhibited much higher dielectric permittivity as compared to pure $MgTiO_3$ and a recorded maximum of ~200 for MTBS5. At, the same time, enhancement in dielectric loss ($tan\delta$) is also noticeable with an increase in *BST* concentration, which is also an important parameter from an application point of view. Optimization of all dielectric parameters is required in these composite ceramics studies. Hence, MTBS1with x = 0.1, composite ceramics exhibited the best microwave dielectric properties with dielectric permittivity of ε_r ~20, dielectric loss of ~ $10^{-4,}$ and $Q \times f_0$ ~ 17,806 at 7.262 GHz. Further, the quality factor ($Q \times f_0$) of the MTBS composite ceramics was also found to be enhanced from 7800 to 17,806 GHz with sintering temperature from 1250 to 1350 °C.

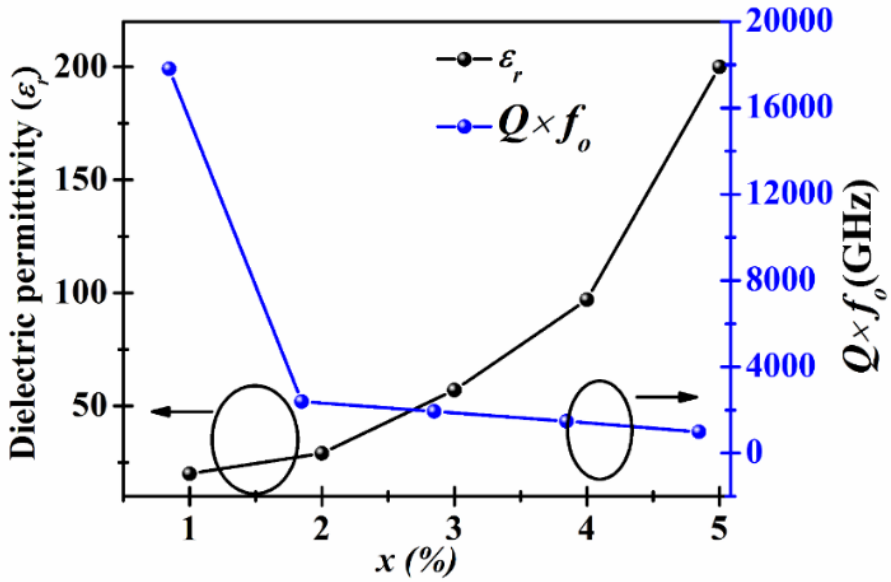

Figure 5.10: Variation of dielectric permittivity and Q × f_0 value with BST concentration.

This improvement in quality factor ($Q \times f_0$) value with sintering temperature can be attributed to increased relative density with sintering temperature, which will result in less conduction loss through the defect states originating from the porous microstructure of the ceramics [26]. It is interesting to note that the addition of *BST* has significantly influenced the microwave dielectric properties. There is a drastic improvement in the dielectric constant at the same time the quality factor degraded as compared to pure *MTO* [152].

5.3.1.3. Broadband dielectric properties:

In Figure 5.11, dielectric responses of MTBS composite ceramics as a function of temperature measured at different frequencies are demonstrated. Unlike pure *MTO* and *BST* ceramics, MTBS and pure *BST* ceramics have exhibited diffused transition. Due to the addition of *BST* ceramics in *MTO* ceramics, the dielectric constant showed an overall enhancement as well as a transition with temperature.

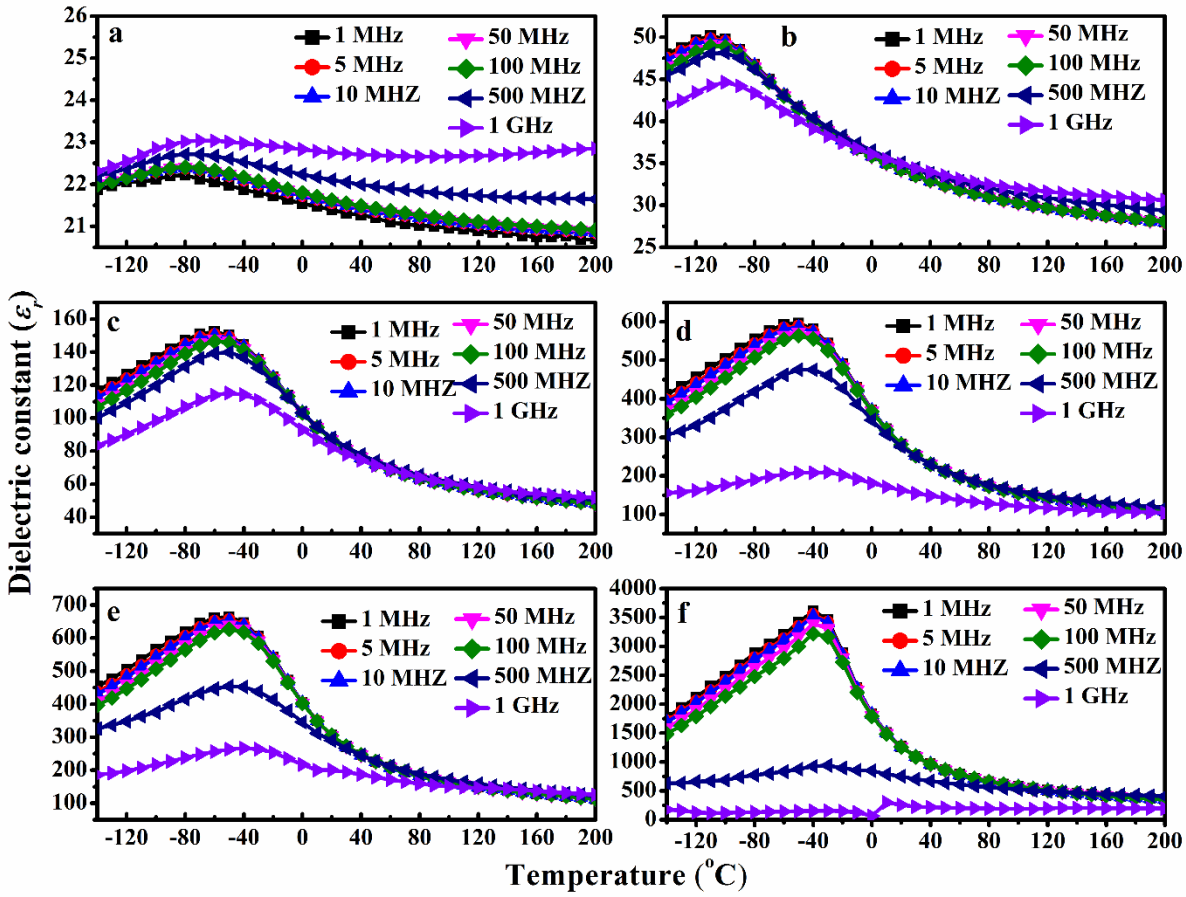

Figure 5.11: Broadband (1 MHz– 1GHz) dielectric response of MBST ceramics as a function of temperature for MTO–BST composite and pure BST ceramics, respectively.

The dielectric constant value is found to be increased abruptly from x = 0.3 to 0.4 as compared to x = 0.1 to 0.3 and this can be attributed to actual individual phase concentrations in the composite ceramics as estimated from Rietveld refinement. As the *BST* concentration increases the transition peak becomes more prominent and the transition temperature (T_C) value shifted towards *BST*'s T_C. These responses indicated a mixed dielectric contribution from both the phases in the *MTO-BST* composite ceramics. From the earlier studies, it is evident that due to the replacement of Mg^{2+} in the acceptor site of ABO_3, the transition temperature of *BST* shifts towards a lower temperature. When Mg replaces Ti on the B site of

perovskite ABO_3 structure and a double ionized oxygen vacancy is formed simultaneously, i.e.,

$$MgO(-TiO_2) \rightarrow Mg_{Ti}^{"} + V_O^{"} + O_O \qquad (5.4)$$

Mg ions along with charged oxygen vacancies induce the local deformation in the perovskite unit cells leading to the reduction of the tetragonal *c/a* ratio and hence, the Curie temperature T_C shifts towards lower temperature [136]. For 10 mol% *BST* composites, the dielectric transition is highly diffused in nature, which has exhibited a broad peak T_C.

In the present study, the dielectric constant has exhibited diffused kinds of transitions with measurement temperature for all the MTBS composite ceramics and such kind of transition is a signature of relaxor ferroelectrics [153]. Further, for the first time two scientists Uchino and Nomura proposed a modified Curie–Weiss law, to probe the nature of this relaxor behavior of ferroelectrics.

The modified Curie Weiss law can be expressed as follows

$$(1/\varepsilon_r - 1/\varepsilon_m) = \frac{(T - T_C)^{\gamma}}{C} \qquad (5.5)$$

where C is the Curie constant, γ is the diffuseness constant and ε_m is the maximum dielectric constant at T_C. Again, the numerical value of diffuseness constant γ lies between 0 to 1 and 1 to 2 for perfect ferroelectric and relaxor ferroelectric materials respectively.

In Figure 5.12 (a-e), the plots for, log ($1/\varepsilon_r$ - $1/\varepsilon_m$) vs log(T-T_C) are shown and the values of γ have been extracted from the slope of the linearly fitted lines for all the MTBS composite ceramics. The obtained γ values varied from 1.01 for x = 0.1 to 1.83 for x = 0.5, as an indication of the relaxor nature of the ceramics as given in Table 5.7. The diffuseness constant γ is increasing with an increase in x, which can be attributed to a larger amount of distortion in the sample.

Figure 5.13(a-e) corresponds to dielectric loss (*tanδ*) as a function of measuring the temperature at various frequencies of the MTBS composite ceramics. The dielectric loss (*tanδ*) was also enhanced due to the addition of *BST* ceramics in the *MTO* matrix. The dielectric loss (*tanδ*) has shown a distinct anomaly near the T_C for all the composite ceramics. For all the composite ceramics it has been observed that the peak of dielectric loss shifts towards higher temperature and the overall value also increases with an increase in the

measuring frequency. As per earlier studies, this behavior of dielectric loss is related to the dielectric relaxation process and the value of dielectric loss implies the concentration of dielectric relaxation units[154]. The MTBS3 sample with x = 0.3, was optimized for further study due to its better structural and microstructural properties.

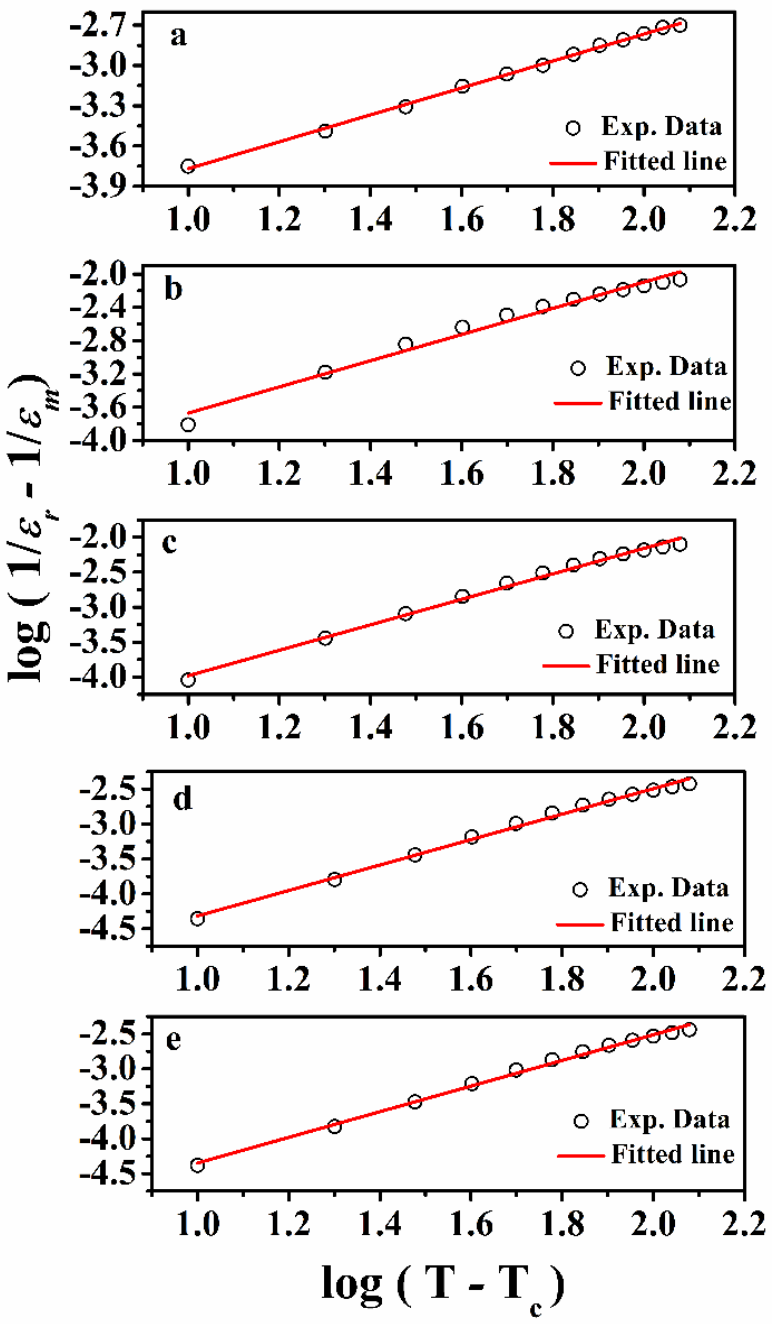

Figure 5.12: The plots of log ($1/\varepsilon_r - 1/\varepsilon_m$) versus log ($T - T_C$) for MTO-BST composite ceramics.

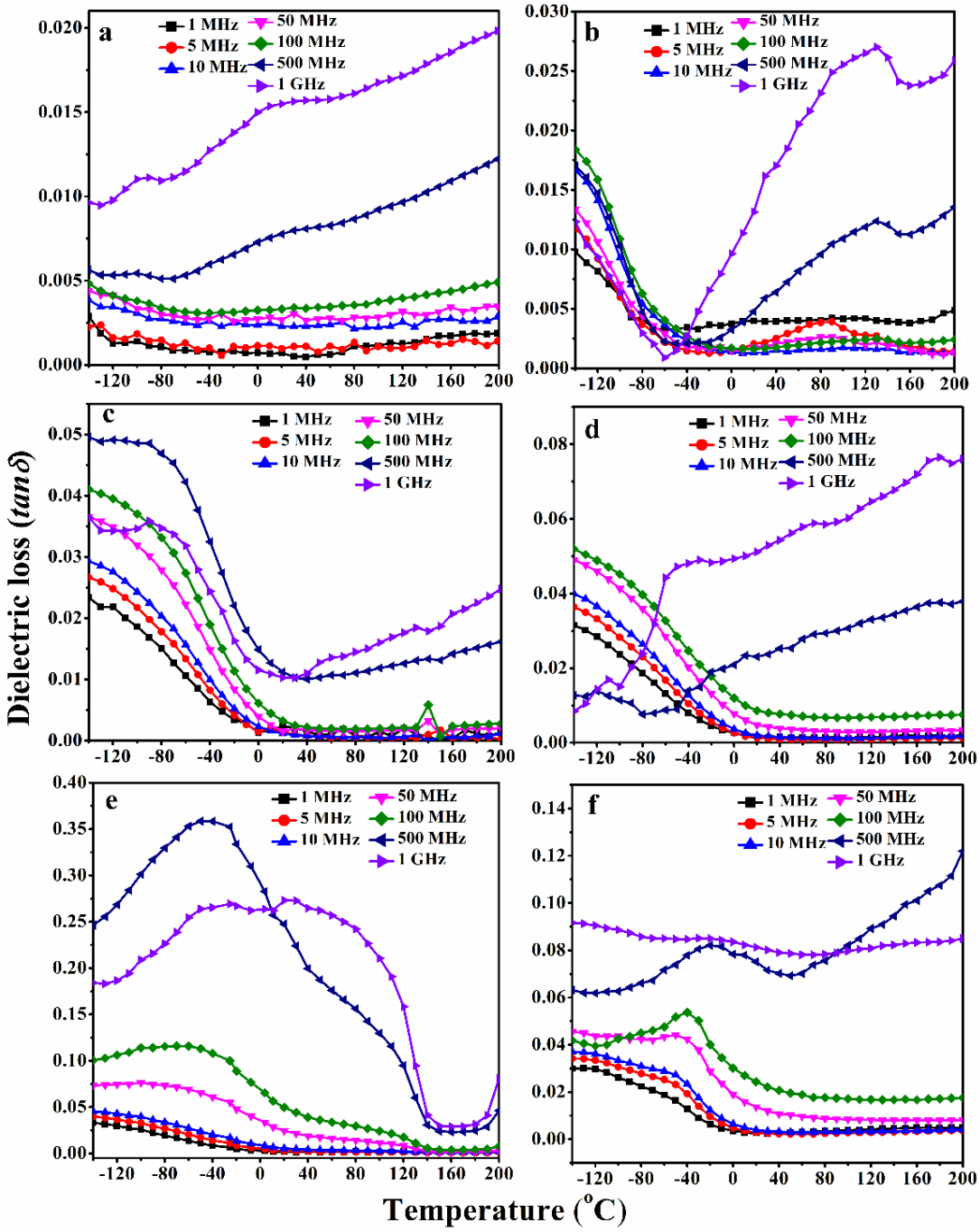

Figure 5.13: Dielectric loss (tanδ) as a function of measuring temperature at various frequencies of the MTBS composite and BST ceramics.

Figure 5.14(a) shows the variation of dielectric permittivity as a function of temperature at various measuring frequencies (1 kHz to 100 kHz) for MTBS3 composite ceramic. The *MTO –BST* composite ceramics have shown significant dependency on temperature, which can be attributed to the temperature-dependent dielectric permittivity of *BST* ceramics. It is observed that there are two regions for temperature-dependent dielectric

permittivity for all the frequency ranges. From room temperature to 200˚C, dielectric permittivity decreases with measurement temperature but with a further rise in temperature there is an improvement in the permittivity, which can be attributed to the phase transition associated with the *BST* phase near room temperature as shown in the previous analysis and thermally activated polarization in the high-temperature region (T >200 ˚C)

Table 5.7: *Obtained dielectric parameters for MTO-BST composite ceramics measured at 1MHz.*

Sample name	T_C (°C)	**Maximum relative dielectric permittivity (ε_r)**	**Diffuseness co-efficient 1.1.1 (γ)**
MTBS1	-81	22	1.002
MTBS2	-107	50	1.574
MTBS3	-62	153	1.822
MTBS4	-51	605	1.821
MTBS5	-50	676	1.834

Figure 5.14(b) and 5.11(c) displayed the dielectric permittivity with frequency in two different temperature ranges (RT to 250 ºC and > 250 ºC)

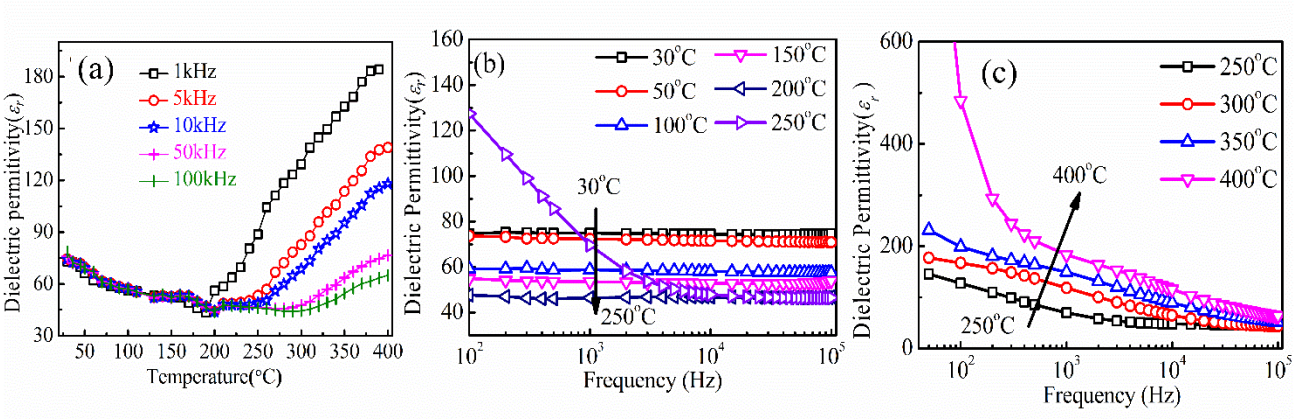

Figure 5.14:(a) Dielectric permittivity variation of MTBS3 as a function of temperature measured at different frequencies, Dielectric permittivity spectra as a function of frequency measured at different temperatures (b) RT to 250˚C and (c) T > 250 ˚C, respectively.

In the lower temperature region (RT to 250˚C), dielectric permittivity has shown minimal variation with frequency, whereas, in the higher temperatures and at lower

frequencies the permittivity exhibited higher values, due to space charge polarization and gradually decrease with frequency and become almost constant as a function of frequency. The variation in dissipation factor as a function of frequency (1 kHz to 100 kHz), measured at different temperatures is shown in figure 5.15(a). The dissipation factor of the sample exhibited a relaxation type of behavior with a broad peak and the shift of the peak value towards higher frequency with an increase in temperature indicates the strong dispersion in the dissipation factor of the sample. The relaxation time can be described by Arrhenius law, i.e.,

$$\omega_m = \omega_0 \exp\left[-\frac{E_a}{k_B T}\right] \tag{5.6}$$

Where, ω_m, ω_0 and E_a denotes the angular frequency for a maximum value of dissipation factor, pre-exponential factor, and activation energy of the sample, respectively.

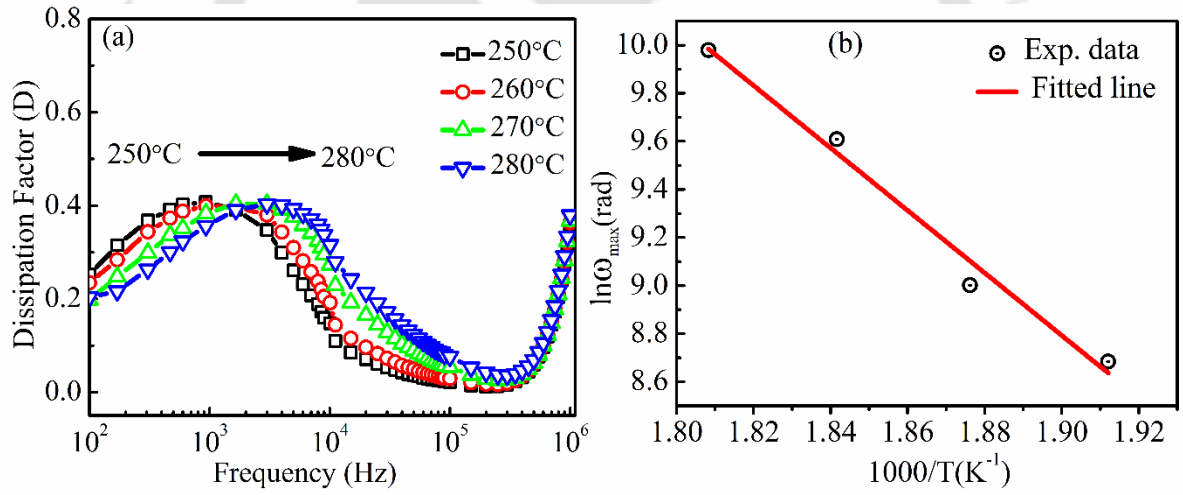

Figure 5.15: (a) Variation of dissipation factor (D) with frequency measured at different temperatures and (b) $ln\omega_{max}$ vs 1000/T plot from dissipation spectra.

Figure 5.15(b), shows the variation of logω to 1000/T of MTBS3 ceramics. The activation energy is calculated from the slope of the fitted line and is found to be 1.12 eV. The obtained activation energy is associated with thermally activated conduction of charge carriers across the grains and grain boundaries. The activation energy (E_a) for conduction around 1 eV corresponds to the migration of oxygen vacancies in perovskites [155]. The dielectric relaxation behavior at higher temperatures corresponds to short-range hopping of oxygen vacancies. In the current study, the activation energy value signifies the presence of conduction by doubly ionized oxygen vacancies in the samples[156].

5.3.1.4. Impedance analysis:

Figure 5.16(a) shows the spectra of MTBS3 ceramic of the imaginary impedance vs. frequency at different measurement temperatures (30 to 400 °C). The imaginary part of the impedance is very high in the lower frequency region and decreases with an increase in frequency. But towards the higher frequency region, the spectra merged for all the measured temperatures.

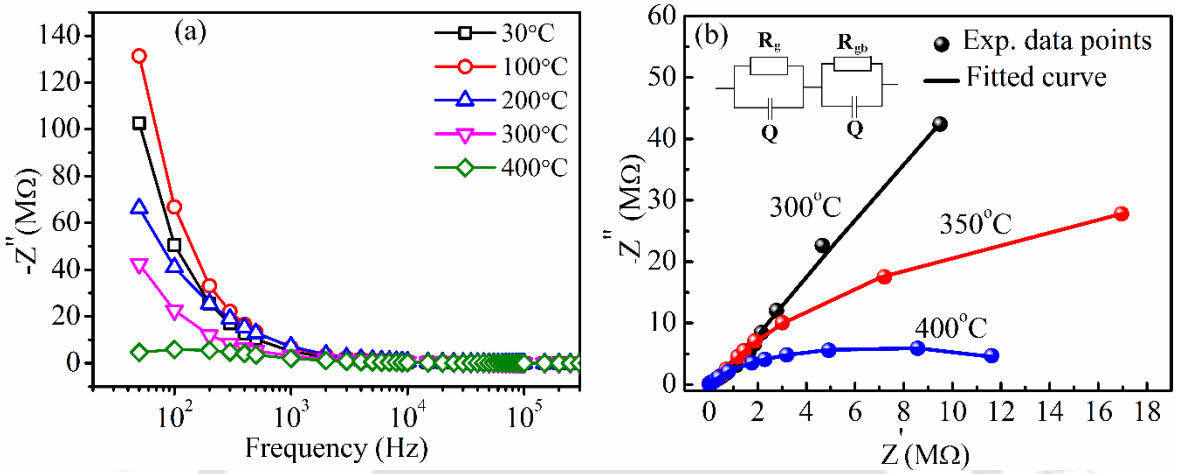

Figure 5.16: (a) Spectra of the imaginary part of impedance as a function of frequency at different measurement temperatures, and (b)Fitted complex impedance spectra and corresponding equivalent electrical circuit given in the inset

At higher frequencies, the drop in the imaginary part of the impedance is due to the release of space charge carriers[157]. This independency of impedance with frequency in the high-frequency region also implies an enhancement in ac conductivity with temperature[89]. Electrical properties exhibited by the ceramics are a compound effect of conduction at various electrically active regions like grains and grain boundaries [158]. This mechanism in ceramics can be understood by the Brick-layer model[96]. In impedance spectroscopy, the Brick-layer model is used to understand conduction in grains and across the grain boundaries. In a polycrystalline, multigrain system the resistivity of grain boundaries can be considered larger than the resistivity of core grains and can be expressed as two components equivalent electrical circuit consisting of a parallel capacitor (C) and resistor (R) connected in series. The complex impedance spectrum is a representation of various relaxation phenomena associated with the sample. Based on such responses, several phenomena were introduced by Debye, Cole–Cole, Cole–Davidson, Havriliak–Negami, etc. All these models can be categorized broadly into Debye and non-Debye type of relaxation representing non-interacting (one body) and interacting (many body) system. In Debye type, dipoles will not

have any interaction with each other as they are separated by a viscous medium. On an application of electric fields, these dipoles will align along the field direction and on removable of the field, the dipoles will reorient back to their initial position. In such cases, impedance spectra will be a perfect semicircle, originating from real axis. Whereas, usually all practical systems are non-Debye type, where there will be interactions among the dipoles present in the system and hence the impedance spectra will be a distorted semicircle originating below the real axis.

The impedance spectra in the present case showed Cole–Cole type relaxation behavior. The mathematical equation for Cole–Cole type for dielectric constant $\varepsilon(\omega)$ at angular frequency ω is can be express as

$$\varepsilon(\omega)-\varepsilon(\infty)\propto\frac{1}{(1+i\omega\tau)^{1-\alpha}} \tag{5.7}$$

where $\varepsilon(\infty)$ and α represent permittivity at high frequency and angle of deviation below the real axis, respectively. In the present case, the relaxation phenomenon is analyzed in the impedance plane using the following equations relating to permittivity and impedance

$$\varepsilon''=\frac{Z'}{\omega C_0(Z'^2+Z''^2)} \tag{5.8}$$

$$\varepsilon^{//}=\frac{Z''}{\omega C_0(Z'^2+Z''^2)} \tag{5.9}$$

where C_0 is the vacuum capacitance. The complex impedance spectra at three different temperatures are fitted using Cole–Cole model circuit. The equivalent circuit for the sample obtained using this model is shown in the inset of Figure 5.16(b).

Table 5.8: The numerical values of resistance and capacitance for MTBS3 extracted from Cole-Cole plot.

Temperature(°C)	R_g *(MΩ)*	Q_1		Q_2		R_{gb}*(MΩ)*
		A_1 ($\times 10^{-10}$)	n_1	A_2($\times 10^{-10}$)	n_2	
300	3910	1.557	0.873	9.175	0.964	0.377
350	83.26	9.157	0.769	10.880	0.908	0.317
400	14.14	11.63	0.767	2.462	0.898	0.133

The numerical values of circuit elements are tabulated in Table 5.8, where Q represents the constant phase element that can behave either as a capacitor or a resistor, depending on

whether n is 0 or 1. The obtained bulk resistance for the circuit is found to be decreased with an increase in temperature, which is the signify negative co-efficient of resistivity. The drop in resistance towards higher temperature occurs due to the release of charges accumulated at the grain boundaries and electrode interfaces contributing to conductivity in the sample[159].

5.3.1.5. Conductivity analysis:

In dielectric ceramics, the loss (dissipation) occurs as a result of conduction in the sample. Thus, the real part of conductivity (σ) can be express in terms of dielectric loss ($\varepsilon^{//}$) as,

$$\sigma = \omega\varepsilon_0\,\varepsilon^{//} \tag{5.10}$$

where, ω and ε_0 are angular frequency and dielectric permittivity in free space, respectively[96]. Ideally, in ceramic systems conductivity diminishes with a decrease in frequency and shows a constant value after a certain frequency. The region where conductivity becomes independent of frequency is referred to as DC conductivity (σ_{dc}). In general, the AC conductivity shows a direct proportionality with frequency and the real part of such conductivity obeys a power law, known as the Almond-West relation, i.e.,

$$\sigma = \sigma_{ac}\left[1+\left(\frac{\omega}{\omega_H}\right)\right]^n \tag{5.11}$$

where ω_H denote the hopping frequency of charge carriers and n is the Jonscher's constant[95]. In AC conductivity if $n \leq 1$, the conduction process follows an ideal ionic process of Debye dielectric dipolar type. For such processes, charge carrier conduction occurs via hopping motion. For the other case, when $n > 1$, there is localized long-range back and forth hopping of charge carriers[160,161].

The AC conductivity spectra of MTBS3 are shown in Figure 5.17 and can be divided into two regions, frequency independent plateau (Region I) and dispersion region (Region II). The frequency-independent plateau region corresponds to dc conductivity σ_{dc} and its numerical value can be obtained by extrapolating the curve towards a lower frequency. The frequency dependence of conductivity in the dispersive region can be expressed by using Jonscher's universal power law[95]

$$\sigma_{tot} = \sigma_{dc} + \sigma_{ac} \tag{5.12}$$

$$\sigma_{ac} = A\omega^S \tag{5.13}$$

where A is the pre-exponential factor and $\omega = 2\pi f$ is the angular frequency and 's' is the power law exponent (ideally, $0 < s < 1$). The dispersive regions were fitted into two different

frequency regions and regions and the obtained variation of s values with measurement temperature is shown in Figure 5.17(b). The dependency of 's' value with temperature is also can be related to the different conduction mechanisms associated with the sample. Temperature independent 's' implies quantum mechanical tunneling (QMT) of charge carriers, 's' will be enhanced with increasing T in case of small polaron conduction mechanism and for correlated barrier hopping (CBH) model 's' would improve with reduction in T and tends to unity at 0 K [162].

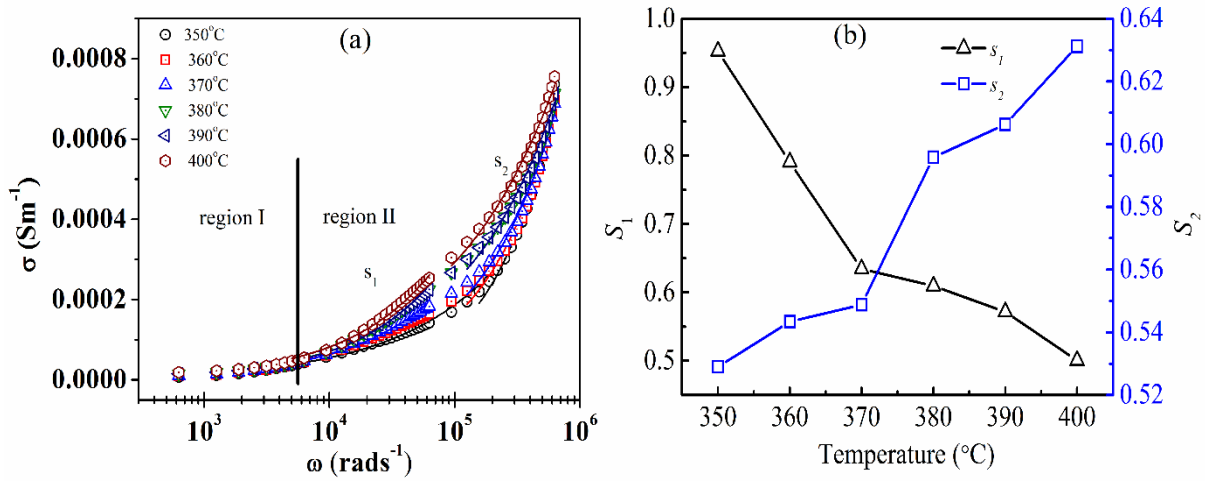

Figure 5.17:: Frequency-dependent conductivity of sintered MTBS3 ceramic with frequency measured at different temperatures.

The obtained values of s_1 (1kHz <ω <100kHz) and s_2 (100kHz <ω <1MHz) are in the range of 0 to 1. Whereas, the values of s_1 decrease with a rise in temperature and s_2 enhanced with an increase in temperature. The obtained values imply the ac-conductivity of the test sample comprises both small polaron and correlated barrier hopping mechanisms. In the low-frequency region, 's_1' signifies translational hopping and in the higher frequency region, s_2 characterizes the presence of localized relaxation[163].

5.3.1.6. Temperature stability analysis:

The change in capacitance over a measurement temperature is an important parameter for a dielectric capacitor. The change in capacitance evaluated from capacitance versus temperature (−30 to +125 °C) curve shown in Figure 5.15 and found to be ∼−54% over the temperature range of (RT) −30 to +85 °C. This obtained value of change in capacitance fulfills the criteria for type-II capacitor[164]. From the above analysis, interesting responses are observed for *MTO-BST* composite ceramics, therefore for microwave integrated circuit

applications, studies on thin films of *MTO* and *BST* composite systems are carried out. In the present work, thin films of *MTO* and *BST* ceramics are studied in a bilayer structure altering stacking order. The detailed results and discussion are presented in the subsequent section

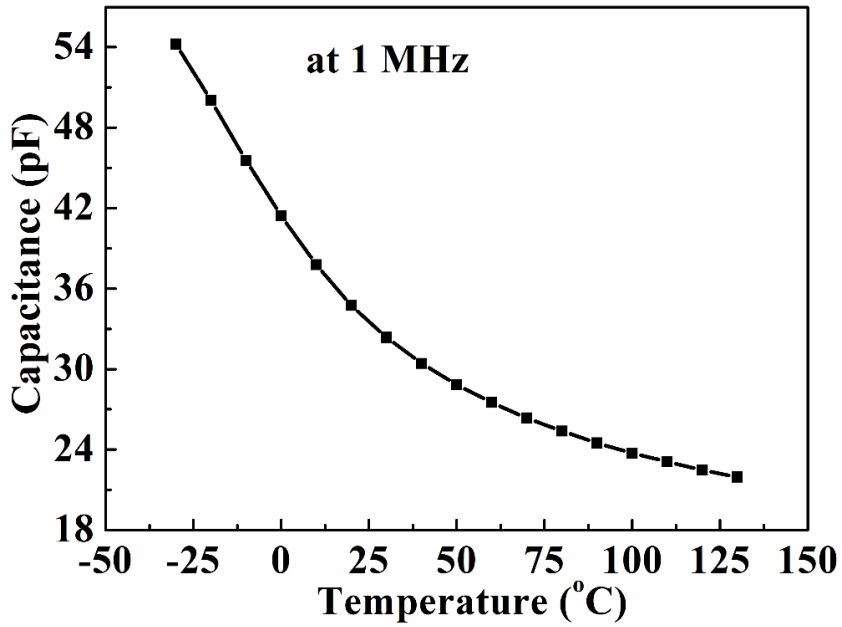

Figure 5.18*: Capacitance vs temperature curve for MTBS3 composite ceramics, measured at 1 MHz.*

5.3.2 $MgTiO_3$ and $Ba_{0.5}Sr_{0.5}TiO_3$ bilayer films:

5.3.2.1 Structural and microstructural analysis:

Figure 5.19 (i-iv) presents the XRD patterns of annealed *BST*, *MTO/BST, BST/MTO,* and *MTO* thin films each of 200 nm thickness deposited on n-type Si substrates. All the films exhibited polycrystalline nature for both the monoliths. The diffraction peaks corresponding to cubic BST (JCPDS no # 00-0390-1395) with Pm-3m space group, and rhombohedral *MTO* (JCPDS # 790831) with $R\bar{3}$ the group are indexed in the pattern (i) and (iv), respectively. The bilayer thin films: *MTO/BST* and *BST/MTO* exhibited both *MTO* and *BST* polycrystalline phases.

However, the peak intensities corresponding to individual phases, viz: *MTO* and *BST* are found to be different depending upon stacking order i.e., *MTO/BST* and *BST/MTO,* respectively. For *MTO/BST,* the peak intensities for both *MTO* and *BST* are almost equivalent, whereas the peak intensity of *BST* is much higher as compared to the *MTO* phase

for *BST/MTO* bi-layer films. This kind of discrepancy could be understood in detail from the theory of the heteroepitaxial growth of films. The differences in lattice parameters of Si ($a = b = c = 5.43$ Å), *MTO* ($a = b = 5.056$Å and $c = 13.89$Å) and *BST* ($a = b = c = 3.94$Å) would lead to stresses (tensile or compressive) on deposited film as a result of lattice misfit (*f*). The lattice misfit (*f*) in the attempt to grow a film on a substrate of dissimilar lattice parameters can be calculated by using the following expression from the lattice parameters of the substrate (a_s) and the film (a_f) [81]

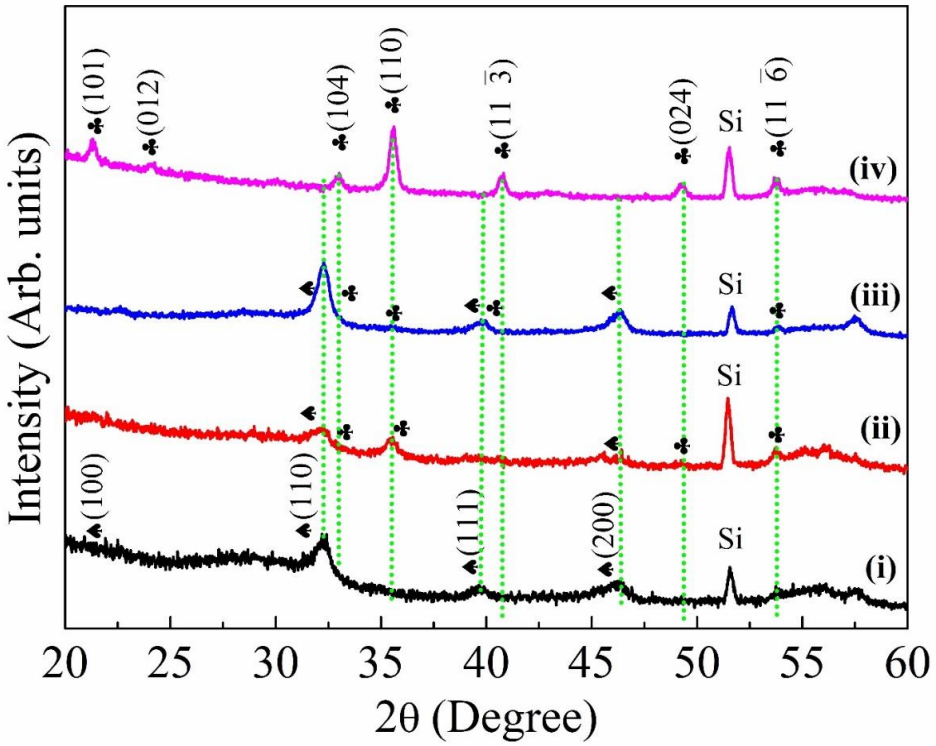

Figure 5.19: (i-iv): XRD patterns of BST, MTO/BST, BST/MTO, and MTO thin films, respectively, and the miller indices are indexed in patterns (i) and (ii) for BST and MTO phase, respectively.

$$\text{Lattice misfit } (f) = \frac{a_s - a_f}{a_f} \times 100\% \qquad (5.14)$$

The obtained lattice mismatches for the four different films were listed in table 5.9. Interestingly, despite of high lattice mismatch between *MTO* and *BST*, the bilayer of *MTO/BST* and *BST/MTO* were successfully grown with accommodation of strain.

Table 5.9: List of lattice misfits (f) and theoretical obtained nature of strain for MTO/Si, BST/Si, MTO/BST/Si, and BST/MTO/Si thin films

Structure	Lattice misfit	Remarks
MTO/Si	*+7.5%*	*Tensile stress on MTO film.*
BST/Si	*-2.7%*	*Compressive stress on BST film.*
MTO/BST/Si	*+56%*	*Tensile stress on MTO film*
BST/MTO/Si	*-31%*	*Compressive stress on BST film*

Further, as shown in Figures 5.20 (a) and (c), the most intense diffraction peak along (110) for MTO deposited on Si substrate showed better crystallinity as compared to that on *BST* coated on Si-substrate. In contrast to that, *BST* deposited on *MTO* (Figure 5.20(d)) coated Si substrate showed better crystallinity than that over Si substrate as shown in Figure 5.20(c).

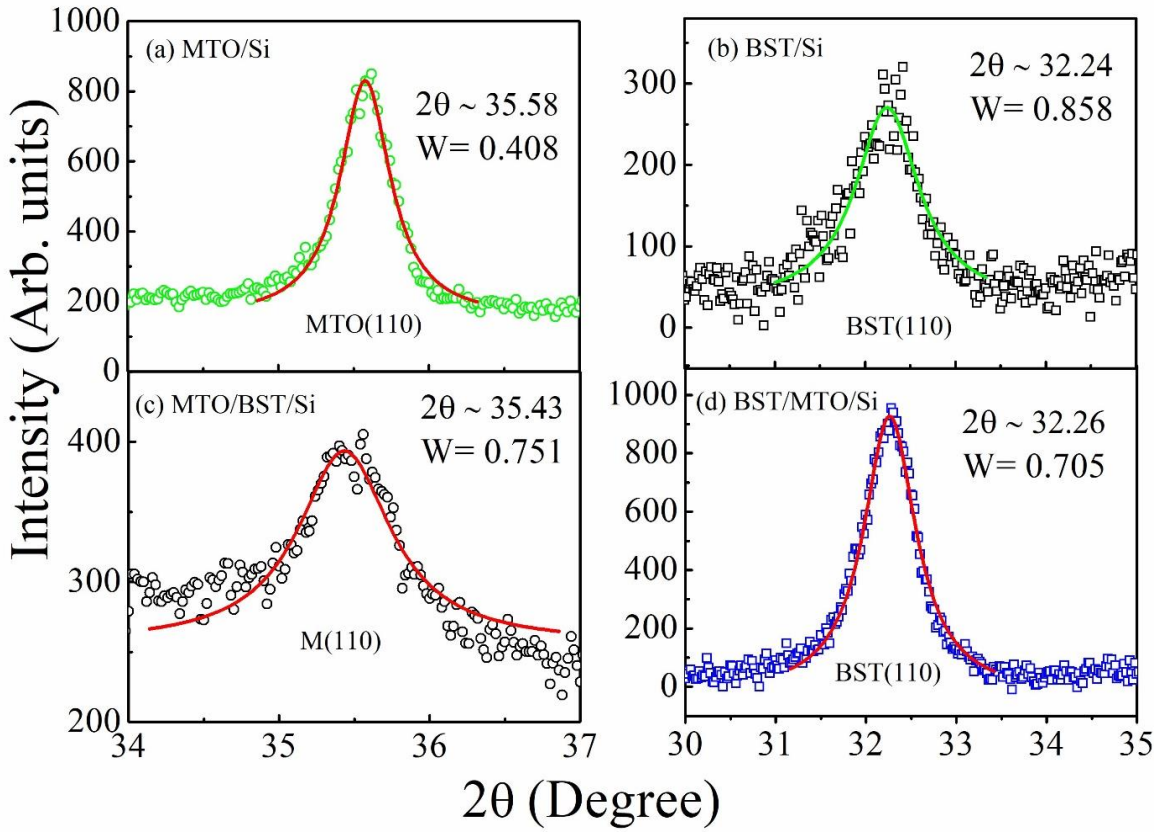

Figure 5.20: The diffraction peak profile along (110) plane of (a-b) MTO and BST deposited on Si, (c) MTO deposited on BST/Si film, and (d) BST deposited on MTO/Si.

These observations can be attributed to differences in the lattice misfit. Moreover, residual lattice strain/stress is a crucial parameter for structural stability in the case of multilayer film

deposition [137]. The origin of residual stress/strain comes from both intrinsic and extrinsic stress/strain in the film. Whereas the origin of extrinsic stress/strain is said to be due to the difference in lattice expansion co-efficient between the consecutive layers, which arises when the deposited films were treated at elevated temperatures (annealing of the film).

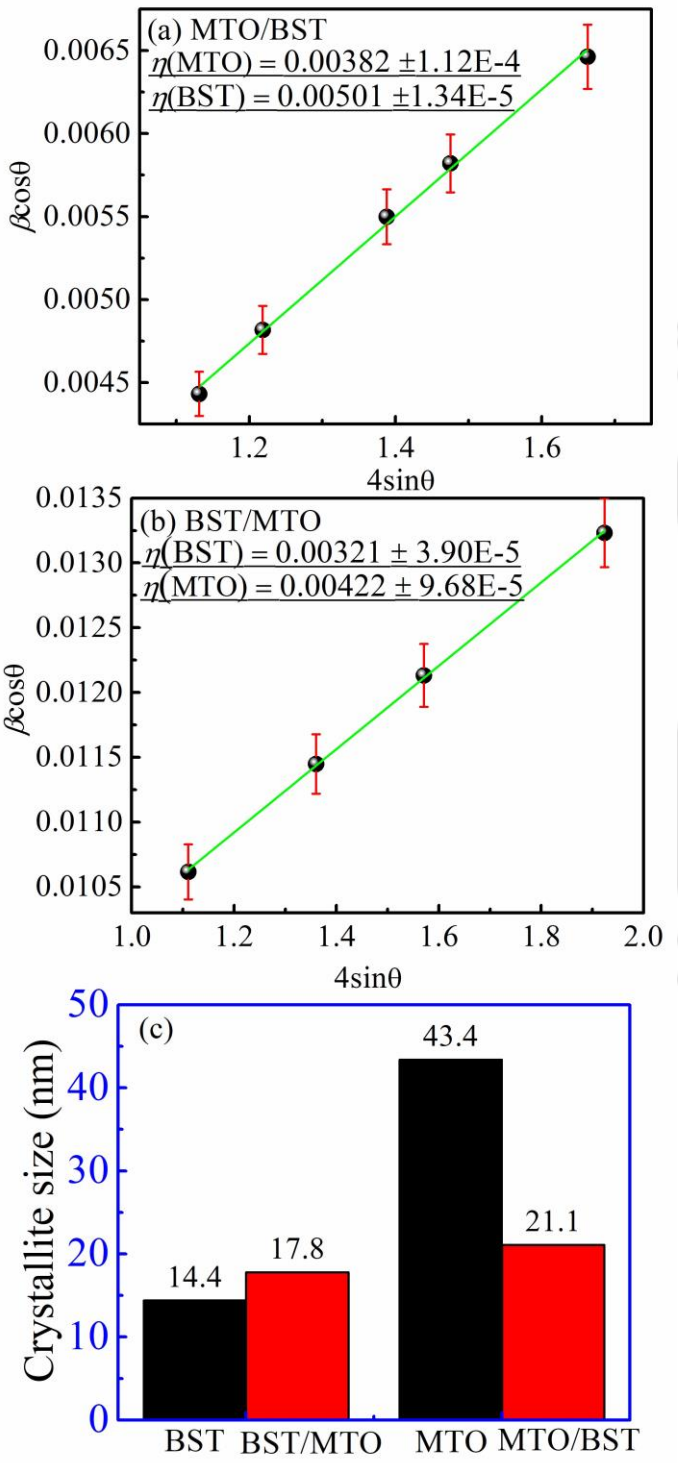

Figure 5.21: W-H plot for MTO/BST and BST/MTO film (a-b), crystallite sizes of BST and MTO deposited on bare Si substrate and MTO/Si and BST/Si substrates, respectively.

In contrast to extrinsic stress/strain, intrinsic stress/strain is a complex parameter to determine due to multiple probable factors. During the growth process, intrinsic stress/strain starts forming and it is unique for a particular deposition technique [165]. In addition, the formation of non-equilibrium structures, and recrystallization also contribute to intrinsic stress/strain. In the current study the residual stress for the annealed *MTO, BST, MTO/BST,* and *BST/MTO* were determined by using Williamson-Hall plots. The peak profile of a material depends on two factors: the crystallite size of the sample and the strain present in the material, and that can be expressed by equations 5.2 and 5.3.

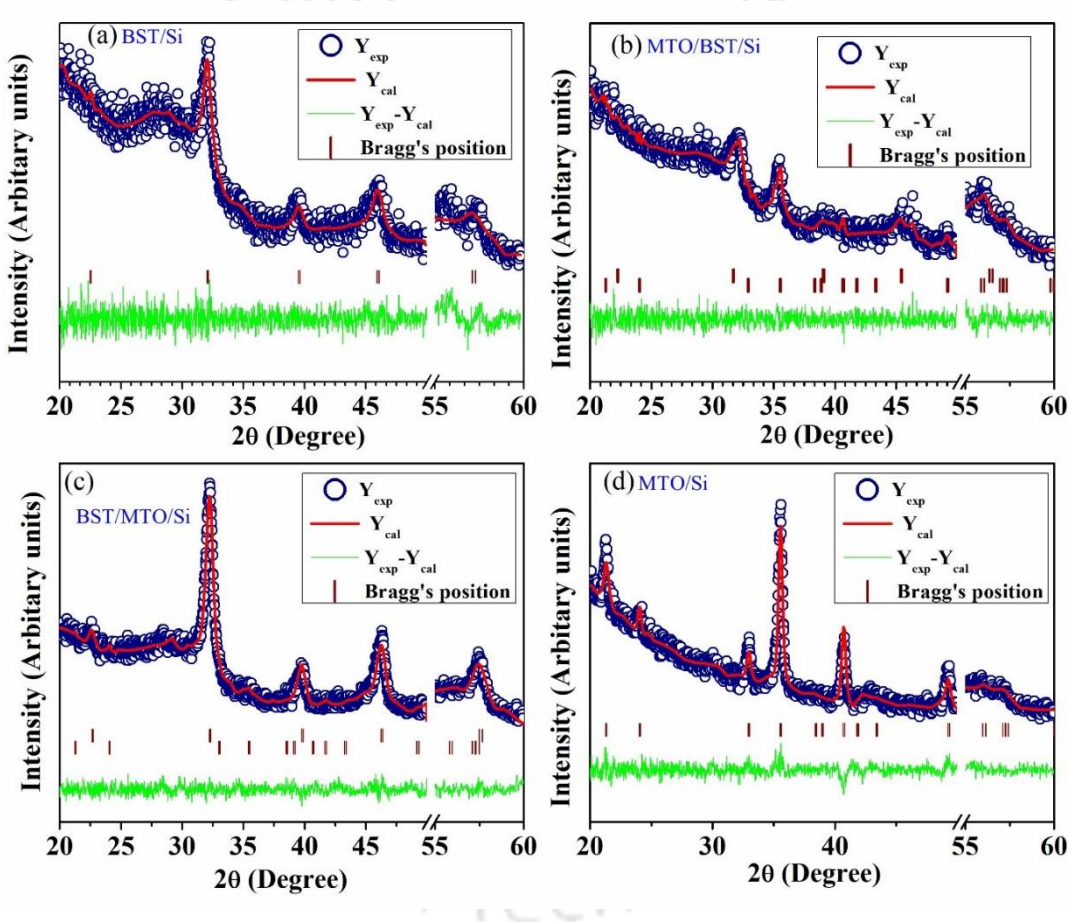

Figure 5.22: Rietveld refined XRD patterns for BST, MTO/BST, BST/MTO, and MTO thin films along with the difference between theoretical and experimental responses, and Bragg's positions.

As shown in figure 5.21(a), the strain for the films was determined by linear fitting in $\beta_{hkl}\cos\theta$ vs. $4\sin\theta$ plot. The obtained residual strain in the *MTO/BST* bilayer is found to be higher (0.0032) as compared to *MTO* film (0.00236). Whereas strain in the *BST* film reduced to 0.0038 from 0.0074 when deposited on *MTO* coated Si than that of bare Si substrate. The

estimated crystallite sizes are also in good agreement with the above results as shown in Figure 5.21 (c). The Rietveld refinement of the XRD patterns for *BST*, *MTO/BST*, *BST/MTO*, and *MTO* thin films are carried out to confirm the phase purity and extract the corresponding lattice parameters, shown in figure 5.22(a-d). The refinements were carried out considering rhombohedral hexagonal symmetry with $R\bar{3}$ (143) space group and cubic symmetry with Pm3m space group (221) for *MTO* and *BST* phase, respectively. The obtained lattice parameters along with refinement parameters are listed in Table 5.10.

Table 5.10: Details of Reitveld refined parameters and lattice parameters of the bilayer films

Name of the Sample	***Refinement parameters***			***MTO***			***BST***	
	χ^2	R_{wp}	R_p	*Fraction (%)*	*a = b (Å)*	*C (Å)*	*Fraction (%)*	*a=b=c (Å)*
MTO	*1.54*	*5.95*	*7.90*	*100*	*5.0503± 0.0031*	*13.8688 ± 0.0075*	--	--
MTO/BST	*1.28*	*4.08*	*5.30*	*96.99*	*5.0576 ± 0.0042*	*13.9083 ± 0.0118*	*3.01*	*3.9957± 0.00314*
BST/MTO	*1.03*	*4.39*	*5.64*	*17.38*	*5.0643 ± 0.0065*	*13.8103 ± 0.0274*	*82.62*	*3.9234± 0.0018*
BST	*1.22*	*4.62*	*5.99*				*100*	*3.9479± 0.0037*

The perfectly fitted diffraction patterns validated the formation of polycrystalline *MTO* and *BST* phases. The lattice parameters, the volumetric fraction of *MTO*, and the *BST* phase in the bi-layer films are estimated from the refinement results and their slight deviations from theoretical lattice parameters as a consequence of heteroepitaxial growth are observed. The *MTO* film deposited on Si and *BST* coated Si exhibited larger lattice parameters than that of theoretical *MTO* lattice as a result of tensile stress ascribed to positive misfit to the bottom layer (refer to Table-5.9). Likewise, lattice parameters of *BST* film deposited on both bare Si and *MTO* coated Si exhibited compressed lattice parameters as obtained in Table-5.10.

The surface topography, a histogram for grain distributions, and 3D images of AFM are presented in figure 5.23(a1, a2, and a3) and (b1, b2, and b3) for *MTO/BST* and *BST/MTO* thin films over an $5\mu m \times 5\mu m$ area. The surface morphology of *MTO* film grown on top of *BST* showed the formation of uneven spherical grains with RMS roughness of ~ 49.2 nm. The observed morphology for *MTO/BST* film suggests island-type growth. On the other hand, *BST* film grown on top of *MTO* film exhibited uniform spike-like morphology and topography with RMS roughness of ~1.82 nm. The respective histograms of particle size distribution also indicate broader particle size distribution in *MTO/BST* as compared to *BST/MTO*. These complement the results obtained from the XRD analysis.

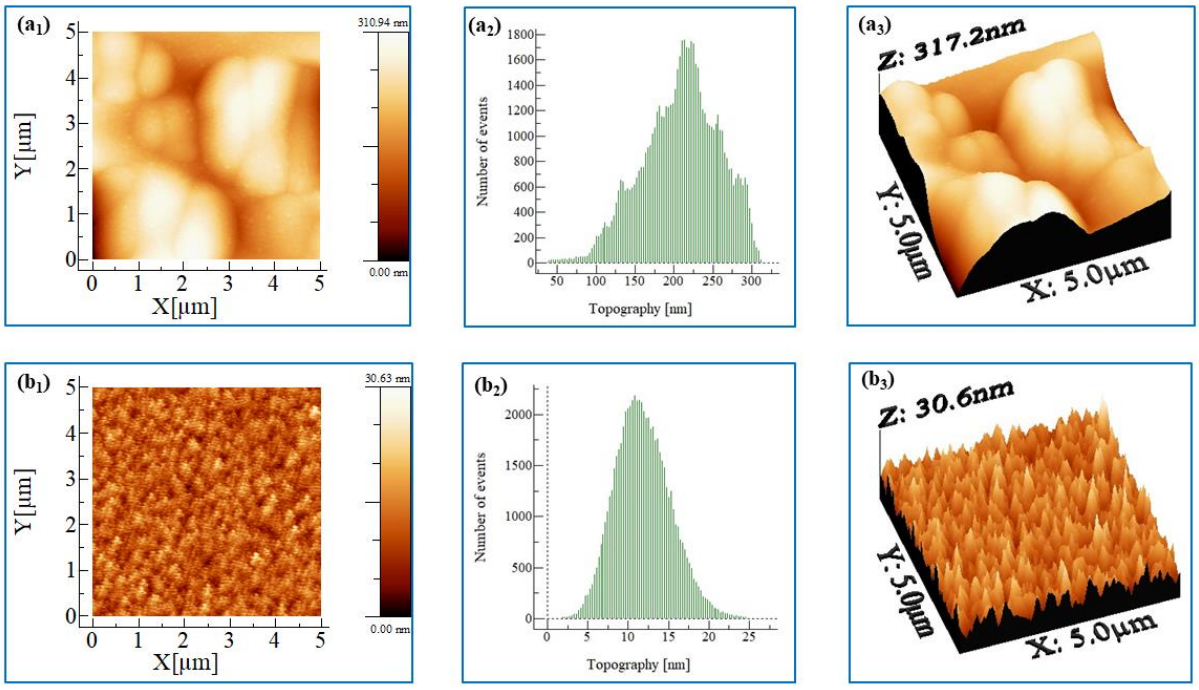

Figure 5.23: Topological image, histograms corresponding to grain distribution, and 3d representation of MTO/BST (a_1, a_2, and a_3) and BST/MTO (b_1, b_2, and b_3), respectively.

5.3.2.2 Dielectric analysis:

Bilayers of *MTO* and *BST* films exhibited interesting responses for dielectric properties depending upon stacking order. Figure 5.24(a-b) presents dispersion in loss tangent and dielectric constant as a function of the frequency of applied field for *MTO/BST/Si* and *BST/MTO/Si* thin films at room temperature. As seen in figure 5.24(a) dielectric constant of *MTO/BST/Si* exhibited a gradual drop at around 2 kHz and 100 kHz, respectively. Around these frequency regions, the dielectric loss tangent showed increments.

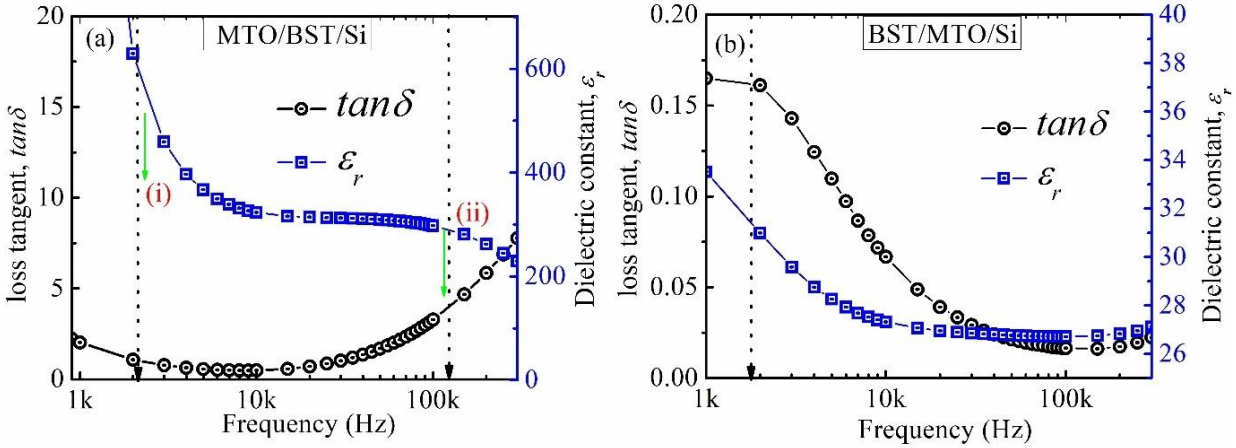

Figure 5.24: (a) Variation of loss tangent (tanδ) and dielectric constant, as a function of the frequency of (a) MTO/BST/Si and (b) BST/MTO/Si thin films measured at room temperature, respectively.

Literature suggests a drop of dielectric constant around 2 kHz and 100 kHz is due to relaxation of space charge polarization and dipolar (orientational) polarization, respectively. The dielectric constant of BST/MTO/Si starts falling around 2 kHz, which can be attributed to the relaxation of space charge polarization and becomes almost constant after 10 kHz in a measured frequency range. As Koop's phenomenological theory suggests, ε_r decayed rapidly in a low-frequency field as a result of relaxation of space charge polarization and became invariant for higher frequency field [166][77]. Space charge polarization is a phenomenon where free charges originated from defects got accumulated in the dielectric to electrode interface [167].

The effective dielectric constant of bilayer thin films of different dielectric constants can be determined by the following expression by considering two capacitors connected in series [168]

$$\varepsilon_r = \frac{\varepsilon_1 \varepsilon_2 (t_1 + t_2)}{\varepsilon_1 t_2 + \varepsilon_2 t_1} \qquad (5.15)$$

where, ε_1, ε_2, and t_1, t_2 are the dielectric constants and thicknesses of the monolayers. The values of ε_r at 100kHz are found to be 323.2 and 27 for *MTO/BST* and *BST/MTO* thin films, respectively. The obtained ε_r for *BST/MTO* bilayer is comparable to the theoretically calculated values by using equation (5.15). In contrast to that, *MTO/BST* bilayer exhibited a huge dielectric constant of 323, which is greater than both *BST* and *MTO* monolayer violating

the equation (5.15). This can be attributed to the formation of an interfacial layer in between the *BST* and *MTO* layer [127,138]. In additional relaxation of the dielectric constant of *MTO/BST/Si* bilayer film around 200 kHz indicated the presence of dipolar polarization. Further irregular surface topography and higher strain estimated from XRD diffraction patterns suggest the possibility of the formation of irregular structures leading to high asymmetry in structure while growing *MTO* film on *BST/Si* film.

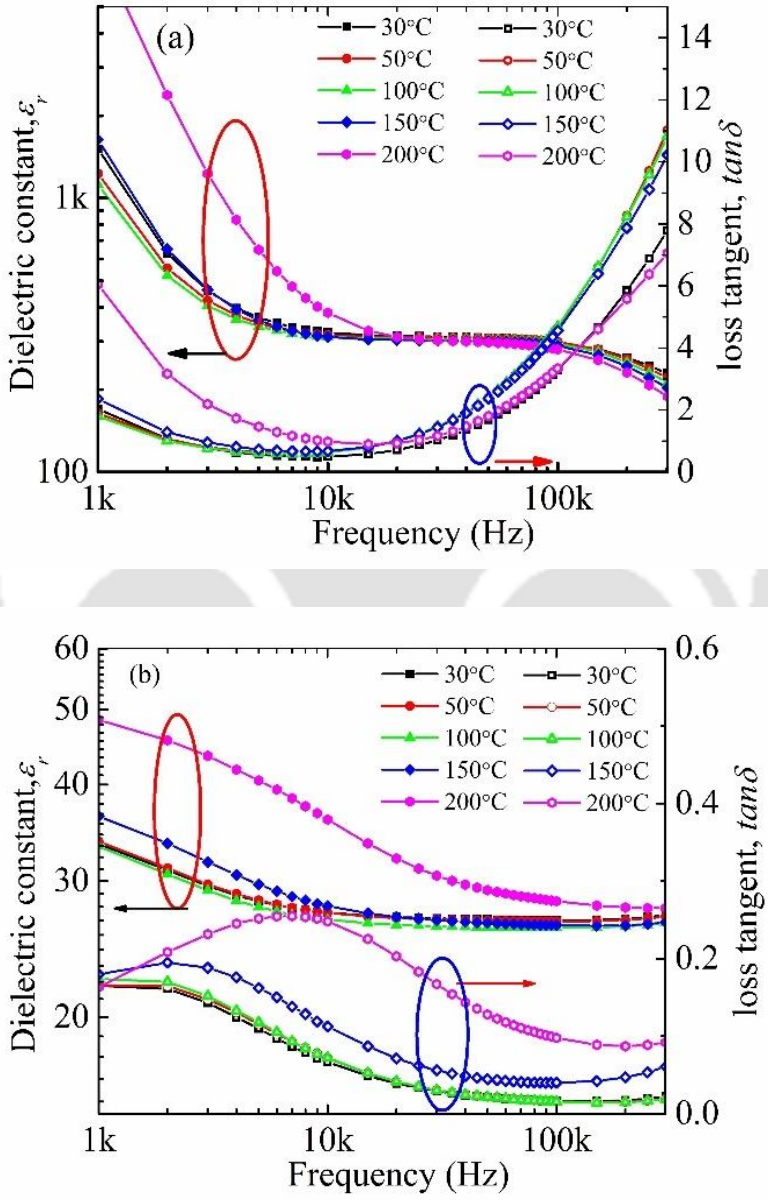

Figure 5.25 (a-b): *Variation of dielectric constant and dissipation factor of MTO/BST/Si and BST/MTO/Si bilayer film at different measuring temperatures, respectively.*

In Figure 5.25(a-b), frequency-dependent ε_r and loss tangent ($tan\delta$) at different measuring temperatures are presented for *MTO/BST/Si* and *BST/MTO/Si* bilayer films,

respectively. For both the bilayers the variations in dielectric constant and loss tangent (*tanδ*) with measuring temperature is insignificant up to 100°C. And above 100°C, the contribution of space charge polarization is found to be increased significantly resulting in higher dielectric constant and loss tangent in the lower frequency region. The observed peaks of loss tangent(*tanδ*) at the lower frequency region signifies relaxation of dipoles, which is further moving towards the higher frequency side with an increase in measuring temperature indicating a thermally activated conduction process in the films[169].

5.3.2.3 Impedance spectroscopy:

Figure 5.26 (a-b) presents the variation of real and imaginary impedance as a frequency of the applied field for *BST, MTO/BST, BST/MTO,* and *MTO* thin films measured at room temperature. In the low-frequency region, dispersion is evident, which decreases with an increase in frequency and becomes almost the same for all the films

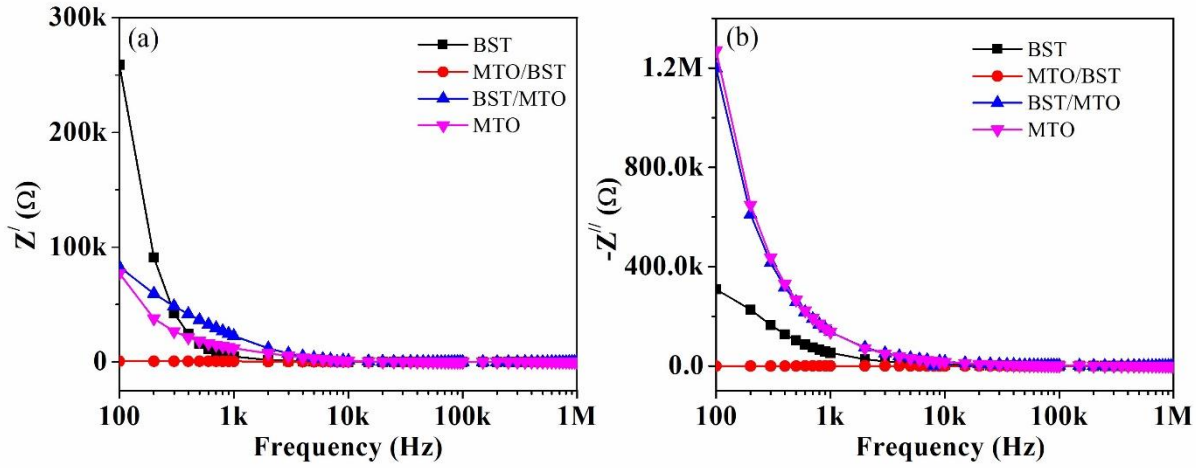

Figure 5.26: Variation of (a) real and (b) imaginary impedance as a function of the frequency of applied field measured for BST, MTO/BST, BST/MTO, and MTO thin films measured at room temperature.

The electrical response of a dielectric sample is highly dependent on its microstructure. Complex impedance spectroscopy i.e., a plot of imaginary impedance to real impedance appears in a combination of successive semicircles in the frequency domain corresponding to different electrically active regions (i.e., grain, grain boundary, and electrode-material interface) of different relaxation times. Generally, first, second, and third semicircular arcs observed at a higher frequency, intermediate frequency and lower frequency region correspond to dielectric relaxation processes in grain, grain boundary region, and electrode interfacial region, respectively. In experimentally obtained spectra, semicircular

arcs corresponding to grain and grain boundary both appear merged. With the help of ZSimpWin software impedance spectra fitted in an electrical circuit, the model provides segregated electrical responses corresponding to different electrically active regions both qualitatively and quantitatively. Among various electrical circuits, which could fit the spectra, a series combination of two parallel resistive components (R) and capacitive component (C) was found to be practically most suitable. In some cases, the use of constant phase element (CPE) in place of C gives a more accurate fitting. In a real system, not a single electrical element is an ideal capacitor or resistor, and the use of CPE in the electrical circuits replicating a real system offers a clearer picture

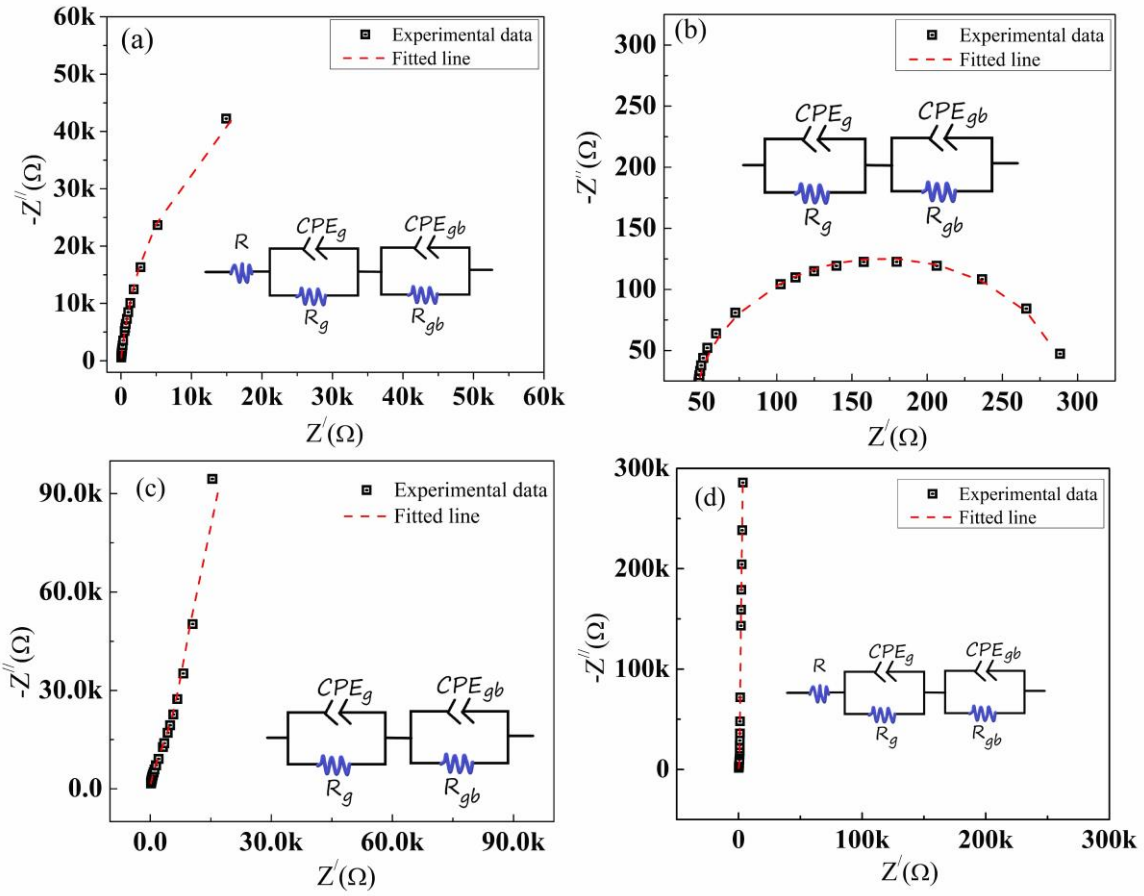

Figure 5.27: Cole-Cole fitted impedance spectra of BST, MTO/BST, BST/MTO, and MTO thin films at 200˚C. Equivalent electric circuits for the Cole-Cole fittings are presented in the insets.

Figure 5.27(a-d) represents fitted impedance spectra of *BST, MTO/BST, BST/MTO,* and *MTO* thin films at 200˚C. The equivalent electrical circuits are shown in the inset of Figure 5.27(a-d). The obtained equivalent circuits for BST and MTO films indicated electrical contribution from all three electrically active regions. However, in the case of bi-

layer *MTO/BST* and *BST/MTO* films contributions from grain and grain boundary regions dominated in the measured frequency range.

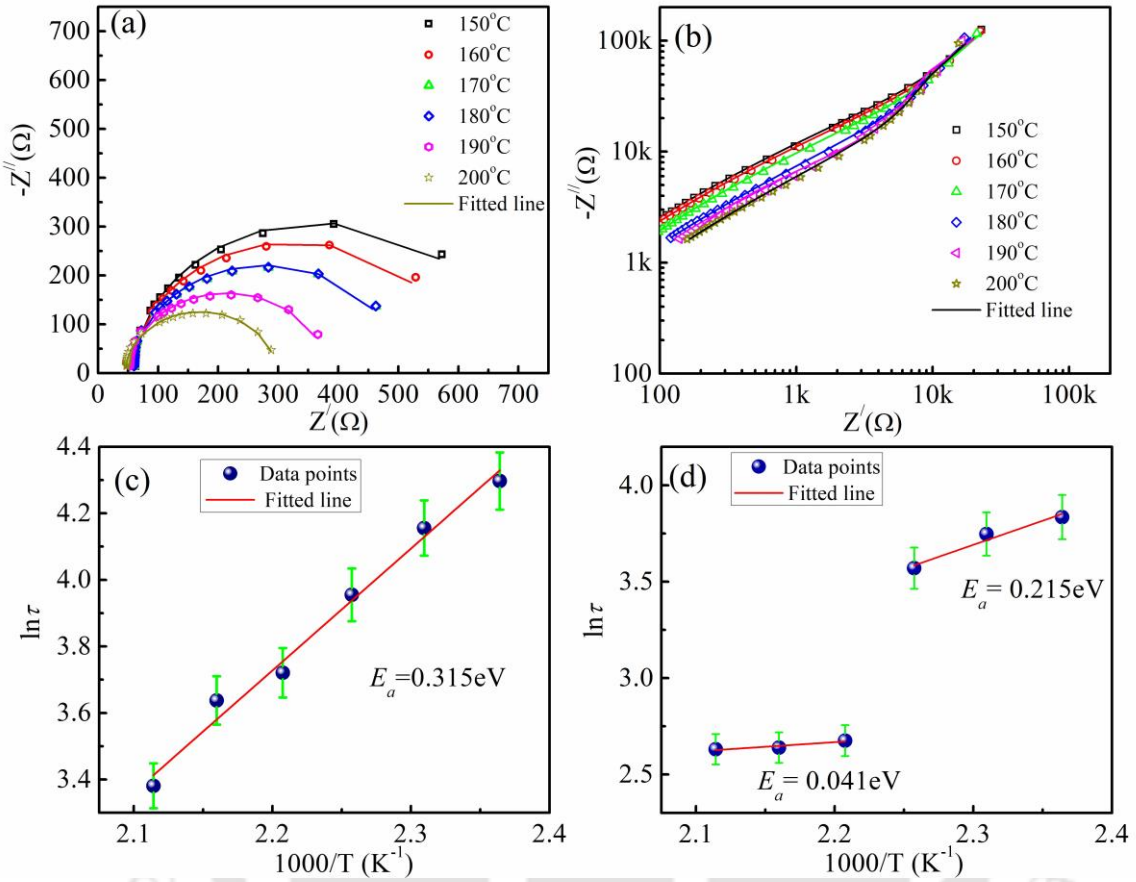

Figure 5.28:(a-b) Cole-Cole fitted impedance spectra and (c-d) variation of dipolar relaxation time (τ) with 1000/T of MTO/BST and BST/MTO film at different measuring temperatures.

Figure 5.28 (a) and (b) present Cole-Cole fitted impedance spectra for *MTO/BST* and *BST/MTO* films for different measuring temperatures (150-200°C). The obtained values of resistances and capacitances are tabulated in Table 5.11. The estimated dipolar relaxation time for both the films is found to be decreasing with an increase in measuring temperature attributed to thermally activated conduction. The activation energy for relaxation time is estimated by fitting the plot using the Arrhenius relation as follows

$$\tau = \tau_o \exp(-\frac{E_a}{k_B T}) \qquad (5.16)$$

where, τ_0, E_a and k_B are prefactor, the activation energy of relaxation process and Boltzmann constant, respectively.

As shown in figure 5.28 (c-d) the plots of lnτ to the inverse of measuring temperature 1/T can be fitted by one or more linear equations, and the corresponding slope is utilized to determine the activation energy of conduction. In the measured temperature range lnτ vs. 1/T plot exhibited a linear behavior with a slope of (3.665) for *MTO/BST* bilayer film with an activation energy of 0.314 eV. However, for *BST/MTO* bilayer film two different activation energies are 0.215 eV and 0.041eV, respectively for lower and higher temperature regions. As the conduction process is thermally activated with an increase in temperature activation energy decreased.

Table 5.11: Grain resistance and capacitance extracted from equivalent circuit fitting and calculated relaxation time at different measuring temperatures

Temperature	*MTO/BST*			*BST/MTO*		
(^oC)	R_g (kΩ)	C_g(nF)	τ (μs)	R_g (kΩ)	C_g(nF)	τ (μs)
150	0.614	119	*73.5*	11.15	4.16	46.31
160	0.536	191	*63.8*	10.45	4.06	42.40
170	0.442	118	*52.2*	8.59	4.13	35.52
180	0.350	118	*41.3*	7.01	2.07	14.52
190	0.327	117	*38*	6.80	2.05	14.00
200	0.250	117	*29.4*	6.34	2.18	13.88

5.3.2.4 Leakage current analysis:

The room temperature leakage current density as a function of the applied field is investigated for *MTO/BST* and *BST/MTO* films and the corresponding J vs. E plots are presented in Figure 5.29 (a). The leakage current for *MTO/BST* and *BST/MTO* is found to be ~10^{-2}A/cm^2 and ~10^{-4}A/cm^2, respectively. Higher leakage current for *MTO/BST* to *MTO/BST* can be attributed to non-uniform grain distribution as well as higher roughness as observed from the AFM analysis. Further, understanding the origin of leakage current is a breakthrough move to have control over excessive leakage current in the construction of an electrical device.

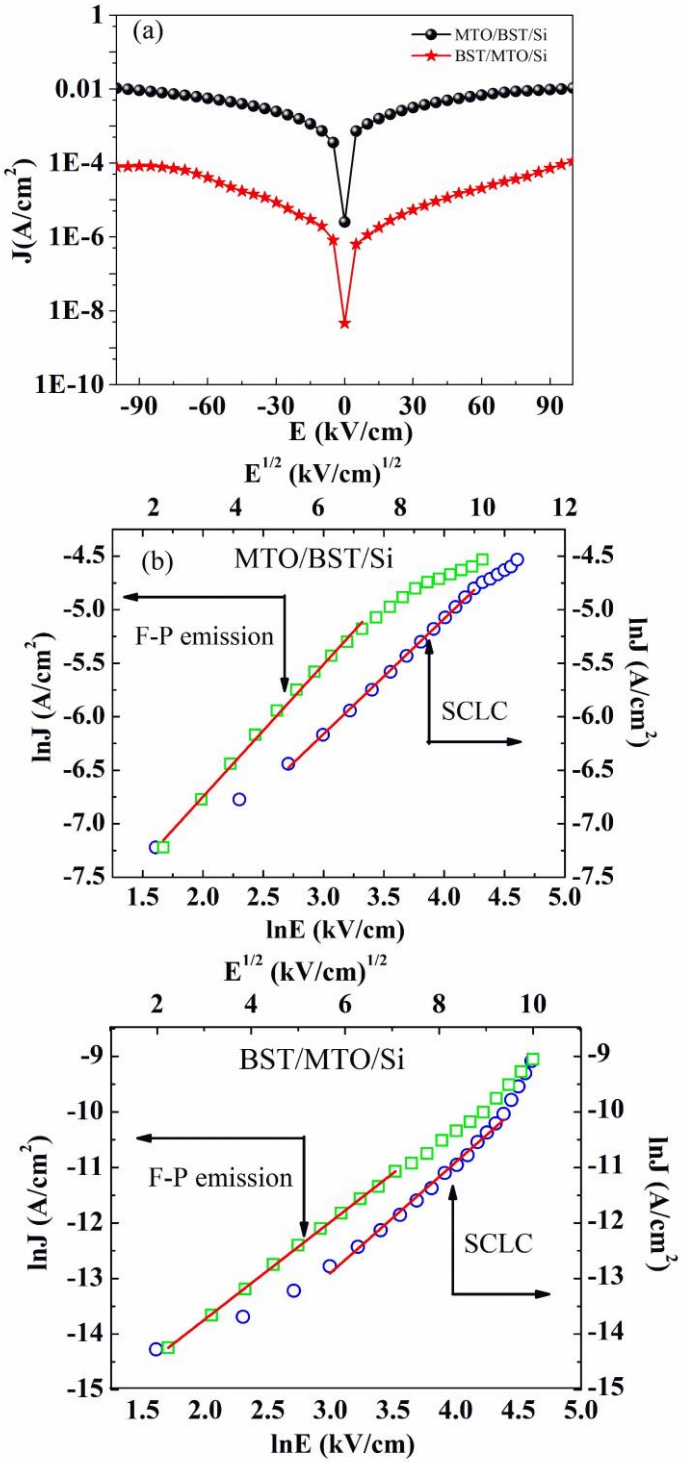

Figure 5.29: (a) Current density with respect to applied field for MTO/BST and BST/MTO film, (b) and (c) lnE vs. lnJ and lnJ vs $E^{1/2}$plots for MTO/BST and BST/MTO film, respectively.

From literature, it has been found that leakage current originates from several sources such as Space charge-limited current, Schottky emission, Poole- Frenkel emission, and Fowler-Nordheim tunneling [12]. The imposed conditions of the present study rule out the possibility of Poole-Frenkel emission since the measurement is carried out at room temperature, and Fowler-Nordheim tunneling as in the present case leakage current is recorded for a moderate field (< 100 kV/cm) [81]. In the electrode (metal) to dielectric interface with small charge carrier concentration, forms a Schottky barrier and leakage current would be due to Schottky emission. Moreover, if the number of charge carriers is very high, the Schottky barrier behaves like Ohmic contact, and the leakage current is dominated by the Space-charge limited current [132].

The plot lnJ vs lnE showed linear variation with a slope near 1 as shown in Figures 5.29(b) and 5.29(c), signifying Space-charge limited conduction mechanism for E > 25 kV/cm[120]. Moreover, lnJ vs. $E^{1/2}$ plot exhibited linear characteristics as shown in the inset of Figure 5.26(b-c) in the lower field region (< 25 kV/cm) Schottky emission dominates. In the presented study, Schottky emission and Space-charge limited current contribute to leakage current. Zhang *et al.* [171] also reported similar leakage studies of $Al_2O_3/TiO_2/Al_2O_3$ capacitors and found that Ohmic behavior dominates in lower field range (<0.2 MV/cm) whereas at higher field range (0.17-0.65 MV/cm) both Schottky and F-P emissions coexisted. Since this study enables the origin of leakage current at different field ranges, leakage current regulation can be realized by careful fabrication and proper choice of electrode material.

5.3.2.5 C-V Characteristics:

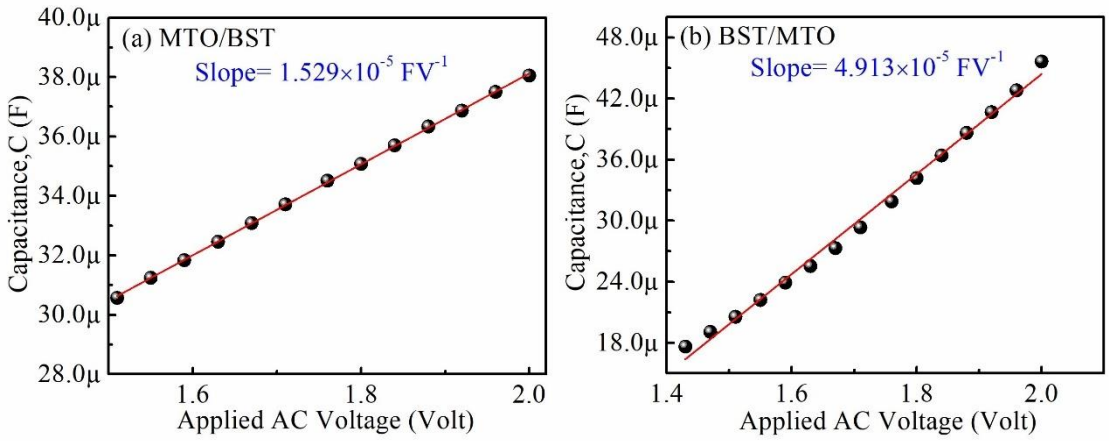

Figure 5.30(a,b): C vs. V for MTO/BST and BST/MTO bilayer thin film measured at 1 kHz.

Variation of dielectric polarization of the MTO/BST and BST/MTO bilayer films to applied AC voltage is studied. A significant variation in capacitance (C) value with applied

AC voltage is observed and C vs. V curve, which is fitted linearly as shown in figure 5.27. The slopes of the C vs. V plot for MTO/BST and BST/MTO bilayer films are found to be 1.529×10^{-5} FV^{-1} and 4.913×10^{-5} FV^{-1}, respectively.

5.4 Summary:

(1-*x*) $MgTiO_3$–*x*$Ba_{0.5}Sr_{0.5}TiO_3$ (for x = 0.1 to 0.5) composite ceramics were successfully prepared by solid-state reaction method. The XRD results also revealed the presence of a mixed-phase # $BaMg_6Ti_6O_{19}$ apart from independent phases of *MTO* and *BST*. The intensities of the mixed phase were found to be enhanced with an increase in BST concentration as well as sintering temperatures. The Raman spectra also complement the XRD results. The microstructures of the composites also showed dependency on BST concentration as well as sintering temperature. The sintering temperature of the *MTO-BST* composite ceramics is optimized as 1350 °C, and the dielectric permittivity is found to be in the range of $\varepsilon_r \approx 20$–200, dielectric loss~10^{-4}–$10^{-3,}$ and $Q\times f_0$~17,806 GHz at 7.262 GHz to 988 GHz at 2.548 GHz. The temperature-dependent dielectric constant for the composite ceramics has exhibited diffused transition as a typical signature of relaxor ferroelectrics due to the compound response of ferroelectric *BST* and linear dielectric *MTO*. The diffuseness constants extracted by modified Curie–Weiss law is found to be 1.002 for x=0.1 and 1.834 for x=0.5, respectively. All the characterizations and analysis MTBS3 sintered at 1350 °C is optimized and exhibited the best behavior with enhanced dielectric permittivity $\varepsilon_r\approx57$, loss of ~ $10^{-3,}$ and $Q\times f_0$ ~ 1,930 at 4.16 GHz. The obtained value of dielectric permittivity is much higher than *MTO* ceramics and lower than pure *BST* ceramics, which may be attributed to the compound response of dielectric polarization from both *MTO* and *BST* grains as well as grains of mixed-phase $BaMg_6Ti_6O_{19}$ ceramics. The Impedance analysis revealed the presence of non-Debye type conductivity relaxation in the sample. The thermal stability of capacitance has been estimated over the temperature range of (RT) −30 to +85 °C and found to be ~−54%. The optimized MTBS3 composite has exhibited high dielectric permittivity with low loss tangent value and temperature stable capacitance favorable for the type-II capacitor in IC applications.

MTO/BST and *BST/MTO* bilayer films have been deposited on the n-type substrate by RF sputtering technique, respectively. *BST/MTO* bi-layer exhibited better structural stability as compared to *MTO/BST* bi-layered film. The AFM analysis complemented the XRD results revealing less RMS roughness and homogeneous topography for *BST/MTO* bi-layers. Further,

the dielectric constant of the *BST/MTO* bi-layer was found to be intermediate to *BST* and *MTO* in agreement with the theory of the parallel combination of individual capacitance in a multilayer structure. In contrast, a huge dielectric constant of *BST/MTO* indicated the accumulation of dipoles in the interface of *MTO* and *BST* layers for structural asymmetry. The equivalent electrical circuit for *MTO/BST and BST/MTO* revealed the contribution of both grain and grain-boundary in electrical responses. Leakage current analysis suggests both Schottky emission and Space-charge limited-assisted leakage current. Further, the obtained value of the slope of C versus V curves for both *MTO/BST* and *BST/MTO* bilayer films revealed tunable dielectric property.

CHAPTER 6: Conclusion and Future Scopes

A detailed study on the structural, microstructural, dielectric, and electrical properties of *MTO*-based composite ceramic materials, in bulk as well as thin film form, was carried out. Three *MTO*-based composite ceramics were prepared by adding *BNO*, *STO*, and *BST* ceramics using the solid-state reaction method. In addition, *MTO-BNO* composite thin films and heterostructures of *MTO* with *STO* and *BST* ceramic thin films were deposited using one of the versatile techniques RF magnetron sputtering.

6.1 Conclusions:

The composite of two different phases having distinct crystallographic features, under ideal conditions, generally tends to form a solid solution. However, the thermal-induced ionic substitution during the material preparation can result in the formation of secondary and mixed phases in the composites. For the studied ceramic composites, the final ceramic product either exhibited only independent constituent ceramic phases or in addition to secondary and mixed phases depending on the type of ceramics added to the *MTO* base. This is attributed to the variation in the interaction of *MTO* with the three different added ceramics. The *MTO-BNO* and *MTO-BST* composites revealed the formation of secondary phase and mixed-phase along with the characteristic *MTO-BNO* and *MTO-BST* phases. The *MTO-STO* composite, on the other hand, showed the independent *MTO* and *STO* phases with a little crystallographic distortion caused by ionic substitution. The structural characteristics and physical properties viz., dielectric constant, electrical conductivity, and optical bandgap of composite ceramics are a combined response of constituent ceramics. For *MTO-BNO* and *MTO-STO* composite ceramics, the negative τ_f value of *MTO* ceramics was successfully tuned near zero at an optimized concentration. However, control over the structural property for *MTO-BNO* composite was challenging. Therefore, *MTO-STO* composite ceramics is more convenient for commercial applications in bulk quantity. The *MTO-BST* composite ceramic also exhibited temperature stable dielectric property for type-II capacitor applications. *MTO*-based thin films also exhibited promising dielectric properties for integrated circuit applications.

The following conclusions were drawn based on the extensive analysis carried out in this study.

***MTO-BNO* composite ceramics and thin films**

- The structural and dielectric properties of the MTO-BNO composite ceramics developed by using the conventional SSR method and microwave sintering process are significantly influenced by the sintering temperature and percentage of BNO content in the composite. The optimum value of the BNO content is 10% (x = 0.1) as the structural properties display anomaly above x =0.1. An increase in the sintering temperature (950-1030 °C), on the other hand, significantly improved the crystallinity, relative density, and microwave dielectric property. The MTO-BNO composite with 10% BNO content (x = 0.1) at a sintering temperature of 1030 °C exhibited excellent structural and dielectric properties, promising for dielectric resonator and antenna applications. At this temperature, the MTO-BNO composite exhibited a maximum relative density of 98% as well as suitable dielectric properties: dielectric constant (ε_r) ~20, loss tangent ($tan\delta$) ~ 10^{-4}, and quality factor ($Q\times f_o$) = 60,230 GHz at 8.25 GHz with τ_f ~ -5 ppm/^{o}C.
- The crystallinity of the annealed 0.9*MTO*-0.1*BNO* thin films is primarily influenced by the ratio of Ar/O_2 in the mixed ambiance during the deposition on n-type Si and SiO_2 substrates by RF reactive magnetron sputtering at 400°C. The deposited thin film exhibited the best post-annealing crystallinity in the mixed ambiance having a 50/50 Ar/O_2 ratio.
- The lattice of the thin film undergoes strain during deposition due to the hetero-epitaxial growth on the substrate. The lattice strain, RMS-roughness, and lattice defects of the deposited films tend to be lower for higher film thicknesses. Thus, better dielectric (microwave as well as low frequency), optical responses, and leakage current control can be achieved by increasing the film thickness.
- The leakage current conductivity of the deposited thin films is primarily caused by non-Debye, and non-overlapping small polaron hopping conduction process. The leakage current can be lowered by minimizing the lattice strain and defects.
-

***MTO-STO* composite ceramics and thin films**

- The *MTO-STO* composite ceramics at the sintering temperature of 1350°C exhibited the best microwave dielectric properties and thermal stability (τ_f ~ 1.76 ppm/K) with an *STO* content of 4%. The dielectric constant showed gradual improvement (18.74 -

85.55) with an increase in the *STO* content and thermal activation which showed no variation over a broad frequency range of (100Hz-100MHz).

- The perusal of Mott's variable range hopping 3-d model revealed the dominance of short-range hopping (< 3 nm) in composite ceramics. The activation energy for conduction is found to be decreasing (172 meV - 83 meV for x = 0.04 -0.5) with *STO* content attributed to the increase in number of density of states from 1.65 ×1019 $eV^{-1}cm^{-3}$ to 3.413×1020 $eV^{-1}cm^{-3}$.
- Three different bi-layer films with varying *MTO* thickness on the top of an *STO* layer with fixed-thickness namely, STMT1, STMT2, and STMT3, were successfully deposited by RF magnetron sputtering. Strain in the lattice structure of the STMT bi-layer film is caused due to the non-epitaxial stacking. The surface morphology was distinctly different for the three STMT bilayers as the strains experienced by the surface layer atoms were different due to the changes in the *MTO* layer thickness.
- An improved microwave dielectric property was obtained for STMT3 film with minimum loss tangent (1.89×10^{-3}) and considerable dielectric constant ~ 65 at 10 GHz. All the films exhibited more than 75% optical transparency and dropped to zero near 300 nm, corresponding to the characteristic absorption edge. Frequency-dependent dispersion of dielectric constant for STMT films followed Maxwell-Wagner and Koop's phenomenological theory. The overall dielectric constant decreases with an increase in *MTO* thickness. The dielectric constant remained almost constant in the measured temperature range (303K-350K) for STMT3 film.
- A shallow leakage current of the order of 10^{-6} A/cm^2 is recorded for a 200 kV/cm field. Further analysis revealed that Schottky conduction and space charge limited mechanisms are responsible in the lower field region and higher field region, respectively.

***MTO-BST* composite ceramics and thin films**

- The $(1-x)$ *MTO*$-x$ *BST* (for x = 0.1 to 0.5) composite ceramics were prepared by using solid state reaction method. The maximum densification was optimized at different sintering temperatures (1250 to 1400°C). The composite ceramics have exhibited diffused transition as a typical signature of relaxor ferroelectrics with

temperature. Modified Curie–Weiss law was implemented and calculated the diffuseness constant to probe the relaxor behavior of the ceramics.

- The Impedance analysis in complex plane showed non-Debye type relaxation behavior. Correlated barrier hopping mechanism is found to be responsible for conduction process at higher frequency region in AC- conductivity analysis. The 0.7 *MTO*-0.3 *BST* composite ceramic sintered at a temperature (Ts) of 1350℃ is optimized as the best composition with 97% relative density, high dielectric permittivity ε_r ~ 57 and moderate quality factor, $Q \times f_0$ = 19,30 GHz at 4.16 GHz. The thermal stability of capacitance over the temperature range of (RT) − 30 to + 85 °C was found to be ~ − 54%.

- The bi-layer thin films of *MTO* and *BST* ceramics were deposited on n-type Si by RF magnetron sputtering technique by altering stacking order. Both the bi-layer thin films exhibited independent *MTO* and *BST* phases. However, residual strain as well as diffraction peak analysis revealed showed better stability in *BST* stacked on *MTO* (*BST/MTO*) to *MTO* stacked *BST* (*BST/MTO)* bi-layer thin film. Topography of *BST/MTO* bilayer exhibited lower rms roughness (1.82 nm) to *MTO/BST* bi-layer rms roughness ~ 49.2.

- The dielectric responses of the two bilayers: *MTO/BST* and *BST/MTO* exhibited interesting role of stacking order. As theoretical estimation, *BST/MTO* bilayer exhibited intermediate dielectric constant and loss (27.3 and~10^{-2}) to *BST*, *MTO* monolayer at 100 kHz. However, the observed dielectric response for *MTO/BST* showed anomaly attributed to generation of dipoles in the interface of individual layers.

- The impedance spectroscopy analysis of the bi-layers revealed contribution of both grain and grain boundary in conduction process.

- The leakage in *MTO/BST* (10^{-2} A/cm^2 at 100 kV/cm) bilayer is higher than that of *BST/MTO* (10^{-4}A/cm^2 at 100 kV/cm) bilayer and Schottky emission and Space-charge limited current contributes to the leakage current.

Table 6.1:*Comparison of dielectric properties of MTO based composite ceramics and thin films.*

Sl no.	Sample details	ε_r	tanδ	τ_f (ppm/K)	τ_ε	Measured frequency
1	*0.9MTO-0.1BNO* composite ceramics	20	10^{-4}	-5		8.254 GHz
	0.9MTO-0.1BNO thin film	14.66	10^{-4}			10 GHz
2	*0.96MTO-0.04STO* composite ceramics	18.74	10^{-5}	+1.76		8.08 GHz
	MTO/STO bilayer thin film	65	10^{-3}			10 GHz
3	*0.7MTO-0.3BST* composite ceramics	57	10^{-4}		54 %	4.16 GHz
	MTO/BST bilayer thin film	27.3	10^{-3}			100 kHz

6.2 Future scopes

The studies on *MTO*-based composite ceramics showed improved microwave dielectric properties for terrestrial applications where temperature fluctuation is inevitable. Similarly, the *MTO*-based thin films also exhibited promising dielectric properties. However, more studies are required to completely understand the *MTO*-based composite ceramics and thin film systems. Some of the future scopes derived from the present study are as follows:

- In this work, the dielectric study of the *MTO-BNO* composite ceramics was carried out only at a single value of *BNO* content i.e., $x = 0.1$. A more rigorous study on the dielectric response of the *MTO-BNO* composite by varying the *BNO* content in the range of $x = 0$ to 0.2 is necessary to develop a comprehensive understanding of the composite system.
- The *MTO-BNO* composite thin films were subjected to the annealing treatment at a temperature of 750- 800 ℃ to achieve better crystallinity. The effect of the annealing temperature, was, however, not considered in the present study. Further, the influence of the argon/oxygen ratio in the deposition chamber on the performance of *MTO-BNO* composite thin films was not dealt with in detail. These two aspects can be addressed in the future to acquire a better insight into the growth dynamics of thin films and the evaluation of corresponding physical properties.

- The compatibility of *MTO-BNO* thin films with the electrode material is crucial for device application purposes, in order to minimize leakage current. A study on the electric properties of composite thin films with different electrode materials, therefore, is of significant importance.
- Multilayer and bilayer *MTO* and *BNO* ceramic thin films are other aspects that can be explored in the future and can be assessed with respect to the *MTO-BNO* composite ceramic thin films.
- *MTO-BST* composite ceramics are proposed for tunable microwave device applications, therefore tunability studies for *MTO-BST* composite ceramics at different measuring temperatures can be explored for terrestrial device application purposes.
- In addition to *MTO/STO* bilayer studies, the multilayer structure of thin alternate *MTO* and *STO* layers would provide a better understanding of heterostructures.
- In addition to *MTO/BST* bilayer studies, the multilayer structure of thin alternate *MTO* and *BST* layers is necessary to understand the observed anomaly in dielectric properties of *MTO/BST* and *BST/MTO* bilayer thin films.
- The effect of substrate material is also important to understand as lattice mismatch affects the structural properties of deposited films.

REFERENCES

[1] *H. Ohsato, Functional advances of microwave dielectrics for next generation, Ceram. Int. 38 (2012) S141–S146. https://doi.org/10.1016/j.ceramint.2011.04.068.*

[2] *M.T. Sebastian, R. Ubic, H. Jantunen, Microwave Materials and Applications, Wiley, 2017.*

[3] *R. Muhammad, Y. Iqbal, C.R. Rambo, H. Khan, Research trends in microwave dielectrics and factors affecting their properties: A review, Int. J. Mater. Res. 105 (2014) 431–439. https://doi.org/10.3139/146.111044.*

[4] *Lord Rayleigh, On the Passage of.Electric Waves through Tubes., 43 (1897) 125–132.*

[5] *H. Sobol, Microwave Communications — An Historical Perspective, IEEE Trans. Microw. Theory Tech. M (1984) 1170–1181.*

[6] *A. Okaya, L.F. Barash, The Dielectric Microwave Resonator*, Proc. IRE. 50 (1962) 2081–2092. https://doi.org/10.1109/JRPROC.1962.288245.*

[7] *K. Wakino, K. Minai, H. Tamura, Microwave Characteristics of (Zr, Sn)TiO_4 and BaO-PbO-Nd_2O_3-TiO_2 Dielectric Resonators, J. Am. Ceram. Soc. 67 (1984) 278–281. https://doi.org/10.1111/j.1151-2916.1984.tb18847.x.*

[8] *N. Ichinose, H. Yamamoto, Effect of additives on microwave dielectric properties in low-temperature firing (Mg,Ca)TiO_3 based ceramics, Ferroelectrics. 201 (1997) 255–262. https://doi.org/10.1080/00150199708228375.*

[9] *S.G. Mhaisalkar, D.W. Readey, S.A. Akbar, Microwave Dielectric Properties of Doped $BaTi_4O_9$, J. Am. Ceram. Soc. 74 (1991) 1894–1898. https://doi.org/10.1111/j.1151-2916.1991.tb07805.x.*

[10] *B. Jancar, D. Suvorov, M. Valant, G. Drazic, Characterization of $CaTiO_3$-$NdAlO_3$ dielectric ceramics, J. Eur. Ceram. Soc. 23 (2003) 1391–1400. https://doi.org/10.1016/S0955-2219(02)00359-X.*

[11] *I.M. Reane, D. Iddles, Microwave dielectric ceramics for resonators and filters in mobile phone networks, J. Am. Ceram. Soc. 89 (2006) 2063–2072. https://doi.org/10.1111/j.1551-2916.2006.01025.X.*

[12] *H. Li, L. Cheng, F. Liu, S. Liu, Crystal defects induced by evaporation of Co and Zn on the structure and microwave properties of $Ba(Co_{0.7}Zn_{0.3})_{1/3}Nb_{2/3}O_3$ ceramics, Ceram. Int. 47 (2021) 17745–17752. https://doi.org/10.1016/j.ceramint.2021.03.095.*

[13] *P. Liao, T. Qiu, J. Yang, X. Lu, Effect of Al_2O_3 addition on microwave dielectric properties of $BaCo_{0.194}Zn_{0.116}Nb_{0.69}O_3$ ceramics, Electron. Mater. Lett. 10 (2014) 121–125. https://doi.org/10.1007/s13391-013-3063-9.*

[14] *H. Wang, F. Zhou, J. Guo, H. Yang, J. Tong, Q. Zhang, Modified BCZN particles filled PTFE composites with high dielectric constant and low loss for microwave substrate applications, Ceram. Int. 46 (2020) 7531–7540. https://doi.org/10.1016/j.ceramint.2019.11.252.*

[15] *A.S.E. Taheri-nassaj, T. Kolodiazhnyi, N. Newman, Origin of dielectric loss in $Ba(Co_{1/3}Nb_{2/3})O_3$ microwave ceramics, J. Am. Ceram. Soc. (2017) 1665–1676. https://doi.org/10.1111/jace.15343.*

[16] *I.M. Reaney, D. Iddles, Microwave Dielectric Ceramics for Resonators and Filters in Mobile Phone Networks, J. Am. Ceram. Soc. 89 (2006) 2063–2072. https://doi.org/10.1111/j.1551-2916.2006.01025.x.*

[17] *Y. Kobayashi, S. Tanaka, Resonant Modes of a Dielectric Rod Resonator Short-Circuited at Both Ends*

by Parallel Conducting Plates, IEEE Trans. Microw. Theory Tech. 28 (1980) 1077–1085. https://doi.org/10.1109/TMTT.1980.1130228.

[18] K.W. Leung, S.A. Long, A. Petosa, A. Ittipiboon, Y. Antar, K.-L. Wong, dielectric resonator antenna, 2008.

[19] T.S. Kumar, A. Kumar, A.R. James, D. Pamu, Enhanced Microwave Dielectric Properties of $MgTiO_3$ Ceramics Prepared by Mechanochemical Method, J. Aust. Ceram. Soc. 47 (2011) 44–48.

[20] H. Tanaka, N. Banba, S. Arai, T. Nishikawa, 2 GHz One Octave-band 90 Degree Hybrid Coupler Using Coupled Meander Line Optimized by 3-D FEM Hiroaki, IEEE MTT-S Dig. (1994) 903–906.

[21] C. Huang, C. Tsai, A. Yang, A. Hsu, Using stepped-impedance dielectric resonators for ism band wireless communication, 44 (2005) 421–423. https://doi.org/10.1002/mop.20654.

[22] R.P. Liferovich, R.H. Mitchell, Mn, Mg, and Zn ilmenite group titanates: A reconnaissance rietveld study, Crystallogr. Reports. 51 (2006) 383–390. https://doi.org/10.1134/S1063774506030047.

[23] M. Jain, S.B. Majumder, Y.I. Yuzyuk, R.S. Katiyar, A.S. Bhalla, F.A. Miranda, F.W. Van Keuls, Dielectric properties and leakage current characteristics of sol-gel derived $(Ba_{0.5}Sr_{0.5})TiO_3$:$MgTiO_3$ thin film composites, Ferroelectr. Lett. Sect. (2003). https://doi.org/10.1080/07315170390274614.

[24] Q.L. Zhang, H. Yang, Low-temperature sintering and microwave dielectric properties of $MgTiO_3$ ceramics, J. Mater. Sci. Mater. Electron. 18 (2007) 967–971. https://doi.org/10.1007/s10854-006-9090-7.

[25] H. Wang, Q. Yang, D. Li, L. Huang, S. Zhao, S. Xu, Sintering Behavior and Microwave Dielectric Properties of $MgTiO_3$ Ceramics Doped with B_2O_3 by Sol-Gel Method, J. Mater. Sci. Technol. 28 (2012) 751–755. https://doi.org/10.1016/S1005-0302(12)60125-X.

[26] T.S. Kumar, D. Pamu, Effect of V_2O_5 on microwave dielectric properties of non-stoichiometric $MgTiO_3$ ceramics, Mater. Sci. Eng. B. 194 (2015) 86–93. https://doi.org/10.1016/j.mseb.2015.01.003.

[27] C. Lee, C. Ou, Y. Lin, C. Huang, C. Su, Structure and microwave dielectric property relations in $(Ba_{1-x}Sr_x)_5Nb_4O_{15}$ system, 27 (2007) 2273–2280. https://doi.org/10.1016/j.jeurceramsoc.2006.07.022.

[28] J.B. Huang, B. Yang, C.Y. Yu, G.F. Zhang, H. Xue, Z.X. Xiong, G. Viola, R. Donnan, H.X. Yan, M.J. Reece, Microwave and terahertz dielectric properties of $MgTiO_3$ – $CaTiO_3$ ceramics, Mater. Lett. 138 (2015) 225–227. https://doi.org/10.1016/j.matlet.2014.09.122.

[29] A. Kan, T. Moriyama, S. Takahashi, H. Ogawa, Microwave Dielectric Properties of LiF- and $CaTiO_3$-Added MgO with Low Dielectric Loss and Near-Zero Temperature Coefficient of Resonant Frequency for Low-Temperature Cofired- Ceramic, Jpn. J. Appl. Phys. 01 (2012).

[30] S. Hao, S. Wu, Y. Hai-yang, Dielectric Properties of B_2O_3 Doped $MgTiO_3$-$CaTiO_3$ System Ceramics, J. Wuhan Univ. Technol. Mater. Sci. Ed. 19 (2004) 62–64.

[31] S. Singh Rajput, S. Keshri, V. Rani Gupta, N. Gupta, V. Bovtun, J. Petzelt, Design of microwave dielectric resonator antenna using MZTO – CSTO composite, Ceram. Int. 38 (2012) 2355–2362. https://doi.org/10.1016/j.ceramint.2011.10.088.

[32] W.W. Cho, K.I. Kakimoto, H. Ohsato, High-Q microwave dielectric $SrTiO_3$-doped $MgTiO_3$ materials with near-zero temperature coefficient of resonant frequency, Jpn. J. Appl. Phys. 43 (2004) 6221–6224. https://doi.org/10.1143/JJAP.43.6221.

[33] M.W. Cole, P.C. Joshi, M.H. Ervin, M.C. Wood, R.L. Pfeffer, Influence of Mg doping on the materials

properties of $Ba_{1-x}Sr_xTiO_3$ thin films for tunable device applications, Thin Solid Films. 374 (2000) 34–41. https://doi.org/10.1016/S0040-6090(00)01059-2.

[34] X. Chou, J. Zhai, X. Yao, Dielectric tunable properties of low dielectric constant

$Ba_{0.5}Sr_{0.5}TiO_3$ - Mg_2TiO_4 microwave composite ceramics, Appl. Phys. Lett. 91 (2007) 2005–2008. https://doi.org/10.1063/1.2784202.

[35] W. Chang, S.W. Kirchoefer, J.M. Pond, J.A. Bellotti, S.B. Qadri, J.H. Haeni, D.G. Schlom, Room-temperature tunable microwave properties of strained $SrTiO_3$ films, J. Appl. Phys. 96 (2004) 6629–6633. https://doi.org/10.1063/1.1813641.

[36] B. Su, T.W. Button, Microstructure and dielectric properties of Mg-doped barium strontium titanate ceramics, J. Appl. Phys. 95 (2004) 1382–1385. https://doi.org/10.1063/1.1636263.

[37] L. Tang, J. Wang, J. Zhai, B. Shen, X. Yao, Dielectric tunable properties of $Ba_{0.5}Sr_{0.5}TiO_3$-$MgMoO_4$ composite ceramics for microwave applications, J. Mater. Sci. Mater. Electron. 24 (2013) 2576–2580. https://doi.org/10.1007/s10854-013-1136-z.

[38] R. Schaller, Technological innovation in the semiconductor industry: A case study of the international technology roadmap for semiconductors (ITRS), Picmet. (2002) 195. https://doi.org/10.1109/picmet.2001.951917.

[39] K. Yim, Y. Yong, J. Lee, K. Lee, H. Nahm, J. Yoo, C. Lee, C.S. Hwang, S. Han, Novel high- κ dielectrics for next-generation electronic devices screened by automated ab initio calculations, (2015) 1–6. https://doi.org/10.1038/am.2015.57.

[40] U.O. Bhagwat, J.J. Wu, A.M. Asiri, S. Anandan, Synthesis of $MgTiO_3$ Nanoparticles for Photocatalytic Applications,Chemistry Select. 4 (2019) 788–796. https://doi.org/10.1002/slct.201803583.

[41] S. Ahn, Y. Lee, Y. Roh, S. Kang, J. Lee, Electrical characterizations of $MgTiO_3$ thin films grown on Si, Integr. Ferroelectr. 31 (2000) 359–366. https://doi.org/10.1080/10584580008215669.

[42] C.Y. Hsiao, C.F. Shih, C.H. Chien, C.L. Huang, Textured magnesium titanate as gate oxide for GaN-based metal-oxide-semiconductor capacitor, J. Am. Ceram. Soc. 94 (2011) 1005–1007. https://doi.org/10.1111/j.1551-2916.2011.04439.x.

[43] C.Y. Hsiao, C.F. Shih, C.H. Chien, C.L. Huang, MgTiO3 (003) thin film deposited on sapphire (0001) by sputtering, J. Am. Ceram. Soc. 94 (2011) 363–366. https://doi.org/10.1111/j.1551-2916.2010.04331.x.

[44] S. Rabha, A.K. Chikkala, P. Dobbidi, Structural and dielectric properties of (1- x) $MgTiO_3$ - x $Ba_5Nb_4O_{15}$ composites by microwave sintering process, Ferroelectrics. 519 (2017). https://doi.org/10.1080/00150193.2017.1361233.

[45] C.-L. Huang, C.-L. Pan, Structure and electrical properties of $MgTiO_3$ thin films deposited by rf magnetron sputtering, J. Vac. Sci. Technol. A Vacuum, Surfaces, Film. 22 (2004) 2440–2445. https://doi.org/10.1116/1.1810164.

[46] J.I. Marulanda, R.A.A. Lima, M.C.R. Carvalho, A.F.L. Almeida, A.B.S. Sombra, L.S. Demenicis, Characterization of dielectric properties of screen-printed $MgTiO_3$-$CaTiO_3$ composite thick films in the microwave frequency range, SBMO/IEEE MTT-S Int. Microw. Optoelectron. Conf. Proc. (2009) 211–214. https://doi.org/10.1109/IMOC.2009.5427598.

[47] *B.D. Lee, K.H. Yoon, E.S. Kim, T.H. Kim, Microwave dielectric properties of $CaTiO_3$ and $MgTiO_3$ thin films, Jpn. J. Appl. Phys. 42 (2003) 6158–6161. https://doi.org/10.1143/JJAP.42.6158.*

[48] *V.M. Ferreira, F. Azough, R. Freer, J.L. Baptista, The effect of Cr and La on $MgTiO_3$ and $MgTiO_3$–$CaTiO_3$ microwave dielectric ceramics V., J. Mater. Res. 12 (1997) 3293–3299. https://doi.org/10.1126/science.235.4784.9.*

[49] *Y. Bian, J. Zhai, Low dielectric loss $Ba_{0.6}Sr_{0.4}TiO_3$/ $MgTiO_3$ composite thin films prepared by a sol-gel process, J. Phys. Chem. Solids. (2014). https://doi.org/10.1016/j.jpcs.2014.02.002.*

[50] *C.H. Lee, I.T. Kim, S.J. Park, MOCVD of $Pb(Zr_xTi_{1-x})O_3$ thin films on $MgTiO_3$/Si substrates and their electrical properties, Integr. Ferroelectr. 12 (1996) 115–123. https://doi.org/10.1080/10584589608013054.*

[51] *L. Gao, J. Zhai, X. Yao, Z. Xu, $MgTiO_3$ and $Ba_{0.60}Sr_{0.40}Mg_{0.15}Ti_{0.85}O_3$ composite thin films with promising dielectric properties for tunable applications, J. Am. Ceram. Soc. 91 (2008) 3109–3112. https://doi.org/10.1111/j.1551-2916.2008.02569.x.*

[52] *S. Lu, Z. Xu, Effect of interlayer thickness on stress and dielectric properties of $MgTiO_3$ modified $(Ba,Sr)TiO_3$ multilayer thin films, Mater. Sci. Forum. 654–656 (2010) 1796–1799. https://doi.org/10.4028/www.scientific.net/MSF.654-656.1796.*

[53] *V.L. Gurevich, A.K. Tagantsev, Advances in Physics Intrinsic dielectric loss in crystals, Adv. Phys. 40 (1991) 719–767.*

[54] *H. Zhao, S. Feng, W. Xu, Y. Shi, Y. Mao, X. Zhu, A rapid chemical route to niobates: Hydrothermal synthesis and transport properties of ultrafine $Ba_5Nb_4O_{15}$, J. Mater. Chem. 10 (2000) 965–968. https://doi.org/10.1039/a909554c.*

[55] *H. Zhuang, Z. Yue, F. Zhao, J. Pei, L. Li, Microstructure and microwave dielectric properties of $Ba_5Nb_4O_{15}$-$BaWO_4$ composite ceramics, J. Alloys Compd. 472 (2009) 411–415. https://doi.org/10.1016/j.jallcom.2008.04.073.*

[56] *D.W. Kim, K.S. Hong, C.S. Yoon, C.K. Kim, Low-temperature sintering and microwave dielectric properties of $Ba_5Nb_4O_{15}$-$BaNb_2O_6$ mixtures for LTCC applications, J. Eur. Ceram. Soc. 23 (2003) 2597–2601. https://doi.org/10.1016/S0955-2219(03)00154-7.*

[57] *C. Anil Kumar, D. Pamu, Microwave dielectric properties of low temperature fired $Ba_5Nb_4O_{15}$ - $BaWO_4$ ceramics supplemented with their own nanoparticles for LTCC applications, Int. J. Appl. Ceram. Technol. 14 (2017) 191–199. https://doi.org/10.1111/ijac.12639.*

[58] *C. Anil Kumar, D. Pamu, Dielectric and Optical Characterization of RF Sputtered $Ba_5Nb_4O_{15}$ - $BaWO_4$ Composite Films for Electronic and Smart Window Applications, J. Electron. Mater. 45 (2016) 3101–3112. https://doi.org/10.1007/s11664-016-4406-8.*

[59] *S.-J.L. Kang, Sintering: densification, grain growth and microstructure, Elsevier, 2004.*

[60] *L.B. Mccusker, R.B. Von Dreele, D.E. Cox, D. Louër, P. Scardi, Rietveld refinement guidelines, J. Appl. Crystallogr. 32 (1999) 36–50. https://doi.org/10.1107/S0021889898009856.*

[61] *E. Smith, G. Dent, Modern Raman spectroscopy: a practical approach, John Wiley & Sons, England, Chichester, 2005.*

[62] *R. Singh, CV Raman and the Discovery of the Raman Effect, Phys. Perspect. 4 (2002) 399–420.*

[63] *A.W. Varnes, F.A. Settle, Inductively coupled plasma mass spectrometry, Handb. Instrum. Tech. Anal.*

Chem. Up. Saddle River, New Jersey, Prentice Hall. (1997) 419–439.

[64] I. Horcas, R. Fernández, J.M. Gómez-Rodríguez, J. Colchero, J. Gómez-Herrero, A.M. Baro, WSXM: A software for scanning probe microscopy and a tool for nanotechnology, Rev. Sci. Instrum. 78 (2007) 13705. https://doi.org/10.1063/1.2432410.

[65] R. Swanepoel, Determination of the thickness and optical constants of amorphous silicon, J. Sci. Instrum. 16 (1983) 1215–1222.

[66] B.G. Bagley, R. Grigorovici, E.N. Economou, M.H. Cohen, K.F. Kirkpatrick, M.H. Freed, E.M. Kirkpatrick, J. Tauc, H. Fritzsche, J.E. Enderby, Amorphous and Liquid Semiconductors., 1973. https://doi.org/10.1080/715120893.

[67] M.T. Sebastian, Dielectric Materials for Wireless Communication, Elsevier, 2008.

[68] B. W. Hakki and P. D. Coleman, A Dielectric Resonator Method of Measuring Inductive Capacities in the Millimeter Range. IEEE Trans. Microwave Theory Technol. 8(1960)402-410..pdf, (n.d.).

[69] B. W. Hakki, P.D. Coleman, A Dielectric Resonator Method of Measuring Inductive Capacities.pdf, IRE Trans. Microw. THEORY Tech. 8 (1960) 402–410.

[70] J. Krupka, K. Derzakowski, B. Riddle, J. Baker-Jarvis, A dielectric resonator for measurements of complex permittivity of low loss dielectric materials as a function of temperature, Meas. Sci. Technol. 9 (1998) 1751–1756. https://doi.org/10.1088/0957-0233/9/10/015.

[71] N. Kumar, M.P. Singh, Telecom Regulatory Authority of India, New Dimens. Fed. Discourse India. (2016) 60–78. https://doi.org/10.4324/9781003032663-5.

[72] B.A. Wechsler, R.B. Von Dreele, Structure refinements of Mg_2TiO_4, $MgTiO_3$ and $MgTi_2O_5$ by time-of-flight neutron powder diffraction, Acta Crystallogr. Sect. B. 45 (1989) 542–549. https://doi.org/10.1107/S010876818900786X.

[73] C. Vineis, P.K. Davies, T. Negas, S. Bell, Microwave dielectric properties of hexagonal perovskites, Mater. Res. Bull. 31 (1996) 431–437. https://doi.org/10.1016/S0025-5408(96)00028-1.

[74] T.S. Kumar, A. Kumar, A.R. James, D. Pamu, Enhanced Microwave Dielectric Properties of $MgTiO_3$ Ceramics Prepared by Mechanochemical Method Enhanced Microwave Dielectric Properties of $MgTiO_3$ Ceramics Prepared by Mechanochemical Method, (2016).

[75] T.S. Kumar, P. Gogoi, A. Perumal, P. Sharma, P. Dobbidi, Effect of Cobalt Doping on the Structural, Microstructure and Microwave Dielectric Properties of $MgTiO_3$ Ceramics Prepared by Semi Alkoxide Precursor Method, J. Am. Ceram. Soc. (2014) 1–6. https://doi.org/10.1111/jace.12851.

[76] M. Oghbaei, O. Mirzaee, Microwave versus conventional sintering: A review of fundamentals, advantages and applications, J. Alloys Compd. 494 (2010) 175–189. https://doi.org/10.1016/j.jallcom.2010.01.068.

[77] R.K. Bhuyan, T. Santhosh Kumar, D. Pamu, J.M. Renehan, M. V. Jacob, Low temperature and broadband dielectric properties of V_2O_5 doped Mg_2TiO_4 ceramics, Mater. Express. 4 (2014) 349–358. https://doi.org/10.1166/mex.2014.1182.

[78] C. Wang, X. Jing, W. Feng, J. Lu, Assignment of Raman-active vibrational modes of $MgTiO_3$, J. Appl. Phys. 104 (2008) 034112. https://doi.org/10.1063/1.2966717.

[79] N.E. Massa, S. Pagola, R. Carbonio, Far-infrared reflectivity and Raman spectra, Phys. Rev. B - Condens. Matter Mater. Phys. 53 (1996) 8148–8150. https://doi.org/10.1103/PhysRevB.53.8148.

[80] Suk-Joong L. Kang, Sintering, First, Elsevier, Book Aid International and Sabre Foundation, 2005.

[81] M. Ohring, Materials science of thin films: deposition and structure, 2002.

[82] T. Santhosh Kumar, R.K. Bhuyan, D. Pamu, Effect of post annealing on structural, optical and dielectric properties of $MgTiO_3$ thin films deposited by RF magnetron sputtering, Appl. Surf. Sci. 264 (2013) 184–190. https://doi.org/10.1016/j.apsusc.2012.09.168.

[83] C.A. Kumar, D. Pamu, Dielectric , optical and electric studies on nanocrystalline

Ba_5 Nb_4O_{15} thin films deposited by RF magnetron sputtering, Appl. Surf. Sci. 340 (2015) 56–63. https://doi.org/10.1016/j.apsusc.2015.02.172.

[84] T.S. Kumar, P. Gogoi, S. Bhasaiah, K.C. James Raju, D. Pamu, Structural, optical and microwave dielectric studies of Co doped $MgTiO_3$ thin films fabricated by RF magnetron sputtering, Mater. Res. Express. 2 (2015) 056403. https://doi.org/10.1088/2053-1591/2/5/056403.

[85] M. DiDomenico Jr, S.H. Wemple, Oxygen-Octahedra Ferroelectrics . I . Theory of Electro-optical and Nonlinear optical Effects, J. Appl. Phys. 40 (1998) 720. https://doi.org/10.1063/1.1657458.

[86] F. Yakuphanoglu, A. Cokurovali, I. Yilmaz, Single-oscillator model and determination of optical constants of some optical thin film materials, Phys. B. 353 (2004) 210–216. https://doi.org/10.1016/j.physb.2004.09.097.

[87] P. Khatri, B. Behera, V. Srinivas, R.N.P. Choudhary, Complex Impedance Spectroscopic Properties of $Ba_3V_2O_8$ Ceramics, Res. Lett. Mater. Sci. 2008 (2008) 1–5. https://doi.org/10.1155/2008/746256.

[88] J. Plocharski and W. Wieczorek, PEO based composite solid electrolyte containing nasicon, Solid State Ionics. 28–30 (1988) 979–982.

[89] B. Tiwari, R.N.P. Choudhary, Study of Impedance Parameters of Cerium Modified Lead Zirconate Titanate Ceramics, IEEE Transcations Dielectr. Electr. Insul. 17 (2010) 5–17.

[90] B. Behera, P. Nayak, R.N.P. Choudhary,Impedance spectroscopy study of $NaBa_2V_5O_{15}$ ceramic, 436 (2007) 226–232. https://doi.org/10.1016/j.jallcom.2006.07.028.

[91] U. Intatha, S. Eitssayeam, J. Wang, T. Tunkasiri, Impedance study of giant dielectric permittivity in $BaFe_{0.5}Nb_{0.5}O_3$ perovskite ceramic, Curr. Appl. Phys. 10 (2010) 21–25. https://doi.org/10.1016/j.cap.2009.04.006.

[92] B. Tang, S. Zhang, X. Zhou, C. Deng, S. Yu, Preparation of pure MgTiO 3 powders and the effect of the $ZnNb_2O_6$ -dope onto the property of $MgTiO_3$ -based ceramics, J. Alloys Compd. 492 (2010) 461–465. https://doi.org/10.1016/j.jallcom.2009.11.140.

[93] L. Zhang, J. Zhou, Z. Wang, D. Davidovi, A single electric relaxation time in Ba_{1-x} $SrxTiO_3$ nanoparticles at low temperatures, Nanotechnology. 18 (2007) 135707. https://doi.org/10.1088/0957-4484/18/13/135707.

[94] A.S. Nowick, B. S. Lim, Analysis of ac conductivity data for Na_20 $3SiO_2$ glass by stretched exponential and Jonscher power-law methods, J. Non-CrystaUine Solids. 172–174 (1994) 1389–1394.

[95] A.K. Jonscher, Analysis of the alternating current properties of ionic conductors, J. Mater. Sci. 13 (1978) 553–562.

[96] W. Almond, D. P., Ducan, G.K., The determination of hopping rates and carrier concentrations in ionic conductors by a new analysis of ac conductivity, Solid State Ionics. 8 (1983) 159–164.

[97] S. Nasri, A. Oueslati, I. Chaabane, M. Gargouri, AC conductivity , electric modulus analysis and

electrical conduction mechanism of $RbFeP_2O_7$ ceramic compound, Ceram. Int. 42 (2016) 14041–14048. https://doi.org/10.1016/j.ceramint.2016.06.011.

[98] A. Ghosh, Frequency-dependent conductivity in bismuth-vanadate glassy semiconductors, Phys. Rev. B. 41 (1990) 1479–1488.

[99] M.F. Kotkata, F.A. Abdel- Wahab, Investigations of the conduction mechanism and relaxation properties of semiconductor Sm doped a-Se films, J. Phys. D. Appl. Phys. 39 (2006) 2059–2066. https://doi.org/10.1088/0022-3727/39/10/013.

[100] M. Dult, R.S. Kundu, S. Murugavel, R. Punia, N. Kishore, Conduction mechanism in bismuth silicate glasses containing titanium, Phys. B Phys. Condens. Matter. 452 (2014) 102–107. https://doi.org/10.1016/j.physb.2014.07.004.

[101] S. Punia, R, Kundu, R. S., Dult,Meenakshi, Murugavel, N. Kishore, Temperature and Frequency Dependent Conductivity of Bismuth Zinc Vanadate Semiconducting Glassy System, J. Appl. Phys. 112 (2012) 083701. https://doi.org/10.1063/1.4759356.

[102] H. Cheng, B. Xu, J. Ma, Preparation of $MgTiO_3$ by an improved chemical co-precipitation method, J. Mater. Sci. Lett. 16 (1997) 1570–1572.

[103] V.M. Ferreira, J.L. Baptism, Preparation and microwave dielectric properties of pure and doped magnesium titanate., Mater. Res. Bull. 29 (1994) 1017–1023.

[104] M.T. Sebastian, R. Ubic, H. Jantunen, Low-loss dielectric ceramic materials and their properties, Int. Mater. Rev. 60 (7) (2015) 392–412. https://doi.org/10.1179/1743280415Y.0000000007.

[105] Z. Liu, J. Lu, Y. Mao, P. Ren, H. Fan, Energy storage properties of $NaNbO_3$-$CaZrO_3$ ceramics with coexistence of ferroelectric and antiferroelectric phases, J. Eur. Ceram. Soc. 38 (2018) 4939–4945. https://doi.org/10.1016/j.jeurceramsoc.2018.07.029.

[106] Z. Liu, H. Fan, J. Lu, Y. Mao, Y. Zhao, Tailored dielectric tunability of alkali niobate-based antiferroelectric/relaxor-ferroelectric composites, J. Eur. Ceram. Soc. 38 (2018) 2871–2878. https://doi.org/10.1016/j.jeurceramsoc.2018.02.026.

[107] S. Rabha, P. Dobbidi, Structural , electrical and dielectric studies on $(1-x)\,MgTiO_3 - xBa_{0.5}Sr_{0.5}TiO_3$ composite ceramics for type-II capacitor applications, J. Mater. Sci. Mater. Electron. 30 (2019) 5327–5341. https://doi.org/10.1007/s10854-019-00875-3.

[108] R.K. Bhuyan, T. Santhosh Kumar, A. Perumal, S. Ravi, D. Pamu, Optical properties of ambient temperature grown nanocrystalline Mg_2TiO_4 thin films, Surf. Coatings Technol. 221 (2013) 196–200. https://doi.org/10.1016/j.surfcoat.2013.01.048.

[109] M. Liu, H. Zhu, Y. Zhang, C. Xue, J. Ouyang, Energy storage characteristics of $BiFeO_3$/$BaTiO_3$ Bi-layers integrated on Si, Materials (Basel). 9 (2016). https://doi.org/10.3390/ma9110935.

[110] S. Yoon, A.E. Maegli, L. Karvonen, S.K. Matam, A. Shkabko, S. Riegg, T. Großmann, S.G. Ebbinghaus, S. Pokrant, A. Weidenkaff, Bandgap tuning in $SrTi(N,O,F)_3$ by anionic-lattice variation, J. Solid State Chem. 206 (2013) 226–232. https://doi.org/10.1016/j.jssc.2013.08.001.

[111] E.A.V. Ferri, J.C. Sczancoski, L.S. Cavalcante, E.C. Paris, J.W.M. Espinosa, A.T. de Figueiredo, P.S. Pizani, V.R. Mastelaro, J.A. Varela, E. Longo, Photoluminescence behavior in $MgTiO_3$ powders with vacancy/distorted clusters and octahedral tilting, Mater. Chem. Phys. 117 (2009) 192–198. https://doi.org/10.1016/j.matchemphys.2009.05.042.

[112] *S. Dagar, A. Hooda, K. Satish, M. Malik, Structural refinement, investigation af dielectric and magnetic properties of NBT doped $BaFe_{12}O_{19}$ novel composite system., J. Alloys Compd. 826 (2020) 154214.*

[113] *B. Reynard, F. Guyot, High-Temperature Properties of Geikielite ($MgTiO_3$-Ilmenite) from High-Temperature High-Pressure Raman Spectroscopy- Some Implications for $MgSiO_3$-Ilmenite, Phys. Chem. Miner. 21 (1994) 441–450.*

[114] *S. Rabha, P. Dobbidi, The impact of thickness on the optical, electrical and dielectric properties of nanocrystalline 0.9 MTO-0.1BNO composite thin films, Appl. Surf. Sci. 489 (2019) 831–840. https://doi.org/10.1016/j.apsusc.2019.05.339.*

[115] *T. Luo, X. Shan, J. Zhao, H. Feng, Q. Zhang, H. Yu, J. Liu, Improvement of quality factor of $SrTiO_3$ dielectric ceramics with high dielectric constant using $Sm_2 O_3$, J. Am. Ceram. Soc. 102 (2019) 3849–3853. https://doi.org/10.1111/jace.16415.*

[116] *D.A. Tenne, A.K. Farrar, C.M. Brooks, T. Heeg, J. Schubert, H.W. Jang, C.W. Bark, C.M. Folkman, C.B. Eom, D.G. Schlom, Ferroelectricity in nonstoichiometric $SrTiO_3$ films studied by ultraviolet Raman spectroscopy, Appl. Phys. Lett. 97 (2010). https://doi.org/10.1063/1.3499273.*

[117] *Z. Wang, V. Kugler, U. Helmersson, N. Konofaos, E.K. Evangelou, S. Nakao, P. Jin, Electrical properties of $SrTiO_3$ thin films on Si deposited by magnetron sputtering at low temperature, Appl. Phys. Lett. 79 (2001) 1513–1515. https://doi.org/10.1063/1.1398321.*

[118] *R.K. Bhuyan, R.K. Mohapatra, G. Nath, B.K. Sahoo, D. Das, D. Pamu, Influence of high-energy ball milling on structural, microstructural, and optical properties of Mg_2TiO_4 nanoparticles, J. Mater. Sci. Mater. Electron. 31 (2020) 628–636. https://doi.org/10.1007/s10854-019-02568-3.*

[119] *S. Ke, P. Lin, H. Fan, H. Huang, X. Zeng, Variable-range-hopping conductivity in high-k $Ba(Fe_{0.5}Nb_{0.5})O_3$ ceramics, J. Appl. Phys. 114 (2013) 104106–104113. https://doi.org/10.1063/1.4821042.*

[120] *S. Pattipaka, A.R. James, P. Dobbidi, Enhanced dielectric and piezoelectric properties of BNT-KNNG piezoelectric ceramics, J. Alloys Compd. 765 (2018) 1195–1208. https://doi.org/10.1016/j.jallcom.2018.06.138.*

[121] *M.Z. Ansari, N. Khare, Thermally activated band conduction and variable range hopping conduction in Cu_2ZnSnS_4 thin films., 025706 (2015). https://doi.org/10.1063/1.4905673.*

[122] *R. Cao, X. Cheng, F. Zhang, L. Su, T. Chen, H. Ao, X. Yu, W. Ruan, Enhanced luminescence properties of $MgTO_3$:Mn^{4+} red-emitting phosphor by adding Ge^{4+} ion and H_3BO_3, J. Mater. Sci. Mater. Electron. 29 (2018) 13005–13010. https://doi.org/10.1007/s10854-018-9421-5.*

[123] *S. Nakamura, M. Senoh, N. Iwasa, S.I. Nagahama, High-power InGaN single-quantum-well-structure blue and violet light-emitting diodes, Appl. Phys. Lett. 67 (1995) 1868. https://doi.org/10.1063/1.114359.*

[124] *S. Rabha, P. Dobbidi, The impact of thickness on the optical, electrical and dielectric properties of nanocrystalline 0.9 MTO-0.1BNO composite thin films, Appl. Surf. Sci. 489 (2019). https://doi.org/10.1016/j.apsusc.2019.05.339.*

[125] *E.A.V. Ferri, T.M. Mazzo, V.M. Longo, E. Moraes, P.S. Pizani, M.S. Li, J.W.M. Espinosa, J.A. Varela, E. Longo, Very intense distinct blue and red photoluminescence emission in $MgTiO_3$ thin films prepared by the polymeric precursor method: An experimental and theoretical approach, J. Phys. Chem. C.*

(2012). https://doi.org/10.1021/jp3021535.

[126] K. Van Benthem, C. Elsässer, R.H. French, Bulk electronic structure of $SrTiO_3$: Experiment and theory, J. Appl. Phys. 90 (2001) 6156–6164. https://doi.org/10.1063/1.1415766.

[127] D. O'Neill, R.M. Bowman, J.M. Gregg, Dielectric enhancement and Maxwell-Wagner effects in ferroelectric superlattice structures, Appl. Phys. Lett. 77 (2000) 1520–1522. https://doi.org/10.1063/1.1290691.

[128] T.S. Kumar, R.K. Bhuyan, A. Perumal, D. Pamu, Effect of process parameters and post annealing temperature on structural and optical properties of $MgTiO_3$thin films deposited by rf magnetron sputtering, in: Springer Proc. Phys., 2013. https://doi.org/10.1007/978-3-642-34216-5_30.

[129] F.M. Pontes, E.J.H. Lee, E.R. Leite, E. Longo, J.A. Varela, High dielectric constant of $SrTiO_3$ thin films prepared by chemical process, J. Mater. Sci. 35 (2000) 4783–4787. https://doi.org/10.1023/A:1004816611050.

[130] S. Dussan, A. Kumar, J.F. Scott, R.S. Katiyar, Effect of electrode resistance on dielectric and transport properties of multiferroic superlattice: A Impedance spectroscopy study, AIP Adv. 2 (2012) 0–11. https://doi.org/10.1063/1.4746026.

[131] B. Nagaraj, S. Aggarwal, T.K. Song, T. Sawhney, R. Ramesh, Leakage current mechanisms in lead-based thin-film ferroelectric capacitors, Phys. Rev. B - Condens. Matter Mater. Phys. 59 (1999) 16022–16027. https://doi.org/10.1103/PhysRevB.59.16022.

[132] M. Abazari, A. Safari, Leakage current behavior in lead-free ferroelectric (K,Na)NbO_3-$LiTaO_3$-$LiSbO_3$ thin films, Appl. Phys. Lett. 97 (2010) 262902. https://doi.org/10.1063/1.3531575.

[133] L.C. Sengupta, S. Sengupta, Novel ferroelectric materials for phased array antennas, IEEE Trans. Ultrason. Ferroelectr. Freq. Control. 44 (1997) 792–797. https://doi.org/10.1109/58.655193.

[134] S.S. Gevorgian, E.L. Kollberg, Do we really need ferroelectrics in paraelectric phase only in electrically controlled microwave devices?, IEEE Trans. Microw. Theory Tech. 49 (2001) 2117–2124. https://doi.org/10.1109/22.963146.

[135] L.C. Sengupta, S. Sengupta, Breakthrough advances in low loss, tunable dielectric materials, Mater. Res. Innov. 2 (1999) 278–282. https://doi.org/10.1007/s100190050098.

[136] S. Ke, H. Fan, W. Wang, G. Jiao, H. Huang, H.L.W. Chan, $MgTiO_3$ doping effect on dielectric properties of $Ba_{0.6}Sr_{0.4}TiO_3$ ceramics via a molten salt process, Compos. Part A Appl. Sci. Manuf. 39 (2008) 597–601. https://doi.org/10.1016/j.compositesa.2007.08.013.

[137] I.C. Noyan, T.C. Huang, B.R. York, Residual stress / strain analysis in thin films by X- ray diffraction, Crit. Rev. Solid State Mater. Sci. 20 (1995) 125–177. https://doi.org/10.1080/10408439508243733.

[138] S. Ge, Z. Ning, Z. Dong, M. Shen, Investigation on dielectric properties of polycrystalline BT/ST multilayer thin films, J. Phys. D. Appl. Phys. 35 (2002) 906–909. https://doi.org/10.1088/0022-3727/35/9/311.

[139] M. Kahn, C. Vallée, E. Defay, C. Dubourdieu, M. Bonvalot, S. Blonkowski, J.R. Plaussu, P. Garrec, T. Baron, Improved electrical properties using $SrTiO_3/Y_2O_3$ bilayer dielectrics for MIM capacitor applications, Microelectron. Reliab. 47 (2007) 773–776. https://doi.org/10.1016/j.microrel.2007.01.029.

[140] B. Forg, C. Richter, J. Mannhart, Field -effect devices utilizing $LaAlO_3$-$SrTiO_3$ interfaces, Appl. Phys.

Lett. 100 (2012) 053506.

[141] D. Hirai, J. Matsuno, H. Takagi, Fabrication of (111)-oriented $Ca_{0.5}Sr_{0.5}IrO_3/SrTiO_3$ superlattices - A designed playground for honeycomb physics, APL Mater. 3 (2015) 0–6. https://doi.org/10.1063/1.4913389.

[142] C.Y. Hsiao, C.F. Shih, C.H. Chien, C.L. Huang, Textured magnesium titanate as gate oxide for GaN-based metal-oxide-semiconductor capacitor, J. Am. Ceram. Soc. 94 (2011) 1005–1007. https://doi.org/10.1111/j.1551-2916.2011.04439.x.

[143] J. Bernard, D. Houivet, J. El Fallah, J.M. Haussonne, $MgTiO_3$ for Cu base metal multilayer ceramic capacitors, 24 (2004) 1877–1881. https://doi.org/10.1016/S0955-2219(03)00461-8.

[144] P. Gogoi, P. Sharma, Microwave and broadband dielectric properties of Ni substituted, J. Mater. Sci. Mater. Electron. (2016). https://doi.org/10.1007/s10854-016-4938-y.

[145] P.S. Sahoo, A. Panigrahi, S.K. Patri, R.N.P. Choudhary, Impedance and modulus spectroscopy studies of $Ba_4SrSmTi_3V_7O_{30}$ ceramics, Mater. Sci. Pol. 28 (2010).

[146] P. Barnes, S. Jacques, M. Vickers, Crystallite Size and Strain, Birkbeck Coll. Univ. London. (2012) 3–5. http://pd.chem.ucl.ac.uk/pdnn/peaks/size.htm.

[147] M. Osada, M. Kakihana, S. Wada, T. Noma, W.S. Cho, Broken symmetry in low-temperature $BaTiO_3$ phases: Strain effects probed by Raman scattering, Appl. Phys. Lett. 75 (1999) 3393–3395. https://doi.org/10.1063/1.125304.

[148] H. Zheng, G.D.C. Csete de Györgyfalva, R. Quimby, H. Bagshaw, R. Ubic, I.M. Reaney, J. Yarwood, Raman spectroscopy of B-site order-disorder in $CaTiO_3$-based microwave ceramics, J. Eur. Ceram. Soc. 23 (2003) 2653–2659. https://doi.org/10.1016/S0955-2219(03)00149-3.

[149] J. Zhang, J. Zhai, H. Jiang, X. Yao, Raman and dielectric study of $Ba_{0.4}$ $Sr_{0.6}$ TiO_3 - $MgAl_2$ O_4 tunable microwave composite, J. Appl. Phys. 104 (2008). https://doi.org/10.1063/1.3000057.

[150] D.C. Harris, M.D. Bertolucci, Symmetry and spectroscopy: An introduction to vibrational and electronical spectroscopy, 1978.

[151] Z. Cheng, X. Wang, S. Dou, H. Kimura, K. Ozawa, Improved ferroelectric properties in multiferroic $BiFeO_3$ thin films through La and Nb codoping, Phys. Rev. B - Condens. Matter Mater. Phys. 77 (2008) 1–4. https://doi.org/10.1103/PhysRevB.77.092101.

[152] J. Sun, X. Chou, J. Zhai, X. Yao, Dielectric and tunable properties of $Ba_{0.6}Sr_{0.4}TiO_3$-Mg_2TiO_4 composite ceramics for phase shifter applications, Ferroelectrics. 356 (2007) 128–133. https://doi.org/10.1080/00150190701511625.

[153] V. V. Shvartsman, D.C. Lupascu, Lead-free relaxor ferroelectrics, J. Am. Ceram. Soc. 95 (2012) 1–26. https://doi.org/10.1111/j.1551-2916.2011.04952.x.

[154] T. Miruszewski, B. Trawiński, M. Gałka, J. Morzy, B. Bochentyn, J. Karczewski, P. Gdaniec, M. Gazda, B. Kusz, Correlation between structural and electrical properties in highly porous $(Y,Sr)(Ti,Nb)O_{3-\delta}$ SOFC anodes, Mater. Sci. Pol. 32 (2014) 331–340. https://doi.org/10.2478/s13536-014-0210-4.

[155] K. Kumar, B. Kumar, Ceramics International 38 (2012) 1157–1165

Effect of Nb-doping on dielectric, ferroelectric and conduction behaviour of lead free $Bi_{0.5}(Na_{0.5}K_{0.5})_{0.5}TiO_3$ ceramic, Ceram. Int. 38 (2012) 1157–1165. https://doi.org/10.1016/j.ceramint.2011.08.045.

[156] G. Singh, V.S. Tiwari, P.K. Gupta, Role of oxygen vacancies on relaxation and conduction behavior of

$KNbO_3$ ceramic, J. Appl. Phys. 107 (2010). https://doi.org/10.1063/1.3309745.

[157] B. Tiwari, R.N.P. Choudhary, Frequency-temperature response of $Pb(Zr_{0.65-x}Ce_xTi_{0.35})O_3$ ferroelectric ceramics: Impedance spectroscopic studies, J. Alloys Compd. 493 (2010) 1–10. https://doi.org/10.1016/j.jallcom.2009.11.120.

[158] and X.-X.H. Tian-Fu Zhang, Xin-Gui Tang,† Qiu-Xiang Liu, Yan-Ping Jiang, Oxygen-Vacancy-Related High Temperature Dielectric Relaxation in $(Pb_{1-x}Ba_x)ZrO_3$ Ceramics, J. Am. Ceram. Soc. (2014) 1–8. https://doi.org/DOI: 10.1111/jace.13317.

[159] T.F. Zhang, X.G. Tang, Q.X. Liu, S.G. Lu, Y.P. Jiang, X.X. Huang, Q.F. Zhou, Oxygen-vacancy-related relaxation and conduction behavior in $(Pb_{1-x}Ba_x)$ $(Zr_{0.95}Ti_{0.05})O_3$ ceramics, AIP Adv. 4 (2014) 0–11. https://doi.org/10.1063/1.4900610.

[160] J.M. Le Meins, O. Bohnke, G. Courbion, Ionic conductivity of crystalline and amorphous $Na_3Al_2(PO_4)_2F_3$, Solid State Ionics. 111 (1998) 67–75. https://doi.org/10.1016/s0167-2738(98)00169-6.

[161] S.H. Chung, K.R. Jeffrey, J.R. Stevens, L. Borjesson, Dynamics of silver ions in $(AgI)_x$-$(Ag_2O_{-n}B_2O_3)_{1-x}$ glasses: A109 Ag nuclear magnetic resonance study glass, Phys. Rev. B. 41 (1990) 6154–6164.

[162] R. Dridi, I. Saafi, A. Mhamdi, A. Matri, A. Yumak, M. Haj Lakhdar, A. Amlouk, K. Boubaker, M. Amlouk, Structural, optical and AC conductivity studies on alloy ZnO-Zn_2SnO_4 (ZnO-ZTO) thin films, J. Alloys Compd. 634 (2015) 179–186. https://doi.org/10.1016/j.jallcom.2015.02.009.

[163] A.A.A. Youssef, The Permittivity and AC Conductivity of the Layered Perovskite $[(CH_3)(C_6H_5)_3P]_2HgI_4$, Zeitschrift Fur Naturforsch. - Sect. A J. Phys. Sci. 57 (2002) 263–269. https://doi.org/10.1515/zna-2002-0510.

[164] Calramic technolgies LLC, The effect of temperature and voltage changes on high voltage ceramic capacitors. www.voltagemultiplers.com

[165] J.M.A.R.K. K. Aite, J. Holleman, The relatisonship between intrinsic stress of silicon nitride films and in generation in a 50 kHz RF discharge, Mater. Res. Soc. 130 (1989) 347–353.

[166] R.N.P.C. Subrat K. Barik, A.K. Singh, Ac impedance spectroscopy and conductivity studies of $Ba_{0.8}Sr_{0.2}TiO_3$ ceramics, Adv. Mater. Lett. 2 (2011) 419–424. https://doi.org/10.5185/amlett.2011.2228.

[167] A. Sasmal, A. Patra, P.S. Devi, S. Sen, Space charge induced augmented dielectric permittivity and improved energy harvesting ability of nano-Ag decorated $ZnSnO_3$ filled PVDF based flexible nanogenerator, Compos. Sci. Technol. 213 (2021) 108916. https://doi.org/10.1016/j.compscitech.2021.108916.

[168] S.K. Sahoo, D. Misra, M. Sahoo, C.A. MacDonald, H. Bakhru, D.C. Agrawal, Y.N. Mohapatra, S.B. Majumder, R.S. Katiyar, Improved dielectric properties and their temperature insensitivity in multilayered $Ba_{0.8}Sr_{0.2}TiO_3/ZrO_2$ thin films, J. Appl. Phys. 109 (2011) 0–6. https://doi.org/10.1063/1.3563576.

[169] S. Narayanan, A.K. Baral, V. Thangadurai, Dielectric characteristics of fast Li ion conducting garnet-type $Li^{5+}2xLa_3Nb_{2-x}Y_xO_{12}$ (x = 0.25, 0.5 and 0.75), Phys. Chem. Chem. Phys. 18 (2016) 15418–15426. https://doi.org/10.1039/c6cp02287a.

[170] M. Ohring, Materials science of thin films deposition and structure, Elsevier, n.d.

[171] G. Zhang, W. Hao, C. Chen, T. Wang, J. Yue, C. Liu, Transparent and flexible capacitors based on nanoaminate $Al_2O_3/TiO_2/Al_2O_3$, Nanoscale Res. Lett. 10 (2015) 76.